

Journal of Electrochemical Science and Engineering

J. Electrochem. Sci. Eng. **15(1)** 2025

Special Issue dedicated to

9th Regional Symposium on Electrochemistry – South East Europe





Open Access : : ISSN 1847-9286

www.jESE-online.org

Editorial

The 9th Regional Symposium on Electrochemistry - South East Europe

Branimir N. Grgur^{1,⊠} and Igor A. Pašti²

¹University of Belgrade - Faculty of Technology and Metallurgy, Department of Physical Chemistry and Electrochemistry, Karnegijeva 4, 11020 Belgrade, Serbia

²University of Belgrade – Faculty of Physical Chemistry, Studentski trg 12-16, 11158 Belgrade, Serbia

Corresponding author: [™] bngrgur@tmf.bg.ac.rs; Tel.: +381-11-330-3681

Received: February 26, 2025; Published: February 27, 2025

The 9th Symposium on Electrochemistry - South East Europe (RSE-SEE 9) was held from June 3 to June 7, 2024, in Novi Sad, the second-largest city in Serbia and the capital of Vojvodina Province. The Symposium took place at the University of Novi Sad, in the Rectorate building, within the university's green campus near the Danube. It gathered electrochemists from the region to discuss recent research and developments in the field. The Electrochemical Division of the Serbian Chemical Society and the Faculty of Technology, University of Novi Sad, organized the event.

The RSE-SEE 9 featured a total of 140 presentations, including 57 oral presentations (44 excluding student contributions), 5 plenary talks, 17 keynote lectures, and 61 posters. The program covered various areas of electrochemistry, with the largest number of contributions in electrocatalysis, which included 2 plenary talks, 2 keynote lectures, 12 oral presentations, and 14 posters. Corrosion and corrosion prevention was another major topic, with 1 keynote lecture, 6 oral presentations, and 6 poster. Electrochemical energy storage was represented by 5 keynote, lectures, 2 oral presentations, and 12 posters. Electrochemistry for environmental applications included 5 oral and 9 poster presentations, while the electrochemistry of new materials had 1 keynote lecture, 4 oral along with 4 poster presentations. Other topics, such as analytical electrochemistry, electrodeposition, interfaces, organic and bioelectrochemistry, and nanoscale electrochemistry, were also well represented.

The Symposium gathered 153 participants from 26 countries across all continents except Australia. The event was supported by four sponsors and included three exhibitors. Additionally, it received funding from the Ministry of Science, Technological Development and Innovations of Republic of Serbia and the Vojvodina Provincial Secretariat.

This special issue of Journal of Electrochemical Science and Engineering brings together full papers based on presentations given at RSE-SEE 9. It includes eleven contributions, comprising two review articles and nine full-length research papers. Covering various areas of electrochemistry, this collection highlights some of the key findings presented at the symposium. The guest editors would like to extend their gratitude to all the authors who contributed to this special issue, which we hope

will further enhance the impact of electrochemistry research in South East Europe and make it more visible to the worldwide community.



Figure 1. Joint photograph of the Symposium participants, taken on June 3rd, 2024.

Given the importance of electrochemistry in modern society, particularly in energy, environmental protection, and the development of new materials, the 9th Symposium on Electrochemistry - South East Europe provided a platform for knowledge exchange and fostered scientific collaboration among researchers from around the world. The next, 10th RSE-SEE, will be held in 2026 in Prague, Czech Republic, continuing the tradition of bringing together experts to discuss the latest advancements and future directions in electrochemical research.



Open Access : : ISSN 1847-9286

www.jESE-online.org

Review

Beyond current frontiers of electrocatalysis

Aleksandar R. Zeradjanin[™]

Max Planck Institute for Chemical Energy Conversion, Stiftstrasse 34-36, Mülheim an der Ruhr, Germany

 $Corresponding \ authors: {}^{\boxtimes}\underline{aleksandar.zeradjanin@cec.mpg.de}; \ \ Tel.: +49-(0)208-306-3726;$

Fax: +49-(0)208-306-3951

Received: December 26, 2024; Accepted: January 10, 2025; Published: January 17, 2025

Abstract

One of the key reasons why the transition to renewable energy sources is progressing slowly is the low efficiency of processes at electrified interfaces where electricity is converted and stored as chemical energy. The challenge behind low efficiency is sluggish electrochemical conversion reactions. To resolve low efficiency, it is necessary to comprehend the intrinsic reasons behind the unusually complex phenomena of converting electrical energy into chemical energy, and vice versa, chemical energy into electrical energy. An important example is the electrolysis of water, where, after decades of research, it is not clear how to significantly accelerate the processes of hydrogen and oxygen generation. Of critical importance for the control of the water electrolysis mechanism is understanding the origins of the electrocatalytic activity. If we ask a key question from a conceptual point of view, namely: what are the origins of electrocatalytic activity? The answer will be, in most cases, as it was 70 years ago. Namely, the paradigm of electrocatalysis is the Sabatier principle, which suggests optimal ("not too strong, not too weak") binding of intermediates as the main prerequisite for a high reaction rate. Conventional wisdom suggests that confirmation of this should be a linear relationship between the adsorption energy of the intermediate and the activation energy, known as the Brønsted-Evans-Polanyi relation. However, recent results show that lowering the activation energy is not necessarily beneficial for increasing the reaction rate. In this work, some fundamentally important questions about the nature of electrocatalytic activity will be raised. Identifying and analyzing these issues can be an important trigger and driver towards efficient water electrolysis and a more comprehensive understanding of electrocatalysis as a scientific field of key importance for the conversion, storage and utilization of energy from renewable sources.

Keywords

Activation energy, preexponential factor, barrier, reactant-catalyst collisions, characteristic vibrations, tunneling

Introduction

Electrocatalysis is the area of electrochemistry that studies the impact of the nature of the electrode material on the rate of the electrochemical reaction [1]. Electrocatalytic reactions involve the formation/cleavage of a chemical bond(s) between the intermediate and the electrode surface (*i.e.*, adsorption of the intermediate), suggesting that the energetics of intermediate formation, including the strength of the chemical bond(s) between the intermediate and the electrode surface, plays an important role in the overall reaction rate. Taking into account the above, it becomes clear why, for more than a century, the paradigm of heterogeneous catalysis, and therefore of electrocatalysis, has been Sabatier's principle [2].

Sabatier's principle postulates that the high rate of the catalytic reaction is due to the optimal binding of intermediates to the electrode surface. Optimal binding of intermediates in qualitative terms implies "not too strong, not too weak" chemical bond. If the chemical bond is too strong, recombination reactions are inhibited, and if the chemical bond is too weak, desorption of reactants/intermediates occurs before products are formed. This qualitative rule is usually manifested graphically through the so-called Balandin-type volcano plots where the kinetics of the reaction is given as a function of the enthalpy of adsorption of intermediates [3,4]. The peak of the volcano plot corresponds to the optimal enthalpy of adsorption. This qualitative consideration received a quantitative interpretation in electrochemistry in the late 1950s, when the exchange current density was expressed mathematically as a function of the standard Gibbs energy of hydrogen adsorption [5]. A graphic illustration of this dependence is the volcano plot, the slope of which depends on the elementary step that determines the overall reaction rate. In other words, the slope of the volcano plot depends on the symmetry factor and intermediate coverage of the elementary step that determines the overall reaction rate. The Balandin-type of volcano plot, as a consequence of Sabatier's principle, was generally accepted in electrocatalysis in the early 1970s, when a sufficient amount of experimental data for d-metals and sp-metals had been accumulated and analyzed, including relatively credible values of the exchange current density for the hydrogen reaction in acidic electrolytes, and relatively problematic values for the energy (i.e. enthalpy change) of metal-hydrogen bond formation ($\Delta H(M-H)$) [6]. The values used are problematic because they came from three different environments: 1) "bulk" interactions during hydride formation, 2) interaction of hydrogen with metal atoms on the surface, but in the gas phase, 3) electrochemical adsorption. The first two experimental environments are not relevant for electrochemistry, while the values obtained in the electrochemical experiment represented the differential values of the activation energy of the Volmer reaction on the investigated metal in relation to the activation energy of the Volmer reaction on mercury. A decade after the publication of the hydrogen volcano plot, by re-analyzing the experimental values of the hydrogen adsorption enthalpy in an electrochemical environment used in the construction of the hydrogen volcano curve, a linear dependence between the exchange current density and the adsorption enthalpy was obtained [7]. This contradiction was the trigger for considering in detail an experimental methodology that would give reliable values of the hydrogen adsorption enthalpy at the liquid/solid interface with an established Galvanic potential difference because computational chemistry did not add enough clarity here [8,9]. One of the possible approaches is the methodology to measure with a Kelvin probe the change in the work function of the metal during the adsorption of hydrogen through the water layer at the metal surface [10]. Having the realistic values of hydrogen adsorption enthalpies for various metals of interest, we could answer several key questions and, based on reliable experimental insights, create a more realistic picture of the nature of electrocatalytic activity.

Some of the most important questions that should be answered in the future are the following:

- 1. whether there is a straightforward relationship between the exchange current density for the hydrogen reaction and the enthalpy of adsorption, and if so, is it a volcano-type relationship or a linear relationship or something else;
- 2. do the trends in the enthalpy of adsorption coincide with the trends in the Gibbs energy of adsorption, that is, what is the influence of the entropy of adsorption on the trends in activity;
- 3. if the relationship between the exchange current density and the enthalpy of adsorption is of the volcano-type, is it possible to overcome the volcano-plot apex and how? At the same time, if the relation between exchange current density and adsorption enthalpy is linear, what approach should be applied to overcome the activity of the most active metals;
- 4. whether the adjustment of the enthalpy of adsorption has a direct effect on the activation energy as predicted by Brönsted-Evans-Polanyi (BEP) relations;
- 5. what is the contribution of the adsorption to the pre-exponential factor through the coverage of intermediates;
- 6. what other parameters from the rate law, besides adsorption energies (*i.e.*, adsorption enthalpy, adsorption free energy and adsorption entropy) have a significant influence on the overall reaction rate either through activation energy or through preexponential factor and with what properties of electrified interface they can be related to. Special emphasis here should be on partial orders of reaction in preexponential factor and activation barrier symmetry coefficient in exponential factor (*i.e.*, activation energy), both well-known kinetic parameters in the conventional expression for the rate law, whose physical meaning was never really resolved.
- 7. if we identify relevant properties of the electrified interface that have a significant impact on the total reaction rate (*i.e.*, through a particular parameter in the rate law), the following question is what material properties are responsible for that and how can they be tuned;
- 8. is it possible to have a separate impact on activation energy and preexponential factor?

 In this work, some of the important questions listed above will be the topic of analysis, with the intention of giving a perspective on how to proceed with the development of electrocatalysis. Currently, experimental data that could resolve the questions listed above are lacking. However, analysis on the conceptual level is very important and represents the first step in achieving in-depth clarification of electrocatalytic mechanisms. The ultimate goal is to gain knowledge on how to sufficiently accelerate key electrocatalytic reactions so they can be utilized efficiently in energy conversion devices and systems.

Results and discussion

Why is a thorough understanding of the hydrogen evolution reaction essential?

Hydrogen evolution reaction (HER) in acidic electrolytes is the simplest electrocatalytic reaction and is naturally a prerequisite for understanding more complex reactions such as oxygen reduction reaction, oxygen evolution reaction, etc. The reaction is given together with the indicated redox potential (for pH 0) in relation to the reference scale of the standard hydrogen electrode, Equation (1):

$$2H^+ + 2e^- \leftrightarrow H_2 \quad E^\circ = 0.00 \text{ V vs. SHE} \tag{1}$$

HER is a reaction during which are exchanged two electrons and two protons, usually on metal surfaces that do not structurally change significantly during the course of the reaction. Exceptions exist for this, like in the case of Pd, where significant bulk absorption impacts surface adsorption properties and this material requires different, more complex treatment [11]. Today, there is

general agreement on the reaction pathway of HER in acidic media. The elementary step in which a proton from the electrolyte reacts on the inner Helmholtz plane with an electron from the Fermi level of the metallic electrocatalyst, forming an intermediate product, is known as the Volmer step (Equation (2)). The Volmer step is followed by an elementary step in which an intermediate recombines with a proton and an electron, forming a hydrogen molecule in one active site and/or an elementary step in which two intermediates recombine, requiring two adjacent active sites. The formation of hydrogen molecules through electrochemical recombination is known as the Heyrovsky step (Reaction 3a), while chemical recombination is known as the Tafel step (Equation (3b)).

$$H^+ + e^- \leftrightarrow H_{ad}$$
 Volmer's degree (2)

$$H_{ad} + H^+ + e^- \leftrightarrow H_2$$
 Heyrovsky stage (3a)

$$2H_{ad} \leftrightarrow H_2$$
 Tafel degree (3b)

Of fundamental importance for catalysis and electrode kinetics is the identification of the elementary step that determines the total reaction rate. It is generally accepted that the elementary step that determines the total reaction rate can be evaluated using the value of the Tafel slope. Conventional wisdom suggests that for weak hydrogen bonding and very low intermediate coverage, the overall rate is determined by the Volmer step, with a Tafel slope of 120 mV/dec. If the Heyrovsky step determines the total reaction rate, which is typical for low to medium coverage with intermediates and the binding is stronger than in the Volmer step, then the Tafel slope is 40 mV/dec. Finally, when the Tafel step determines the overall rate, which is typical for moderately strong binding of intermediates and medium to high coverages, then the slope is typically 30 mV/dec or can reach 120 mV dec⁻¹ if the coverage with intermediates approaches a monolayer. The Tafel slope, which determines how easy it is to alter reaction rate with overpotential for the given solvent (i.e. water), essentially depends on the nature of the electrode material, where besides the impact of intermediate coverage, of particular importance is shape/steepness of activation barrier that is described by symmetry factor. The symmetry factor, which determines how easy it is to change the height of the barrier with a potential, essentially depends on the nature of the electrode material, but in a way that remains unknown to us for decades. Practically all diagnostic criteria of electrode kinetics (i.e. partial orders of reaction, stoichiometric number and charge transfer coefficient for multi-electron reactions) depend on the nature of the electrode material, but in a way that we still cannot comprehend. This was the reason why many kinetic studies did not make any significant contribution to the design of new, superior electrode materials and the reason why, over time, there is a growing interest in a correlative approach where the search for material properties (i.e. descriptors) that could relate with reaction rate appears to be much more realistic strategy [12,13]. The correlative approach has been visibly intensified in the last twenty years, which coincides with the rise of computational chemistry [14]. Many descriptors have been investigated, whereas most descriptors lack a show of how exactly they contribute to the activation process and what their direct link to the rate law is. On that road, it was important to introduce and define interfacial descriptors that are essentially different than material descriptors because they are strictly the result of the interaction of electrode with electrolyte [15,16]. A rational approach would imply that the property of the material (i.e. material descriptor) is related to the property of the electrified interface (i.e. interfacial descriptor), which ultimately should be related to the total reaction rate through some of the parameters in the rate law. At the same time, the descriptors should contribute to understanding the activation process.

Heuristic model of proton adsorption activation process

If we analyze the electrified electrode/electrolyte phase boundary during proton adsorption (Figure 1), using the heuristic model, we can notice that there are four important processes relevant to the formation of intermediate, as discussed previously in detail [10,15,17]:

- 1. The metallic electrode is treated as an equipotential surface and electron source, where electronic energy is described by the Fermi level or work function of the metal. Water molecules have two non-bonding electron pairs on the oxygen atom, where one of them is energetically less stable and forms a covalent bond with the metal surface (M-OH₂). The consequence of established chemical bond is metal-specific interfacial water structure that can also be described, despite the significant thermal motion of water molecules (i.e. vibrations and rotations of chemical bonds and water dipole flip), by preferential water molecule orientation. Preferential water molecule orientation reflects a statistical probability because the water bilayer is in a dynamic state. Water orientation, besides metal-water bond strength, depends on the strength of the electric field in the double layer (i.e. interfacial electric field). The electric field strength in the double layer is proportional to the potential difference between the potential of zero charge and the actual/applied potential. The stronger the metal-water bond and the larger the interfacial potential difference (i.e. as more positive), the more significant the orientation of water with hydrogen towards the metal surface will be. In other words, the covalent metal-water interaction that primarily dictates the structure of water in the double layer will be modulated by the electrostatic interaction as a secondary interaction that additionally affects the structure and dynamics of water molecules in a double layer;
- 2. The movement of protons from the outer Helmholtz plane to the inner Helmholtz plane (IHP). In reality, the proton "jumps" from one solvation shell to another in a non-linear motion, where in one instance, it will be positioned close to the metal surface so that electron transfer is likely. In essence, this interaction is a proton-electric field interaction, which depends significantly on the structure of the water in the double layer, which in turn depends significantly on the strength of the metal-water interaction and the strength of the interfacial electric field;
- 3. When the proton, including its solvation shell, is located at the IHP, then the deformation/reorganization of the solvation shell (including the reorganization of water molecules on the metal surface) is necessary as a prerequisite for electron transfer or proton-electron interaction. Deformation/reorganization of the solvation shell is actually a proton-water interaction that is influenced by the water structure, which is again influenced by the strength of the metal-water bond and the strength of the interfacial electric field;
- 4. Finally, when the water molecules on the metal surface, as well as the solvation shell around the proton, are reorganized in such a way that the positive charge of the proton is exposed to the negatively charged metal surface, electron transfer will occur, resulting in the formation of a chemical bond (M-H). The formation of the M-H bond is a metal-proton interaction. However, exposure of the positive charge of protons to the negatively charged surface depends on the stability of the solvation shell, which also depends on the structure of interfacial water that is again influenced by the strength of the metal-water bond and the strength of the interfacial electric field. So, in summary, we have three key covalent interactions: metal-water (solvent), metal-proton, and solvent-proton. These three covalent interactions can be modulated by the electrostatic interactions, which originate from the interfacial electric field. When we apply cathodic polarization, the surface of the metal becomes increasingly negatively charged proportionally to the applied potential, the water molecule's orientation with hydrogen towards the surface of the

electrode becomes statistically more probable and importantly the concentration of protons increases in the double layer. Practically, electrostatic interactions add to the above-mentioned existing covalent interactions. The contribution of electrostatic interactions depends on the interfacial electric field strength, which is directly proportional to the difference between the potential of zero charge and the actual/applied potential. Bearing all this in mind, the activation process of intermediate formation depends on the energetics of interactions: metal-water, metal-proton and proton-water, and the potential of zero charge. Individual or combined, these four properties of the phase boundary should be brought, if possible, into a direct relationship with experimentally available measurable physico-chemical quantities and with parameters in the rate law.

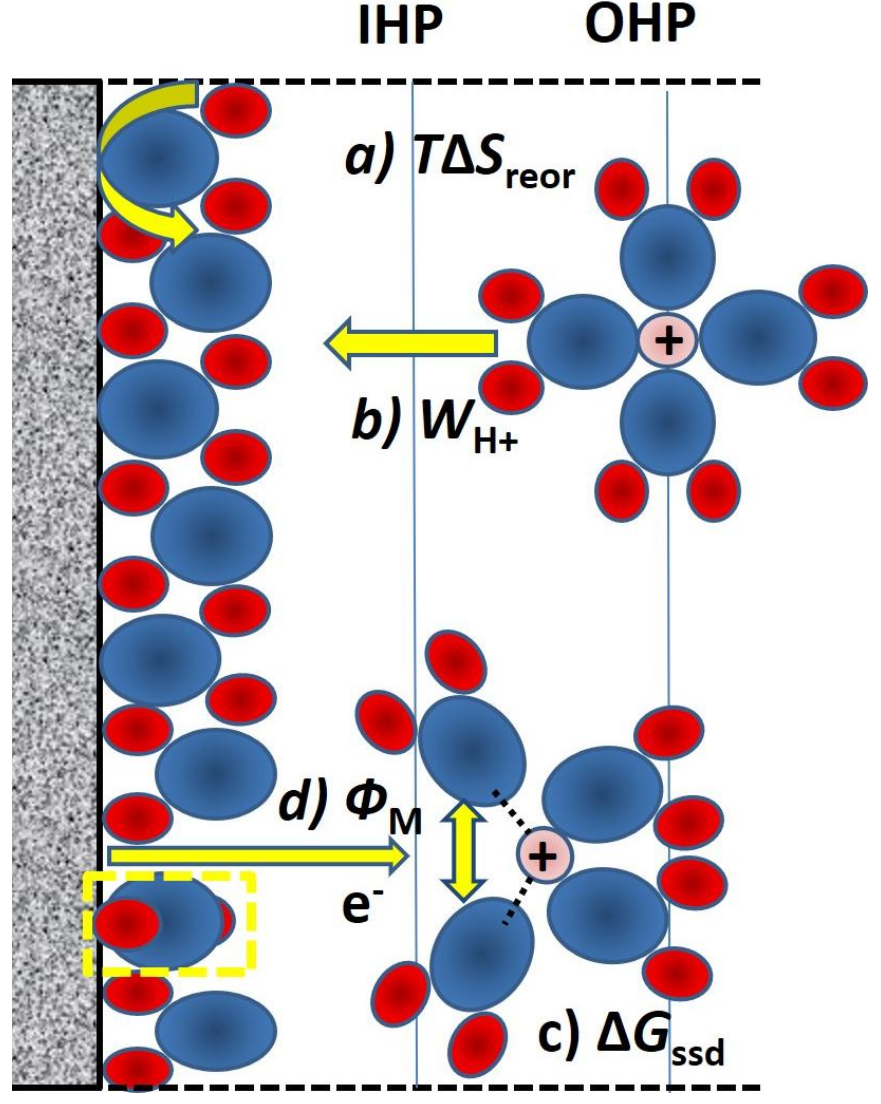


Figure 1. Structural changes of the electric double layer during proton adsorption at the solid/liquid phase boundary including: (a) reorganization of water molecules in the electric double layer under the influence of covalent metal-water interaction and the strength of the interfacial electric field, given as the average change in the entropy of the reorganization of water in proximity of the solvation shell (ΔS_{reor}), (b) average work invested on transferring proton (W_{H+}) from the outer Helmholtz plane (OHP) to the inner Helmholtz plane (IHP), (c) the average free energy of deformation/reorganization of the solvation shell in the inner Helmholtz plane (ΔG_{ssd}) in combination with further reorganization of water in the double layer in the proximity of the solvation shell, and (d) electron transfer from the Fermi level of the metal to a proton with a partially deformed solvation shell with partially exposed positive charge, driven by work function of the metal (Φ_m). Color code: metal surface—grey, oxygen—blue, hydrogen from water—red, proton and adsorbed proton—pale red. The space between the first and second layers of water in the double layer is intentionally left for clarity. Yellow dashed rectangular indicates that besides water dipole flip important is water molecule rotation

Three out of four mentioned interactions (*i.e.* metal-water, metal-proton and potential of zero charge) are strongly electrode material dependent, while proton-water interaction is strongly electrolyte dependent. If we utilize the same electrolyte to investigate different metals (*i.e.* electrode materials), then proton-water interaction is irrelevant to the investigation. However, we can alter the properties of solvent [18], use different counterions [19], use additives and/or impurities [20], so proton-water interaction can be a very relevant parameter for HER kinetics.

Phase boundary dynamics during hydrogen evolution reaction through the prism of the preexponential frequency factor

In electrocatalysis, the activation process is generally much better understood than the collision process. Therefore, the pre-exponential frequency factor is a much bigger unknown than the processes contributing to the activation energy. For electrocatalytic reactions like HER reaction rate is usually defined with the following expression (Equation (4)) [17]:

$$j_{0} = nFc_{H^{+}}^{p} (1 - \theta)^{q} k_{\text{et}} \exp\left(\frac{-\beta FE_{\text{rev}}}{RT}\right) \exp\left(\frac{-\gamma \left(\left(\Delta G_{H_{\text{ad}}}\right)_{\theta=0} + r\theta\right)}{RT}\right)$$
(4)

where: j_0 - exchange current, n - number of exchanged electrons, F - Faraday's constant, c_{H^+} - concentration of protons, p - partial order with respect to proton concentration, q - partial order with respect to number of available active sites, θ - total coverage including intermediates and eventual blocking species, β - symmetry factor, E_{rev} - reversible potential, R - universal gas constant, T - temperature, $(\Delta G_{Had})_{\theta=0}$ - the change in free-energy of adsorption at zero coverage, r - the interaction parameter. The interaction parameter originates in lateral interactions of intermediates (assisted with surrounding water molecules/dipoles) and can be positive (for repulsive interactions) or negative (for attractive interactions) and can have a great impact on the overall value of the free-energy of adsorption (i.e. $(\Delta G_{H_{ad}})_{\theta \neq 0} = (\Delta G_{H_{ad}})_{\theta = 0} + r\theta$ - the change in free-energy of adsorption at defined coverage), γ - Bronsted-Evans-Polanyi (BEP) coefficient. Conventional wisdom suggests that electrocatalytic activity is a result of a balance established by $(\Delta G_{Had})_{\theta \neq 0}$ vs. $(1-\theta)$, where for very exergonic adsorption, the resulting activation energy should be very low while the coverage should be very high and consequently, preexponential factor should be low. Conversely, for very endergonic adsorption, the resulting activation energy should be high while coverage should be low and consequently, the preexponential factor should be high. This is in accordance with the Sabatier principle. The HER exchange current has its highest value when Had formation is thermoneutral and entropy-driven ($(\Delta G_{Had})_{\theta \neq 0} = 0$). Activity trends based on this assumption are nowadays widely accepted. Some authors introduce in the exponential factor two additional parameters: the potential at the outer Helmholtz plane in reference to the potential of the electrolyte bulk, (what can be brought into correlation with the potential of zero charge) as well as the reorganization energy of the solvent, what according to discussion linked to Figure 1 seems to be justified [21]. In the preexponential factor, the same authors also include the density of states at the Fermi level, the distance between the inner and outer Helmholtz plane as well as the overlapping integral between wave functions of reactant and atoms of the electrocatalysts, suggesting a role of quantum mechanics in electrocatalysis [21]. Quantum mechanics was introduced to electrochemistry approximately a century ago [22]. Developments included both, electron transfer studies [23] and proton transfer studies [24], as well as studies on electrocatalytic reactions like HER [25], nevertheless, works were predominantly based on theoretical and/or computational chemistry. Importantly, the mentioned works did not focus on the preexponential frequency factor of electrocatalytic reactions, which is essential for understanding interfacial dynamics intermediate/product formation.

From Equation (4), it seems that the preexponential factor, besides partial orders of the reaction and the coverage by intermediates, which are understood as classical chemical effects, depends on the electron transfer rate constant. The electron transfer rate constant, for outer sphere reactions according to the semi-classical treatment of electron transfer, is defined as following (Equation (5)) [26,27]:

$$k_{\rm et} = \kappa_{\rm el} \Gamma_{\rm n} \nu_{\rm n} \exp\left(\frac{-\Delta G^*}{RT}\right) \tag{5}$$

where $k_{\rm et}$ - the electron transfer rate constant, ΔG^* - the standard free energy of activation when Galvani's potential difference is zero and, according to Marcus theory is only solvent dependent; $\kappa_{\rm el}$ - electron transfer coefficient ($\kappa_{\rm el} \leq 1$) refers to the probability of electron tunneling, which depends on the strength of the interaction between the reactant and the electrode; Γ_n - the nuclear tunneling factor ($\Gamma_n \ge 1$) which corrects the electron transfer rate for reactants (protons) that react without completely overcoming the classical barrier; v_n - the nuclear frequency factor that represents the frequency of energy barrier attempts and is generally associated with bond vibrations and solvent motions, which are relevant for the transformation of the reactant into the activated complex and the transformation of the activated complex into the product. As mentioned above, the model given by Equation (5) was initially proposed for outer sphere reactions, not for electrocatalytic reactions. However, it introduces a very interesting platform for understanding interfacial dynamics. The preexponential factor generally in electrochemistry was discussed in more detail relatively recently [28]. On the one hand, it is understood that if the interaction between the metal valence band and frontier orbital of adsorbate species is strong, then the electron transfer coefficient that refers to the probability of electron tunneling is equal one, and that should be the case for the most of relevant d-metals that are used as HER electrocatalysts. On the other hand, the nuclear tunneling factor is a parameter that can significantly differ amongst different d-metals. Proton tunneling has been discussed relatively thoroughly in the past. However, it was never considered essential for HER electrode kinetics or generally essential for rates of electrocatalytic reaction [29-32]. Rare are authors in the past that had intuition and understanding that preexponential factor should be investigated thoroughly [33] and that it can be related to the nature of electrode material, potential and reaction mechanism [34]. Some initial experimental results illustrated substantially divergent values for activation energies and preexponential factor in a case of HER on Pt when comparing the results of different research groups [35,36]. Interestingly, the results of high-temperature kinetic experiments in the case of oxygen reduction reaction (ORR) were very similar between the two leading research groups at that time, but the interpretation was essentially different. Namely, the enhancement of ORR at Pt alloyed by 3d-metals was coupled with an unexpected increase in activation energy [37]. One research group interpreted that as a consequence of reduced total coverage by adsorbed intermediate and/or blocking species [38], like in heterogeneous gas-phase catalysis [39]. In contrast, the other group interpreted that obtained coverage by adsorbed intermediate and/or blocking species becomes even higher [40,41]. Latter interpretation implicitly suggested the rate of ORR strongly depends on the preexponential frequency factor, however, due to some other contributor to the preexponential factor than the coverage with intermediates and/or blocking species. Based on this experimental results it was proposed that the eventual role of the preexponential factor is equally important as activation energy or even more important for electrocatalytic rates [42,43]. Finally, taking all this into consideration, systematic HER high-temperature electrochemistry experiments were conducted on a series of d-metals in acidic and alkaline media for the first time recently [44,45]. Results showed very interesting tendencies (Figure 2a): a) preexponential frequency factor strongly depends on the



nature of the electrocatalytic material, b) for the most active metals for HER, activation energies have intermediate to high values and at the same time intermediate to high values of preexponential frequency factor c) preexponential frequency factors span over ten orders of magnitude suggesting that divergent behavior of metals should not be due to difference in coverage, d) slope of dependence E_{act} vs. log A has almost identical value in acidic and alkaline media and it is around 5.6-5.8 kJ mol⁻¹. Exact physical meaning for this slope remains unknown, but it seems that represents some kind of universal limitation, like compensation effect in heterogenous gas-phase catalysis [39]. Dependence shown in Figure 2a is first straightforward illustration of compensation effect in electrocatalysis and proof that preexponential frequency factor has to be considered very thoroughly to understand the nature of electrocatalytic activity.

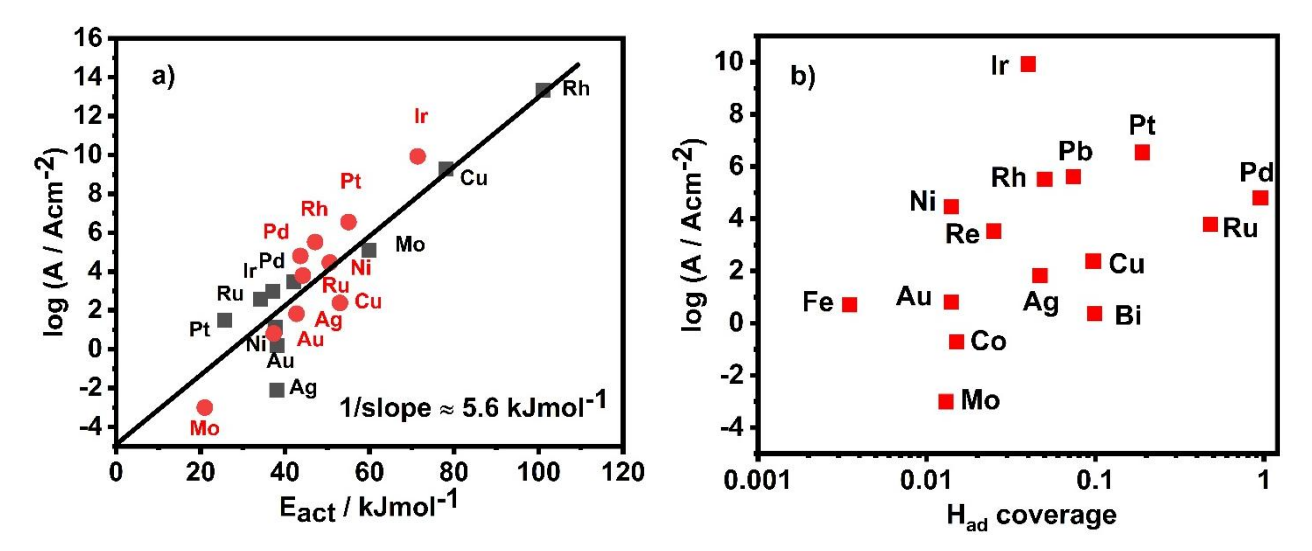


Figure 2. Relation between preexponential frequency factor and some important inerfacial kinetic parameters, including: (a) activation energy in acidic electrolyte (0.1 M HClO₄) and alkaline electrolyte (0.1 M KOH). Data related to acidic electrolyte (red circles) are extracted from [44] under the terms and conditions of the Creative Commons Attribution 4.0 International License. Published by American Chemical Society (2022). Data related to the alkaline electrolyte (black rectangular) are extracted from [45] under the terms and conditions of the Creative Commons Attribution 4.0 International License. Published by Wiley (2021). (b) intermediate coverage in acidic electrolyte. Data are extracted from [46] under the terms and conditions of the Creative Commons Attribution 4.0 International License. Published by Wiley (2024).

When comparing HER in acidic and alkaline media, Au, Ag, Ru and Pd are at approximately similar positions for both electrolytes, while the other six metals are distributed differently, which indicates that HER in alkaline media follows a completely different kind of mechanism, as discussed recently in more detail [46]. At the same time, when analyzing the relation between preexponential frequency factor and H_{ad} intermediate coverage (Figure 2b), we could say there is a certain relation between them, but it is not straightforward to be explanatory why preexponential frequency factor for different metals span over ten orders of magnitude, because H_{ad} intermediate coverage for the same metals span in the best case three orders of magnitude. The partial order of reaction also has a role (Equation (4), however, partial order of reaction is practically never greater than three because the effective collision of ions or molecules of the reactant with the electrocatalyst surface has to happen with specific orientation and specific frequency. Even if partial order of reaction would be three, still if concentrated electrolytes are utilized, the contribution of partial order of reaction to the total value of preexponential frequency factor or to the total value of exchange current suggests enhancement by order of magnitude or maximum two orders of magnitude, what cannot explain divergent behavior of various metals.

From Equation (5), it seems that the focus has to be on proton tunneling and on the nuclear frequency factor. The precondition for tunneling is that the vibrational quantum is much larger than the thermal quantum (i.e., $h_{V_b} >> k_b T$, where h -Planck constant, k_b - Boltzmann constant, T - temperature and v_b - vibrational frequency). When we talk about proton tunneling, important to stress is that the probability of tunneling increases if a wave function of the initial state of proton significantly overlaps with a wave function of the final state of proton and that is the case for metals that are weakly binding hydrogen [47]. Interestingly, previously, it was predicted by the microkinetic analysis that to uplift the apex of the HER "volcano"-plot, M-H bond formation should be endergonic in reference to thermoneutral conditions (ΔG_{Had}) $_{\theta=0}$ [7]. In that scenario, the tunneling distance is rather large and would require long-range polarization effects, including cooperative orientational displacements of solvent dipoles. On that basis, the general expectation is that metals with weak M-H bond will have large wave function overlap (Figure 3a), a high probability of tunneling and, therefore, a high preexponential frequency factor, but also, according to the compensation effect plot (Figure 2a), high activation energy. At the same time, if we observe potential energy curves (Figure 3b), it is possible that the metal that binds hydrogen more strongly, despite the downshift of the potential energy curve, has an equal or even higher activation barrier than the metal that binds hydrogen weakly, due to more emphasized curvature (i.e. more emphasized steepness) of the potential energy curve. This is an important observation because it provides a qualitative framework for decoupling activation energy and preexponential frequency factors. The exact nature of the compensation effect is not resolved; however, what links the collision process and activated complex is the shape of the potential barrier that depends on the shape of potential energy curves. Potential energy curves can be more or less steep, can be of a parabolic shape or Morse-type potential curve, etc. The essential question is: what controllable interfacial properties determine or impact the shape of potential curves and potential barrier? In the rate law, the symmetry factor is the parameter related to the shape and steepness of the potential barrier, although how to alter or tune the symmetry factor remains unknown. In other words, it remains unknown what interfacial descriptors and material descriptors are dictating the value of the symmetry factor.

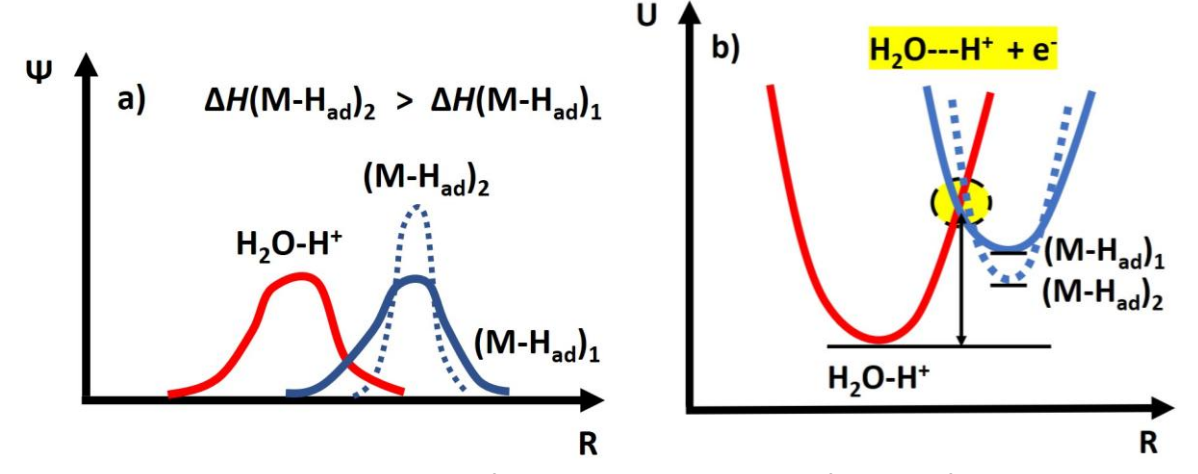


Figure 3. Schematic representation of the overlap between wave function of proton in the electrolyte (i.e. proton bonded to water molecule) and wave functions for the two metals with different metal-hydrogen bond strength and coresponding potential energy diagram: (a) illustration of more significant overlap of wave function in case of metal that adsorbs hydrogen weakly (i.e. lower enthalpy change of M-H bond formation) (b) possible up-lifting of intersection point (i.e. barrier height) in a case of stronger M-H bonding, because of more emphasized curvature (i.e. more emphasized steepness) of potential energy curve

As stated above, besides proton tunneling, it is important to address the nuclear frequency factor. The nuclear frequency factor is introduced for outer sphere reactions, meaning that it is related to bond vibrations and solvent motions. If we make an analogy with electrocatalytic reactions, the bond vibrations of adsorbed intermediates, besides solvent motions, are important. For example, an interesting observation is that characteristic vibrations of adsorbed intermediates and products in the case of chlorine evolution reaction are in the same narrow region like characteristic vibrations/phonons of many transition metal oxides that are investigated as electrocatalysts [48]. An analogy can be drawn for the metals, for which we cannot estimate characteristic lattice vibrations using vibrational spectroscopies, but they exist and could probably be accessed via inelastic neutron scattering. The question is, what are the consequences when oxide phonon or characteristic metal lattice vibrations, individual or collective, interact with characteristic vibration of electrocatalyst-intermediate bond (i.e., M-H bond). If we observe the electrocatalyst surface (i.e., M-M bond) and adsorbed intermediate/reactant (i.e., M-H bond) as two interacting harmonic oscillators, question is rising: is it possible to reach certain resonance state that can contribute to bond cleavage/formation? Based on these premises and experimental insights, including characteristic vibrational frequency-based "volcano"-plot, it was proposed more than a decade ago that electrocatalysis is a resonance phenomenon [48]. Interestingly, while this point of view in electrocatalysis is practically completely disregarded, in heterogeneous thermal catalysis, several orders of magnitude reaction rate enhancement was relatively recently shown at externally imposed "resonance frequencies" [49]. Continuous variation of the catalyst binding energy over varying frequencies ($10^{-6} < f < 10^{11} \text{ s}^{-1}$) reveals a band of resonance frequencies [50]. It was postulated that catalytic surface resonance occurs when the frequency of the applied surface state switching waveform matches the natural frequency of the catalytic kinetics [49]. In the electrocatalysis, in the case of chlorine evolution reaction, it was shown that the characteristic vibrational frequency (i.e. phonon with highest Raman shift) of the best electrocatalyst (i.e. RuO₂) is almost identical to bond vibration of adsorbed intermediate in rate determining step (i.e. CI-O) [48]. The difference between resonance phenomena observed in electrocatalysis [48] and resonance phenomena in thermal heterogeneous catalysis [50] is that enhancement of reaction rate by resonance in heterogeneous thermal catalysis is based on the application of external excitation fields, while enhancement of reaction rate by resonance, in electrocatalysis, should be a consequence of the design of electrocatalyst bulk structure and surface structure. Besides this, the enhancement of reaction rate by resonance in heterogeneous thermal catalysis was related mostly to minimizing activation energy, while the enhancement of reaction rate by resonance in electrocatalysis should be related to preexponential frequency factor [42] or the tuning of the interplay between preexponential frequency factor and activation energy [7].

On this trace, search for the answer on how to identify and what dictates nuclear frequency factor for electrocatalytic reactions (or what characteristic vibrations of intermediates, solvent and electrocatalyst surface are relevant for reaction rate control) should be one of the central research directions. In Figure 4 a schematic illustration of how different vibrations impact different elementary steps of HER is given. For the Volmer step, relevant are H₂O-H⁺ vibrations in the solvation shell and lattice vibrations (Figure 4a); for the Heyrovsky step, relevant are H₂O-H⁺ vibrations in solvation shell and M-H bond vibrations (Figure 4b); for Tafel step relevant are two neighboring M-H bond vibrations (Figure 4c). As we already can conclude from the values of Tafel slopes of elementary steps that activation energies of elementary steps have diverse values, similar can be concluded for the preexponential factors of elementary steps. The usual approach to electrode

kinetics is to search for a rate-determining step (RDS) and then try to accelerate RDS. However, despite one of the elementary steps having the lowest rate, it is possible that some other step, especially one that precedes RDS, has a much lower preexponential frequency factor or much higher activation energy than RDS and that for significant acceleration of total electrocatalytic rate, it is necessary to optimize reaction mechanism beyond just accelerating RDS. Here, it would be very useful to analyze the temperature dependence of elementary steps of HER and, for every elementary step, to obtain preexponential frequency factor and activation energy. This kind of analysis cannot be found today in electrochemistry and electrocatalysis literature.

Resolving concepts analyzed above would generate important knowledge to fully understand how to enhance the preexponential frequency factor without necessarily increasing activation energy. That would be essential in further enhancing HER kinetics and minimizing or even circumventing the compensation effect [7,51]. Of course, it would be ideal if it is possible to simultaneously enlarge the preexponential frequency factor and reduce activation energy. Understanding the mechanism of destabilizing the solvation shell on that pathway would be important. If two reactants are within the distance of the van der Waals radius, then a relatively small expenditure of energy to overcome the repulsive forces would lead to a significant increase in the tunneling probability. That essentially requires a very high concertation of protons in the double layer, if possibly already at HER reversible potential.

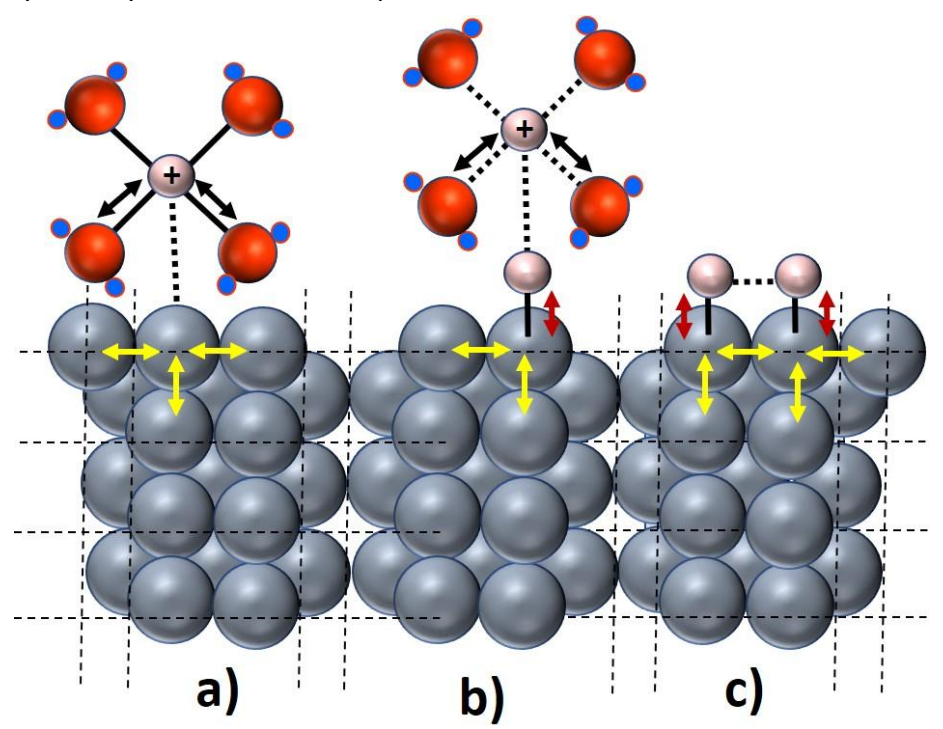


Figure 4. Schematic illustration how different vibrations impact different elementary steps of HER (a) for Volmer step relevant are H₂O-H⁺ vibrations in solvation shell (black arrows) and lattice vibrations (yellow arrows) (b) for Heyrovsky step relevant are H₂O-H⁺ vibrations in solvation shell (black arrows) and M-H bond vibrations (red arrows) (c) for Tafel step relevant are two neighboring M-H bond vibrations (red arrows). Color code: metal surface—grey, oxygen—red, hydrogen from blue—red, proton and adsorbed proton—pale red

Besides high concentration of protons in the double layer, probably there is preferential interfacial water ice-like structure that will make the destabilization of the solvation shell more probable [52]. Behavior and the exact role of water in dynamic processes at electrocatalytic interfaces remains elusive. However, there is no doubt that it contributes to both the activation and collision processes or, in other words, to activation energy and to preexponential frequency factors,

respectively. Nevertheless, it seems that for the enhancement of HER kinetics, it is required to have: 1) M-H bonding weaker than the apex of a conventional "volcano", 2) a high concentration of protons in the double layer so that the solvation shells around protons are getting destabilized. This can assure that although M-H bonding is not strong, coverage with adsorbed intermediates at the electrocatalyst surface will be high, facilitating a recombination reaction. This strategy requires further understanding of preexponential frequency factor or activation entropy for electrocatalytic reactions, and despite some new insights being offered [7,17,28,42,51] and some new important data being generated [15,36,44-46,52-55], it is still an almost completely unexplored area.

Relevant structure-activity relations as a cornerstone of rational electrocatalyst design

As indicated above, the mechanistic analysis could not appear sufficiently practical from the point of view of material science. Therefore, appropriate structure-activity relations are essential for rational catalyst design as the ultimate tool to sufficiently accelerate key electrocatalytic reactions to be utilized efficiently in energy conversion devices and systems. The fact is that experimental data that could resolve essential questions listed in the introduction section are lacking, but they could be generated in the next 5-7 years systematically. Despite this, analysis on a conceptual level is the essential initial step toward in-depth comprehension of electrocatalytic mechanisms. Being aware that some of the concepts are challenging to be fully absorbed by the targeted reader (e.g., links between electrode kinetics and quantum mechanics), in this sub-section, an effort is made to expand the discussion on how future experimental studies could validate the proposed models and concepts as well as to provide more explicit connections between the proposed theoretical insights and their practical implications for electrocatalytic performance. To simplify the analysis, for the purpose of better clarity, a table summarizing the key unresolved questions, expectations and proposed experimental technique/methodology is shown (Table 1).

Most of the essential issues mentioned in Table 1 are already discussed and are all related to intrinsic electrocatalytic properties of materials and/or electrified interface. Questions 1-7 are related to activation energy; questions 8-14 are related to preexponential frequency factor; questions 15 and 16 are related to the interplay between activation energy and preexponential factor. The one that we did not mention in the text, which has been routinely avoided for years, is the challenge of the effective surface area [57,58]. Namely, when we analyze the intrinsic activity of gas-evolving reactions like HER, it is not relevant total number of active sites at open circuit conditions but the number of available active sites at working conditions (i.e., total number of active sites minus an average number of active sites covered with gas-bubbles at defined overpotential). Methodologies for the effective surface area were proposed more than a decade ago [57,58], and some were relatively recent [59]. By disregarding effective surface area, we obtain "intrinsic activity" that is inaccurate, and we are actually underestimating the activity of electrocatalytic material. So, if we attend to establish relevant structure-activity relations, the essential step is to adequately estimate intrinsic electrocatalytic activity. Further, it is essential to identify interfacial properties/descriptors that can be analogue to the properties used to describe heuristic model (e.g. quantities in scheme of activation process in Figure 1). Identified interfacial descriptors should be: 1) measurable, 2) if possible related to some parameter in the rate law and 3) related to some material property/descriptor (i.e., property of electrode or electrolyte) that can be tuned. Considering that material descriptors is what material scientist can tune it would be very important that electrocatalytic investigations are done on single crystals, because majority of kinetic parameters listed in the Table 1 (or in the rate law) will be well defined on single crystal facets, including those properties that are responsible for interfacial

dynamics. In this context, it is worth to mention that spatio-temporal oscillations with characteristic visual patterns recorded by photoemission electron microscopy (PEEM) were only visible on single crystal facets [60]. Of course, this should not exclude studies on polycrystalline materials and/or real high-surface-area catalysts because intrinsic kinetic properties of polycrystalline materials (*e.g.,* Tafel slope) can be not only different but also superior in comparison to any single crystal constituent [61].

Table. 1 Summary of the key unresolved questions, expectations and proposed experimental techniques//methodologies. Used abreviations for quantitites and techniques are explained in the text related to the rate law (see Eqs (4) and (5)), except those that are well known in physico-chemical and electrochemistry literature. Questions 1-7 are related to activation energy; questions 8-14 are related to preexponential frequency factor; questions 15 and 16 are related to interplay between activation energy and preexponential factor and quesiton 17 is related to methodological approach relevant for evaluation of intrinsic electrocatalytic activity

	Question	Expectation	Experimental approach
1	Shape of relation $\log j_0$ vs. $\Delta H_{H_{ad}}$	"Volcano"-type or linear or	Kelvin probe (KP) [10]
2	$\Delta H_{H_{ad}}$ vs. $\Delta G_{H_{ad}}$ or role of ΔS_{ad}	Significant impact of ΔS_{Had} on activity trends	High temperature hydrodynamic LSV [44,46]
3	BEP relative (ΔH_{Had} vs. E_{act}) valid or no	If not, that suggests role of solvent for E _{act}	KP [10] and high T hydrodynamic LSV [44]
4	$\Delta H_{\text{H}_2\text{O}_{\text{ad}}}$ trends for various metals	Strongly metal-dependent, strongly impacts $E_{\rm act}$	KP [10] and DFT [56]
5	Values and nature of β	Strongly metal-dependent	Hydrodynamic LSV
6	Values and nature of γ	Should be the same for different metals?	KP [10] and high <i>T</i> hydrodynamic LSV [44]
7	Values and nature of r	Strongly metal-dependent	Hydrodynamic LSV
8	Nature of partial orders f	Strongly metal-dependent	Hydrodynamic LSV
9	Potential dependent $ heta_{\!\scriptscriptstyleH_ad}$	Strongly metal-dependent	Hydrodynamic LSV
10	Intermediate vibrations	Metal dependent	Vibrational spectroscopy (e.g. Raman)
11	Lattice vibrations	Strongly metal/oxide-dependent	Vib. spectr. or inelastic neutron scattering (INS)
12	Solvent vibrations	Probably metal-dependent	THz vibrational spectroscopy
13	Nuclear tunneling factor	metal-dependent	kinetic isotope separation factor
14	Nuclear frequency factor	metal-dependent	?
15	Log A and E _{act} of elementary steps	strongly metal-dependent	High <i>T</i> hydrodynamic LSV
16	How to overcome "volcano"-apex	possible <i>via</i> interplay of elementary rate constants	hydrodynamic LSV [7,46]
17	Effective surface area	material and morphology- dependent	CV + SECM, [57] or EIS ?

An important example is given schematically in Figure 5, where activation energy is "dissected" into four interfacial descriptors related to known material properties. From the heuristic model (see Figure 1 and Eqs. (4) and (5), we concluded that for efficient HER activation, it is essential to have optimal M-H bond strength (*i.e.*, weaker than at thermoneutral binding conditions) and high interfacial concentration of protons with destabilized solvation shells. This suggests four interfacial descriptors: M-H bond strength, M-H₂O bond strength, H⁺-OH₂ bond strength and E_{pzc} . While M-H bond strength can be related to d-band center (ε_d) and E_{pzc} can be related to work function (\mathcal{O}_m), the other two interfacial descriptors (*i.e.*, M-H₂O bond strength and H⁺-OH₂ bond strength) cannot be in a straightforward manner related to some material properties.

Even in the case of the d-band center, it can be questioned is it really a reliable material descriptor for M-H bond strength. According to the Newns-Anderson model [62], M-H adsorption energy is related to a minimum of three parameters: the bandwidth, the coupling strength between the electrocatalyst surface and the adsorbed proton, and the energy difference between the d-band center and the protons valence orbital. Only when the first two parameters are constant for various metals inside a homologous group of metals (e.g., 3d-metals) does the d-band center correlate approximately to the adsorption energy in a linear fashion. So, for the HER activation process, we could say that we identified relevant interfacial descriptors, but we still need to dedicate substantial time to discovering relevant material descriptors. This is a good illustration that, despite some widely accepted views that are oversimplifying reality, we have to make a thorough effort to understand the nature of electrocatalytic activity.

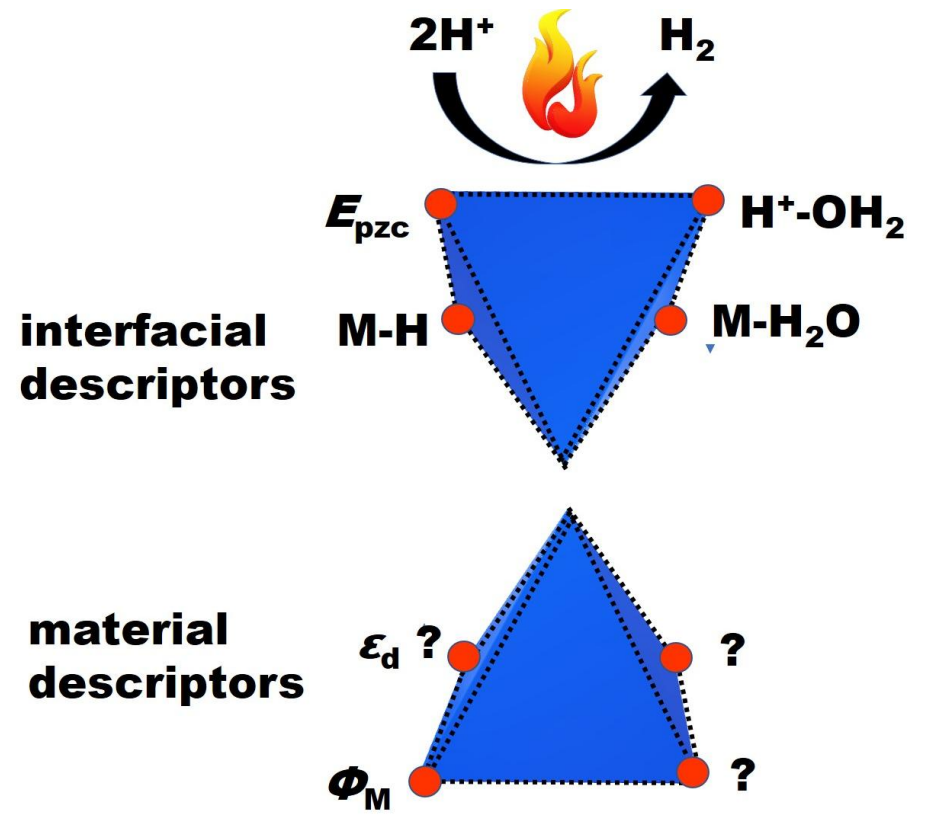


Figure 5. Relation between interfacial descriptors and material descriptors for the case of HER activation process. While M-H bond strength can be related to d-band center (ϵ_d) and ϵ_{pzc} can be related to work function (Φ_m), the other two interfacial descriptors (i.e. M-H₂O bond strength and H⁺-OH₂ bond strength) cannot be in straightforward manner related to some material properties

In the end, it can be said that some of the listed important scientific questions (see Table 1) are close to being answered, while some will require several years. For example, close to realization during 2025 will be systematic experimental measurements of M-H bond strengths for various relevant metals using Kelvin probe, as well as systematic trends for partial orders extracted from electrochemical measurements. At the same time, some other scientific questions listed in Table 1 will require new specific experiments in the design process. Proper, straightforward and sufficiently convincing experimental proofs will require time because systematic datasets with electrochemical or spectro-electrochemical data, which are the building block for relevant analysis after all these years, are practically not available in the existing literature.

Conclusions

Today, electrocatalysis research has almost entirely gone toward materials science, looking for new, more active and stable electrocatalysts, but in most cases, without clear guidelines, design principles and new mechanical insights or conceptual improvements. In this work, an important discussion was conducted on achieving a breakthrough in electrocatalysis of water splitting and electrocatalysis in general. The complexity of electrocatalysis was pointed out and why hydrogen evolution in acidic electrolytes was identified as a necessary model reaction. Furthermore, the analysis focused on catalytic descriptors and how to connect them with the rate law and the activation process to establish a new, more relevant type of structure-activity relationship. It is recognized that the dynamic aspects of the electrode/electrolyte phase boundary are of special importance, which requires an in-depth understanding of the activation process and an in-depth comprehension of collision processes between reactants, intermediates and active sites at the catalyst surface. Understanding contributors to the activation energy, contributors to the preexponential frequency factor and their mutual interaction was of special importance. It is important to emphasize that fundamentally important unknowns in the understanding of electrocatalysis have been identified, and aspects that need to be investigated in the future have been highlighted in order to obtain a comprehensive dynamic picture of electrocatalytic processes. In the long run, this appears to be the only reasonable path towards rational electrocatalyst design.

Acknowledgment: This article reflects some important aspects of the plenary lecture held at 9th Regional Symposium on Electrochemistry - South East Europe (RSE-SEE) and it is dedicated to Prof. J.O'M. Bockris, one of the world's leading electrochemists, a member of Serbian Academy of Science (SASA) and an important pillar in the development of the Belgrade School of Electrochemistry.

References

- [1] A. Frumkin, N. Polianovskaya, I. Bagotskaya, N. Grigoryev, Electrocatalysis and electrode surface properties, *Journal of Electroanalytical Chemistry and Interfacial Electrochemistry* **33** (1971) 319-328. https://doi.org/10.1016/S0022-0728(71)80120-1
- [2] P. Quaino, F. Juarez, E. Santos, W. Schmickler, Volcano plots in hydrogen electrocatalysis uses and abuses, *The Beilstein Journal of Nanotechnology* **5** (2014) 846-854. https://doi.org/10.3762/bjnano.5.96
- [3] A. A. Balandin, The multiplet theory of catalysis. Structural factors in catalysis, *Russian Chemical Reviews* 31 (1962) 589-614. https://doi.org/10.1070/RC1962v031n11ABEH001323
- [4] A. A. Balandin, The multiplet theory of catalysis energy factors in catalysis, *Russian Chemical Reviews* **33** (1964) 258-275. https://doi.org/10.1070/RC1964v033n05ABEH001407
- [5] R. Parsons, The rate of electrolytic hydrogen evolution and the heat of adsorption of hydrogen, *Transactions of the Faraday Society* 54 (1958) 1053. https://doi.org/10.1039/tf9585401053
- [6] S. Trasatti, Work function, electronegativity, and electrochemical behaviour of metals, Journal of Electroanalytical Chemistry and Interfacial Electrochemistry **39** (1972) 163-184. https://doi.org/10.1016/S0022-0728(72)80485-6
- [7] A. R. Zeradjanin, J.-P. Grote, G. Polymeros, K. J. J. Mayrhofer, A Critical Review on Hydrogen Evolution Electrocatalysis: Re-exploring the Volcano-relationship, *Electroanalysis* **28** (2016) 2256-2269. https://doi.org/10.1002/elan.201600270
- [8] J. K. Nørskov, T. Bligaard, A. Logadottir, J. R. Kitchin, J. G. Chen, S. Pandelov, U. Stimming, Trends in the Exchange Current for Hydrogen Evolution, *Journal of The Electrochemical Society* **152** (2005) J23. https://doi.org/10.1149/1.1856988



- [9] E. Santos, P. Quaino, W. Schmickler, Theory of electrocatalysis: hydrogen evolution and more, *Physical Chemistry Chemical Physics* 14 (2012) 11224. https://doi.org/10.1039/c2cp40717e
- [10] A. R. Zeradjanin, I. Spanos, J. Masa, M. Rohwerder, R. Schlögl, Perspective on experimental evaluation of adsorption energies at solid/liquid interfaces, *Journal of Solid State Electrochemistry* **25** (2021) 33-42. https://doi.org/10.1007/s10008-020-04815-8
- [11] A. R. Zeradjanin, P. Narangoda, I. Spanos, J. Masa, R. Schlögl, Expanding the frontiers of hydrogen evolution electrocatalysis-searching for the origins of electrocatalytic activity in the anomalies of the conventional model, *Electrochimica Acta* **388** (2021) 138583. https://doi.org/10.1016/j.electacta.2021.138583
- [12] O. A. Petrii, G. A. Tsirlina, Electrocatalytic activity prediction for hydrogen electrode reaction: intuition, art, science, *Electrochimica Acta* 39 (1994) 1739-1747. https://doi.org/10.1016/0013-4686(94)85159-X
- [13] J. M. Jaksic, N. M. Ristic, N. V. Krstajic, M. M. Jaksic, Electrocatalysis for hydrogen electrode reactions in the light of fermi dynamics and structural bonding FACTORS—I. individual electrocatalytic properties of transition metals, *International Journal of Hydrogen Energy* 23 (1998) 1121-1156. https://doi.org/10.1016/S0360-3199(98)00014-7
- [14] A. Holewinski, J.-C. Idrobo, S. Linic, High-performance Ag-Co alloy catalysts for electrochemical oxygen reduction, *Nature Chemistry* **6** (2014) 828-834. https://doi.org/10.1038/nchem.2032
- [15] A. R. Zeradjanin, A. Vimalanandan, G. Polymeros, A. A. Topalov, K. J. J. Mayrhofer, M. Rohwerder, Balanced work function as a driver for facile hydrogen evolution reaction comprehension and experimental assessment of interfacial catalytic descriptor, *Physical Chemistry Chemical Physics* 19 (2017) 17019-17027. https://doi.org/10.1039/C7CP03081A
- [16] N. Dubouis, A. Grimaud, The hydrogen evolution reaction: from material to interfacial descriptors, *Chemical Science* **10** (2019) 9165-9181. https://doi.org/10.1039/C9SC03831K
- [17] A. R. Zeradjanin, How to further accelerate key electrocatalytic reactions? Missing pieces of the roadmap toward efficient water electrolysis, in: Encyclopedia of Solid-Liquid Interfaces, K. Wandelt, G. Bussetti Eds., Elsevier, 2024: pp. 36-52. https://doi.org/10.1016/B978-0-323-85669-0.00110-0
- [18] Y. Li, A. Malkani, R. Gawas, S. Intikhab, B. Xu, M. Tang, J. Snyder, Interfacial Water Manipulation with Ionic Liquids for the Oxygen Reduction Reaction, *ACS Catalysis* **13** (2023) 382-391. https://doi.org/10.1021/acscatal.2c04914
- [19] D. Strmcnik, D. F. Van Der Vliet, K.-C. Chang, V. Komanicky, K. Kodama, H. You, V. R. Stamenkovic, N. M. Marković, Effects of Li ⁺, K ⁺, and Ba ²⁺ Cations on the ORR at Model and High Surface Area Pt and Au Surfaces in Alkaline Solutions, *The Journal of Physical Chemistry Letters* **2** (2011) 2733-2736. https://doi.org/10.1021/jz201215u
- [20] D. Y. Chung, P. P. Lopes, P. Farinazzo Bergamo Dias Martins, H. He, T. Kawaguchi, P. Zapol, H. You, D. Tripkovic, D. Strmcnik, Y. Zhu, S. Seifert, S. Lee, V. R. Stamenkovic, N. M. Markovic, Dynamic stability of active sites in hydr(oxy)oxides for the oxygen evolution reaction, *Nature Energy* **5** (2020) 222-230. https://doi.org/10.1038/s41560-020-0576-y
- [21] P. Searson, P. Nagarkar, R. Laianision, The effect of density of states, work function and exchange integral of polycrystalline and single crystal surfaces on the hydrogen evolution reaction, *International Journal of Hydrogen Energy* **14** (1989) 131-136. https://doi.org/10.1016/0360-3199(89)90002-5
- [22] R. W. Gurney, The quantum mechanics of electrolysis, *Proceedings of the Royal Society A* **134** (1931) 137-154. https://doi.org/10.1098/rspa.1931.0187
- [23] P. Siders, R. A. Marcus, Quantum effects in electron-transfer reactions, *Journal of the American Chemical Society* **103** (1981) 741-747. https://doi.org/10.1021/ja00394a003

- [24] R. R. Dogonadze, Z. D. Urushadze, Semi-classical method of calculation of rates of chemical reactions proceeding in polar liquids, *Journal of Electroanalytical Chemistry and Interfacial Electrochemistry* **32** (1971) 235-245. https://doi.org/10.1016/S0022-0728(71)80189-4
- [25] E. Santos, A. Lundin, K. Pötting, P. Quaino, W. Schmickler, Hydrogen evolution and oxidation—a prototype for an electrocatalytic reaction, *Journal of Solid State Electrochemistry* **13** (2009) 1101-1109. https://doi.org/10.1007/s10008-008-0702-4
- [26] M. J. Weaver, Dynamical solvent effects on activated electron-transfer reactions: principles, pitfalls, and progress, *Chemical Reviews* 92 (1992) 463-480. https://doi.org/10.1021/cr00011a006
- [27] M. J. Weaver, G. E. McManis, Dynamical solvent effects on electron-transfer processes: recent progress and perspectives, *Accounts of Chemical Research* **23** (1990) 294-300. https://doi.org/10.1021/ar00177a005
- [28] Z. He, Y. Chen, E. Santos, W. Schmickler, The Pre-exponential Factor in Electrochemistry, Angewandte Chemie International Edition **57** (2018) 7948-7956. https://doi.org/10.1002/anie.201800130
- [29] B. E. Conway, Some considerations on the role of proton tunneling in certain charge transfer processes, *Canadian Journal of Chemistry* **37** (1959) 178-189. https://doi.org/10.1139/v59-025
- [30] J. O. Bockris, D. B. Matthews, Proton Tunneling in the Hydrogen-Evolution Reaction, *The Journal of Chemical Physics* **44** (1966) 298-309. https://doi.org/10.1063/1.1726461
- [31] J. O. Bockris, D. B. Matthews, The mechanism of electrolytic hydrogen evolution—evidence for the participation of proton tunneling, *Electrochimica Acta* **11** (1966) 143-162. https://doi.org/10.1016/0013-4686(66)80003-8
- [32] M. Salomon, B. E. Conway, Classical and quantum-mechanical effects in electrochemical proton discharge, and the kinetics at low temperatures, *Discussions of the Faraday Society* **39** (1965) 223. https://doi.org/10.1039/df9653900223
- [33] R. Parsons, The kinetics of electrode reactions and the electrode material, *Surface Science* **2** (1964) 418-435. https://doi.org/10.1016/0039-6028(64)90083-4
- [34] R. Parsons, Effect of electrode material on the product of a branched electrochemical reaction, *Discussions of the Faraday Society* **45** (1968) 40. https://doi.org/10.1039/df9684500040
- [35] N. M. Marković, B. N. Grgur, P. N. Ross, Temperature-Dependent Hydrogen Electrochemistry on Platinum Low-Index Single-Crystal Surfaces in Acid Solutions, *The Journal of Physical Chemistry B* **101** (1997) 5405-5413. https://doi.org/10.1021/jp970930d
- [36] Z.-D. He, J. Wei, Y.-X. Chen, E. Santos, W. Schmickler, Hydrogen evolution at Pt(111) activation energy, frequency factor and hydrogen repulsion, *Electrochimica Acta* **255** (2017) 391-395. https://doi.org/10.1016/j.electacta.2017.09.127
- [37] A. B. Anderson, J. Roques, S. Mukerjee, V. S. Murthi, N. M. Markovic, V. Stamenkovic, Activation Energies for Oxygen Reduction on Platinum Alloys: Theory and Experiment, *The Journal of Physical Chemistry B* **109** (2005) 1198-1203. https://doi.org/10.1021/jp047468z
- [38] V. R. Stamenkovic, B. Fowler, B. S. Mun, G. Wang, P. N. Ross, C. A. Lucas, N. M. Markovic, Improved Oxygen Reduction Activity on Pt3Ni(111) via Increased Surface Site Availability, *Science* 315 (2007) 493-497. https://doi.org/10.1126/science.1135941
- [39] D. Teschner, G. Novell-Leruth, R. Farra, A. Knop-Gericke, R. Schlögl, L. Szentmiklósi, M. G. Hevia, H. Soerijanto, R. Schomäcker, J. Pérez-Ramírez, N. López, In situ surface coverage analysis of RuO₂-catalysed HCl oxidation reveals the entropic origin of compensation in heterogeneous catalysis, *Nature Chemistry* 4 (2012) 739-745. https://doi.org/10.1038/nchem.1411



- [40] M. Wakisaka, H. Suzuki, S. Mitsui, H. Uchida, M. Watanabe, Increased Oxygen Coverage at Pt–Fe Alloy Cathode for the Enhanced Oxygen Reduction Reaction Studied by EC–XPS, *The Journal of Physical Chemistry C* **112** (2008) 2750-2755. https://doi.org/10.1021/jp0766499
- [41] N. Wakabayashi, M. Takeichi, H. Uchida, M. Watanabe, Temperature Dependence of Oxygen Reduction Activity at Pt–Fe, Pt–Co, and Pt–Ni Alloy Electrodes, *The Journal of Physical Chemistry B* **109** (2005) 5836-5841. https://doi.org/10.1021/jp046204+
- [42] A.vR. Zeradjanin, Is a major breakthrough in the oxygen electrocatalysis possible?, *Current Opinion in Electrochemistry* **9** (2018) 214-223. https://doi.org/10.1016/j.coelec.2018.04.006
- [43] A. R. Zeradjanin, J. Masa, I. Spanos, R. Schlögl, Activity and Stability of Oxides During Oxygen Evolution Reaction---From Mechanistic Controversies Toward Relevant Electrocatalytic Descriptors, *Frontiers in Energy Research* **8** (2021) 613092. https://doi.org/10.3389/fenrg.2020.613092
- [44] A. R. Zeradjanin, P. Narangoda, J. Masa, R. Schlögl, What Controls Activity Trends of Electrocatalytic Hydrogen Evolution Reaction?—Activation Energy *Versus* Frequency Factor, *ACS Catalysis* **12(19)** (2022) 11597-11605. https://doi.org/10.1021/acscatal.2c02964
- [45] P. Narangoda, I. Spanos, J. Masa, R. Schlögl, A. R. Zeradjanin, Electrocatalysis Beyond 2020: How to Tune the Preexponential Frequency Factor, *ChemElectroChem* 9 (2022). https://doi.org/10.1002/celc.202101278
- [46] A. R. Zeradjanin, P. Narangoda, J. Masa, On the Origins of Intrinsic Limitations of Electrocatalytic Hydrogen Evolution in Alkaline Media, *ChemCatChem* 16 (2024) e202400634. https://doi.org/10.1002/cctc.202400634
- [47] R. R. Dogonadze, L. I. Krishtalik, The Fundamental Step in Electrode Reactions, *Russian Chemical Reviews* **44** (1975) 938-945. https://doi.org/10.1070/RC1975v044n11ABEH002399
- [48] A. R. Zeradjanin, N. Menzel, P. Strasser, W. Schuhmann, Role of Water in the Chlorine Evolution Reaction at RuO₂-based Electrodes-Understanding Electrocatalysis as a Resonance Phenomenon, *ChemSusChem* **5** (2012) 1897-1904. https://doi.org/10.1002/cssc.201200193
- [49] M. A. Ardagh, O. A. Abdelrahman, P. J. Dauenhauer, Principles of Dynamic Heterogeneous Catalysis: Surface Resonance and Turnover Frequency Response, *ACS Catalisis* **9** (2019) 6929-6937. https://doi.org/10.1021/acscatal.9b01606
- [50] M. A. Ardagh, T. Birol, Q. Zhang, O. A. Abdelrahman, P. J. Dauenhauer, Catalytic resonance theory: superVolcanoes, catalytic molecular pumps, and oscillatory steady state, *Catalysis Science & Technology* 9 (2019) 5058-5076. https://doi.org/10.1039/C9CY01543D
- [51] A. R. Zeradjanin, Understanding entropic barriers, *Nature Energy* **9** (2024) 514-515. https://doi.org/10.1038/s41560-024-01502-0
- [52] A. R. Zeradjanin, G. Polymeros, C. Toparli, M. Ledendecker, N. Hodnik, A. Erbe, M. Rohwerder, F. La Mantia, What is the trigger for the hydrogen evolution reaction? towards electrocatalysis beyond the Sabatier principle, *Physical Chemistry Chemical Physics* **22** (2020) 8768-8780. https://doi.org/10.1039/D0CP01108H
- [53] C. G. Rodellar, J. M. Gisbert-Gonzalez, F. Sarabia, B. Roldan Cuenya, S. Z. Oener, Ion solvation kinetics in bipolar membranes and at electrolyte-metal interfaces, *Nature Energy* **9** (2024) 548-558. https://doi.org/10.1038/s41560-024-01484-z
- [54] F. Sarabia, C. Gomez Rodellar, B. Roldan Cuenya, S. Z. Oener, Exploring dynamic solvation kinetics at electrocatalyst surfaces, *Nature Communications* 15 (2024) 8204. https://doi.org/10.1038/s41467-024-52499-9
- [55] L. Chen, Q. Xu, S. W. Boettcher, Kinetics and mechanism of heterogeneous voltage-driven water-dissociation catalysis, *Joule* **7** (2023) 1867-1886. https://doi.org/10.1016/j.joule.2023.06.011

- [56] X.-Y. Li, A. Chen, X.-H. Yang, J.-X. Zhu, J.-B. Le, J. Cheng, Linear Correlation between Water Adsorption Energies and Volta Potential Differences for Metal/water Interfaces, *The Journal of Physical Chemistry Letters* **12** (2021) 7299-7304. https://doi.org/10.1021/acs.jpclett.1c02001
- [57] A.R. Zeradjanin, Frequent Pitfalls in the Characterization of Electrodes Designed for Electrochemical Energy Conversion and Storage, *ChemSusChem* **11** (2018) 1278-1284. https://doi.org/10.1002/cssc.201702287
- [58] A. R. Zeradjanin, E. Ventosa, A. S. Bondarenko, W. Schuhmann, Evaluation of the Catalytic Performance of Gas-Evolving Electrodes using Local Electrochemical Noise Measurements, *ChemSusChem* **5** (2012) 1905-1911. https://doi.org/10.1002/cssc.201200262
- [59] T. Lochner, M. Perchthaler, F. Hnyk, D. Sick, J. P. Sabawa, A. S. Bandarenka, Analysis of the Capacitive Behavior of Polymer Electrolyte Membrane Fuel Cells during Operation, *ChemElectroChem* **8** (2021) 96-102. https://doi.org/10.1002/celc.202001146
- [60] G. Ertl, Reactions at Surfaces: From Atoms to Complexity (Nobel Lecture), *Angewandte Chemie International Edition* **47** (2008) 3524-3535. https://doi.org/10.1002/anie.200800480
- [61] Y. Matsumoto, E. Sato, Electrocatalytic properties of transition metal oxides for oxygen evolution reaction, *Materials Chemistry and Physics* **14** (1986) 397-426. https://doi.org/10.1016/0254-0584(86)90045-3
- [62] D. M. Newns, Self-Consistent Model of Hydrogen Chemisorption, *Physical Review* **178** (1969) 1123-1135. https://doi.org/10.1103/PhysRev.178.1123

© 2025 by the authors; licensee IAPC, Zagreb, Croatia. This article is an open-access article distributed under the terms and conditions of the Creative Commons Attribution license (https://creativecommons.org/licenses/by/4.0/)



Open Access:: ISSN 1847-9286 www.jESE-online.org

Mini review

In situ and operando characterization techniques for nanocatalyst-based electrochemical hydrogen evolution reactions

Anaclet Nsabimana¹, Yiran Guan²,⊠, Guobao Xu²,3,≣

¹Chemistry Department, College of Science and Technology, University of Rwanda, P.O. Box: 3900, Kigali, Rwanda

²State Key Laboratory of Electroanalytical Chemistry, Changchun Institute of Applied Chemistry, Chinese Academy of Sciences, Jilin 130022, China

³School of Chemistry and Applied Engineering, University of Science and Technology of China, Hefei, Anhui 230026, China

Corresponding authors: $\[\] \underline{guanyr@ciac.ac.cn}; \[\] \underline{guobaoxu@ciac.ac.cn}; \]$ Tel.: +86-431-85262747;

Fax: +86-431-85262747

Received: October 13, 2024; Accepted: December 16, 2024; Published: December 25, 2024

Abstract

The hydrogen evolution reaction is important in energy conversion and storage. This has led to the design of different types of catalysts and production setups. Understanding the status of the catalysts and reaction mechanisms motivated researchers to adopt the operando/in situ techniques. Herein, we present a brief overview of the recent (from 2020) advances in the use of in situ and operando characterization techniques, such as in situ X-ray absorption spectroscopy, X-ray photoelectron spectroscopy, X-ray diffraction analysis, IR spectroscopy, electrochemical Raman spectroscopy, online inductively coupled plasma - mass spectroscopy, differential electrochemical mass spectroscopy, optical microscopy, electron microscopy, electrochemical atomic microscopy, electrochemical scanning tunneling microscopy, and scanning electrochemical microscopy, in the electrochemical hydrogen evolution reaction. Representative examples of the applications of these techniques are also provided. Challenges in this field and future perspectives are discussed.

Keywords

Electrocatalyst; *operando* technique; *in situ* characterization techniques; hydrogen evolution reaction

Introduction

The growth of the population and standards of living style increase the consumption of energy. Moreover, the use of fossil fuels is linked to environmental pollution and global warming. This motivated researchers to find sustainable and green energy. Hydrogen is one of the most promising

sustainable and clean energy carriers, and it yields only water as a byproduct without any polluting emissions [1]. It is considered a potential fuel as it can be used as fuel free from carbon emissions, as an energy carrier, a storage medium, and in fuel cells [2]. Hydrogen is the best option for sustainable and secure energy because of its high energy density of 142.351 MJ kg⁻¹ and its zero-emission profile [3].

Hydrogen produced using electrocatalytic water splitting has attracted ever-growing attention compared to the traditional method through steam from fossil fuels [4]. Hydrogen is obtained through the hydrogen evolution reaction (HER). The HER is the cathodic water electrolysis reaction, which can be performed in an acidic or alkaline medium [5]. In an alkaline solution, the HER reaction pathway is similar to that in an acidic environment but two to three orders of magnitude slower than that in an acidic medium [6]. For the synthesis of highly efficient HER electrocatalysts, several key characteristics, such as Gibbs free energy, minimum overpotentials in electrochemical HER, reduced Tafel slop, and enhanced exchange current density in electro-catalytical water splitting, *etc*, are sought [7].

Electrocatalysis has been fundamental in improving energy efficiency, reducing environmental impacts and carbon emissions, and promoting a more sustainable approach to meeting global energy demands [8]. However, its production efficiency through electrolysis of water is very low to be economically competitive because of the high energy consumption and low hydrogen evolution rate [1]. For this reason, more research has been conducted to increase efficiency and reduce energy consumption to develop alternative low-cost electrocatalysts with high efficiency. Nanomaterials with various chemical and physical structures are among the most promising electrocatalysts for HER. They are utilized for electrocatalysis due to their attractive properties, including high surface area, high catalytic activity and favourable nanoscale effects [8].

HER is a pivotal process in renewable energy conversion and storage systems, including electrolyzers, which transform and store intermittent renewable electricity into chemical energy by generating hydrogen [9]. However, it interferes with other energy production and conversion processes, such as N2- and CO2-reducing electrolyzers, batteries and, supercapacitors. Thus, understanding the structure and reaction mechanisms of electrocatalysts at electrode-electrolyte interfaces is crucial for the advancement of renewable energy technologies [8]. It is very important to understand the hydrogen adsorption and absorption mechanisms on the electrode surface because, for a constant HER rate at the electrode surface, the required overpotential decreases when the energetics of adsorption of reaction intermediates on the electrode surface is favorable [10]. Also, the electrocatalytic reactions are highly influenced by the morphology and surface composition of nanosized catalysts, with the electronic structure and atomic arrangement often determining their electrocatalytic performance [8]. Even though traditional characterization techniques provide some information, they are not suitable for real-time study of the nanocatalysts used in HER [11]. The ex situ characterization comparison between the pre- and post-chemical states of the catalyst in specific electrochemical reactions cannot always guarantee a meaningful trend and relevance between the chemical variation of the catalyst and electrochemical activity [12]. Thus, the need to address the working structure of a catalyst under reaction or working conditions has given rise to the development of in situ and operando methods [13,14]. To achieve that, the specialized reaction cells were integrated into conventional characterization instruments to facilitate the study of catalytic materials during the reactions, enabling the combination of data from conventional characterization of a sample under reaction conditions with simultaneous measurements of its catalytic performance.

This study provides a brief overview of recent advances in the application of the *in situ* and *operando* characterization techniques, such as *in situ* X-ray absorption spectroscopy, X-ray

photoelectron spectroscopy, X-ray diffraction (XRD) analysis, IR spectroscopy, electrochemical Raman spectroscopy, online inductively coupled plasma - mass spectroscopy, differential electrochemical mass spectroscopy, optical microscopy, electron microscopy, electrochemical atomic microscopy, electrochemical scanning tunneling microscopy, and scanning electrochemical microscopy, in the electrochemical hydrogen evolution reaction. Examples are also provided for each characterization technique.

In situ and operando characterization techniques for electrochemical hydrogen evolution reactions

X-ray adsorption spectroscopy

The energy of the X-rays is high enough to excite core-level electrons to higher unoccupied states. X-ray absorption spectroscopy (XAS) is one technique for measuring changes in X-ray absorption or fluorescence [8]. XAS is a technique that gathers data on the interactions between incoming X-rays and the core electrons within atoms [15]. XAS spectra can be categorized into three distinct regions, which are the pre-edge region, X-ray absorption near edge structure (XANES), and extended X-ray absorption fine structure (EXAFS) [8,15]. XANES provides element-specific insights into the electronic structure, bonding geometry of the absorbing atom, and the density of unoccupied states [15]. In general, the spectrum of this region is located between the edge and 50 eV above the threshold [16]. On the other hand, EXAFS offers insights into local structures, including bond distances and coordination numbers around the absorbing atoms [15]. In situ/operando XAS is utilized to identify the electronic and geometric structures of electrocatalysts within electrode networks, particularly to elucidate the structure of active catalytic sites on oxide-based catalysts [16]. It provides detailed information about their electronic structures, coordination environments, and site symmetry, which are particularly effective in distinguishing different elements within multimetallic metal oxides [8].

Ding at al. [17] utilized XAS and near-ambient pressure X-ray photoelectron spectroscopy to reveal that NiS undergoes an *in-situ* phase transition to a mixed phase of Ni₃S₂ and NiO, creating highly active synergistic dual sites at the Ni₃S₂/NiO interface (Figure 1). The results showed that the interfacial Ni is the active site for water dissociation and OH* adsorption, while the interfacial S is the active site for H* adsorption and H₂ evolution [17]. Consequently, the in-situ formation of Ni₃S₂/NiO interfaces allowed NiS electrocatalysts to achieve an overpotential of only 95 \pm 8 mV at a current density of 10 mA cm⁻².

Using operando EXAFS and XANES, Tang et al. [18] studied the Pt single-site catalysts and demonstrated that when a negatively biased potential is applied, the Pt–N bonds break first and then the Pt–Cl bonds follow. Pt is reduced from platinum(II) to metallic platinum(0) by the onset of the hydrogen-evolution reaction at 0 V. Furthermore, there was an increase in Pt–Pt bonding, which indicates the formation of Pt agglomerates.

Wang et al. [19] utilized Pt single atoms anchoring on the nitrogen-carbon substrate (PtSA/N-C) to investigate the dynamic structure of Pt single-atom centers during the HER process using in situ/operando synchrotron X-ray absorption spectroscopy and X-ray photoelectron spectroscopy. This helped to identify the intriguing structural reconstruction at the atomic level in the PtSA/N-C when it underwent repetitive cyclic voltammetry and linear sweep voltammetry scanning. It was demonstrated that the Pt-N bonding tends to be weakened under cathodic potentials, inducing some Pt single atoms to dynamically aggregate to form small clusters during the HER.

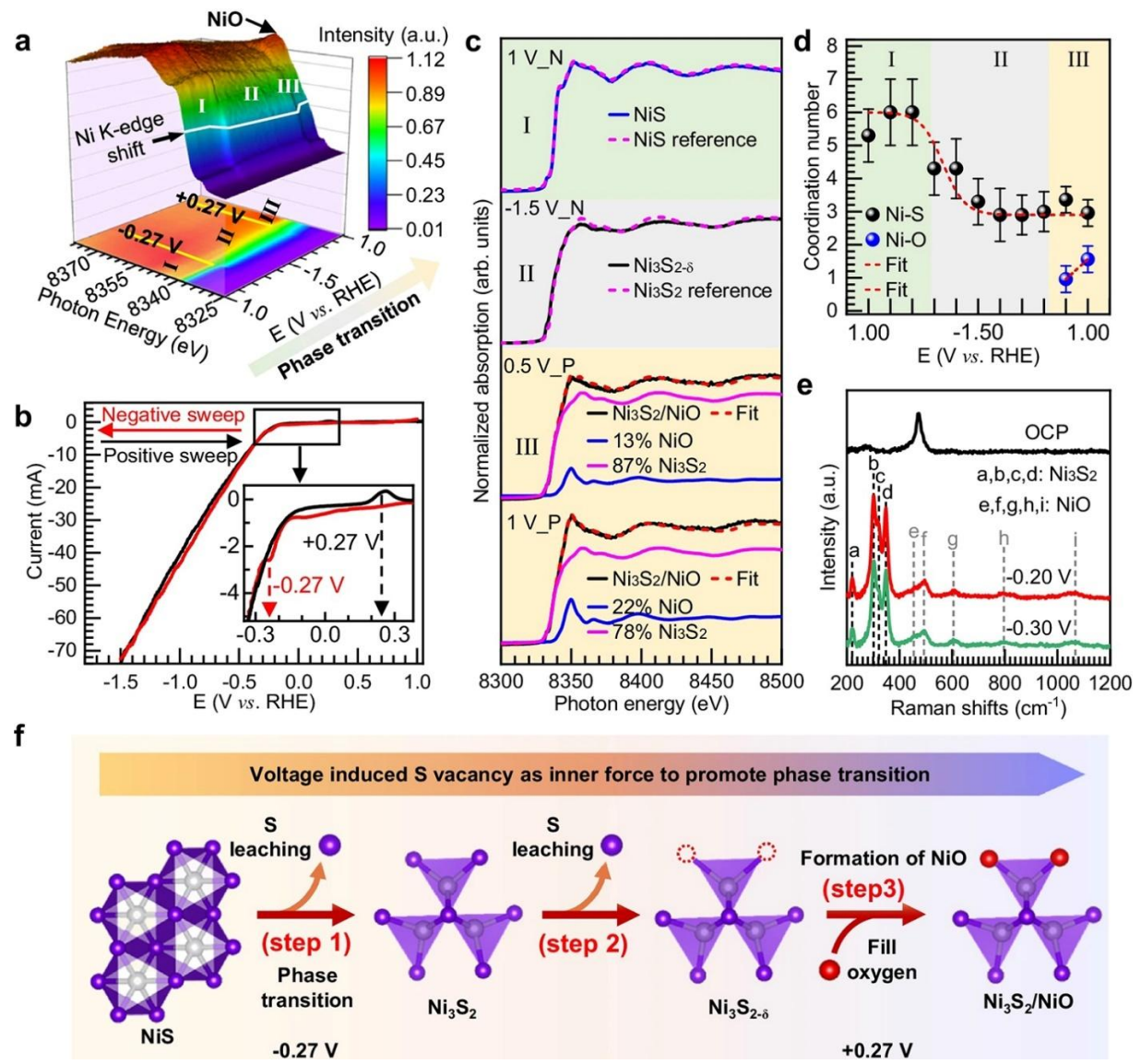


Figure 1. (a) Operando Ni K-edge XAS for NiS catalyst as a function of applied voltages (Top: 3-dimensional view of Ni K-edge XAS spectra; bottom: 2-dimensional projection from a 3-dimensional view).

(b) Corresponding CV profile used for the operando XAS measurement (Inset: magnified region marked in the rectangular box). (c) Ni K-edge XAS spectra at specific applied voltages of +1.00, -1.50, +0.50 and +1.00 V (V_N means V in negative sweep and V_P means V in positive sweep of CV) in region I, II, and III respectively, extracted from (a), and their linear combination of Ni₃S₂ and NiO. (d) Coordination number of Ni as a function of applied voltages. (e) Operando Raman spectroscopy of NiS at different applied voltages. (f) Illustration for phase transition of NiS catalyst during HER measurement. Reproduced from Ref. [17]

X-ray photoelectron spectroscopy

X-ray photoelectron spectroscopy (XPS) is a surface-sensitive quantitative technique able to provide detailed information on the element-specific chemistry and electronic state of the sample [15]. It is one of the most powerful techniques enabling the understanding of the elemental composition and chemical states of the surface of materials [20]. However, the requirement of the ultra-high vacuum condition at the electrode-electrolyte interface challenges the application of *in situ* XPS [15]. This led to the development of the ambient pressure XPS (APXPS), which is also a beneficial tool for the *in-situ* characterization of photoelectrochemical and electrochemical systems [20].

Liu et al. [21] used in situ and ex situ transmission electron microscopy (TEM) in combination with in situ XPS to study the encapsulation of metallic iridium nanoparticles (NPs) by carbon in an Ir/C

catalyst (Figure 2). The real-time atomic-scale imaging visualized particle reshaping and increased carbon support graphitization upon heating Ir/C in a vacuum. The *in situ* TEM results revealed that carbon overcoating grows over Ir NPs during heating, starting from *ca*. 550 °C. With the carbon overlayers formed, no sintering and migration of Ir NPs is observed at 800 °C, yet the initial Ir NPs sinter at or below 550 °C. The catalytic activity and stability of the encapsulated Ir NPs in the HER were higher than that of the initial (nonencapsulated) state of Ir/C.

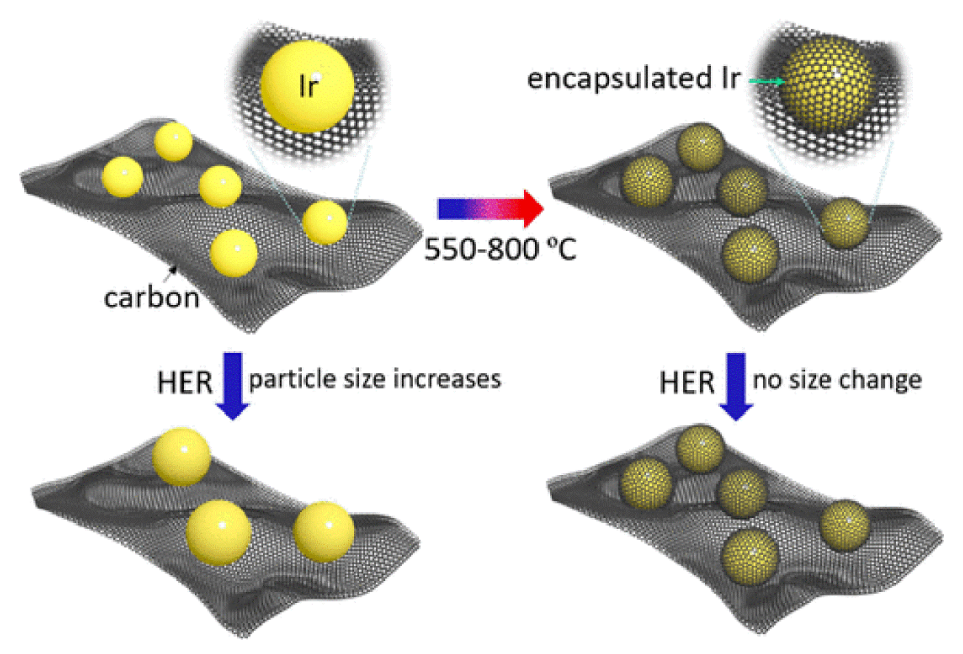


Figure 2. Carbon encapsulation of supported metallic iridium nanoparticles for HER. Reproduced from Ref. [21]

X-ray diffraction

XRD is a technique that can monitor the catalyst structural evolution by examining the degree of crystallinity, type of phase structure, and size of crystallite particles [15]. *In situ* XRD analysis was used to study the real-time change of crystal structure during the HER reaction processes [22]. *Operando* XRD has been reported to be a useful tool for the determination of the phase transformation of nanocatalyst for HER [23].

Zhai et al. [24] applied operando synchrotron X-ray powder diffraction (SXRD) in the NiSe₂ electrocatalyst system to reveal an *in situ* phase transformation from cubic NiSe₂ to hexagonal NiSe (Figure 3).

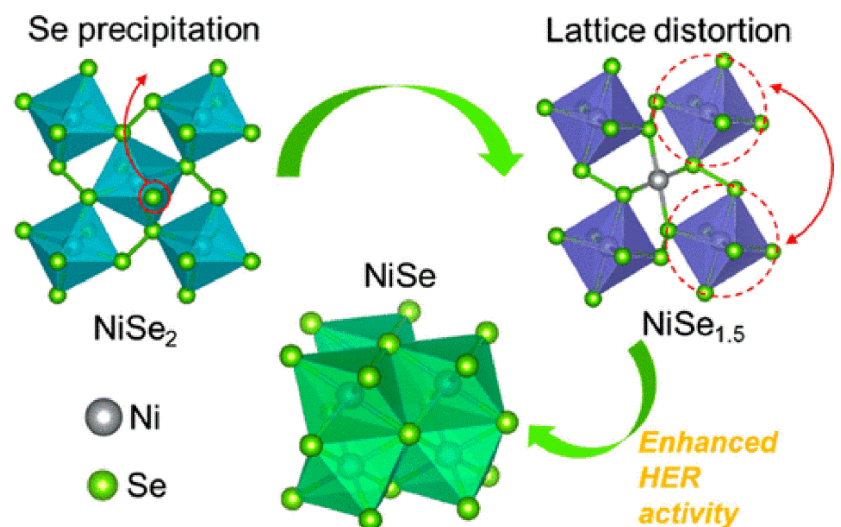


Figure 3. In situ phase transformation on nickel-based selenides for enhanced hydrogen evolution reaction in alkaline medium. Reproduced from Ref. [24]

The NiSe phase showed an enhanced catalytic activity and the *operando* Raman spectroscopy was used to verify the decomposition of NiSe₂ during HER. This work unravels the underlying phase transition of electrocatalyst on reductive conditions in an alkaline medium and highlights the significance of identifying the intrinsic active sites under realistic reaction conditions.

IR spectroscopy

Operando IR-based techniques are sometimes employed as complementary methods to investigate intermediate species formed on the catalyst surface during electrochemical reactions and to determine the catalytic reaction mechanisms [16]. The operando or in situ versions of these techniques require fast and highly sensitive detection of target species and have been used to monitor the HER. Two cell configurations, internal and external cell designs, are utilized to perform the in situ/operando characterization of electrochemical reactions using IR-based techniques (Figure 4) [16]. For the internal cell design, a layer of catalyst is deposited over an IR-transparent crystal using electroless or sputtering deposition (Figure 4A), making the catalyst layer thickness limited to a few nanometers, whereas for the external cell design (Figure 4B), the working electrode is positioned close to the prism allowing to achieve the efficient characterization of solution species and adsorbates with a stronger IR illumination and possibility to use different types of electrode materials.

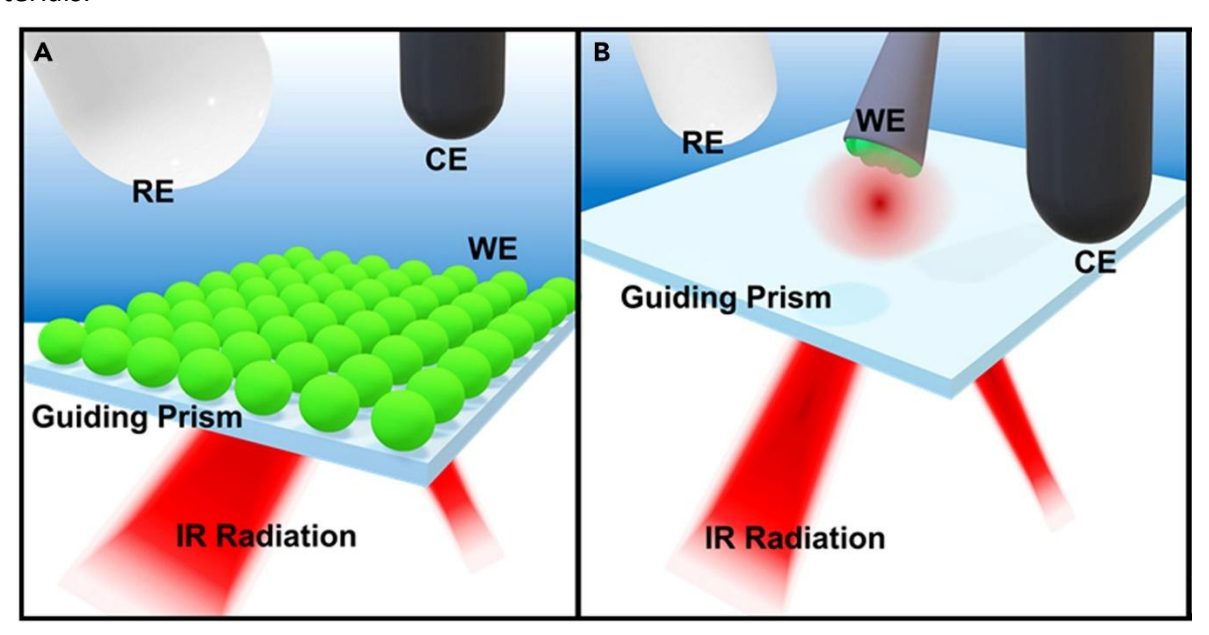


Figure 4. Schematic illustration of operando IR spectroscopy: (A) Internal and (B) external IR cell designs for in situ electrochemical studies. Reproduced from ref. [16]

Tan et al. [25] proposed a practical method for engineering a local acid-like reaction environment to design highly efficient alkaline HER catalysts. By virtue of multiple physicochemical interactions between the substrate, metal active site, and reaction intermediate, they selected Pt/MgO as the prototypical example to construct an acid-like reaction environment in an alkaline medium. *Operando* Raman spectroscopy, synchrotron radiation Fourier transformed infrared spectroscopy (SR-FTIR) spectroscopy and X-ray absorption near-edge spectroscopy (XANES) confirmed the generation of massive amounts of H_3O^+ intermediates on the MgO surface and accumulation around negatively-charged Pt (Pt $^{\delta-}$). This engineered local acid-like reaction environment (in an alkaline medium) led to an extraordinary HER performance with a significantly low overpotential of 39 mV at 10 mA cm $^{-2}$, much better than the value of 62 mV for 20 wt.% Pt/C and close to the acidic HER

behavior of 20 wt.% Pt/C (33 mV). This system also has tenfold higher mass activity than the 20 wt.% Pt/C electrodes in an alkaline medium and 2.5-fold higher than that of 20 wt.% Pt/C in acidic medium at -39 mV vs. RHE. Experimental characterizations and first-principles calculations suggest that the oxygen vacancy-rich MgO is favorable for water dissociation, and the electronic interaction between the MgO and Pt nanoparticles drives electron transfer from VO-MgO to Pt, giving rise to the formation of negatively charged Pt $^{\delta-}$ species. Then, the Pt $^{\delta-}$ accelerates H $_3$ O $^+$ migration and an acid-like environment is formed around the Pt $^{\delta-}$ in an alkaline medium, thus boosting the HER in this alkaline medium.

Raman spectroscopy

In general, operando Raman spectroscopy is performed to identify the active species and reaction intermediate, active site, and phase transitions during the reaction [16]. Thanks to this characterization, the catalyst states, the reaction intermediates, and products during the gas-involved reactions can be detected non-destructively [22].

Zhou et al. [26] monitored the origin of MoSe2-electrocatalytic HER activity using the quasioperando XPS and in situ Raman spectroscopy. The results clearly revealed dynamic evolution of both Mo and Se species on the MoSe₂ electrode surface to promote HER activity and maintain longterm catalytic stability.

Johnson *et al.* [27] utilized the *in situ/operando* Raman spectroelectrochemistry (Raman-SEC) combined with density functional theory (DFT) calculations to probe the HER mechanism of the Ti₃C₂ MXene catalyst in aqueous media. In acidic electrolytes, the -O- termination groups are protonated to form Ti-OH bonds, followed by protonation of the adjacent Ti site, leading to hydrogen formation. DFT calculations show that the large overpotential is due to the lack of an optimum balance between O and Ti sites. In neutral electrolytes, H₂O reduction occurs on the surface, leading to surface protonation and hydrogen formation. This results in an overcharging of the structure, leading to the observed large HER overpotential. Bazan-Aguilar *et al.* reported an effortless and low-cost method to obtain highly active Ni foam-based electrocatalysts toward the HER in alkaline media from commercial and low-cost Ni-foam material [28]. The *in-situ* Raman-SEC (Figure 5) and differential electrochemical mass spectrometry achieve a deep understanding of the kinetics and reaction mechanism.

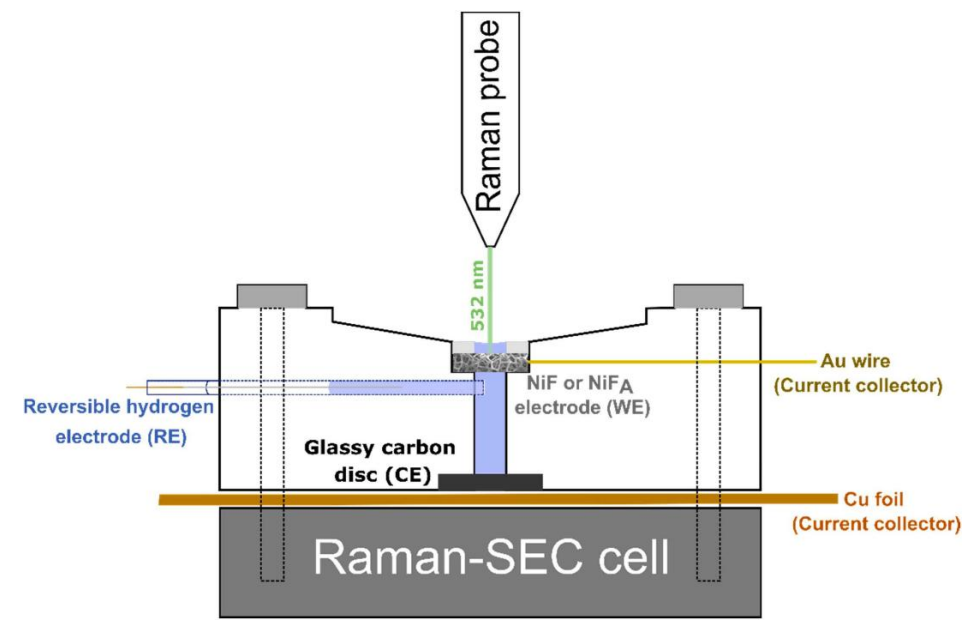


Figure 5. Schematic illustration of the in-situ Raman spectroelectrochemical cell. Reproduced from Ref. [28]

Inductively coupled plasma mass spectroscopy

Inductively coupled plasma mass spectroscopy (ICP-MS) is a quantitative elemental analysis technology that detects various elements [20]. This technique has been used to monitor the *operando/in situ* HER. For example, Aymerich-Armengol *et al.* [29] conducted a comprehensive study on the stability of MoS₂ nanocatalysts under both open circuit potential and HER conditions, with and without Rhenium dopants. This involved a combination of *ex situ* electrochemical degradation and *operando* characterization using SFC-ICPMS (Figure 6). The obtained results were correlated with the evolution of morphology and chemical composition shown by microscopy imaging and spectroscopy at identical locations, XPS, XAS, and calculated Pourbaix diagrams. The *operando* SFC-ICPMS results revealed a stability window from -0.05 to -0.3 V *vs.* RHE for HER operation in sulfuric acid. In addition, the quantitative analysis showed that Re-doped MoS₂ nanocatalysts possess greater stability against dissolution under HER conditions. They also exhibit a wider electrochemical stability window against Re dissolution at anodic potentials, making them more durable for use in acidic electrolyzers compared to pure MoS₂ nanocatalysts.

Coupling of the electrochemical flow cell (EFC) with an ICP-MS device (EFC-ICP-MS) is a powerful method for tracking the online dissolution of metals during electrochemical reactions [30]. It is a powerful electroanalytical technique that provides significant information on the dissolution behavior of the catalysts [31]. It also helps to understand the mechanism of degradation under operating conditions [32,33]. Smiljanić *et al.* monitored the electrochemical stability and degradation mechanisms of a commercial Pd/C catalyst using EFC-ICP-MS [34]. To achieve that, HER was used as a test reaction to observe the corresponding impact of the degradation on the activity of Pd/C. The results of this work emphasized the importance of a systematic study of the durability of Pd nanocatalysts, as this may present a limiting factor for their application in energy conversion devices.

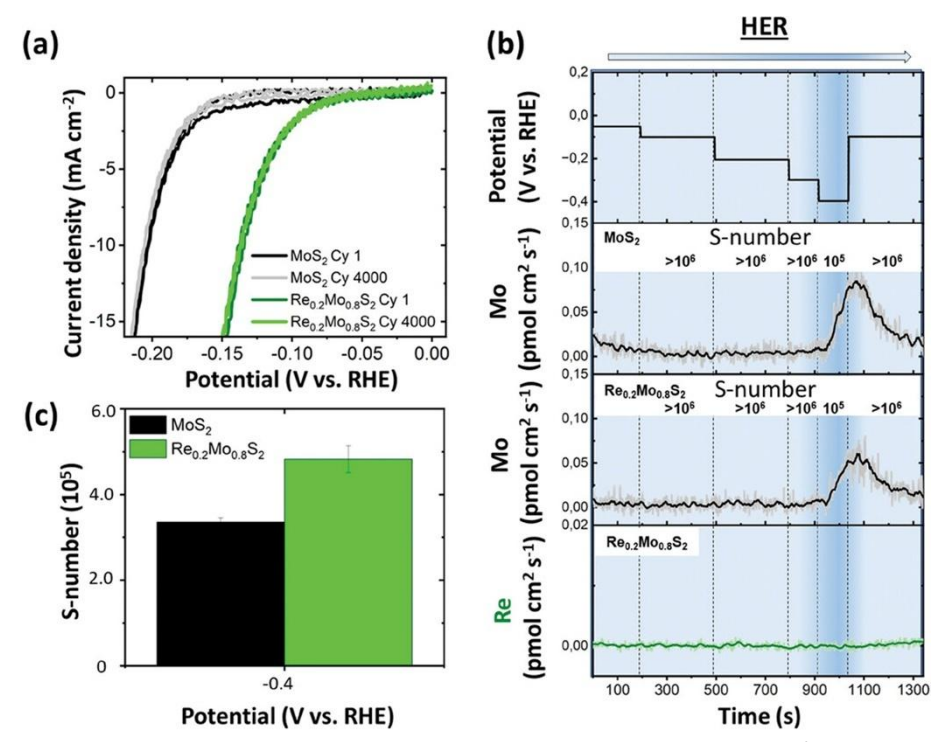


Figure 6. (a) Cyclic voltammograms comparing the HER performance of MoS₂/CP and Re_{0.2}Mo_{0.8}S₂/CP electrodes at cycle 1 and cycle 4000. (b) Operando SFC-ICPMS data illustrating the Mo and Re dissolution at different HER potentials. (c) S-number of MoS₂ and Re_{0.2}Mo_{0.8}S₂ at -0.4 V_{RHE}. Reproduced from Ref. [29]

Electrochemical impedance spectroscopy

Electrochemical impedance spectroscopy (EIS) is one of the effective methods for investigating electrocatalytic reaction kinetics and the properties of the electrode/electrolyte interface [15]. Its *in situ* and non-invasive nature makes it suitable for studying underlying mechanisms and performance under actual catalytic operating conditions [16]. This is the method used in many HER reactions [12,16,35]. For example, Smiljanić *et al.* [30] developed an attractive strategy to suppress Pt dissolution by using an organic matrix tris(aza)-pentacene (TAP) as an alternative support material for Pt. The results of the *in situ* EIS measurements (Figure 7) showed that the improved stability of Pt/TAP was a consequence of the potential-dependent conductivity of TAP support.

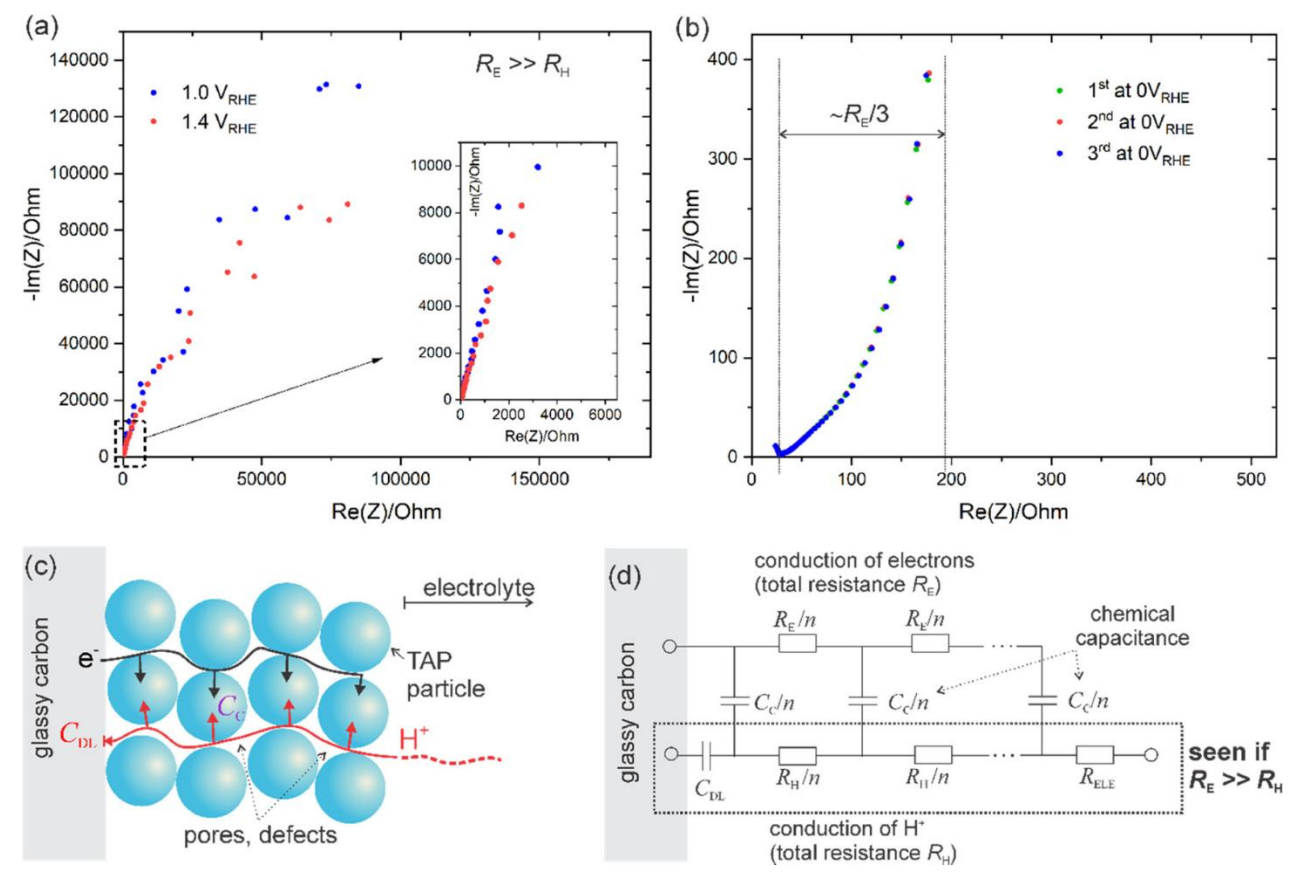


Figure 7. Impedance spectra measured at (a) high and (b) low potentials vs RHE; (c) Illustration of ionic and electronic transport and insertion in the defect-rich TAP film deposited on a glassy carbon electrode; and (d) transmission line model corresponding to the transport/insertion mechanism(s) in panel (c).

Reproduced from Ref. [30]

Optical microscopy

It has been reported that optical microscopy can be used to investigate the electrolytic HER mechanism. Lemineur *et al.* [36] used interference reflection microscopy (IRM) to probe *operando* an ensemble of individual NPs and the surface gas nanobubbles (NBs) they generate under electrochemical activation (Figure 8). Taking advantage of the high spatial and high temporal resolution of such optical nanoscope, the position of both the nano-catalysts and the NBs are tracked dynamically. In addition, modeling the optical response of gas NBs in the IRM configuration allowed evaluating dynamically the size and shape of the NBs during their production, enabling us to discuss the growth mechanism of gas NBs from single catalytic colloidal Pt NPs. It is shown that the Pt NPs are rapidly electrically disconnected by the NBs, which are still continuously growing.

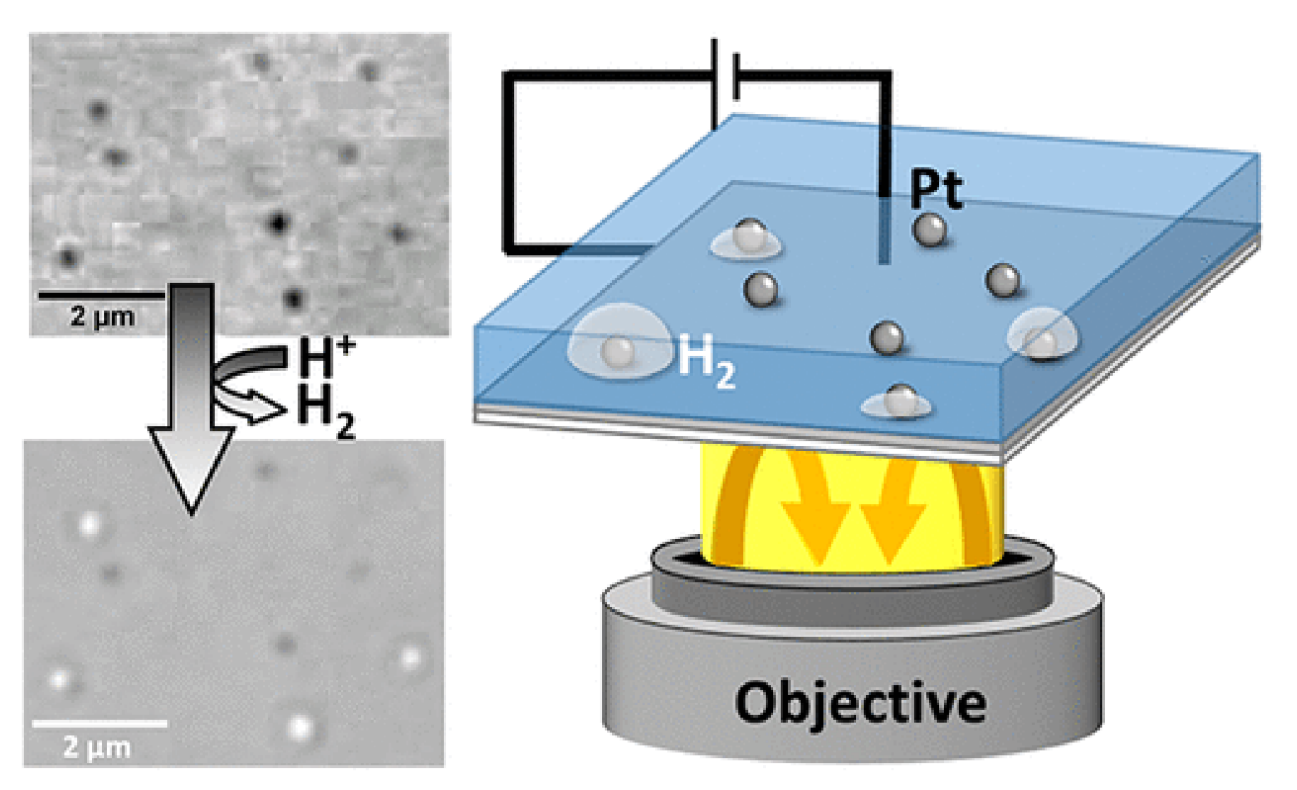


Figure 8. Imaging and quantifying the formation of single nanobubbles at single Pt nanoparticles during the hydrogen evolution reaction. Reproduced from Ref. [36]

Transmission electron microscopy

TEM is a technique that combines electron diffraction, imaging, and spectroscopic tools to provide valuable details on the morphology, crystalline structure, and chemical composition of materials [11]. It is used to characterize nanocatalysts, and recently, scientists have shown that it is possible to use it to monitor electrochemical reactions in real time.

In situ TEM is now a fast-growing field of research with numerous possibilities to study samples under applied heat, light excitation, stress, electric or magnetic fields, and electrochemical control [37]. In comparison with other in situ/operando techniques, the in situ/operando TEM is relatively new, and it helps capture the information of individual atoms or molecules under reaction conditions [38]. It can enhance our fundamental understanding of electrocatalytic processes and catalyst degradation mechanisms in their native environments without the need for freezing or drying the samples [8]. This technique provides the information with atomic, molecular and sometimes nanoscale/microscale resolutions depending on the sample system's nature and the instrumental measurement configuration [38]. It is well-suited to provide unique insights into interfacial electrocatalytic process-ses, offering nanometer-scale or higher resolution, as well as detailed information on composition and chemical bonding [8]. For HER, a reaction involving a catalyst for liquid reactants, a liquid cell, has been developed to allow the presence of liquid and the potential control of the electrode [38].

Fu et al. [39] reported an interesting edge optimization strategy to enhance the catalytic activity of two-dimensional metal phosphorus trichalcogenides (MPTs). With in situ reconstructed amorphous surface, MPTs could intrinsically offer better catalytic performance for alkaline hydrogen production (Figure 9). Trace Ru (0.81 wt.%) was doped into NiPS₃ nanosheets for alkaline HER. Using in situ electrochemical TEM technique, they confirmed that the amorphization process on the edges of NiPS₃ is critical for achieving superior activity.

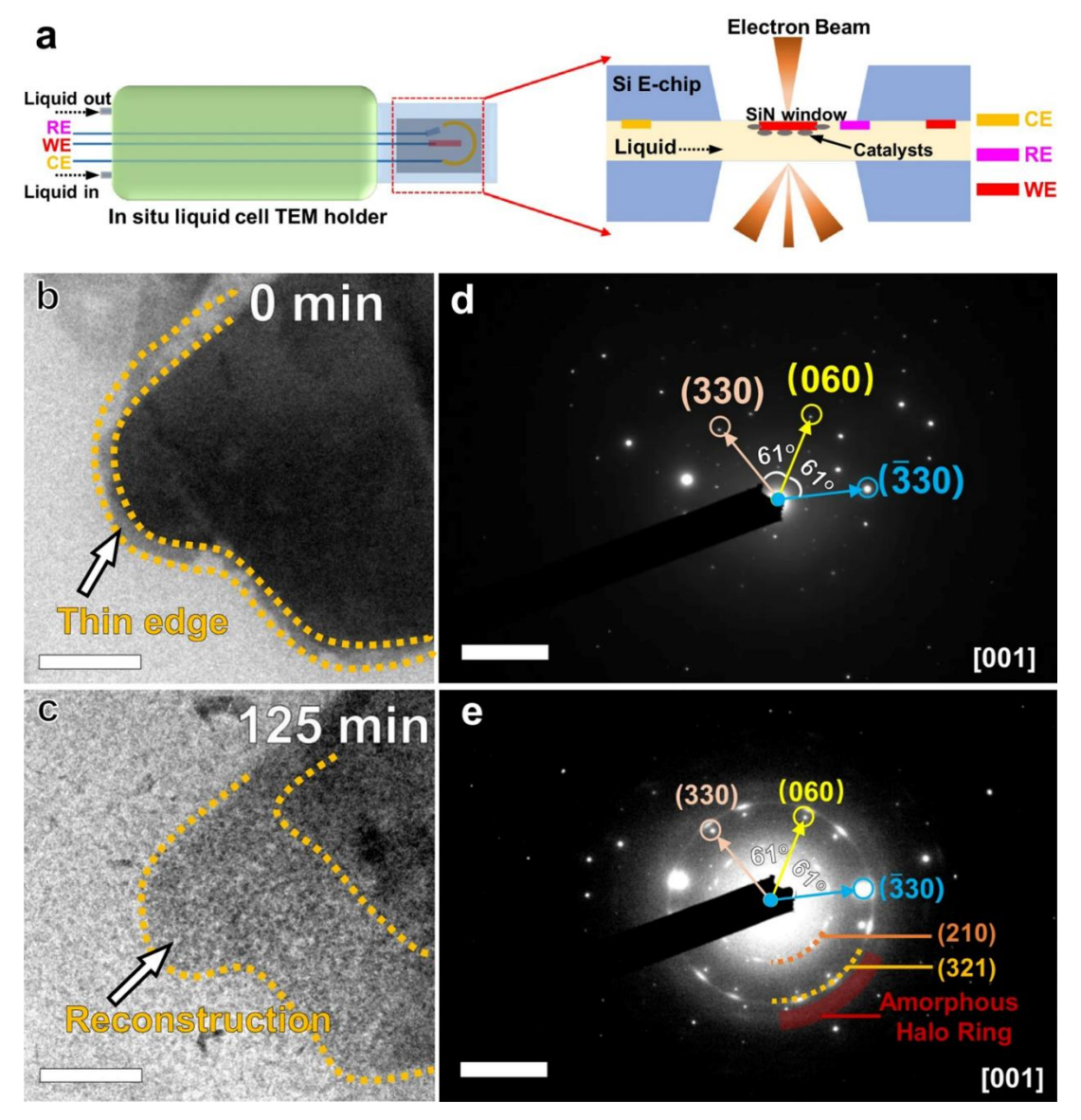


Figure 9. The structural evolution of Ru-NiPS₃ NSs during the HER process: (a) Schematic illustration of the in situ electrochemical liquid cell TEM holder and the liquid cell. In situ liquid TEM image (scale bar: 0.2 μm) of Ru-NiPS₃ NSs; (b) before and (c) after chronopotentiometry test; (d), (e) corresponding SAED for (b) and (c), respectively. Reproduced from Ref. [39]

Electrochemical scanning tunneling microscopy

Electrochemical scanning tunneling microscopy (EC-STM) is another tool providing the information which can help to improve hydrogen production. For example, Kluge *et al.* [40] used electrochemical scanning tunnelling microscopy under reaction conditions (EC-STM) to show that, by using this technique, it is possible to *in situ* visualize the active sites of highly oriented pyrolytic graphite for the HER. This technique was applied to highly ordered pyrolytic graphite in HER conditions. The results showed that at atomic resolution, the most active sites in an acidic medium are located near edge sites and defects, while the basal planes remain inactive.

Lunardon *et al.* reported in details the principles of the EC-STM method, focusing on the HER (Figure 10) [41]. They demonstrated that the quantitative analysis of the noise in the tunneling current allows quantifying the local onset potential and provides information about the microscopic mechanism of electrochemical reactions on sub-nanometric electrocatalytic sites, such as chemically heterogeneous flat interfaces, nanoparticles, and even single-atom defects.

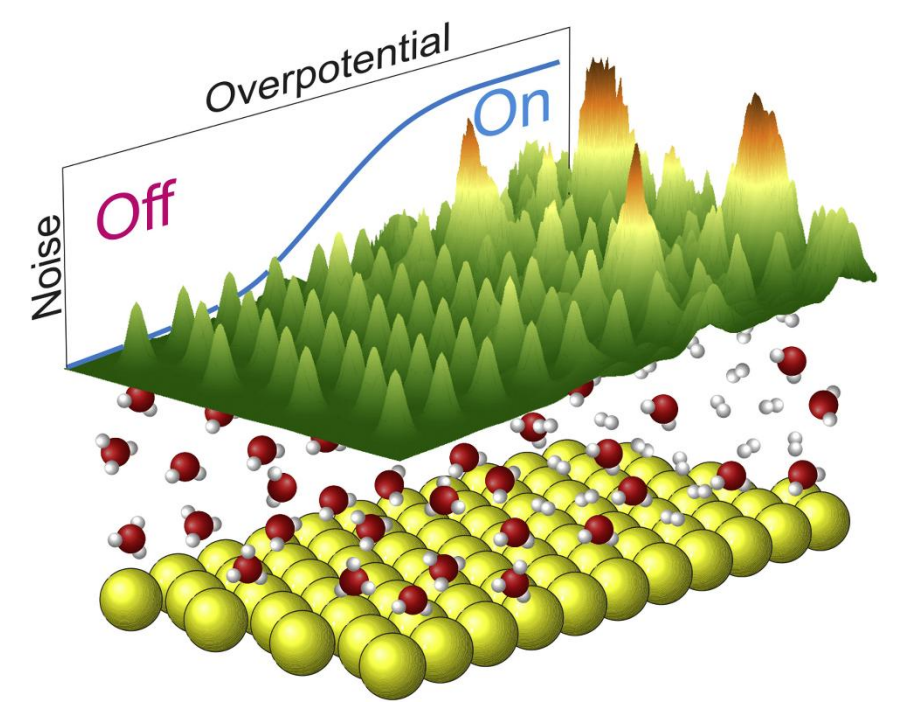


Figure 10. Monitoring the recorded EC-STM signal noise under reaction condition. Reproduced from Ref. [41]

Scanning electrochemical microscopy

Scanning electrochemical microscopy (SECM), a technique conceived by Bard and co-workers in 1986, offers unique and powerful functionality for electrocatalysis applications, and its instrument-tation is comparatively simple, inexpensive, and commercially available [8]. The instrumentation of SECM includes a probe (or tip) electrode, a bipotentiostat for independently controlling the potentials of the probe and substrate, micropositioners for scanning the probe in the *xyz* directions, and a computer to manage the system [42]. SECM is able to inspect local topography and electrochemical activity independently and simultaneously while revealing versatility towards a range of different interfaces and experimental conditions [43].

Ciocci *et al.* [44] reported the investigation of the electrochemical behavior of ITO under optoelectrochemical monitoring in scanning electrochemical cell microscopy, SECCM, configuration during the HER in 5 mM of H₂SO₄, a concentration for which the ITO electrode remains stable (Figure 11).

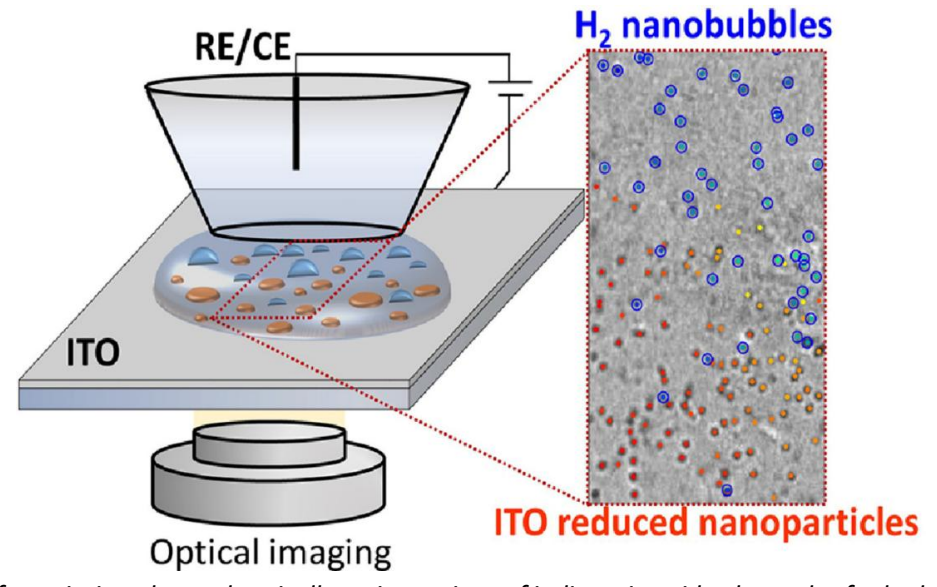


Figure 11. Differentiating electrochemically active regions of indium tin oxide electrodes for hydrogen evolution and reductive decomposition reactions using an in situ optical microscopy approach. Reproduced from Ref. [44]

The *in situ* optical monitoring through IRM allowed discriminating the formation of H_2 nanobubbles, NBs and the formation of In(0) nanoparticles, NPs, issued from the HER and the ITO electrochemical reduction, respectively. Segregation in electrode potential and space between NBs and NPs formation on the ITO electrode is observed, attributed to the intrinsic variation of the ITO conductivity. That variation was further evidenced by changing the droplet cell position on the ITO substrate and through SECM investigation. Besides, the onset potential of the NPs formation was shifted toward less negative potentials when the conductivity of the ITO increases, whereas the onset potential of the H_2 formation remained mostly unchanged.

Conclusions and future perspectives

HER is an important process in renewable energy conversion and storage systems, including electrolyzers, which transform and store intermittent renewable electricity into chemical energy by generating hydrogen. Researchers are doing their best to find solutions to challenges hindering the competitive commercialization of hydrogen energy. One of the ways to achieve this is to exploit the advantages of the *operando/in situ* characterization techniques. This has shown good progress, and research is still being done.

Recently, machine learning and artificial intelligence have been used to find the solutions to the problems we encounter and even improve technology. Their incorporation in the studies on monitoring nanocatalyst-based electrochemical HER will accelerate successful hydrogen energy production and commercialization. The miniaturization of the characterization equipment is another important parameter in this field. Volatile electrolytes disturb the functioning of some characterization instruments, e.g. they lead to the poor special resolution and contrast of TEM [45]. The consideration of the reduction of the radiolysis of water, attempting electrode preparation methods, using compressive sensing software, exploration of various electrolytes, minimizing the electron beam induced damage, and controlling the liquid film thickness, may lead to the solution. In addition, the integration of multiple operando/in situ techniques is suitable as one technique cannot provide all the necessary information. Also, the combination of theoretical calculations and experimental studies will contribute more. The integration of machine learning algorithms and automated data analysis for large data sets will bring much improvement [46].

Acknowledgments: This work was financially supported by the National Natural Science Foundation of China (22004116 and 22272036) and CAS President's International Fellowship Initiative (PIFI).

References

- [1] S. Shiva Kumar, V. Himabindu, Hydrogen production by PEM water electrolysis A review, Materials Science for Energy Technologie. **2** (2019) 442-454. https://doi.org/10.1016/j.mset.2019.03.002
- [2] H. Ishaq, I. Dincer, Comparative assessment of renewable energy-based hydrogen production methods, *Renewable and Sustainable Energy Review*. **135** (2021) 110192. https://doi.org/10.1016/j.rser.2020.110192
- [3] F. Sun, J. Qin, Z. Wang, M. Yu, X. Wu, X. Sun, J. Qiu, Energy-saving hydrogen production by chlorine-free hybrid seawater splitting coupling hydrazine degradation, *Nature Communications* **12** (2021) 4182. https://doi.org/10.1038/s41467-021-24529-3
- [4] Y. Wang, T. Williams, T. R. Gengenbach, B. Kong, D. Zhao, H. Wang, C. Selomulya, Unique Hybrid Ni₂P/MoO₂@MoS₂ Nanomaterials as Bifunctional Non-Noble-Metal Electro-Catalysts for Water Splitting, *Nanoscale* **44** (2017) 17349-17356. https://doi.org/10.1039/C7NR06186B

- [5] D. Liu, G. Xu, H. Yang, H. Wang, B. Y. Xia, Rational Design of Transition Metal Phosphide-Based Electrocatalysts for Hydrogen Evolution, *Advanced Functional Materials* **33** (2023) 2208358. https://doi.org/10.1002/adfm.202208358.
- [6] F. Liu, C. Shi, X. Guo, Z. He, L. Pan, Z. Huang, X. Zhang, J. Zou, Rational Design of Better Hydrogen Evolution Electrocatalysts for Water Splitting: A Review, *Advanced Science* **9** (2022) 2200307. https://doi.org/10.1002/advs.202200307.
- [7] A. Mondal, A. Vomiero, 2D Transition Metal Dichalcogenides-Based Electrocatalysts for Hydrogen Evolution Reaction, *Advanced Functional Materials*. 32 (2022) 2208994. https://doi.org/10.1002/adfm.202208994
- [8] Y. Yang, Y. Xiong, R. Zeng, X. Lu, M. Krumov, X. Huang, W. Xu, H. Wang, F. J. Disalvo, J. D. Brock, D. A. Muller, H. D. Abrunã, *Operando* Methods in Electrocatalysis, *ACS Catalysis* 11 (2021) 1136-1178. https://doi.org/10.1021/acscatal.0c04789
- [9] A. H. Shah, Z. Zhang, Z. Huang, S. Wang, G. Zhong, C. Wan, A. N. Alexandrova, Y. Huang, X. Duan, The role of alkali metal cations and platinum-surface hydroxyl in the alkaline hydrogen evolution reaction, *Nature Catalysis* **5** (2022) 923-933. https://doi.org/10.1038/s41929-022-00851-x
- [10] J. Proost, A. Delvaux, In-situ monitoring of hydrogen absorption into Ni thin film electrodes during alkaline water electrolysis, *Electrochimica Acta* 322 (2019) 134752. https://doi.org/10.1016/j.electacta.2019.134752
- [11] S. Ramasundaram, S. Jeevanandham, N. Vijay, S. Divya, P. Jerome, T. H. Oh, Unraveling the Dynamic Properties of New-Age Energy Materials Chemistry Using Advanced *In Situ* Transmission Electron Microscopy, *Molecules* 29 (2024) 4411. https://doi.org/10.3390/molecules29184411
- [12] X. Li, H.-Y. Wang, H. Yang, W. Cai, S. Liu, B. Liu, In Situ/Operando Characterization Techniques to Probe the Electrochemical Reactions for Energy Conversion, Small Methods 2 (2018) 1700395. https://doi.org/10.1002/smtd.201700395
- [13] S. W. Chee, T. Lunkenbein, R. Schlögl, B. R. Cuenya, *In situ* and *operando* electron microscopy in heterogeneous catalysis—insights into multi-scale chemical dynamics, *Journal of Physics: Condensed Matter* **33** (2021) 153001. https://doi.org/10.1088/1361-648X/abddfd
- [14] Y. Deng, B. S. Yeo, Characterization of Electrocatalytic Water Splitting and CO₂ Reduction Reactions Using *In Situ/Operando* Raman Spectroscopy, *ACS Catalysis* **7** (2017) 7873-7889. https://doi.org/10.1021/acscatal.7b02561
- [15] S. Zuo, Z. P. Wu, H. Zhang, X. W. Lou, *Operando* Monitoring and Deciphering the Structural Evolution in Oxygen Evolution Electrocatalysis, *Advanced Energy Materials* **12** (2022) 2103383. https://doi.org/10.1002/aenm.202103383
- [16] B. Y. Kaplan, A. C. Kırlıoğlu, M. Alinezhadfar, M. A. Zabara, N. R. Mojarrad, B. Iskandarani, A. Yürüm, C. S. Ozkan, M. Ozkan, S. A. Gürsel, Hydrogen production via electrolysis: *Operando* monitoring and analyses, *Chemical Catalysis* 3 (2023) 100601. https://doi.org/10.1016/j.checat.2023.100601
- [17] X. Ding, D. Liu, P. Zhao, X. Chen, H. Wang, F. E. Oropeza, G. Gorni, M. Barawi, M. García-Tecedor, V. A. de la Peña O'Shea, J. P. Hofmann, J. Li, J. Kim, S. Cho, R. Wu, K. H. L. Zhang, Dynamic restructuring of nickel sulfides for electrocatalytic hydrogen evolution reaction, *Nature Communications* 15 (2024) 5336. https://doi.org/10.1038/s41467-024-49015-4
- [18] P. Tang, H. J. Lee, K. Hurlbutt, P. Y. Huang, S. Narayanan, C. Wang, D. Gianolio, R. Arrigo, J. Chen, J. H. Warner, M. Pasta, Elucidating the Formation and Structural Evolution of Platinum Single-Site Catalysts for the Hydrogen Evolution Reaction, *ACS Catalysis* **12** (2022) 3173-3180. https://doi.org/10.1021/acscatal.1c05958
- [19] J. Wang, H. Y. Tan, T. R. Kuo, S. C. Lin, C. S. Hsu, Y. Zhu, Y. C. Chu, T. L. Chen, J. F. Lee, H. M. Chen, *In Situ* Identifying the Dynamic Structure behind Activity of Atomically Dispersed



- Platinum Catalyst toward Hydrogen Evolution Reaction, *Small* **17** (2021) 2005713. https://doi.org/10.1002/smll.202005713
- [20] S. Pishgar, S. Gulati, J. M. Strain, Y. Liang, M. C. Mulvehill, J. M. Spurgeon, *In Situ* Analytical Techniques for the Investigation of Material Stability and Interface Dynamics in Electrocatalytic and Photoelectrochemical Applications, *Small Methods* **5** (2021) 2100322. https://doi.org/10.1002/smtd.202100322.
- [21] P. Liu, A. Klyushin, P. Chandramathy Surendran, A. Fedorov, W. Xie, C. Zeng, X. Huang, Carbon Encapsulation of Supported Metallic Iridium Nanoparticles: An *in Situ* Transmission Electron Microscopy Study and Implications for Hydrogen Evolution Reaction, *ACS Nano* **17** (2023) 24395-24403. https://doi.org/10.1021/acsnano.3c10850
- [22] Y. He, S. Liu, M. Wang, Q. Cheng, H. Ji, T. Qian, C. Yan, Advanced *In Situ* Characterization Techniques for Direct Observation of Gas-Involved Electrochemical Reactions, *Energy & Environmental Materials* **6** (2023) e12552. https://doi.org/10.1002/eem2.12552
- [23] O. M. Magnussen, J. Drnec, C. Qiu, I. Martens, J. J. Huang, R. Chattot, A. Singer, *In Situ* and *Operando* X-ray Scattering Methods in Electrochemistry and Electrocatalysis, *Chemical Reviews* **124** (2024) 629-721. https://doi.org/10.1021/acs.chemrev.3c00331
- [24] L. Zhai, T.W. Benedict Lo, Z. Xu, J. Potter, J. Mo, X. Guo, C. C. Tang, S. C. Edman Tsang, S. P. Lau, In Situ Phase Transformation on Nickel-Based Selenides for Enhanced Hydrogen Evolution Reaction in Alkaline Medium, ACS Energy Letters 5 (2020) 2483-2491. https://doi.org/10.1021/acsenergylett.0c01385
- [25] H. Tan, B. Tang, Y. Lu, Q. Ji, L. Lv, H. Duan, N. Li, Y. Wang, S. Feng, Z. Li, C. Wang, F. Hu, Z. Sun, W. Yan, Engineering a local acid-like environment in alkaline medium for efficient hydrogen evolution reaction, *Nature Communications* 13 (2022) 2024. https://doi.org/10.1038/s41467-022-29710-w
- [26] L. Zhou, C. Yang, W. Zhu, R. Li, X. Pang, Y. Zhen, C. Wang, L. Gao, F. Fu, Z. Gao, Y. Liang, Boosting Alkaline Hydrogen Evolution Reaction via an Unexpected Dynamic Evolution of Molybdenum and Selenium on MoSe₂ Electrode, *Advanced Energy Materials* **12** (2022) 2202367. https://doi.org/10.1002/aenm.202202367
- [27] D. Johnson, H. E. Lai, K. Hansen, P. B. Balbuena, A. Djire, Hydrogen evolution reaction mechanism on Ti₃C₂ MXene revealed by *in situ/operando* Raman spectroelectrochemistry, *Nanoscale* **14** (2022) 5068-5078. https://doi.org/10.1039/d2nr00222a
- [28] A. Bazan-Aguilar, G. García, E. Pastor, J. L. Rodríguez, A. M. Baena-Moncada, *In-situ* spectroelectrochemical study of highly active Ni-based foam electrocatalysts for hydrogen evolution reaction, *Applied Catalysis B: Environmental* **336** (2023) 122930. https://doi.org/10.1016/j.apcatb.2023.122930
- [29] R. Aymerich-Armengol, M. Vega-Paredes, Z. Wang, A. M. Mingers, L. Camuti, J. Kim, J. Bae, I. Efthimiopoulos, R. Sahu, F. Podjaski, M. Rabe, C. Scheu, J. Lim, S. Zhang, *Operando* Insights on the Degradation Mechanisms of Rhenium-Doped and Undoped Molybdenum Disulfide Nanocatalysts During Hydrogen Evolution Reaction and Open-Circuit Conditions, *Advanced Functional Materials* (2024) 2413720. https://doi.org/10.1002/adfm.202413720
- [30] M. Smiljanić, M. Bele, L. J. Moriau, J. F. Vélez Santa, S. Menart, M. Šala, A. Hrnjić, P. Jovanovič, F. Ruiz-Zepeda, M. Gaberšček, N. Hodnik, Suppressing Platinum Electrocatalyst Degradation via a High-Surface-Area Organic Matrix Support, ACS Omega 7 (2022) 3540-3548. https://doi.org/10.1021/acsomega.1c06028
- [31] M. Smiljanić, A. Hrnjić, N. Maselj, M. Gatalo, P. Jovanovič, N. Hodnik, *Advanced electro-chemical methods for characterization of proton exchange membrane electrocatalysts*, in: *Polymer Electrolyte-Based Electrochemical Devices*, M. Lo Faro, S. Campagna Zignani, Eds., Elsevier Inc., 2024, pp. 49-90 https://doi.org/10.1016/B978-0-323-89784-6.00002-4

- [32] L. Moriau, T. Đukić, V. Domin, R. Kodym, M. Prokop, K. Bouzek, M. Gatalo, M. Šala, N. Hodnik, Towards improved online dissolution evaluation of Pt-alloy PEMFC electrocatalysts via electrochemical flow cell ICP-MS setup upgrades, *Electrochimica Acta* **487** (2024) 144200. https://doi.org/10.1016/j.electacta.2024.144200
- [33] P. Jovanovič, A. Pavlišič, V. S. Šelih, M. Šala, N. Hodnik, M. Bele, S. Hočevar, M. Gaberšček, New insight into platinum dissolution from nanoparticulate platinum-based electrocatalysts using highly sensitive *in situ* concentration measurements, *ChemCatChem* **6** (2014) 449-453. https://doi.org/10.1002/cctc.201300936
- [34] M. Smiljanić, M. Bele, L. Moriau, F. Ruiz-Zepeda, M. Šala, N. Hodnik, Electrochemical Stability and Degradation of Commercial Pd/C Catalyst in Acidic Media, *Journal of Physical Chemistry C* **125** (2021) 27534-27542. https://doi.org/10.1021/acs.jpcc.1c08496
- [35] W. Du, Y. Shi, W. Zhou, Y. Yu, B. Zhang, Unveiling the *In Situ* Dissolution and Polymerization of Mo in Ni4Mo Alloy for Promoting the Hydrogen Evolution Reaction, *Angewandte Chemie International Edition* **60** (2021) 7051-7055. https://doi.org/10.1002/anie.202015723
- [36] J.-F. Lemineur, P. Ciocci, J.-M. Noël, H. Ge, C. Combellas, F. Kanoufi, Imaging and Quantifying the Formation of Single Nanobubbles at Single Platinum Nanoparticles during the Hydrogen Evolution Reaction, *ACS Nano* **15** (2021) 2643-2653. https://doi.org/10.1021/acsnano.0c07674
- [37] N. Hodnik, G. Dehm, K. J. J. Mayrhofer, Importance and Challenges of Electrochemical *in Situ* Liquid Cell Electron Microscopy for Energy Conversion Research, *Accounts of Chemical Research* **49** (2016) 2015-2022. https://doi.org/10.1021/acs.accounts.6b00330
- [38] H. Cheng, S. Wang, G. Chen, Z. Liu, D. Caracciolo, M. Madiou, S. Shan, J. Zhang, H. He, R. Che, C. Zhong, Insights into Heterogeneous Catalysts under Reaction Conditions by *In Situ/Operando* Electron Microscopy, *Advanced Energy Materials* 12 (2022) 2202097. https://doi.org/10.1002/aenm.202202097
- [39] Q. Fu, L. W. Wong, F. Zheng, X. Zheng, C. S. Tsang, K. H. Lai, W. Shen, T. H. Ly, Q. Deng, J. Zhao, Unraveling and leveraging in situ surface amorphization for enhanced hydrogen evolution reaction in alkaline media, *Nature Communications* 14 (2023) 6462. https://doi.org/10.1038/s41467-023-42221-6
- [40] R. M. Kluge, R. W. Haid, I. E. L. Stephens, F. Calle-Vallejo, A.S. Bandarenka, Monitoring the active sites for the hydrogen evolution reaction at model carbon surfaces, *Physical Chemistry Chemical Physics* **23** (2021) 10051-10058. https://doi.org/10.1039/d1cp00434d
- [41] M. Lunardon, T. Kosmala, C. Durante, S. Agnoli, G. Granozzi, Atom-by-atom identification of catalytic active sites in *operando* conditions by quantitative noise detection, *Joule* **6** (2022) 617-635. https://doi.org/10.1016/j.joule.2022.02.010
- [42] D. Wang, J. Wu, L. Jiao, L. Xie, *In situ* identification of active sites during electrocatalytic hydrogen evolution, *Nano Research* **16** (2023) 12910-12918. https://doi.org/10.1007/s12274-023-5686-y
- [43] D. Valavanis, P. Ciocci, I. J. McPherson, G. N. Meloni, J.-F. Lemineur, F. Kanoufi, P. R. Unwin, *Operando* Electrochemical and Optical Characterization of the Meniscus of Scanning Electrochemical Cell Microscopy (SECCM) Probes, *ACS Electrochemistry* (2024) https://doi.org/10.1021/acselectrochem.4c00029.
- [44] P. Ciocci, J.-F. Lemineur, J.-M. Noël, C. Combellas, F. Kanoufi, Differentiating electrochemically active regions of indium tin oxide electrodes for hydrogen evolution and reductive decomposition reactions. An *in situ* optical microscopy approach, *Electrochimica Acta* **386** (2021) 138498. https://doi.org/10.1016/j.electacta.2021.138498
- [45] Z.-H. Xie, Z. Jiang, X. Zhang, Promises and Challenges of *In Situ* Transmission Electron Microscopy Electrochemical Techniques in the Studies of Lithium Ion Batteries, *Journal of The Electrochemical Society* **164** (2017) A2110-A2123. https://doi.org/10.1149/2.1451709jes



[46] A. R. Kamšek, F. Ruiz-Zepeda, A. Pavlišič, A. Hrnjić, N. Hodnik, Bringing into play automated electron microscopy data processing for understanding nanoparticulate electrocatalysts' structure-property relationships, *Current Opinion in Electrochemistry* **35** (2022) 101052. https://doi.org/10.1016/j.coelec.2022.101052

©2024 by the authors; licensee IAPC, Zagreb, Croatia. This article is an open-access article distributed under the terms and conditions of the Creative Commons Attribution license (https://creativecommons.org/licenses/by/4.0/)



Open Access:: ISSN 1847-9286 www.jESE-online.org

Original scientific paper

Polyaniline prepared by Fe₃O₄ catalysed eco-friendly synthesis as electrocatalyst for efficient water electrolysis

Jadranka Milikić¹, Jana Mišurović¹,², Lazar Rakočević³, Igor A. Pašti¹, Gordana Ćirić-Marjanović¹ and Biljana Šljukić¹,⊠

¹University of Belgrade - Faculty of Physical Chemistry, Studentski trg 12-16, 11158, Belgrade, Serbia ²Now at University of Montenegro, Faculty of Metallurgy and Technology, Cetinjski put, bb, 81000 Podgorica, Montenegro

³University of Belgrade, "VINČA" Institute of Nuclear Sciences, National Institute of the Republic of Serbia, Mike Petrovića Alasa 12-14, 11000, Belgrade, Serbia

Corresponding authors: [™]*biljka@ffh.bg.ac.rs*

Received: July 22, 2024; Accepted: September 9, 2024; Published: October 30, 2024

Abstract

Preparing cost-effective and highly active catalysts for electrocatalytic hydrogen evolution reaction is crucial for developing hydrogen-based technologies. Hence, four conductive polyanilines, prepared by the environmentally-friendly approach using Fe₃O₄ nanoparticles/ H_2O_2 as the catalyst/main oxidant system (PANI/Fe₃O₄), were investigated for the first time as electrocatalysts for hydrogen evolution reaction (HER) in acidic media (0.1 M H_2SO_4) by using voltammetry and chronoamperometry. PANI/Fe₃O₄ electrodes exhibited Tafel slope values in the -171 to -246 mV dec⁻¹ range depending on the synthesis conditions – Fe₃O₄/aniline mass ratio and polymerization time. The sample PANI/Fe₃O₄-II(3) prepared with shorter reaction time and higher Fe₃O₄/aniline mass ratio showed the best electrocatalytic behaviour reflected in the lowest onset potential (-0.286 V), the lowest overpotential to reach a current density of -10 mA cm⁻², the highest current density, the lowest HER activation energy (10 kJ mol⁻¹), and the lowest charge-transfer resistance (5.3 Ω) under HER conditions. Materials were characterized by scanning electron microscopy with energy dispersive X-ray spectroscopy, X-ray photoelectron spectroscopy and electrochemical impedance spectroscopy, and differences in their electrocatalytic HER performance were explained by differences in their content of Fe₃O₄, surface and electrical properties. Moreover, the possibility of using PANI/Fe₃O₄-II(3) as HER electrocatalyst in a wider range of pH (i.e. in alkaline media as well) and as a bifunctional electrocatalyst, i.e. for oxygen evolution reaction beside HER, was also examined.

Kevwords

Hydrogen evolution reaction; oxygen evolution reaction; conducting polymers; transition metal oxides; electrocatalysis

Introduction

Intensive research in electrochemistry is devoted to finding the appropriate way to transform and store hydrogen energy [1-5]. The electrochemical hydrogen evolution reaction (HER) is probably the most important reaction to produce hydrogen (H_2) in a simple, clean, and efficient way. HER mechanism in acidic media takes two possible pathways: Volmer-Heyrovsky (Eqs. 1 and 2) or Volmer-Tafel pathway (Eqs. 1 and 3) [6]:

$$H_3O^+ + e^- + * \rightarrow H_{ads} + H_2O$$
 Volmer reaction (1)

$$H_3O^+ + e^- + H_{ads} \rightarrow H_2 + H_2O + *$$
 Heyrovsky reaction (2)

$$H_{ads} + H_{ads} \rightarrow H_2 + *$$
 Tafel reaction (3)

where * represents an active site on the surface of the electrocatalyst.

Many electrocatalysts have been tested for HER, where platinum (Pt) is the most active, demonstrating fast HER kinetics with low overpotential and high current densities [5]. Still, the application of this metal on an industrial scale is limited because of its high price. Finding an appropriate electrocatalyst for HER that is inexpensive and efficient, with good performance and stability during HER, is vital for future applications in the industry and energy systems. Electrocatalysts based on nonprecious metals such as iron (Fe), nickel (Ni), cobalt (Co), and copper (Cu) are investigated for HER in both acidic and alkaline solutions [7-11]. Composites of MoCoFeS (MCFS) with different amounts of reduced graphene oxide (rGO), MCFS/rGO, were examined for HER in acidic media (0.5 M H₂SO₄) [10]. It was shown that MCFS/rGO electrocatalysts with a mass ratio of rGO up to 0.4 have good HER activity with high current densities and low Tafel slopes of ca. 50 to 60 mV dec⁻¹ [10]. Fe, Co, and Fe-Co alloy encapsulated in nitrogen-doped carbon nanotubes (CNTs) were characterised for HER by voltammetry and density functional theory (DFT) calculations in acidic media [6]. HER activity of these electrocatalysts significantly increased with increasing the amount of nitrogen. Fe-Co alloy showed the best performance for HER with the smallest overpotential and the onset potential value of ca. 70 mV vs. RHE in 0.1 M H₂SO₄ [6]. Iron phosphide (FeP) nanoparticles synthesised by phosphorization of α-Fe₂O₃ showed excellent HER performance and stability in 0.5 M H₂SO₄ due to the change of surface-charge-transfer resistance [12]. Fe_{1.89}Mo_{4.11}O₇/MoO₂ showed good stability during HER in both acidic and alkaline media [13]. The Tafel slope and an exchange current density were calculated to be -47 and 0.072 mA cm⁻², respectively, in acidic media [13]. A hybrid composite consisting of Fe₃C nanorods encapsulated in N-doped carbon nanotubes (CNTs) was presented as a good HER electrocatalyst in both alkaline and acidic media with Tafel slope of -113 and -97 mV dec⁻¹ in these media, respectively [14]. Fe₃O₄ on graphite sheets were synthesized by one-pot hydrothermal method and exhibited favourable HER kinetics in alkaline media with low Tafel slope of -78 mV dec⁻¹, as well as long-term stability under HER conditions [15].

Conductive polymers have broad applications in electrochemical energy conversion and storage [16]. Polyaniline (PANI), as a low-cost conductive polymer, has excellent chemical and physical properties and a delocalized π -conjugated structure [17,18]. It can be easily synthesized [18-20] and combined with other active materials, improving the electrocatalytic activity, conductivity, and stability [17,21,22]. PANI was shown to be a useful electrode material for promoting HER [23-26] and oxygen evolution reaction (OER) [27-31] over a wide pH range. It is frequently used as metal electrocatalyst support due to its advantages, such as good flexibility, variety of controllable morphologies, and ability to provide more active sites [32,33]. It was also reported that the conductive PANI is favourable for HER due to its sufficient protonated sites [33]. For instance, several electrocatalysts combining PANI polymer and semiconductor Na₄Ge₉O₂₀ as a support for low amounts of Pt nano-

particles (Pt NPs) were investigated for HER in 0.5 M H_2SO_4 [17]. 5 wt.% Pt/Na₄Ge₉O₂₀-PANI gave an overpotential of -33 mV, *i.e.*, close to that of commercial 20 wt.% Pt/C electrocatalyst (21 mV), demonstrating that PANI and Pt NPs improve HER kinetics due to the increased number of transferring electrons and active sites [17]. RuO₂-Ta₂O₅/PANI composite presented the HER catalytic process by Volmer-Heyrovsky mechanism where Tafel slope was found to be -69.2 mV dec⁻¹ and the overpotential amounted to -185 mV in 0.5 M H_2SO_4 [34]. Nevertheless, the electrocatalysis of HER using PANI-based materials with low concentrations of non-noble metals was not addressed in detail, and such studies could pave the way toward the development of low-cost electrocatalysts for acidic water electrolysis as non-noble metals (Fe, Co, Ni) are generally unstable in acidic media.

The common method for synthesizing PANI is the chemical oxidative polymerization of aniline, most frequently using the powerful oxidant ammonium peroxydisulfate (APS) [18]. This type of reaction also gives undesired inorganic by-products (*e.g.* ammonium hydrogen sulphate) that should be removed by the post-synthetic treatments. For the most environmentally friendly polymerization of aniline, the best oxidizing agent would be hydrogen peroxide (H₂O₂) since the product of its reduction is water. However, due to the low reactivity of H₂O₂, its usage for efficient aniline polymerization leading to PANI of high electrical conductivity needs the addition of a suitable catalyst. Different catalysts were explored for this purpose, such as transition metal salts [35] and peroxidase-type enzymes [20,36].

In this study, four PANI/Fe₃O₄ materials were synthesized under different reaction conditions via environmentally friendly aniline oxidative polymerization by using H_2O_2 as a main oxidant, Fe₃O₄ NPs as a catalyst, and a very small amount of ammonium peroxydisulfate (APS) [37] were examined as electrocatalysts for HER in acidic media (0.1 M H_2SO_4) by voltammetry and chronoamperometry. The surface and electrical properties of materials, determined by scanning electron microscopy with energy dispersive X-ray analysis (SEM-EDX), X-ray photoelectron spectroscopy (XPS), and electrochemical impedance spectroscopy (EIS), were correlated with their electrocatalytic performance. The possibility of using PANI/Fe₃O₄ as HER electrocatalyst in a wider pH range and as a bifunctional electrocatalyst, *i.e.*, for OER beside HER, was also examined.

Experimental

PANI/Fe₃O₄ materials were prepared by the oxidative chemical polymerization of aniline monomer (monomer solution containing 0.2 M aniline hydrochloride, formed *in situ*, and 0.2 M HCl obtained by mixing specified amounts of aniline (1.824 ml) and HCl (3.357 ml) in water (100 ml) with eco-friendly oxidant H₂O₂ (0.25 M) and a small amount of APS (0.1 mM), in the presence of catalytic amounts of Fe₃O₄ NPs, by the procedures reported in [37]. Fe₃O₄ NPs were synthesized by the procedure described in [37], starting from the aqueous solution of ferric chloride hexahydrate and ferrous sulphate heptahydrate and performing precipitation of Fe₃O₄ NPs by NH₄OH. H₂O₂ was successfully used as the main oxidant thanks to Fe₃O₄ NPs, which served as a catalyst, while a small amount of added APS enabled efficient initiation [37]. All PANI/Fe₃O₄ samples were prepared at mole ratios [H₂O₂]/[aniline] = 1.25 and [APS]/[aniline] = 0.0005. Samples synthesized at mass ratio Fe₃O₄ NPs/aniline of 0.0015 were denoted PANI/Fe₃O₄-I(3) and PANI/Fe₃O₄-II(3) and PANI/Fe₃O₄-II(7), where the labels (3) and (7) refer to polymerization times of 3 days and 7 days, respectively.

LCR meter, model LCR-6100 (GW Instek, Taiwan) at room temperature and constant frequency (1.0 kHz) on a pellet pressed between two stainless steel pistons (under pressure of \sim 4 MPa by a manual hydraulic press) was used for measuring the electrical conductivity of powdered samples [37].

The morphology of the samples and their elemental composition were characterized by SEM-EDX using a scanning electron microscope JEOL JSM-660LV, along with elemental mapping. Prior to the analysis, samples were coated with a thin layer of gold using LEICA SCD005 Sputter Coater.

XPS analysis was performed using SPECS Systems with XP50M X-ray source for Focus 500 X-ray monochromator and PHOIBOS 100/150 analyser using AlK α (1486.74 eV) anode at a 12.5 kV and 32 mA as a source. Survey spectra (1000 - 0 eV binding energy) were recorded with a constant pass energy of 40 eV, step size 0.5 eV, and dwell time of 0.2 s in the FAT mode. Detailed spectra of C 1s, N 1s, and O 1s were recorded with a constant pass energy of 20 eV, step size of 0.1 eV, and dwell time of 2s in the FAT mode.

The catalytic inks were prepared by ultrasonically dispersing powder mixtures of each of the four samples (4 mg) and commercial Vulcan XC72 conductive carbon black (1 mg) in 2 wt.% polyvinylidene fluoride solution in N-methyl-2-pyrrolidone (125 μ l). 10 μ L of each ink was deposited onto a glassy carbon tip and dried at 110 °C overnight.

Electrochemical measurements were performed using PAR 273A Princeton Potentiostat/Galvanostat in a one-compartment glass cell of 50 ml volume. Pt wire or graphite rod served as a counter electrode, and saturated calomel electrode (SCE) served as a reference electrode. All potentials within this paper were converted to the reversible hydrogen electrode (RHE) scale. $0.1~M~H_2SO_4$ solution was used as an electrolyte.

HER polarization curves were recorded at 2 mV s⁻¹ and different temperatures from 25 to 75 °C using a Haake F3 bath. Chronoamperometric (CA) curves of all PANI/Fe₃O₄ electrocatalysts were recorded at a potential 0.1 V more negative than the onset potential for 1 h.

Cyclic voltammetry (CV) measurements of four PANI/Fe $_3$ O $_4$ electrocatalysts were performed in 0.1 M H $_2$ SO $_4$ saturated with nitrogen at different scan rates ranging from 10 to 300 mV s $^{-1}$. Electrochemical impedance spectroscopy (EIS) measurements were conducted in the frequency range from 100 kHz to 0.1 Hz, with 5 mV amplitude, at different potentials.

HER polarization curves were also recorded in 8 M KOH as an electrolyte, with this concentration corresponding to the KOH concentration used in industrial alkaline water electrolysers. Finally, polarization curves were recorded under oxygen evolution reaction conditions at 10 mV s⁻¹ in both $0.1 \, \text{M} \, \text{H}_2 \text{SO}_4$ and $8 \, \text{M} \, \text{KOH}$.

Results and discussion

Electrical conductivity and morphology of PANI/Fe₃O₄ electrocatalysts

A detailed characterization of PANI/Fe₃O₄ samples showed that the products obtained were PANIs in their conductive form, emeraldine salt (ES) [37]. This finding, together with the presence of Fe₃O₄ NPs in all samples (although in very small, catalytic amounts), makes these materials promising candidates for HER. Samples PANI/Fe₃O₄-II(3) and PANI/Fe₃O₄-II(7), synthesized at a higher mass ratio of Fe₃O₄ NPs/aniline (0.015), exhibited good electrical conductivities of 10 and 15 mS cm⁻¹, respectively. Conversely, the other two samples, PANI/Fe₃O₄-I(3) and PANI/Fe₃O₄-I(7), which were prepared at lower mass ratio Fe₃O₄ NPs/ aniline (0.0015), showed lower conductivities of 4.6 and 7.3 mS cm⁻¹, respectively [37]. SEM images reveal mutually similar morphology of PANI/Fe₃O₄ samples, which is predominantly granular, with irregularly shaped particles (Figure 1A, 1C, 1E, 1G).

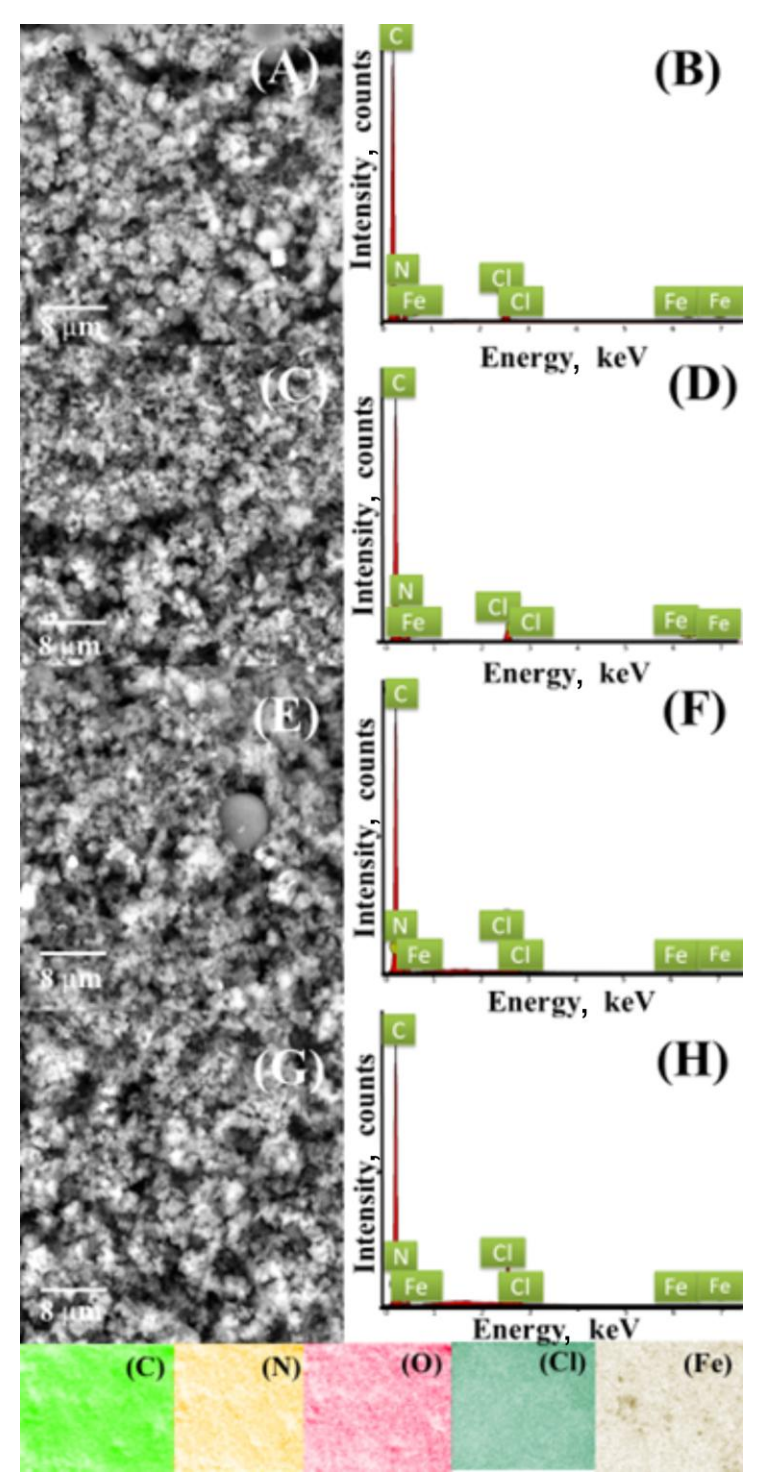


Figure 1. A, C, E, G: SEM images of four PANI/Fe₃O₄ electrocatalysts. B, D, F, H: their corresponding EDX spectra with elemental mapping of PANI/Fe₃O₄-I(3)

EDX analysis (Figure 1B, 1D, 1F, 1H) confirmed the presence of C, N, Fe, O, and Cl, with their distribution evidenced by elemental mapping. The presence of chlorine could be expected since the monomer solution contained aniline hydrochloride and HCl in excess so that Cl⁻ ions are incorporated in the final PANI/Fe₃O₄ mainly as dopant anions in PANI-ES conducting form. The presence of chlorine covalently bound to aromatic rings (C-Cl) is also possible [38]. The presence of Fe revealed by EDX in the samples follows previous XRD analysis where diffractograms of PANI/Fe₃O₄ samples showed peaks characteristic for the crystalline magnetite and confirmed incorporation of Fe₃O₄ NPs in the PANI matrix during synthesis [37]. Fe amount was determined by EDX mapping to be 0.64, 0.46, 0.35 and 0.25 wt.% for II(3), I(3), II(7), and I(7) samples, respectively, revealing that

longer polymerization time led to decrease in Fe content, as might be expected due to increased yield of PANI.

XPS survey spectra for PANI/Fe₃O₄ samples are shown in Figure 2A. They confirm the presence of C, N, O, and Cl in all four samples by their characteristic peaks. Peaks of Fe are not visible in any of the spectra. The most likely reason is that a thin layer of PANI covers Fe (from Fe₃O₄ NPs used in catalytic amounts). Therefore, as a strictly surface analysis, XPS could not detect Fe. All four samples show similar survey spectra that originate from PANI. The atomic percentages of 80.3, 10.8, 5.3, and 3.6 % were obtained for C, N, O, and Cl elements, respectively, derived from survey XPS spectra for the PANI/Fe₃O₄-II (3) sample. The peak at *ca.* 200 eV corresponds to Cl 2p, where chlorine can exist in the form of ionic (Cl⁻) or covalent (C-Cl) species whose peak positions are close, *ca.* 198 and 200 eV, respectively, similar to what was reported for PANI-ES doped with HCl [39].

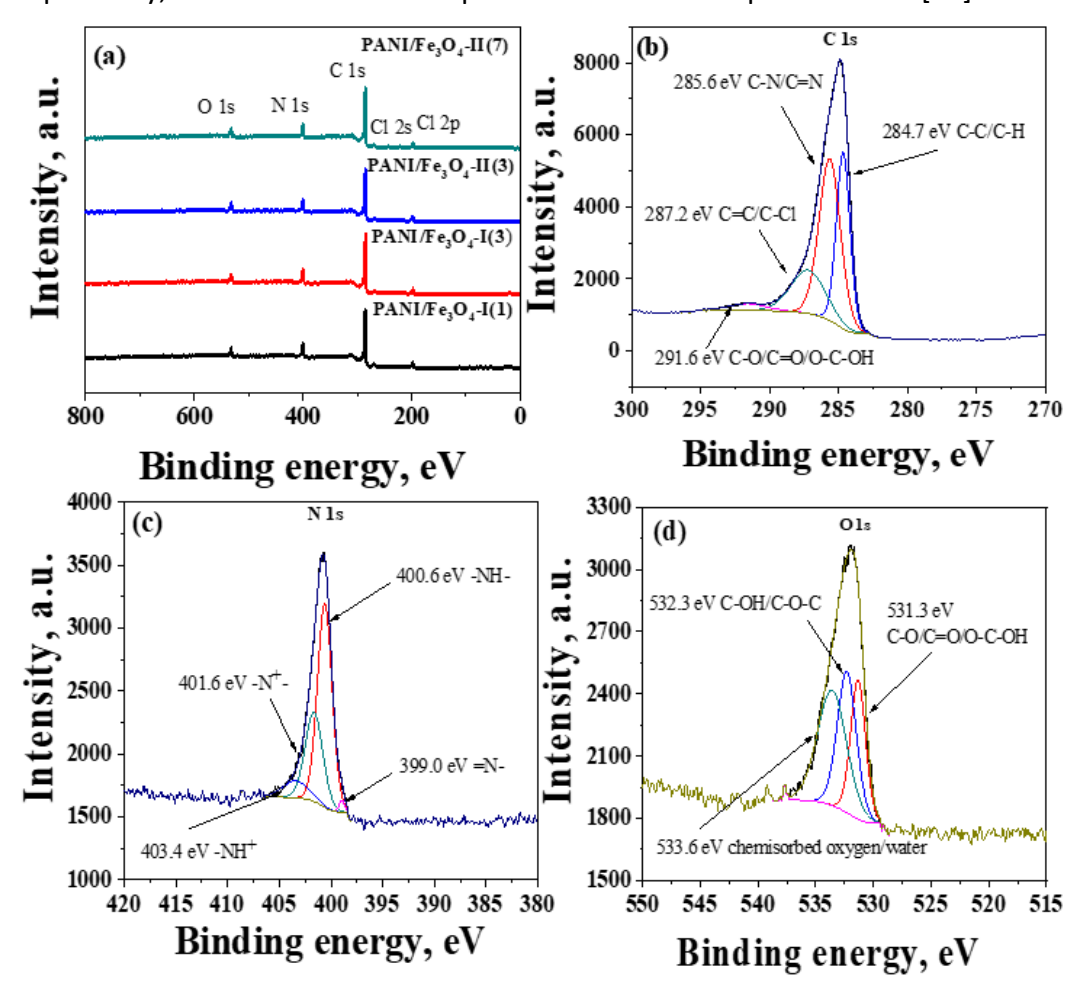


Figure 2. A: XPS survey spectra for all PANI/Fe $_3O_4$ samples; B: Detailed XPS spectra of C 1s; C: Detailed XPS spectra of O 1s

Detailed XPS C 1s signal for sample PANI/Fe $_3O_4$ -II(3), which showed the highest electrocatalytic activity (see below), is shown in Figure 2B. Carbon peak can be deconvoluted into four components. The small intensity component at 291.6 eV originates from carbon-oxygen bonds in C-O, C=O, or O-C-OH groups at similar binding energies. The component at 287.2 eV corresponds to either a double C=C bond or a carbon bound to chlorine (C-Cl) located at similar binding energies. The third component at 285.6 eV originates from bonds of carbon and nitrogen in polaron and bipolaron PANI structures, C-N⁺ and C=N⁺. The last component at 284.8 eV corresponds to either C-C or C-H bond in the PANI backbone structure [40-43].

High-resolution N 1s spectrum for sample PANI/Fe₃O₄-II(3) is shown in Figure 2C. Spectra can be deconvoluted into four components. Components at 403.4, 401.6, 400.6 and 399.0 eV can be attributed to positively charged N species -NH $^+$ and -N $^+$ -, benzenoid amine -NH- and quinonoid imine =N- functional groups, respectively. These functional groups correspond to the PANI structure confirming the nature of the surface of samples [39].

Detailed XPS spectra of O 1s for sample PANI/Fe₃O₄-II(3) (Figure 2D) can be deconvoluted into three components. The component at 533.6 eV is attributed to oxygen originating from chemisorbed water on the surface of PANI. The component at 532.3 eV is attributed to different carbonoxygen C-OH or C-O-C bonds, and a component at 531.3 eV that is also assigned to either C-O, C=O or O-C-OH bonds [39], where C=O (for example, present in benzoquinone species) can be formed by partial hydrolysis of reaction intermediates during PANI synthesis [18].

All the detailed spectra confirm that the surface of the samples consists of a layer of PANI polymer that covers the entire surface and is overlayed over any present Fe.

Percentages for each functional group present in high-resolution XPS spectra of C 1s, N 1s and O 1s for PANI/Fe₃O₄-II(3) are summarized in Table 1.

C 1s	C-C/C-H	C-N/C=N	C=C/C-CI	C-O/C=O/C-OH
 Content, %	31.5	45.4	19.8	3.3
N 1s	=N-	-NH-	-N ⁺ -	-NH⁺
 Content, %	59.0	30.8	8.9	1.3
 O 1s	C-O/C=O/O-C-OH	C-O-C/C-OH	Chemisorbed water	
 Content, %	25.7	33.1	41.2	

Table 1. Content of individual functional groups for PANI/Fe₃O₄-II(3) derived from detailed XPS spectra

Investigation of HER and OER at PANI/Fe₃O₄ electrocatalysts

The HER onset potentials in 0.1 M H_2SO_4 , defined as the potential to reach a current density of -1 mA cm⁻² [44], increased in the order PANI/Fe₃O₄-II(3) (-0.286 V) < PANI/Fe₃O₄-II(7) (-0.397 V) < PANI/Fe₃O₄-I(7) (-0.564 V) < PANI/Fe₃O₄-I (3) (-0.598 V), (Figure 3A). The highest current densities are obtained for PANI/Fe₃O₄-II(3), followed by PANI/Fe₃O₄-II(7), PANI/Fe₃O₄-I(7) and PANI/Fe₃O₄-I(3). The HER overpotential at the current density of -10 mA cm⁻² (η_{10}) for PANI/Fe₃O₄-II(3) is found to be -444 mV (current density of -10 mA cm⁻² was not reached using the other three studied materials). This overpotential was determined as a difference between the potential to reach -10 mA cm⁻² and the equilibrium potential value of the hydrogen electrode (*i.e.* referred to 0 V vs. RHE).

Tafel slope (*b*) and the exchange current density (*j*₀) values for HER at four studied materials were calculated to estimate HER kinetics and their values are presented in Table 2. Tafel slope values increased in the order PANI/Fe₃O₄-II(7) (-171 mV dec⁻¹) < PANI/Fe₃O₄-II(3) (-182 mV dec⁻¹) < PANI/Fe₃O₄-I(7) (-204 mV dec⁻¹) < PANI/Fe₃O₄-I(3) (-246 mV dec⁻¹). The Tafel slopes higher than the theoretically expected values might originate in the uncompensated resistance along with the limited number of active sites of PANI/Fe₃O₄ electrocatalysts where protons could be adsorbed. Namely, Tafel slope takes value of 30, 40 or 120 mV dec⁻¹ for Tafel, Heyrovsky or Volmer step, respectively, being the rate determining step. The observed resistance might arise from the wiring, solution and substrate, as well as from a slow charge transport [45] and it is further examined by EIS (page 9, last paragraph). PANI/Fe₃O₄-II(3) gave the highest exchange current density (37 μ A cm⁻²) followed by PANI/Fe₃O₄-I(7), PANI/Fe₃O₄-I(3) and PANI/Fe₃O₄-II(7) electrocatalysts.

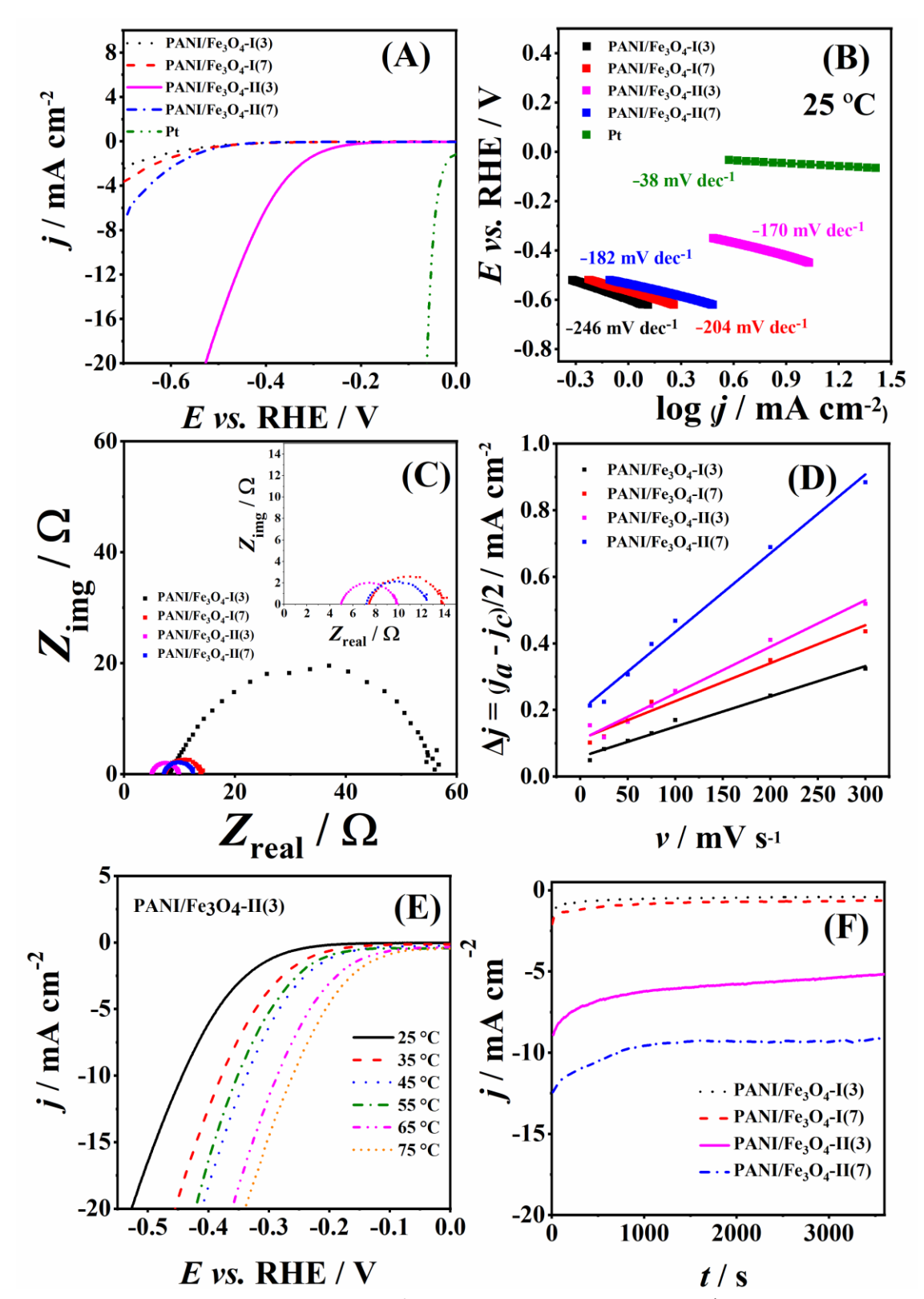


Figure 3. A: polarization curves of four PANI/Fe₃O₄ electrocatalysts at 2 mV s⁻¹ and 25 °C (IR-corrected); B: their corresponding Tafel plots; C: their Nyquist plots at -0.5 V; D: their $\Delta j = ((j_a - j_c)/2)$ as a function of polarisation rate; E: polarization curves of PANI/Fe₃O₄-II(3) at temperatures from 25 to 75 °C at 2 mV s⁻¹ (IR-corrected); F: chronoamperometric curves of four PANI/Fe₃O₄ electrocatalysts. All measurements were done in 0.1 M H₂SO₄ (N₂-saturated electrolyte in the case of D)

PANI/Fe₃O₄-II(3) showed the best performance for HER in terms of the lowest onset potential, the highest current densities, the lowest value of η_{10} , and the highest exchange current density, followed by PANI/Fe₃O₄-II(7). On the other hand, PANI/Fe₃O₄-I(3) and PANI/Fe₃O₄-I(7) showed high

HER onset potential, low current densities, and low exchange current densities (Table 2), thus exhibiting poor HER activity. Some of the possible reasons for this difference in the four electrocatalysts' activity for HER are the differences in their electrical conductivities and charge transfer kinetics [46], along with differences in their hydrogen and reaction intermediates adsorption energy [47] and bonding [48]. PANI/Fe₃O₄-II(3) and PANI/Fe₃O₄-II(7) have one order of magnitude higher electrical conductivities compared to those of PANI/Fe₃O₄-I(3) and PANI/Fe₃O₄-I(7). Still, polycrystalline Pt as a benchmark HER electrocatalyst showed significantly better HER kinetic parameters compared with the presented PANI/Fe₃O₄ electrocatalysts in acidic media (Table 2). On the other hand, Pt has a much higher price than PANI/Fe₃O₄ electrodes.

Table 2. Comparison of HER performance of PANI/Fe $_3O_4$ with other non-noble metal-based electrocatalysts in acidic media

Electrocatalyst	Electrolyte	b / mV dec ⁻¹	<i>j</i> ₀ / μA cm ⁻²	Reference
PANI/Fe ₃ O ₄ -I(3)	0.1 M H ₂ SO ₄	-246	3.6	This work
PANI/Fe ₃ O ₄ -I(7)	0.1 M H ₂ SO ₄	-204	1.7	This work
PANI/Fe ₃ O ₄ -II(3)	0.1 M H ₂ SO ₄	-182	37.0	This work
PANI/Fe ₃ O ₄ -II(7)	0.1 M H ₂ SO ₄	-170	0.72	This work
Pt	0.5 M H ₂ SO ₄	-38	460	This work
MCFS/rGO1/GC ^c	0.5 M H ₂ SO ₄	-202.6	/	[10]
Fe _{1.89} Mo _{4.11} O ₇ /MoO ₂	0.5 M H ₂ SO ₄	-47	72.0	[13]
Fe/MoO ₂	0.5 M H ₂ SO ₄	-128	/	[13]
Fe₃C@NCNT	0.5 M H₂SO ₄	-97	/	[14]
RuNi-NSs@PANI ^g	0.5 M H ₂ SO ₄	-73.1	-	[22]
PANI/CoNiPeNF ^h	0.5 M H ₂ SO ₄	-80	-	[47]
β-INS nanosheets ^a	0.5 M H ₂ SO ₄	-48	14.0	[49]
Fe₂N/rGO	0.5 M H ₂ SO ₄	-161	370.0	[50]
Fe _{4.5} Ni _{4.5} S ₈ ^b	0.5 M H ₂ SO ₄	-72	/	[51]
NHPBA ^d	0.5 M H ₂ SO ₄	-157	/	[52]
Fe-WOxP ^e	0.5 M H ₂ SO ₄	-80	156.0	[53]
FeP (1:1) ^f	0.5 M H ₂ SO ₄	-82	/	[54]
FeP (1:4) ^f	0.5 M H ₂ SO ₄	-69	/	[54]
Ni-PANI	0.5 M H ₂ SO ₄	-131 to -147	0.119 to 0.239	[55]

^airon-nickel sulfide (INS); ^ba direct 'rock' electrode; ^cMoCoFeS supported reduced graphene oxide deposited on glassy carbon (MCFS/rGO/GC; ^dnickel hydroxide array with K₃[FeIII(CN)₆] (NHPBA); ^eiron-doped tungsten oxide nanoplate/reduced graphene oxide nanocomposite (Fe-WOxP); ^firon phosphide pristine; ^gRu-doped Ni(OH)₂ nanosheets; ^hNickel foam

A higher electrical conductivity, *i.e.*, lower charge-transfer resistance of PANI/Fe₃O₄-II(3) and PANI/Fe₃O₄-II(7), was confirmed by EIS measurements in 0.1 M H₂SO₄, Figure 3C. The electrolyte resistance (R_s) as the first point of Nyquist plots of PANI/Fe₃O₄-II(3), PANI/Fe₃O₄-II(7), PANI/Fe₃O₄-I(7), and PANI/Fe₃O₄-I(3) is found to be similar, *i.e.*, 5.1, 7.2, 7.5, and 8.3 Ω , respectively, indicating well-maintained geometry of the experimental setup. The charge-transfer resistance (R_{ct}) was determined to be 4.8, 5.3, and 6.3 Ω for PANI/Fe₃O₄-II(3), PANI/Fe₃O₄-II(7) and PANI/Fe₃O₄-I(7), respectively. A much higher R_{ct} value of 47.8 Ω was determined for PANI/Fe₃O₄-II(3). It can be seen that PANI/Fe₃O₄-II(3) showed very low R_{ct} steaming from the presence of the highest amount of Fe (determined by EDX mapping) and the strong electronic coupling of PANI with Fe₃O₄ [46]. Moreover, it was suggested that the interaction between PANI and Fe₃O₄ lowers the contact resistance and further impacts HER adsorption/desorption of reaction intermediates. This assumption is consistent with highest content of Fe in PANI/Fe₃O₄-II(3) measured by EDX, as well as with higher content of Fe₃O₄ NPs revealed by XRD measurements [37] in PANI/Fe₃O₄-II(3) (mass ratio Fe₃O₄/aniline = 0.015) than in PANI/Fe₃O₄-I(3) (mass

ratio Fe₃O₄/aniline = 0.0015), both samples synthesized with the same polymerization time. These results support-the importance of Fe₃O₄ NPs content and PANI and Fe₃O₄ interactions for HER activity of PANI/Fe₃O₄ material. Namely, theoretical considerations by DFT have confirmed that the Gibbs free energy of hydrogen adsorption, as one of the main indicators of material's activity towards catalysis of HER, is reduced in the presence of PANI [47].

Thus, in addition to electrical conductivity, herein observed favourable HER kinetics at PANI/Fe₃O₄-II(3) may be explained by the synergistic effect of PANI and Fe₃O₄ NPs. PANI stabilizes metal/metal oxide NPs [48]. Furthermore, it has been suggested that during HER in acidic media, PANI with abundant electrons on N atoms effectively weakens the bonding of H⁺ in H₃O⁺ ions and captures H⁺, forming protonated amine groups [48]. These H⁺ may easily transfer from the protonated amine groups to the surface of metal oxide NPs with a low transfer barrier. Homogeneously distributed Fe₃O₄ NPs of 10 to 50 nm size [19] in PANI/Fe₃O₄-II(3) represent numerous active sites. Finally, the H atoms adsorbed on metal oxide react mutually, generating H₂ gas.

To compare the number of active sites at four PANI/Fe₃O₄ electrocatalysts, their effective surface area (ESA) is evaluated by calculating the double-layer capacitance ($C_{\rm cl}$). $C_{\rm cl}$ is calculated from cyclic voltammetry plotting the difference $\Delta j = (j_a - j_c)/2$ at 0.1 V vs. sweep rate (Figure 3D) [48] and it is found to be 2.4, 1.4, 1.1 and 0.9 μ F cm⁻² for PANI/Fe₃O₄-II(7), PANI/Fe₃O₄-II(3), PANI/Fe₃O₄-II(7) and PANI/Fe₃O₄-II(3), respectively. The obtained $C_{\rm cl}$ value of PANI/Fe₃O₄-II(3) indicates its higher ESA and more active sites for HER compared to PANI/Fe₃O₄-I(3) and PANI/Fe₃O₄-I(7) electrocatalysts.

Furthermore, EPR spectra of PANI/Fe₃O₄ samples previously showed that the intensity of signal originating from Fe₃O₄ NPs decreased with increasing polymerization time for both series of samples (I and II, prepared with mass ratio Fe₃O₄ NPs/aniline of 0.0015 and 0.015, respectively) [19], suggesting that the amount of incorporated Fe₃O₄ NPs relative to the amount of PANI is higher in PANI/Fe₃O₄-II(3) than that in PANI/Fe₃O₄-II(7). This is expected as the PANI yield increases with polymerization time while the total amount of Fe₃O₄ NP catalysts in the reaction system does not change. A higher amount of Fe₃O₄ NPs in PANI/Fe₃O₄-II(3) leads to more pronounced synergistic effects of PANI and Fe₃O₄ NPs toward HER in this sample compared to PANI/Fe₃O₄-II(7). Finally, it should be noted that PANI/Fe₃O₄-II(3) also showed better electrocatalytic performance for HER in comparison with some non-noble metal-based electrocatalysts presented in the literature, Table 2.

Figure 3E shows the polarization curves of PANI/Fe₃O₄-II(3) in 0.1 M H₂SO₄ at a range of temperatures from 25 to 75 °C. Increased cathodic current densities from -23.5 to -60.0 mA cm⁻² were reached with increasing temperature from 25 to 75 °C. The same behaviour was observed for the rest of the PANI/Fe₃O₄ electrocatalysts. Current density values recorded at different temperatures were used to construct the Arrhenius' regressions, ln j vs. T^{-1} , for all electrocatalysts and their slopes were used for the calculation of the apparent activation energy (E_a^{app}) using the Arrhenius equation (Equation 4) [56,57].

$$\frac{\partial \ln |j|}{\partial (1/T)} = \frac{\Delta E_a^{\text{app}}}{R} \tag{4}$$

where R is the universal gas constant. The obtained E_a^{app} values increased in the order PANI/Fe₃O₄-II(3) (10 kJ mol⁻¹) < PANI/Fe₃O₄-II(7) (23 kJ mol⁻¹) < PANI/Fe₃O₄-II(7) (39 kJ mol⁻¹). The lowest E_a^{app} of PANI/Fe₃O₄-II(3) correlates well with its best electrocatalytic activity toward HER.

Chronoamperometric curves of four PANI/Fe₃O₄ electrocatalysts are presented in Figure 3F, where a similar current density trend was observed during the polarization study. Namely, PANI/Fe₃O₄-II(3) and PANI/Fe₃O₄-II(7) gave higher current densities during HER than PANI/Fe₃O₄-I(7)

and PANI/Fe₃O₄-I(3). PANI/Fe₃O₄-II(3) showed a current density decrease of ca. 21 % during the first 15 min, remaining constant. Some degree of variation in current density with time can originate in the generation of hydrogen gas bubbles at the electrode surface and change in the H⁺/H₂ concentration [58]. Moreover, it has been reported that PANI improves stability and reduces current density retention in acidic media by its amino groups capturing H⁺, thus keeping it from disrupting the catalyst structure [18].

Activity for HER in electrolytes of a wide pH range could broaden the electrocatalyst's application [23,47]. Hence, the HER performance of PANI/Fe₃O₄-II(3) was also investigated in an 8 M KOH solution as a typical solution used in alkaline industrial water electrolysers, Figure 4A. It could be seen (Figure 4A and 4B) that the activity of PANI/Fe₃O₄-II(3) for HER is notably lower in alkaline than in acidic media as HER onset potential in alkaline media (ca. -0.620 V) was found to be ca. 330 mV more negative than that in acidic media (-0.289 V). Additionally, the current density reached at -0.5 V in alkaline media (-0.2 mA cm⁻²) was strikingly lower than in acidic media (-12.0 mA cm⁻²).

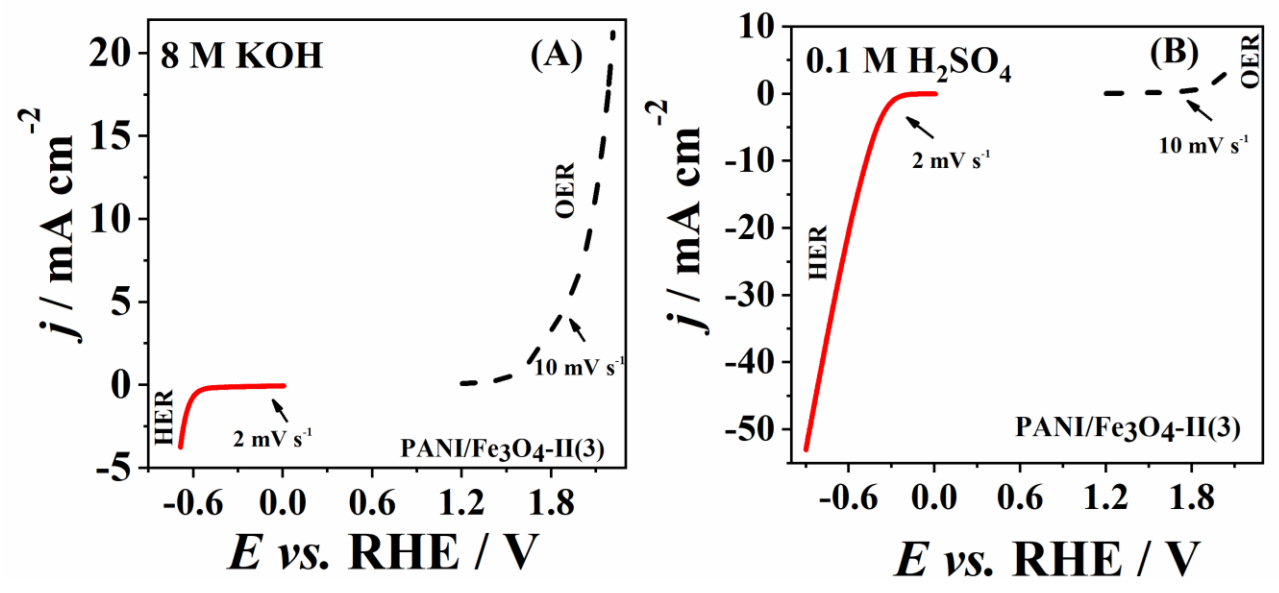


Figure 4. A: polarization curves of PANI/Fe $_3O_4$ -II(3) electrocatalyst in 8 M KOH for HER and OER; B: polarization curves of PANI/Fe $_3O_4$ -II(3) electrocatalyst in 0.1 M H $_2SO_4$ for HER and OER

Furthermore, activity for anode reaction, *i.e.*, oxygen evolution reaction (OER), could broaden the electrocatalyst applicability as a bifunctional electrocatalyst in water electrolysers [59]. Therefore, the OER performance of PANI/Fe₃O₄-II(3) was examined in both acidic (0.1 M H₂SO₄) and alkaline (8 M KOH) media. In the case of OER, higher activity was observed in alkaline than in acidic media in terms of ca. 290 mV less positive onset potential (1.60 V in alkaline media vs. 1.89 V in acidic media) and ca. three times higher current densities reached (7.4 mA cm⁻² at 2.0 V in alkaline media vs. 2.4 mA cm⁻² in acidic media). Tafel slopes of PANI/Fe₃O₄-II(3) electrocatalyst during OER were determined to be 328 and 289 mV dec⁻¹ in alkaline and acidic media, respectively.

Thus, the results obtained in this study suggest that PANI/Fe₃O₄-II(3) is a highly active, low-cost electrocatalyst for HER, which is crucial for efficient, large-scale water-splitting production of hydrogen.

Conclusions

Four PANI/Fe₃O₄ electrocatalysts were tested for HER in acidic media (0.1 M H_2SO_4). The sample PANI/Fe₃O₄-II(3) showed the highest electrocatalytic activity with HER onset potential ca. 300 mV

lower than in the case of three other electrocatalysts (-0.286 V vs. -0.397, -0.564 and -0.598 V for PANI/Fe₃O₄-II(7), PANI/Fe₃O₄-I(7) and PANI/Fe₃O₄-I(3), respectively) and the highest current density. EIS revealed the lowest charge transfer resistance R_{ct} in the case of PANI/Fe₃O₄-II(3), which, along with its high effective surface area/high content of active sites (as evaluated from C_{dl} value) and the lowest HER activation energy (as calculated from the temperature dependence of current density) could explain its highest HER activity. In addition, the highest content of Fe is measured by EDX for PANI/Fe₃O₄-II(3) sample. Linking PANI and Fe₃O₄ NPs introduced a strong coupling and synergistic effect, a 3D structure with a plethora of exposed active sites, and facile permeation of the electrolyte. Thus, PANI is believed to capture the intermediate H⁺ ions and steam their reduction to H₂. The electrocatalytic activity of PANI/Fe₃O₄-II(3) for HER in alkaline media (8 K KOH) as well as for OER in both alkaline and acidic media was explored, offering the possibility of broadening this material's application as bifunctional electrocatalyst in water electrolysers.

Acknowledgements: The authors would like to thank the Science Fund of the Republic of Serbia, grant number 7750219, Advanced Conducting Polymer-Based Materials for Electrochemical Energy Conversion and Storage, Sensors and Environmental Protection-AdConPolyMat (IDEAS program), as well as the Ministry of Science, Technological Development and Innovation, contracts no. 451-03-65/2024-03/200146 and 451-03-66/2024-03/200146.

References

- [1] L. Huang, Y. Hou, Z. Yu, Z. Peng, L. Wang, J. Huang, B. Zhang, L. Qian, L. Wu, Z. Li, Pt/Fe-NF electrode with high double-layer capacitance for efficient hydrogen evolution reaction in alkaline media, *International Journal of Hydrogen Energy* **42(15)** (2017) 9458-9466. https://doi.org/10.1016/j.ijhydene.2017.02.055
- [2] Y. Pan, M. Wen, Noble metals enhanced catalytic activity of anatase TiO₂ for hydrogen evolution reaction, *International Journal of Hydrogen Energy* **43(49)** (2018) 22055-22063. https://doi.org/10.1016/j.ijhydene.2018.10.093
- [3] F. Wang, X. Yang, B. Dong, X. Yu, H. Xue, L. Feng, A FeP powder electrocatalyst for the hydrogen evolution reaction, *Electrochemistry Communications* **92** (2018) 33-38. https://doi.org/10.1016/j.elecom.2018.05.020
- [4] H. Wang, X. Wang, D. Yang, B. Zheng, Y. Chen, Co_{0.85}Se hollow nanospheres anchored on N-doped graphene nanosheets as highly efficient, nonprecious electrocatalyst for hydrogen evolution reaction in both acid and alkaline media. *Journal of Power Sources* **400** (2018) 232-241. https://doi.org/10.1016/j.jpowsour.2018.08.027
- [5] X. Yue, C. Zhong, S. Huang, Y. Jin, C. He, Y. Chen, P.K. Shen, K_{0.4}TaO_{2.4}F_{0.6} Nanocubes as Highly Efficient Noble Metal-Free Electrocatalysts for Hydrogen Evolution Reaction in Acidic Media. *Electrochimica Acta* **245** (2017) 193-200. https://doi.org/10.1016/j.electacta.2017.05.145
- [6] J. Deng, P. Ren, D. Deng, L. Yu, F. Yang, X. Bao, Highly active and durable non-precious-metal catalysts encapsulated in carbon nanotubes for hydrogen evolution reaction. *Energy & Environmental Science* **7** (2014) 1919-1923. https://doi.org/10.1039/c4ee00370e
- [7] P. Zhang, M. Wang, H. Chen, Y. Liang, J. Sun, L. Sun, A Cu-Based Nanoparticulate Film as Super-Active and Robust Catalyst Surpasses Pt for Electrochemical H₂Production from Neutral and Weak Acidic Aqueous Solutions. *Advanced Energy Materials* 6 (2016) 1502319. https://doi.org/10.1002/aenm.201502319
- [8] A.L. Roy, A.M. Shaw, L. Rajagopal, C.H. Strohbehn, S.W. Arendt, K.L. Sauer, Use of minimal-text posters to improve the microbial status of leafy greens and food contact surfaces in foodservice sites serving older adults. *Food Protection Trends* **36** (2016) 125-132. https://doi.org/10.1021/ja403440e



- [9] Y. Li, H. Wang, L. Xie, Y. Liang, G. Hong, H. Dai, MoS₂ nanoparticles grown on graphene: An advanced catalyst for the hydrogen evolution reaction, *Journal of the American Chemical Society* **133** (2011) 7296-7299. 7299. https://doi.org/10.1021/ja201269b
- [10] M.B. Askari, P. Salarizadeh, M. seifi, S.M. Rozati, A. Beheshti-Marnani, H. Saeidfirozeh, MoCoFeS hybridized with reduced graphene oxide as a new electrocatalyst for hydrogen evolution reaction. *Chemical Physics Letters* **711** (2018) 32-36. https://doi.org/10.1016/j.cplett.2018.09.025
- [11] J. Ding, H. Yang, S. Zhang, Q. Liu, H. Cao, J. Luo, X. Liu, Advances in the Electrocatalytic Hydrogen Evolution Reaction by Metal Nanoclusters-based Materials. *Small* **18** (2022) 2204524. https://doi.org/10.1002/smll.202204524
- [12] J. Milikić, M. Vasić, L. Amaral, N. Cvjetićanin, D. Jugović, R. Hercigonja, B. Šljukić, NiA and NiX zeolites as bifunctional electrocatalysts for water splitting in alkaline media. *International Journal of Hydrogen Energy* **43** (2018) 18977-18991. https://doi.org/10.1016/j.ijhydene.2018.08.063
- [13] Z. Hao, S. Yang, J. Niu, Z. Fang, L. Liu, Q. Dong, S. Song, Y. Zhao, A bimetallic oxide Fe_{1.89}Mo_{4.11}O₇ electrocatalyst with highly efficient hydrogen evolution reaction activity in alkaline and acidic media. *Chemical Science* 9 (2018) 5640-5645. https://doi.org/10.1039/c8sc01710g
- [14] L. Zhang, Y. Chen, P. Zhao, W. Luo, S. Chen, M. Shao, Fe₃C Nanorods Encapsulated in N-Doped Carbon Nanotubes as Active Electrocatalysts for Hydrogen Evolution Reaction. Electrocatalysis 9 (2018) 264-270. https://doi.org/10.1007/s12678-017-0425-3
- [15] R. Atchudan, T.N.J. Immanuel Edison, S. Perumal, R. Vinodh, N. Muthuchamy, Y.R. Lee, One-pot synthesis of Fe₃O₄@graphite sheets as electrocatalyst for water electrolysis. *Fuel* **277** (2020) 118235. https://doi.org/10.1016/j.fuel.2020.118235
- [16] J. Wang, L. Ji, X. Teng, Y. Liu, L. Guo, Z. Chen, Decoupling half-reactions of electrolytic water splitting by integrating a polyaniline electrode. *Journal of Materials Chemistry A* **7** (2019) 13149-13153. https://doi.org/10.1039/c9ta03285a
- [17] M. Wang, L. Jiang, Q. Li, X. Zhou, PANI-modified Pt/Na₄Ge₉O₂₀ with low Pt loadings: Efficient bifunctional electrocatalyst for oxygen reduction and hydrogen evolution. *International Journal of Hydrogen Energy* **44** (2019) 31062-31071. https://doi.org/10.1016/j.ijhydene.2019.10.021
- [18] G. Ćirić-Marjanović, Recent advances in polyaniline research: Polymerization mechanisms, structural aspects, properties and applications. *Synthetic Metals* **177** (2013) 1-47. https://doi.org/10.1016/j.synthmet.2013.06.004
- [19] G. Ćirić-Marjanović. *Polyaniline Nanostructures*, in: A. Eftekhari (Ed.), Nanostructured Conduct. Polym., John Wiley & Sons, Hoboken, New Jersey, 2010: pp. 19-98. https://doi.org/10.1002/9780470661338.ch2
- [20] T. Fujisaki, K. Kashima, S. Serrano-Luginbühl, R. Kissner, D. Bajuk-Bogdanović, M. Milojević-Rakić, G. Ćirić-Marjanović, S. Busato, E. Lizundia, P. Walde, Effect of template type on the preparation of the emeraldine salt form of polyaniline (PANI-ES) with horseradish peroxidase isoenzyme C (HRPC) and hydrogen peroxide. *RSC Advances* **9** (2019) 33080-33095. https://doi.org/10.1039/c9ra06168a
- [21] M.S. Biserčić, B. Marjanović, B.A. Zasońska, S. Stojadinović, G. Ćirić-Marjanović, Novel microporous composites of MOF-5 and polyaniline with high specific surface area. *Synthetic Metals* **262** (2020) 116348. https://doi.org/10.1016/j.synthmet.2020.116348
- [22] D. Wang, L. Yang, H. Liu, D. Cao, Polyaniline-coated Ru/Ni(OH)₂ nanosheets for hydrogen evolution reaction over a wide pH range. *Journal of Catalysis* 375 (2019) 249-256. https://doi.org/10.1016/j.jcat.2019.06.008

- [23] Z. Duan, K. Deng, C. Li, M. Zhang, Z. Wang, Y. Xu, X. Li, L. Wang, H. Wang, Polyaniline-coated mesoporous Rh films for nonacidic hydrogen evolution reaction. *Chemical Engineering Journal* **428** (2022) 132646. https://doi.org/10.1016/j.cej.2021.132646
- [24] B.B. Kamble, S.K. Jha, K.K. Sharma, S.S. Mali, C.K. Hong, S.N. Tayade, Redox active MoO₃-Polyaniline hybrid composite for hydrogen evolution reaction and supercapacitor application. *International Journal of Hydrogen Energy* **48** (2023) 29058-29070. https://doi.org/10.1016/j.ijhydene.2023.04.089
- [25] H. Ashassi-Sorkhabi, A. Kazempour, S. Moradi-Alavian, E. Asghari, J.J. Lamb, 3D nanostructured nickel film supported to a conducting polymer as an electrocatalyst with exceptional properties for hydrogen evolution reaction. *International Journal of Hydrogen Energy* **48** (2023) 29865-29876. https://doi.org/10.1016/j.ijhydene.2023.04.139
- [26] T.N. Amirabad, A.A. Ensafi, K.Z. Mousaabadi, B. Rezaei, M. Demir, Binder-free engineering design of Ni-MOF ultrathin sheet-like grown on PANI@GO decorated nickel foam as an electrode for in hydrogen evolution reaction and asymmetric supercapacitor. *International Journal of Hydrogen Energy* **48** (2023) 29471-29484. https://doi.org/10.1016/j.ijhydene.2023.04.159
- [27] X. Chen, Y. Chen, Z. Shen, C. Song, P. Ji, N. Wang, D. Su, Y. Wang, G. Wang, L. Cui, Self-crosslinkable polyaniline with coordinated stabilized CoOOH nanosheets as a high-efficiency electrocatalyst for oxygen evolution reaction. *Applied Surface Science* **529** (2020) 147173. https://doi.org/10.1016/j.apsusc.2020.147173
- [28] Y. Zou, Y. Huang, L.W. Jiang, A. Indra, Y. Wang, H. Liu, J.J. Wang. Polyaniline coating enables electronic structure engineering in Fe₃O₄ to promote alkaline oxygen evolution reaction. *Nanotechnology* **33** (2022) 155402. https://doi.org/10.1088/1361-6528/ac475c
- [29] V. Ashok, S. Mathi, M. Sangamithirai, J. Jayabharathi, Regulated Bimetal-Doped Polyaniline: Amorphous-Crumple-Structured Viable Electrocatalyst for an Efficient Oxygen Evolution Reaction. *Energy and Fuels* **36** (2022) 14349-14360. https://doi.org/10.1021/acs.energyfuels.2c03022
- [30] Z. Xue, Y. Wang, M. Yang, T. Wang, H. Zhu, Y. Rui, S. Wu, W. An, In-situ construction of electrodeposited polyaniline/nickel-iron oxyhydroxide stabilized on nickel foam for efficient oxygen evolution reaction at high current densities. *International Journal of Hydrogen Energy* **47** (2022) 34025-34035. https://doi.org/10.1016/j.ijhydene.2022.08.023
- [31] Y. Duan, Z. Huang, J. Ren, X. Dong, Q. Wu, R. Jia, X. Xu, S. Shi, S. Han, Highly efficient OER catalyst enabled by in situ generated manganese spinel on polyaniline with strong coordination. *Dalton Transactions* **51** (2022) 9116-9126. https://doi.org/10.1039/d2dt01236g
- [32] U. Stamenović, N. Gavrilov, I.A. Pašti, M. Otoničar, G. Ćirić-Marjanović, S.D. Škapin, M. Mitrić, V. Vodnik, One-pot synthesis of novel silver-polyaniline-polyvinylpyrrolidone electrocatalysts for efficient oxygen reduction reaction. *Electrochimica Acta* **281** (2018) 549-561. https://doi.org/10.1016/j.electacta.2018.05.202
- [33] H. Wang, J. Lin, Z.X. Shen, Polyaniline (PANi) based electrode materials for energy storage and conversion. *Journal of Science: Advanced Materials and Devices* **1** (2016) 225-255. https://doi.org/10.1016/j.jsamd.2016.08.001
- [34] C.W. Kuo, J.C. Chang, B.W. Wu, T.Y. Wu, Electrochemical characterization of RuO₂- Ta₂O₅/polyaniline composites as potential redox electrodes for supercapacitors and hydrogen evolution reaction. *International Journal of Hydrogen Energy* **45** (2019) 22223-22231. https://doi.org/10.1016/j.ijhydene.2019.08.059
- [35] Y. Chen, Q. Zhang, X. Jing, J. Han, L. Yu, Synthesis of Cu-doped polyaniline nanocomposites (nano Cu@PANI) via the H₂O₂-promoted oxidative polymerization of aniline with copper salt. Materials Letters **242** (2019) 170-173. https://doi.org/10.1016/j.matlet.2019.01.143



- [36] I. Pašti, M. Milojević-Rakić, K. Junker, D. Bajuk-Bogdanović, P. Walde, G. Ćirić-Marjanović, Superior capacitive properties of polyaniline produced by a one-pot peroxidase/H₂O₂-triggered polymerization of aniline in the presence of AOT vesicles. *Electrochimica Acta* **258** (2017) 834-841. https://doi.org/10.1016/j.electacta.2017.11.133
- [37] J. Mišurović, M. Mojović, B. Marjanović, P. Vulić, G. Ćirić-Marjanović, Magnetite nanoparticles-catalysed synthesis of conductive polyaniline. *Synthetic Metals* **257** (2019) 116174. https://doi.org/10.1016/j.synthmet.2019.116174
- [38] J. Stejskal, R.G. Gilbert, Polyaniline. Preparation of a conducting polymer(IUPAC Technical Report), *Pure and Applied Chemistry* **74** (2002) 857-867. https://doi.org/10.1351/pac200274050857
- [39] E.T. Kang, K.G. Neoh, K.L. Tan, Polyaniline: A polymer with many interesting intrinsic redox states. *Progress in Polymer Science* **23** (1998) 277-324. https://doi.org/10.1016/S0079-6700(97)00030-0
- [40] P. Ahuja, S.K. Ujjain, I. Arora, M. Samim, Hierarchically Grown NiO-Decorated Polyaniline-Reduced Graphene Oxide Composite for Ultrafast Sunlight-Driven Photocatalysis. *ACS Omega Journal* **3** (2018) 7846-7855. https://doi.org/10.1021/acsomega.8b00765
- [41] S. Golczak, A. Kanciurzewska, M. Fahlman, K. Langer, J.J. Langer, Comparative XPS surface study of polyaniline thin films. *Solid State Ionics* **179** (2008) 2234-2239. https://doi.org/10.1016/j.ssi.2008.08.004
- [42] H. Peng, G. Ma, K. Sun, J. Mu, X. Zhou, Z. Lei, A novel fabrication of nitrogen-containing carbon nanospheres with high rate capability as electrode materials for supercapacitors. *RSC Advances* **5** (2015) 12034-12042. https://doi.org/10.1039/c4ra11889h
- [43] S. Cho, O.S. Kwon, S.A. You, J. Jang, Shape-controlled polyaniline chemiresistors for high-performance DMMP sensors: Effect of morphologies and charge-transport properties.

 Journal of Materials Chemistry A 1 (2013) 5679-5688. https://doi.org/10.1039/c3ta01427d
- [44] H.A. Bandal, A.R. Jadhav, A.H. Tamboli, H. Kim, Bimetallic iron cobalt oxide self-supported on Ni-Foam: An efficient bifunctional electrocatalyst for oxygen and hydrogen evolution reaction. *Electrochimica Acta* **249** (2017) 253-262. https://doi.org/10.1016/j.electacta.2017.07.178
- [45] A.P. Murthy, J. Theerthagiri, J. Madhavan, K. Murugan, Highly active MoS₂/carbon electrocatalysts for the hydrogen evolution reaction Insight into the effect of the internal resistance and roughness factor on the Tafel slope. *Physical Chemistry Chemical Physics* **19** (2017) 1988-1998. https://doi.org/10.1039/C6CP07416B
- [46] N. Lingappan, I. Jeon, W. Lee, Polyaniline induced multi-functionalities in interfacially coupled electrocatalysts for hydrogen/oxygen evolution reactions. *Journal of Materials Chemistry A* **11** (2023) 17797-17809. https://doi.org/10.1039/d3ta02389c
- [47] F. Meng, Y. Yu, D. Sun, S. Lin, X. Zhang, T. Xi, C. Xu, H. Ouyang, W. Chu, L. Shang, Q. Su, B. Xu, Three-Dimensional Needle Branch-like PANI/CoNiP Hybrid Electrocatalysts for Hydrogen Evolution Reaction in Acid Media. *ACS Applied Energy Materials Journal* **4** (2021) 2471-2480. https://doi.org/10.1021/acsaem.0c03033
- [48] Q. Dang, Y. Sun, X. Wang, W. Zhu, Y. Chen, F. Liao, H. Huang, M. Shao, Carbon dots-Pt modified polyaniline nanosheet grown on carbon cloth as stable and high-efficient electrocatalyst for hydrogen evolution in pH-universal electrolyte. *ACS Applied Energy Materials Journal* **257** (2019) 117905. https://doi.org/10.1016/j.apcatb.2019.117905
- [49] C.C.L.L. McCrory, S. Jung, I.M. Ferrer, S.M. Chatman, J.C. Peters, T.F. Jaramillo, Benchmarking Hydrogen Evolving Reaction and Oxygen Evolving Reaction Electrocatalysts for Solar Water Splitting Devices. *Journal of the American Chemical Society* **137** (2015) 4347-4357. https://doi.org/10.1021/ja510442p

- [50] P. Yu, L. Wang, Y. Xie, C. Tian, F. Sun, J. Ma, M. Tong, W. Zhou, J. Li, H. Fu, High-Efficient, Stable Electrocatalytic Hydrogen Evolution in Acid Media by Amorphous Fe_xP Coating Fe₂N Supported on Reduced Graphene Oxide. *Small* **14** (2018) 1801717. https://doi.org/10.1002/smll.201801717
- [51] B. Konkena, K.J. Puring, I. Sinev, S. Piontek, O. Khavryuchenko, J.P. Dürholt, R. Schmid, H. Tüysüz, M. Muhler, W. Schuhmann, U.P. Apfel, Pentlandite rocks as sustainable and stable efficient electrocatalysts for hydrogen generation. *Nature Communications* **7** (2016) 12269. https://doi.org/10.1038/ncomms12269
- [52] Y. Ge, P. Dong, S.R. Craig, P.M. Ajayan, M. Ye, J. Shen, Transforming Nickel Hydroxide into 3D Prussian Blue Analogue Array to Obtain Ni₂P/Fe₂P for Efficient Hydrogen Evolution Reaction, Advanced Energy Materials 8 (2018) 1800484. https://doi.org/10.1002/aenm.201800484
- [53] T.H. Wondimu, G.C. Chen, D.M. Kabtamu, H.Y. Chen, A.W. Bayeh, H.C. Huang, C.H. Wang, Highly efficient and durable phosphine reduced iron-doped tungsten oxide/reduced graphene oxide nanocomposites for the hydrogen evolution reaction. *International Journal of Hydrogen Energy* **43** (2018) 6481-6490. https://doi.org/10.1016/j.ijhydene.2018.02.080
- [54] L. Tian, X. Yan, X. Chen. Electrochemical Activity of Iron Phosphide Nanoparticles in Hydrogen Evolution Reaction. *ACS Catalysis Journal* **6** (2016) 5441-5448. https://doi.org/10.1021/acscatal.6b01515
- [55] D.A. Dalla Corte, C. Torres, P.D.S. Correa, E.S. Rieder, C.D.F. Malfatti. The hydrogen evolution reaction on nickel-polyaniline composite electrodes. *International Journal of Hydrogen Energy* **37** (2012) 3025-3032. https://doi.org/10.1016/j.ijhydene.2011.11.037
- [56] J. Milikić, G. Ćirić-Marjanović, S. Mentus, D.M.F. Santos, C.A.C. Sequeira, B. Šljukić, Pd/c-PANI electrocatalysts for direct borohydride fuel cells. *Electrochimica Acta* **213** (2016) 298-305. https://doi.org/10.1016/j.electacta.2016.07.109
- [57] A.J. Bard, L.R. Faulkner, *Electrochemical Methods: Fundamentals and Applications*, 2nd ed., John Wiley & Sons, New York, United States, 2001, p. 864. ISBN 978-0471043720
- [58] B. Kurt Urhan, H. Öztürk Doğan, T. Öznülüer Özer, Ü. Demir, Palladium-coated polyaniline nanofiber electrode as an efficient electrocatalyst for hydrogen evolution reaction.

 International Journal of Hydrogen Energy 47 (2022) 4631-4640.

 https://doi.org/10.1016/j.ijhydene.2021.11.101
- [59] C. Feng, M.B. Faheem, J. Fu, Y. Xiao, C. Li, Y. Li, Fe-Based Electrocatalysts for Oxygen Evolution Reaction: Progress and Perspectives. *ACS Catalysis Journal* **10** (2020) 4019-4047. https://doi.org/10.1021/acscatal.9b05445

© 2024 by the authors; licensee IAPC, Zagreb, Croatia. This article is an open-access article distributed under the terms and conditions of the Creative Commons Attribution license (https://creativecommons.org/licenses/by/4.0/)



Open Access :: ISSN 1847-9286 www.jESE-online.org

Original scientific paper

Functionalization of FeCoNiCu medium entropy alloy via nitridation and anodic oxidation for enhanced oxygen evolution and glycerol oxidation

Luka Suhadolnik^{1,⊠}, Milutin Smiljanić^{1,™}, Marjan Bele¹, Mejrema Nuhanović¹, Matjaž Finšgar², Nik Maselj¹, Daniela Neumüller³, Lidija D. Rafailović³ and Nejc Hodnik^{1,4,™}

¹Department of Materials Chemistry, National Institute of Chemistry, Hajdrihova 19, SI-1000 Ljubljana, Slovenia

²Faculty of Chemistry and Chemical Engineering, University of Maribor, Smetanova 17, 2000 Maribor, Slovenia

³Department of Materials Science, Chair of Materials Physics, University of Leoben, Jahnstrasse 12, 8700, Leoben, Austria

⁴Institute of Metals and Technology, Ljubljana 1000, Slovenia

Corresponding authors: □luka.suhadolnik@ki.si; □milutin.smiljanic@ki.si; □nejc.hodnik@ki.si

Received: December 27, 2024; Accepted: February 5, 2025; Published: February 18, 2025

Abstract

Medium entropy alloys (MEAs) have emerged as a promising class of materials for electrocatalysis due to their tunable properties and exceptional catalytic performance. This study successfully functionalized a bulk FeCoNiCu alloy using a combined anodic oxidation (AO) and nitridation (NT) approach to produce a highly porous, thin-film catalyst. The hierarchical structure formed during the surface treatments enhances the material's specific surface area and alters the oxidation states of the constituent metals, creating abundant active sites. The electrocatalytic performance of the modified bulk FeCoNiCu electrode was evaluated for both the oxygen evolution reaction (OER) and glycerol oxidation reaction (GOR) in an alkaline electrolyte. Remarkably, the AO-NT-treated catalyst exhibited superior activity for OER, surpassing commercial IrOx benchmarks with lower overpotential requirements. For GOR, the FeCoNiCu electrode demonstrated excellent performance by significantly reducing energy input compared to OER, highlighting its potential as a dual-purpose catalyst for alkaline water splitting. Post-reaction product analysis via NMR confirmed the formation of value-added chemicals, with formic acid identified as the main product. These results underline the feasibility of surface-modified MEAs for sustainable energy and chemical production applications, offering a cost-effective alternative to noble metal-based catalysts.

Kevwords

Medium entropy alloy, surface modification, electrocatalysis, oxygen evolution reaction, glycerol oxidation

Introduction

Medium entropy alloys (MEAs), a subset of compositionally complex materials (CCMs), have emerged as an exciting new class of materials due to their unique microstructures and tunable properties [1]. Unlike conventional alloys, MEAs typically combine three to five elements in nearequiatomic proportions, resulting in complex atomic arrangements that provide an exceptional synergy of mechanical, thermal, chemical, and electronic properties [2,3]. The inherent flexibility in elemental composition allows MEAs to exhibit unique features such as high hardness, excellent corrosion resistance, remarkable thermal stability, and unique catalytic properties, making them promising candidates for various applications [4-6]. However, the general shortcoming of CCMs is that they usually come with low specific surface area, which impedes their practical applications in electrocatalysis. To address this, further adjustments of the MEAs' properties can be achieved through surface modifications such as anodic oxidation (AO) and nitridation (NT). AO is known for its relative simplicity and the possibility to create highly porous structures with enlarged surface area, while NT introduces nitrides and oxynitrides into the material, which can significantly improve electronic properties, hardness, wear resistance, and thermal stability. When applied in tandem, these two surface treatments can synergistically boost the overall properties of MEAs, unlocking new possibilities for their applications [7].

Electrocatalysis is one of the fields where the application of CCMs has become particularly attractive due to the constant pursuit of improved catalytic materials [8]. The concept of green hydrogen energy is particularly attractive, and the development of active, durable, and affordable electrocatalysts for electrochemical water splitting is crucial [9]. The bottleneck in water electrolysis is the anodic oxygen evolution reaction (OER), which is kinetically sluggish and takes place under harsh conditions (elevated potentials, extreme pH, and high temperatures), therefore demanding the usage of precious metals catalysts such as Ir and Ru (and their oxides) [10]. To overcome these issues, two strategies can be applied: (i) to develop non-noble catalysts for OER able to compete with Ir- and Ru-based benchmarks; (ii) to substitute OER with some other less energy-demanding anodic reaction, such as glycerol oxidation reaction (GOR) [11,12]. Both strategies can be covered by exact and guided synthesis and modifications of CCMs to yield unique active sites thanks to the fine-tuning of the composition and morphology of these catalysts. Our recent study showcased the potential of the combination of NT-AO applied to FeCoNiCuZn alloy to produce a tuned structure with exceptional electrocatalytic activity for water oxidation in alkaline electrolytes [7]. While NT only slightly improved the activity of starting FeCoNiCuZn alloy, subsequent AO boosted its performance even beyond commercial IrOx reference catalysts and placed it among the bestperforming non-noble catalysts for OER in the literature. This was explained by the significant increase in the catalysts' surface area and changes in the composition of the CCM induced by NT-AO. Specifically, NT-AO treatment removed Cu and Zn, resulting in a hierarchically connected pore structure, where larger pores are interlinked with smaller ones formed due to fluorides in the AO electrolyte, while also altering the oxidation states of the constituent metals. In the case of GOR, noble metal catalysts such as Pt, Pd, and Au are highly effective, offering excellent catalytic properties and stability [13]. Nickel-based materials offer cost-effective alternatives with promising GOR activity, especially when paired with cobalt, which further boosts catalytic performance [14,15]. Combining non-noble and noble metals into multi-metallic and alloy catalysts, such as bimetallic PtAg [16] or Ni₈₀Pd₂₀ [17], can also enhance catalytic efficiency through synergistic effects. Although MEAs and CCMs are generally gaining increasing attention in electrocatalysis, their application in GOR remains underexplored [18]. The vast potential for incorporating various elements into CCMs offers a broad field for experimentation, with many influences on catalytic performance yet to be understood. Future research should focus on testing a wider range of CCMs for reactions such as GOR to fully exploit their potential and enhance the efficiency and selectivity of these processes. For instance, HEA - CoNiCuMnMo nanoparticles synthesized on carbon cloth have shown high efficiency in glycerol oxidation reaction, with molybdenum sites coordinated by manganese, molybdenum, and nickel identified as key catalytic centres [19]. Another study reported Ptdecorated FeCoNiCuMn HEA nanocatalysts with a superior GOR performance compared to Pt/C, which was ascribed to the composition of HEA, providing better CO poisoning features on Ptsites [20]. These studies show a high potential for HEA in GOR catalysis and underscore the need for further exploration in this domain [19].

In this study, a highly porous, thin film electrocatalyst was synthesized by surface modification of the FeCoNiCu bulk electrode and tested for both GOR and OER in an alkaline electrolyte. The starting FeCoNiCu CCM was modified using the AO-NT procedure, and the obtained thin film exhibited promising catalytic properties for both OER and GOR. The catalyst was thoroughly analysed to confirm its composition, structure, and electrocatalytic performance, providing important insights for future optimization and practical applications. While further studies are necessary, the results demonstrate that the FeCoNiCu bulk alloy electrode, modified by the NT-AO approach, represents a very promising concept for developing highly active anodes for alkaline water electrolysis.

Experimental Section

Catalyst preparation

The catalyst was prepared following conditions reported by Suhadolnik *et al.* [7]. Briefly, a compositionally complex FeCoNiCu alloy was produced by arc-melting high-purity elements in a Tigetter Ar atmosphere, followed by multiple heating and cooling cycles for homogeneity. The alloy was nitridized at 700 °C for 30 minutes in ammonia flow, then anodized at 50 V for 5 minutes in a custom electrochemical cell using the freshly prepared electrolyte.

Catalyst characterization techniques

SEM and SEM-EDS analysis: The surface morphology of the catalyst was examined under the conditions previously reported by Suhadolnik *et al.* [21].

XRD analysis: The catalyst was characterized using X-ray diffraction as described by Suhadolnik *et al.* [7]. Phase identification was carried out with the X'Pert HighScore Plus software, utilizing the ICDD PDF-4+ 2024 database [21].

XPS analysis: The surface composition of the compositionally complex sample was analysed using X-ray photoelectron spectroscopy (XPS) using a Supra+ instrument equipped with an Al K_{α} excitation source. Spectra were acquired and processed using ESCApe 1.5 software. XPS measurements were performed at a 90° take-off angle using 160 eV pass energy (survey spectrum). The binding energy ($E_{\rm B}$) scale was corrected using the C-C/C-H peak in the C 1s spectrum, which is located at 284.8 eV. The size of the XPS analysis spot was 300 by 700 μ m.

ToF-SIMS analysis: Depth profiling was performed using a ToF-SIMS M6 instrument (IONTOF, Münster, Germany) equipped with a Bi liquid metal ion gun and a Cs⁺ sputtering source. The primary Bi⁺ ion beam was operated at 30 keV (1.0 pA), while sputtering was performed using 2 keV Cs⁺

(205 nA). Sputtering was performed over an area of 500 by 500 μ m, while the analysis was performed in the middle of the sputter crater on an area of 300 by 300 μ m. Spectra were acquired and processed using SurfaceLab 7.3 software (IONTOF, Münster, Germany).

NMR experiments were performed on a Bruker AVANCE NEO 600 MHz spectrometer equipped with a 5 mm BBFO probe. Spectra was measured in deuterated water (D_2O , Sigma Aldrich). ¹H NMR spectra were referenced on 3-(Trimethylsilyl) propionic-2,2,3,3-d₄ acid sodium salt (TMSPA) (δ = 0.00 ppm) and water present in the sample (δ = 4.79 ppm). The samples were prepared by sampling 100 µL of the electrolyte after the electrolysis and adding 500 µl of D_2O .

Electrochemical analysis: Electrochemical measurements were performed for both OER and GOR at ambient temperature in a single-compartment electrochemical cell with a three-electrode setup. The prepared catalyst was mounted in a custom-made Teflon holder, identical to the one used during anodization, and served as the working electrode. A HydroFlex reversible hydrogen electrode (RHE, Gaskatel GmbH) was used as the reference electrode, while a glassy carbon rod functioned as the counter electrode. A potentiostat (SP-300, Biologic) was used to control the potential. All voltammetric experiments included compensation (85 %) for the ohmic drop determined via electrochemical impedance spectroscopy (EIS) at high frequencies. A double-layer capacitance (C_{dl}) approach was used to assess the electrochemical surface area of our catalyst, as described elsewhere [7]. Briefly, cyclic voltammetry (CV) was applied at different scan rates (20, 50, 100, 200, and 300 mV s⁻¹) in the potential range between 0.25 and 0.35 V_{RHE}. Using linear dependence between $\Delta j = j_a - j_c$ at E = 0.3 V_{RHE} and scan rate, the $C_{\rm dl}$ value was extracted. Linear sweep voltammetry (LSV) was performed in 1 M KOH for OER and in 1 M KOH with 0.1 M glycerol for GOR, over a potential range of 1.2 to 1.6 V vs. RHE (scan rate of 2 mV s⁻¹). Chronoamperometric (CA) measurements for GOR were conducted at various potentials in 1 M KOH containing 0.1 M glycerol. For OER activity comparison, a benchmark IrO_x catalyst was used (Premion, Alfa Aesar). The powdered catalyst was mixed with Milli-Q water (1 mg / 1 ml ratio) to form the uniform catalyst ink, which was then drop-casted (20 µL) onto glassy carbon (5 mm in diameter) rotating disk (RDE) resulting in catalyst loading of 102.04 μg cm⁻². After drying, IrO₂ films were covered with 5 μL of Nafion:Isopropanol mixture (volumetric ratio 1/50) to ensure adhesion. The electrochemical procedure included 20 cycles at a scan rate of 50 mV s⁻¹, ranging from 0.05 to 1.45 V, followed by an activity assessment through linear sweep voltammetry (LSV) recorded from 1.2 to 1.6 V at 2 mV s⁻¹. Both the activation and activity measurements were conducted in an argon-saturated electrolyte.

Results and discussion

Morphology, composition, and structure of the compositionally complex catalyst

The surface morphology of the catalyst was characterized using SEM (Figure 1a). The SEM micrographs, taken at various magnifications, reveal that the film is highly porous with a large surface area, exhibiting a hierarchical pore structure. The presence of both larger macropores and smaller mesopores is crucial for enhancing the exposure of active sites, which, through improved mass transport, enhances the adsorption-desorption dynamics of reactants and products [22]. This hierarchical porosity provides sufficient accessibility for larger molecules, while the high surface area of the mesopores supports effective catalytic reactions by increasing the number of accessible active sites. Moreover, the interconnected nature of the porous network may aid in the diffusion of reactants and the removal of products, reducing diffusion limitations and enhancing overall catalytic performance [23].

The XRD pattern of the catalyst is presented in Figure 1b. The diffractogram shows only peaks corresponding to the underlying FeCoNiCu alloy substrate, indicating that the highly oxidized porous film formed on top lacks sufficient crystallinity to generate distinct diffraction peaks. Due to the complexity of this multi-component alloy system and the absence of comprehensive reference cards in the XRD database for such complex materials, it is challenging to definitively assign specific peaks to individual phases. However, based on the composition determined by SEM-EDS and XPS analyses (as shown in Table 1), we can infer the presence of a single phase in the film. The amorphous nature of the oxidized film results from the synthesis conditions, which can lead to a disordered structure without sufficient crystallinity, i.e. a common characteristic of highly porous materials [24].

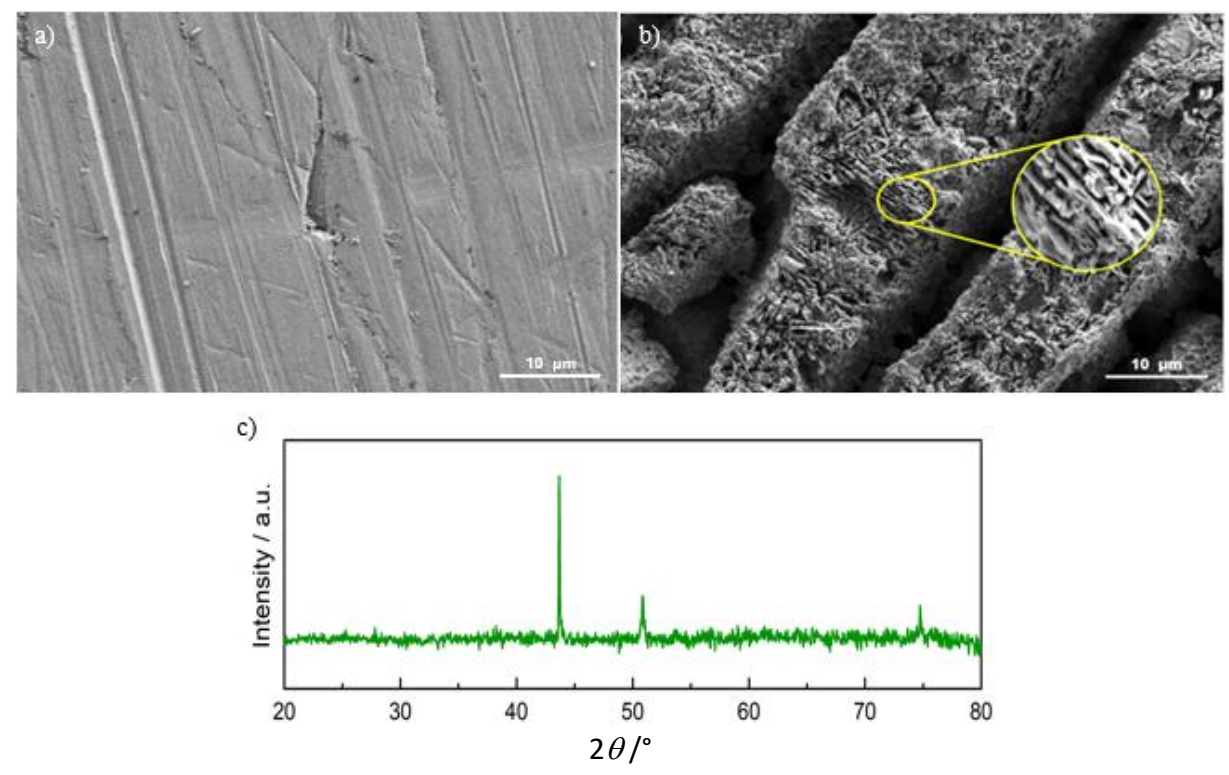


Figure 1. SEM micrographs showing: a) the initial alloy used for catalyst preparation, and b) the catalyst prepared with nitridation and anodization of the alloy shown at two magnifications. Inset circle diameter is 7 μ m. c) XRD diffractogram of the catalyst showing peaks related to the compositionally complex alloy

The XPS analysis confirmed the presence of Fe, Co, and Ni on the surface, while Cu was not detected (XPS survey spectrum in Figure 2). This indicates that Cu is either not present in the top few nanometres, *i.e.* the depth analysed by the XPS technique, or its concentration is below the detection limit of the XPS technique. However, as explained below, Cu was detected using ToF-SIMS, as this analytical technique has a significantly lower detection limit than XPS. The XPS survey spectrum shows intense Fe, Co, and Ni peaks with several XPS-induced LMM Auger peaks. However, the Fe 2p and Co 2p peaks overlap with other XPS-induced Auger peaks (Figure 2), a well-documented challenge in XPS analysis of alloy systems containing these elements. The intense O 1s peak indicates significant surface oxidation, while the presence of the C 1s peak indicates surface contamination, likely from adventitious carbonaceous species adsorbed from the environment after sample preparation during sample transfer to the XPS spectrometer.

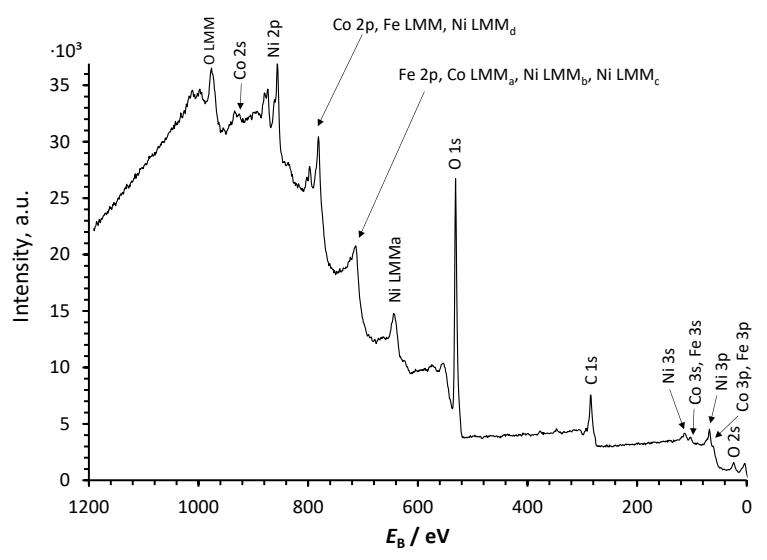


Figure 2. The XPS survey spectrum of the sample showing signals for Fe-, Co-, Ni-, C-, and O-containing species. The XPS surface analysis was performed after the electrocatalytic glycerol oxidation tests

Figure 3 presents the negative ion 3D ToF-SIMS images of the catalyst surface. In ToF-SIMS analysis, the M⁻ signal for a given element can originate from its metallic form (M), oxide (MO), and/or hydroxide (MOH). The MO⁻ signal primarily reflects metal oxides but can also include contributions from metal hydroxides. Similarly, the MOH⁻ signal primarily indicates metal hydroxides, although metal oxides can also contribute to this signal (by attaching very mobile hydrogen). The ToF-SIMS images show that Fe, Co, and Ni oxides/hydroxides dominate the catalyst surface (represented by the MO⁻ and MOH⁻ signals). In contrast, Cu oxides and hydroxides are detected at lower intensity. This distribution suggests that anodic oxidation primarily facilitates the formation of Fe, Co, and Ni oxides/hydroxides while Cu either dissolves, migrates, or forms sub-surface layers during the treatment.

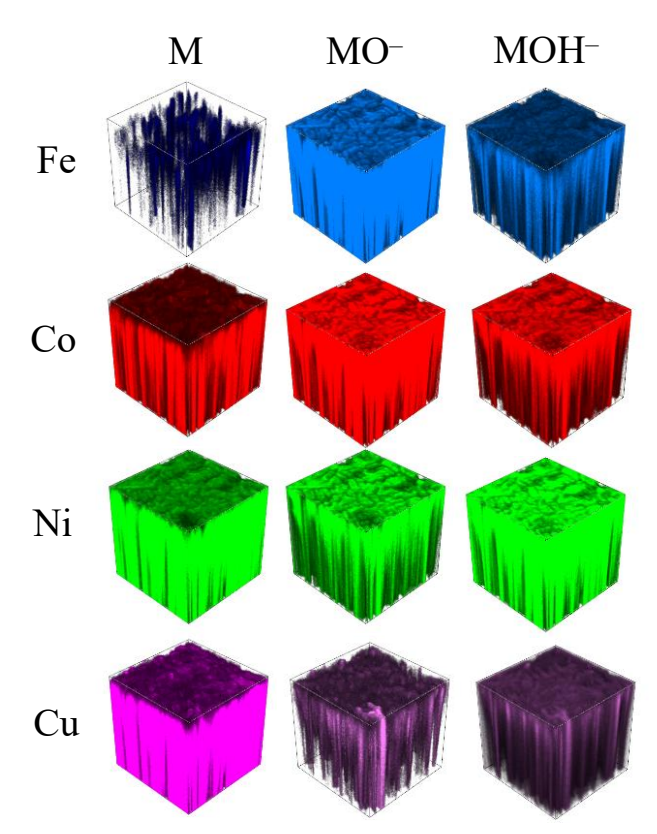


Figure 3. 3D ToF-SIMS images showing M^- (M = Ni, Fe, Ni or Co), and the corresponding signal for MO^- and MOH^- . The analysis was performed after the electrocatalytic glycerol oxidation tests

Another explanation for the lower Cu presence could be selective leaching during anodic oxidation, leading to Cu depletion from the outermost layer. This effect aligns with the known behaviour of Cu under oxidative conditions, where more noble elements like Fe, Co, and Ni tend to stabilize on the surface. The transformation from metallic states to oxides and hydroxides reflects the anticipated outcome of anodic oxidation, which alters surface chemistry and enhances porosity and surface area, contributing to improved catalytic activity.

SEM-EDS analysis shows that the catalyst film is primarily composed of oxygen, iron, cobalt, and nickel, with Ni being the most abundant metal (Table 1). The EDS mapping analysis (Supplementary material, Figure S1) reveals a uniform elemental distribution. The significant presence of Ni, along with Fe and Co, suggests the formation of mixed metal oxides, which are known to enhance the catalytic activity of oxygen evolution reaction due to the availability of numerous Ni- and Co-based active sites and multiple oxidation states [25]. Copper is detected only in trace amounts, likely because it was removed during the anodic oxidation process, which, more importantly, also contributed to the increased porosity of the film.

Table 1. The chemical composition in of the compositionally complex catalyst was determined with SEM-EDS.

Analysis was performed after the electrocatalytic glycerol oxidation tests.

		(Content, at.%		
Analysis	Fe	Co	Ni	Cu	0
EDS	13.0	13.1	19.1	1.3	51.5

Electrocatalytic glycerol oxidation performance

The electrocatalytic performance of FeCoNiCu catalyst was determined in 1 M KOH (Titripur, Merck) in the absence and the presence of 0.1 M glycerol (Figure 3a). The electrocatalytic performance of FeCoNiCu catalyst was determined first for OER in 1 M KOH and compared to the IrO_x benchmark, as shown in Figure 3. Besides a clear advantage in terms of cost, the treated FeCoNiCu catalyst is also more active than IrO_x as it needs 54 mV less overvoltage to reach a current density of 10 mA cm⁻². This comparison exemplifies the applicability of NT-AO-treated CCMs as OER catalysts. Furthermore, the same catalyst was tested for GOR, as shown in Figure 4. At the current density of 50 mA cm⁻², the voltage difference between GOR and OER is 140 mV, which shows a significant decrease in the energy input needed to drive glycerol-assisted water splitting. A comparison of hereby developed material with recent literature data is given in Table S1. The determined $C_{\rm cl}$ value for NT-AO-Treated FeCoNiCu catalyst was equal to 1.0 mF cm⁻² (see Figure S2), which is significantly lower compared to other literature reports on similar catalysts. This could indicate that despite necessitating a higher potential to reach the current density of 10 mA cm⁻², the active sites present in NT-AO-treated FeCoNiCu have high specific activity. Therefore, by increasing the number of exposed active sites, the performance of the FeCoNiCu catalyst can be further boosted.

Product profiling during GOR was conducted using chronoamperometry at different potential values, as shown in Figure 4b. Based on the polarization curves in Figure 4a, it can be proposed that OER occurs at a negligible extent compared to GOR at the potentials used for chronoamperometric tests, as the significant OER currents are measured only at potentials above 1.5 V_{RHE} . Except at the potential of 1.35 V_{RHE} , the measured current densities show that significant glycerol oxidation takes place at the FeCoNiCu catalyst. The main products during glycerol oxidation experiments are expected to be liquid, and NMR was used to analyze the product distribution.

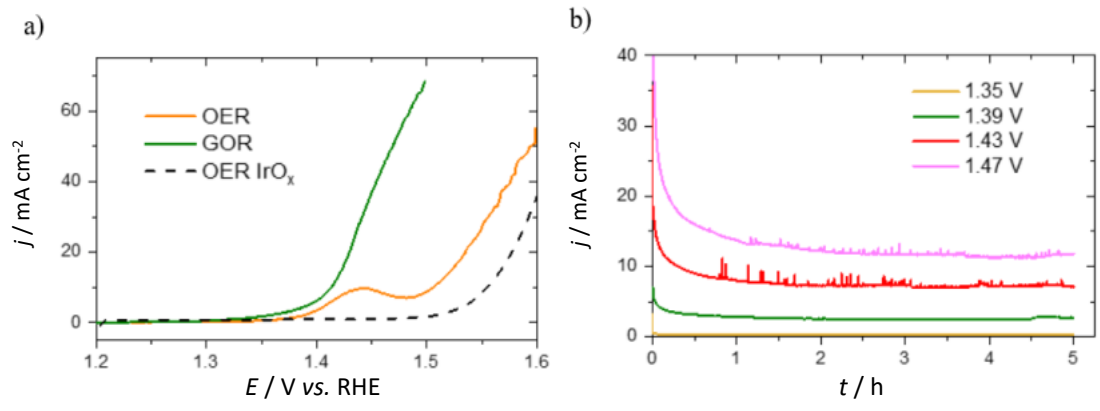


Figure 4. a) LSV polarization curves in 1 M KOH and 1 M KOH with 0.1 M glycerol. b) Chronoamperometric glycerol oxidation at varied potentials in 1 M KOH solution containing 0.1 M glycerol

After each potential hold, $100\,\mu\text{L}$ of electrolyte was sampled, and ^1H NMR spectra were measured (Figure S3). The conversion of starting glycerol was low due to the large relative volume of the cell compared to the working electrode surface area. Using ^1H NMR, 1,2-propanediol and formic acid (FA) were determined as the main electrolysis products. The amount of 1,2-propanediol remained constant at different applied potentials, whereas the relative amount of formic acid increased with increasing potential (Table 2). This suggests that the main product of electrolysis at applied potentials was formic acid.

Table 2. Relative conversions of starting glycerol at different potential holds after 5 hours. The conversions are calculated based on the integrals of distinct peaks for each compound

WE not ontial Vive BUE	Glycerol conversion, %	Content of formic acid, %	Content of
WE potential, V VS. KHE		Content of formic acid, %	1,2-propanediol, %
1.35	1.21	0.27	0.94
1.39	1.83	0.83	1.00
1.43	2.41	1.58	0.83
1.49	3.96	2.90	1.06

Conclusion

In this study, a FeCoNiCu compositionally complex alloy was successfully modified through nitridation (NT) and anodic oxidation (AO), resulting in a highly porous, thin film electrocatalyst with enhanced activity for both the oxygen evolution reaction (OER) and glycerol oxidation reaction (GOR). The synergistic effects of surface treatments yielded a hierarchical structure with significantly increased surface area and optimized active sites, improving catalytic performance. The NT-AO-treated FeCoNiCu catalyst demonstrated good OER activity compared to commercial IrO_x benchmarks by achieving lower overpotential requirements in an alkaline electrolyte. The catalyst showcased outstanding performance for glycerol oxidation, effectively lowering the energy input needed for water splitting by substituting OER with GOR. Product analysis during GOR confirmed the formation of formic acid and 1,2-propanediol as key products, highlighting its potential for value-added chemical production. These findings demonstrate that NT-AO surface modification is a powerful strategy for enhancing the electrocatalytic performance of medium entropy alloys and expanding their application in clean energy conversion technologies. Further optimization and testing could unlock the full potential of FeCoNiCu and similar systems for industrial-scale applications in water electrolysis and glycerol valorisation.



Supplementary material: Additional data are available electronically on article page of the journal's website: https://pub.iapchem.org/ojs/index.php/JESE/article/view/2637, or from the corresponding author upon request.

Acknowledgments: The provision of financial support for the research and the preparation of the manuscript by the Slovenian Research Agency (ARIS) within the research programs P2-0393, P2-0118, and I0-0003 and projects MN-0022, N2-0155, J2-3041, N2-0248, and N2-0337 is gratefully acknowledged. Authors further acknowledge funding from the NATO Science for Peace and Security Program (Grant G6230). The authors also thank Edi Kranjc (Department of Inorganic Chemistry and Technology, National Institute of Chemistry, Slovenia) for the X-ray powder-diffraction measurements. The project is co-financed by the Republic of Slovenia, the Ministry of Education, Science and Sport, and the European Union under the European Regional Development Fund.

References

- [1] X. Du, X. Ma, X. Ding, W. Zhang, Y. He, Enhanced high-temperature oxidation resistance of low-cost Fe-Cr-Ni medium entropy alloy by Ce-adulterated, *Journal of Materials Research and Technology* **16** (2022) 1466-1477. https://doi.org/10.1016/j.jmrt.2021.12.087
- [2] D. Wang, L. Liu, M. Chen, H. Zhuang, Electrical and thermal transport properties of medium-entropy SiyGeySnx alloys, Acta *Materialia*199 (2020) 443-452. https://doi.org/10.1016/j.actamat.2020.08.053
- [3] F. Cao, P. Munroe, Z. Zhou, Z. Xie, Medium entropy alloy CoCrNi coatings: Enhancing hardness and damage-tolerance through a nanotwinned structuring, *Surface and Coatings Technology* **335** (2018) 257-264. https://doi.org/10.1016/j.surfcoat.2017.12.021
- [4] X. Wang, C. Yang, Y. Zhang, D. Xiong, S. Xu, L. Wang, L. Jiang, P. B. Sorokin, P.K. Chu, Medium-entropy alloy MoCoCu-P as an efficient bifunctional catalyst for water splitting, *Journal of Alloys and Compounds* 988 (2024) 174332. https://doi.org/10.1016/j.jallcom.2024.174332
- [5] S. Shuang, G. J. Lyu, D. Chung, X. Z. Wang, X. Gao, H. H. Mao, W. P. Li, Q. F. He, B. S. Guo, X. Y. Zhong, Y. J. Wang, Y. Yang, Unusually high corrosion resistance in MoxCrNiCo medium entropy alloy enhanced by acidity in aqueous solution, *Journal of Materials Science & Technology* **139** (2023) 59-68. https://doi.org/10.1016/j.jmst.2022.07.061
- [6] L. Wang, Y. Jiao, R. Liu, D. Wang, Z. Yu, Y. Xi, K. Zhang, S. Xu, H. Liu, L. Wen, X. Xiao, W. Zhang, J. Ji, A Review of Mechanical Properties and Improvement Methods of Medium Entropy Alloys at High Temperature, *Journal of Metals* **76** (2024) 353-361. https://doi.org/10.1007/s11837-023-06217-3
- [7] L. Suhadolnik, M. Bele, M. Smiljanić, G. Dražić, L. D. Rafailović, D. Neumüller, M. Šala, A. Logar, N. Hodnik, M. Gaberšček, J. Kovač, U. Trstenjak, T. Montini, M. Melchionna, P. Fornasiero, Enhancing oxygen evolution functionality through anodization and nitridation of compositionally complex alloy, *Materials Today Chemistry* **35** (2024) 101835. https://doi.org/10.1016/j.mtchem.2023.101835
- [8] V. Strotkötter, Y. Li, A. Kostka, F. Lourens, T. Löffler, W. Schuhmann, A. Ludwig, Selfformation of compositionally complex surface oxides on high entropy alloys observed by accelerated atom probe tomography: a route to sustainable catalysts, *Material Horizons* 11 (2024) 4932-4941. https://doi.org/10.1039/d4mh00245h
- [9] Z. J. Baum, L. L. Diaz, T. Konovalova, Q. A. Zhou, Materials Research Directions Toward a Green Hydrogen Economy: A Review, ACS Omega 7 (2022) 32908-32935. https://doi.org/10.1021/acsomega.2c03996
- [10] E. A. Moges, K. Lakshmanan, C. Y. Chang, W. S. Liao, F. T. Angerasa, W. B. Dilebo, H. G. Edao, K. T. Tadele, D. D. Alemayehu, B. D. Bejena, C. B. Guta, C. C. Chang, M. C. Tsai, W. N. Su, B. J. Hwang, Materials of Value-Added Electrolysis for Green Hydrogen Production, *ACS*

- Materials Letters Journal **6** (2024) 4932-4954. https://doi.org/10.1021/acsmaterialslett.4c01173
- [11] H. H. Dong, Y. X. Zhu, Y. G. Li, J. Y. Liang, Y. Tan, X. Y. Zhang, H. M. Jiang, L. Lin, Z. M. Sun, Recent advances in glycerol valorization through electrocatalytic methods, *Tungsten* **6** (2024) 696-710. https://doi.org/10.1007/s42864-024-00281-1
- [12] Q. Wang, J. Li, Y. Li, G. Shao, Z. Jia, B. Shen, Non-noble metal-based amorphous high-entropy oxides as efficient and reliable electrocatalysts for oxygen evolution reaction, *Nano Research* **15** (2022) 8751-8759. https://doi.org/10.1007/s12274-022-4179-8
- [13] T. Li, D.A. Harrington, An Overview of Glycerol Electrooxidation Mechanisms on Pt, Pd and Au, *ChemSusChem* **14** (2021) 1472-1495. https://doi.org/10.1002/CSSC.202002669
- [14] C. Li, H. Li, B. Zhang, H. Li, Y. Wang, X. Wang, P. Das, Y. Li, X. Wu, Y. Li, Y. Cui, J. Xiao, Z.-S. Wu, Efficient Electrocatalytic Oxidation of Glycerol to Formate Coupled with Nitrate Reduction over Cu-Doped NiCo Alloy Supported on Nickel Foam, *Angewandte Chemie International Edition* **63** (2024) e202411542. https://doi.org/10.1002/ANIE.202411542
- [15] L. Fan, B. Liu, X. Liu, N. Senthilkumar, G. Wang, Z. Wen, Recent Progress in Electrocatalytic Glycerol Oxidation, *Energy Technology* **9** (2021) 2000804. https://doi.org/10.1002/ENTE.202000804
- [16] Y. Zhou, Y. Shen, J. Xi, X. Luo, Selective Electro-Oxidation of Glycerol into Dihydroxyacetone by PtAg Skeletons., *ACS Appplied Materials & Interfaces Journal* **11** (2019) 28953-28959. https://doi.org/10.1021/ACSAMI.9B09431
- [17] M. S. E. Houache, K. Hughes, A. Ahmed, R. Safari, H. Liu, G. A. Botton, E. A. Baranova, Electrochemical Valorization of Glycerol on Ni-Rich Bimetallic NiPd Nanoparticles: Insight into Product Selectivity Using in Situ Polarization Modulation Infrared-Reflection Absorption Spectroscopy, ACS Sustainable Chemistry & Engineering Journal 7 (2019) 14425-14434. https://doi.org/10.1021/acssuschemeng.9b01070
- [18] H. Yao, Y. Wang, Y. Zheng, X. Yu, J. Ge, Y. Zhu, X. Guo, High-entropy selenides: A new platform for highly selective oxidation of glycerol to formate and energy-saving hydrogen evolution in alkali-acid hybrid electrolytic cell, Nano Research **16** (2023) 10832-10839. https://doi.org/10.1007/s12274-023-5842-4
- [19] L. Fan, Y. Ji, G. Wang, J. Chen, K. Chen, X. Liu, Z. Wen, High Entropy Alloy Electrocatalytic Electrode toward Alkaline Glycerol Valorization Coupling with Acidic Hydrogen Production, Journal of the American Chemical Society 144 (2022) 7224-7235. https://doi.org/10.1021/jacs.1c13740
- [20] Y. Li, J. Hong, Y. Shen, Application of platinum-based high-entropy-alloy nanoparticles for electro-oxidation of formic acid and glycerol, *International Journal of Hydrogen Energy* **82** (2024) 448-455. https://doi.org/10.1016/J.IJHYDENE.2024.07.229
- [21] L. Suhadolnik, M. Bele, M. Čekada, P. Jovanovič, N. Maselj, A. Lončar, G. Dražić, M. Šala, N. Hodnik, J. Kovač, T. Montini, M. Melchionna, P. Fornasiero, Nanotubular TiOxNy-Supported Ir Single Atoms and Clusters as Thin-Film Electrocatalysts for Oxygen Evolution in Acid Media, *Chemistry of Materials* **35** (2023) 2612-2623. https://doi.org/10.1021/ACS.CHEMMATER.3C00125
- [22] W. Zhang, Z. Qu, X. Li, Y. Wang, D. Ma, J. Wu, Comparison of dynamic adsorption/desorption characteristics of toluene on different porous materials, *Journal of Environmental Sciences* **24** (2012) 520-528. https://doi.org/10.1016/S1001-0742(11)60751-1
- [23] R. Luque, A. Ahmad, S. Tariq, M. Mubashir, M. Sufyan Javed, S. Rajendran, R. S. Varma, A. Ali, C. Xia, Functionalized interconnected porous materials for heterogeneous catalysis, energy conversion and storage applications: Recent advances and future perspectives, *Materials Today* **73** (2024) 105-129. https://doi.org/10.1016/J.MATTOD.2023.05.001



- [24] X. H. Yan, P. K. Liaw, Y. Zhang, Order and Disorder in Amorphous and High-Entropy Materials, *Metallurgical and Materials Transactions A* **52** (2021) 2111-2122. https://doi.org/10.1007/s11661-021-06250-4
- [25] K. Kim, T. Kang, M. Kim, J. Kim, Exploring the intrinsic active sites and multi oxygen evolution reaction step via unique hollow structures of nitrogen and sulfur co-doped amorphous cobalt and nickel oxides, *Chemical Engineering Journal* **426** (2021) 130820. https://doi.org/10.1016/J.CEJ.2021.130820

© 2025 by the authors; licensee IAPC, Zagreb, Croatia. This article is an open-access article distributed under the terms and conditions of the Creative Commons Attribution license (https://creativecommons.org/licenses/by/4.0/)



Open Access:: ISSN 1847-9286 www.jESE-online.org

Original scientific paper

Exploring the impact of Al-based electrolytes on the charge storage behaviour of vine shoots derived carbon

Jana Mišurović^{1,⊠}, Aleksandra Gezović Miljanić¹, Veselinka Grudić¹, Robert Dominko², Milica Vujković^{3,4}

¹University of Montenegro - Faculty of Metallurgy and Technology, Cetinjski put bb, 81000 Podgorica, Montenegro

²National Institute of Chemistry, Hajdrihova 19, SI-1000, Ljubljana, Slovenia

³University of Belgrade - Faculty of Physical Chemistry, Studentski trg 12-16, 11158 Belgrade, Serbia ⁴Center for Interdisciplinary and Multidisciplinary Studies, University of Montenegro, Podgorica, Montenegro

Corresponding author: [™]janam@ucq.ac.me

Received: October 15, 2024; Accepted: November 30, 2024; Published: December 11, 2024

Abstract

A new concept for affordable supercapacitors based on Al aqueous electrolytes was proposed recently. This study provides a deeper insight into the cyclic performance of vine shoots-derived activated carbon using three different 1 M aqueous electrolytes: Al₂(SO₄)₃, Al(NO₃)₃ and AlCl₃. Cyclic voltammetry (CV), galvanostatic cycling and impedance measurements have shown that the type of anion causes the differences in the rate capability and long-term cyclability. Although CV deviation is provoked by aggravated sulphate penetration into pores upon switching at higher currents, Al₂(SO₄)₃ emerged as the most promising electrolyte solution due to the best cycling stability of the 1.5 V full cell over 15,000 cycles. Intensive oxidation of the positive electrode during initial cycling, induced by nitrates reduction, is the main reason for the fastest capacitance drop observed in $Al(NO_3)_3$. Therefore, the capacitance values of the carbon cell measured after 5,000 cycles in $Al(NO_3)_3$ (75 F g⁻¹) are two times lower than the corresponding values in $Al_2(SO_4)_3$ and $AlCl_3$ (131 and 127 F g^{-1} , respectively). The oxidation becomes more pronounced only after 10,000 cycles in AlCl₃, thus causing a notable capacitance drop, which is not evidenced in Al₂(SO₄)₃. Al₂(SO₄)₃-based cell can withstand 15,000 with good specific capacitance/energy retention.

Keywords

Al-based supercapacitors; aqueous electrolyte; cyclic stability aspect

Introduction

The viticulture industry produces large amounts of carbon-rich bio-waste and represents a valuable feedstock for the development of a broad material selection with many specific applications. Various byproducts of the grape processing lines have been investigated for different energy-related and environmental applications [1-6]. Vineyard pruning residues, vine shoots, make the most of the dry-basis waste, which takes up enormous space and is most often disposed of by incineration. To prevent the negative effects of this practice, new sustainable alternatives are required. Until now, vine shoot-derived carbons have been considered for the adsorption of different substances [7-10] and energy-related applications, including supercapacitors [11-13]. Especially, carbon derived from vine shoots emerged as a promising electrode for versatile aqueous-based supercapacitors [13].

In addition to the electrode material, the electrolyte significantly determines the overall performance of supercapacitor cell. Several advantages related to conductivity, viscosity, toxicity, and flammability push aqueous electrolytes before conventional organic ones. Nonetheless, thermodynamic limitations on workable voltage window (1.23 V) make them inferior to the organic electrolyte (≈ 2.7 V typically for acetonitrile or propylene carbonate mixed with an organic salts). Typical acidic (H_2SO_4) and alkaline (NaOH) aqueous electrolytes usually allow only a maximal operating voltage of 1 V.

The use of neutral salts based on sulphates (Li_2SO_4 , K_2SO_4 , Na_2SO_4) [14-17] and nitrates (typically LiNO₃) [18-20] stretches the potential window up to ≈ 2 V, with an operative voltage of 1.5 V delivering stable capacitance. Studying the mechanism of carbon-based supercapacitors in these electrolytes, Frackowiak *et al.* [18] concluded that Li_2SO_4 appeared to be the most promising electrolyte. More precisely, the interplay between variables, including the type of material, binder, current collector, hydrogen storage ability, ion solvent and ion-pore interaction, determines the final performance. For instance, the type of electrolyte anions (sulphates or nitrates) may cause the different hydrogen storage capabilities of the carbon and different redox processes occurring at the interface upon prolonged cycling to 1.8 V [18]. This leads to the higher initial energy/power density for LiNO₃-based supercapacitors but lower stability due to additional nitrate-related redox reactions.

Recently, acidic $Al_2(SO_4)_3$ was proposed as an additional approach capable of opening water boundaries beyond the thermodynamic stability window [13]. To the best of our knowledge, no comparative and detailed studies about using different Al-based aqueous electrolyte formulations for supercapacitors have been reported so far. Herein, three different Al-based electrolyte formulations were used to examine the performance of vine shoots-derived carbon. The role of anions $(SO_4^{2-}, NO_3^-, Cl^-)$ on the performance and long-term stability of high voltage Al-based symmetric AC_{vs} supercapacitors was investigated.

Experimental

Material preparation

Activated carbon was obtained by the carbonization of winemaking industry waste, vine shoots, via a previously reported two-step route [13]. Vine shoots collected in the area near Podgorica, Montenegro, were washed, chopped, ground and dried in the air to be prepared for carbonization. First, the precursor was heated for 2 h at a lower temperature (300 °C) under Ar atmosphere with a heating rate of 5 °C min⁻¹. Second, the obtained material was mixed with ZnCl₂ in a mass ratio 1:3, respectively, and carbonized for another 2 h at 700 °C under Ar atmosphere (heating rate of

 $5~^{\circ}$ C min⁻¹). The final product was thoroughly washed with 4 M HCl, hot distilled water, and cold distilled water to remove zinc residues and chlorides completely. In further text, the obtained carbon is designated AC_{vs}700.

Material characterization

XRD of AC_{vs}700 was measured on Rigaku MiniFlex600 X-ray diffractometer operating in parafocusing Brag-Brentano geometry. The source of X-ray Cu-K α radiation was coupled to a D/teX Ultra2 MF semiconductor strip-type detector with direct detection. The operating conditions of the instrument were a voltage of 40 kV and a current of 15 mA. The sample was mounted on a Silica support and the diffractogram was recorded in the 10 to 80° 2 θ angle range, with a step of 0.01°, at a data acquisition rate of 10.00°/min.

SEM micrographs were obtained using SEM FEI Scios2 dual beam system.

Electrochemical methods

Cyclic voltammetry (CV) was performed by using Gamry 1010E Potentiostat/Galvanostat in a typical three-electrode configuration, where saturated calomel electrode (SCE) and platinum foil served as reference and counter electrodes, respectively. The working electrode was a glassy carbon rod with active material ($AC_{vs}700$) slurry distributed evenly on its surface. For all measurements, the slurry was prepared by mixing the active material with a binder (5 wt.% Nafion in ethanol/water = 95/5 weight ratio, Sigma Aldrich) in the mass ratio 95 : 5 and adding the appropriate amount of ethanol to form a viscous mixture. It was further treated ultrasonically until the desired flow was obtained and transferred to a glassy carbon surface in a very thin layer (mass loading was kept at \approx 1 to 1.5 mg cm⁻²). CV measurements were performed at different scan rates within the electrochemical stability window of the used electrolyte.

Galvanostatic charge/discharge measurements were performed using a BTS 8.0 Battery Analyzer Neware 5 V 100 mA in a two-electrode configuration using glassy carbon as current collectors. Comparative charge/discharge curves were measured first at a common current density of 1 A $\rm g^{-1}$ for 5 cycles and afterward, at 5 A $\rm g^{-1}$ for 15,000 cycles with the upper cut-off voltage of 1.5 V. Based on these measurements, the specific capacitance of the electrode ($\it C_s$ in F $\rm g^{-1}$) was calculated according to Equation (1):

$$C_{\rm s} = \frac{2(I\Delta t)}{IJm} \tag{1}$$

with I / A being the discharge current, Δt / s discharge time, U / V the maximal voltage window and m / g the mass of the active material at a single electrode. The specific energy density of the constructed supercapacitor cells (E_s / Wh kg⁻¹) was calculated based on the mass of both electrodes (active materials) according to Equation (2):

$$E_{\rm s} = \frac{1}{8}C_{\rm s}U^2 \tag{2}$$

Electrochemical impedance measurements were performed on Gamry 1010E Potentiostat/Galvanostat in a previously described three-electrode configuration using a typical frequency interval of 10^{-2} to 10^{5} Hz and AC voltage amplitude of 5 mV. For impedance measurements after the cycling stability test (5000, 10,000 and 15,000 cycles), the previously glavanostatically cycled electrodes were transferred to a three-electrode cell in a common electrolyte. The impedance spectra of both pristine and cycled electrodes were obtained at the fixed potential of 0.1 V corresponding to the redox process.

The complex impedance analysis was performed by applying Equations (3) to (5):

$$C(\omega) = -C_{\rm re}(\omega) - jC_{\rm im}(\omega) \tag{3}$$

$$C_{\rm re}(\omega) = -Z''(\omega) / \omega |Z(\omega)|^2 \tag{4}$$

$$C_{\text{im}}(\omega) = -Z'(\omega) / \omega |Z(\omega)|^2 \tag{5}$$

 $C_{re}(\omega)$ corresponds to the real part of the complex capacitance $C(\omega)$, in which a low-frequency value converges with the DC capacitance obtained by CV or galvanostatic measurements. $C_{im}(\omega)$, as an imaginary component of the complex capacitance $C(\omega)$, represents resistive losses that lead to energy dissipation.

All measurements were performed in 1 M $Al_2(SO_4)_3$, 1 M $Al(NO_3)_3$ and 1 M $AlCl_3$ electrolytes and at room temperature. Their electrical conductivity and pH were measured using Seven Compact pH/Conductometer S213 Mettler Toledo.

Results and discussion

ACvs700 microstructural characterization

Typical XRD of activated carbon, including reflections at 24 and 43° (2 θ) indexed to (002) and (100) planes of graphite, is observed for ACvs700, Figure 1a. Broad and low-intensity diffraction peaks indicate its amorphous nature. The interplanar distance (002) estimated using Bragg's law amounts to 0.036704 nm, which aligns with the activated carbon structure [21]. SEM figure reveals irregular AC_{vs} micrometre agglomerates composed of nanoparticles embedded into deep holes formed during the liberation of gases during ZnCl₂-assisted activation. Material developed a high BET surface area of 1494 m² g⁻¹ with high microporosity (Dubinin-Radushkevich method, $V_{\text{micro}} = 0.548 \text{ cm}^3 \text{ g}^{-1}$) and mesoporosity fraction (Dollimore and Heal method $V_{\text{meso}} = 0.254 \text{ cm}^3 \text{ g}^{-1}$).

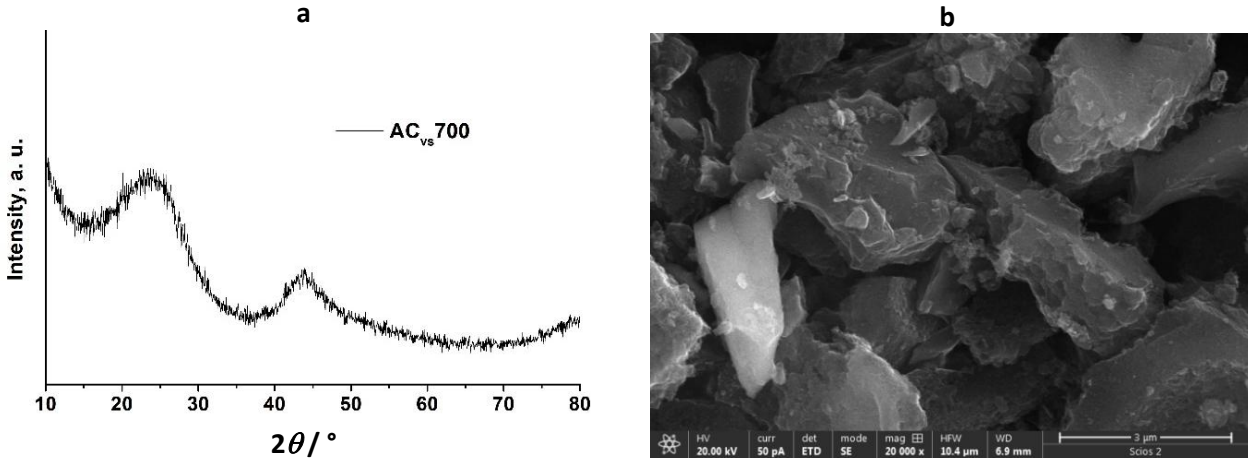


Figure 1. XRD pattern a) and SEM image b) of AC_{vs}700

Interfacial redox processes in Al-based electrolytes

Redox processes of $AC_{vs}700$ in 1 M Al-containing aqueous electrolytes ($Al_2(SO_4)_3$, $Al(NO_3)_3$ and $AlCl_3$) were characterized in a three-electrode configuration by CV at different scan rates (Figure 2 and Figure S1). Figure 2 shows the capacitive behaviour of $AC_{vs}700$ in all three electrolytes comparatively at a lower, medium, and higher scan rate. A similar current response was observed for all electrolytes at lower scan rates, Figure 2a. Due to their acidity, typical hydroquinone/quinone-related redox peaks observed at $0.15/0.08 \, \text{V} \, vs$. SCE can be recognized [22,23]. Additionally, in $Al(NO_3)_3$, there is a deviation at negative potentials in the form of a small cathodic peak (-0.4 V vs. SCE), which appears before the hydrogen evolution reaction, belonging to the reduction of NO_3^{-1} in an acidic medium [24]. As the scan rate increases (Figures 2b and 2c), the anion influence becomes more pronounced in the way that sulphates deviate from chlorides and nitrates.

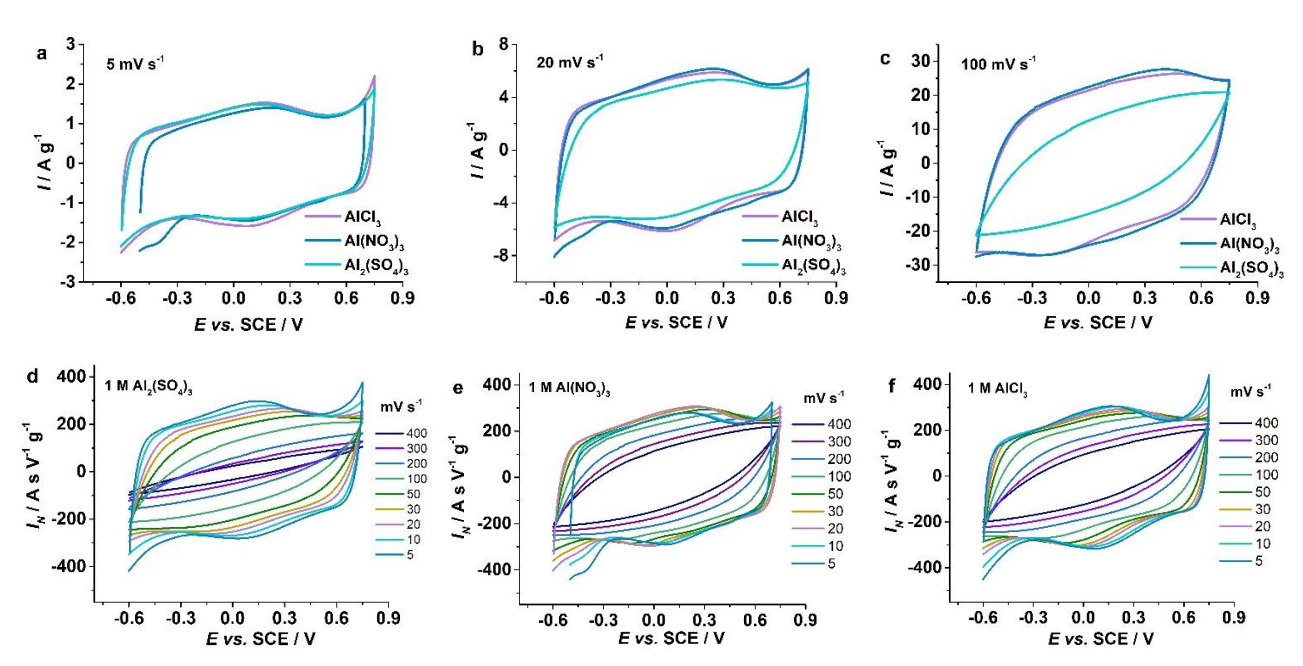


Figure 2. Cyclic voltammograms of AC_{vs}700 in 1 M Al-based electrolytes at the scan rates of (a) 5 mV s⁻¹, (b) 20 mV s⁻¹ and (c) 100 mV s⁻¹ and (d), (e), (f) their scan rate-normalized form for at all scan rates

To explain this behaviour, it is worth considering that AC_{vs}700 has a large specific surface area of $S_{BET} = 1494 \text{ m}^2 \text{ g}^{-1}$, relying on developed micro- (0.548 cm³ g⁻¹) and mesoporosity (0.254 cm³ g⁻¹), with wide micropore size distribution profile ≈ 0.5 -0.7 nm ($D_{max} = 0.5$ nm) [13]. Namely, the correlation of these properties with the size of the used electrolyte ions could be beneficial. The differences in electrochemical behaviour of AC_{vs}700 in various Al-ion-based electrolytes can be explained by the larger hydrated radius of SO₄²⁻, which causes their retarded adsorption and diffusion through the pores, while the smaller and similar radius of NO₃⁻ and Cl⁻ does not impede these processes as much [25,26]. Although the absolute radius of the hydrated specific (SO₄²⁻, NO₃⁻ and Cl⁻) anions is not consistent in literature (depending on the used approach and conditions taken into account) [25-27], the relation between their radii follows the same trend ($SO_4^{2-} > NO_3^{-} > Cl^{-}$). The micropores with a maximal diameter (0.5 nm) are less available for large SO₄²⁻ ions (the calculated diameter of solvated ions can reach values up to 0.533 nm [25]), which leads to a decrease in the number of ions that enter the total pores volume. Additionally, the measured electrical conductivity of Al₂(SO₄)₃ is more than four times lower than that of AlCl₃ and Al(NO₃)₃, resulting in slower movement of ions at higher scan rates, Table 1. A clear representation of this behavior is given by the scan rate-normalized CV graphs (Figure 1d, 1e and 1f), where it can be seen how, in Al₂(SO₄)₃, the voltammograms lose shape as the scan rate increases. On the other hand, in AlCl₃ and Al(NO₃)₃, these changes are much less pronounced.

Table 1. Measured electrical conductivities and pH values of 1 M $Al_2(SO_4)_3$, $Al(NO_3)_3$ and $AlCl_3$.

Electrolyte	1 M Al ₂ (SO ₄) ₃	1 M Al(NO ₃) ₃	1 M AlCl ₃
Conductivity, mS cm ⁻¹	25.733	104.751	114.199
рН	3.04	1.85	2.13

Comparative CV measurements implicate better rate capability in $AlCl_3$ and $Al(NO_3)_3$ while revealing the main obstacles for double layer formation in $Al_2(SO_4)_3$ electrolyte at extremely high currents. Still, their influence on the long-term stability of the material in a supercapacitor should be considered and examined in more detail.

To characterize the interface of pristine AC_{vs}700 electrode in 1 M Al₂(SO₄)₃, Al(NO₃)₃ and AlCl₃ (Figure 3a), Nyquist diagrams were measured at the potential of redox maxima. They show characteristic shapes of carbon electrodes. The high-frequency x-intercept typically belongs to the bulk electrolyte resistance, while the small semicircle, appearing in the high to mid-frequency range $(10^6-38.11 \text{ Hz for Al}(NO_3)_3, 10^6-139.2 \text{ Hz for AlCl}_3 \text{ and } 10^6-5.197 \text{ Hz for Al}_2(SO_4)_3, \text{ Figure 3a inset}),$ corresponds to the interfacial impedance between electrode and bulk solution including the contact impedance between material and current collector, ion transport processes into pores, and charge transfer resistance (R_{ct}) [28,29]. Different diameters of the semicircle indicate the prevailing role of the kinetic hindrance effects in its appearance, determined by the type of electrolyte ions. The highest resistance value for Al₂(SO₄)₃ is governed by the lowest ionic conductivity, Table 1, and the highest hydration enthalpy of SO₄²⁻ anion [28]. There is no such correlation when it comes to Al(NO₃)₃ and AlCl₃, where the inversed behaviour was observed. A slightly larger high-frequency resistance point of AlCl₃ vs. Al(NO₃)₃ (despite better conductivity), as well as a somewhat smaller semicircle diameter (despite larger hydration enthalpy of Cl⁻ vs. NO₃-), is probably the consequence of the poorer wettability of Cl⁻ vs. NO₃⁻ due to higher hydrophobicity [29]. The almost vertical region that prevails in the Nyquist diagram reflects a good pseudocapacitive behaviour of the material in all three types of electrolytes.

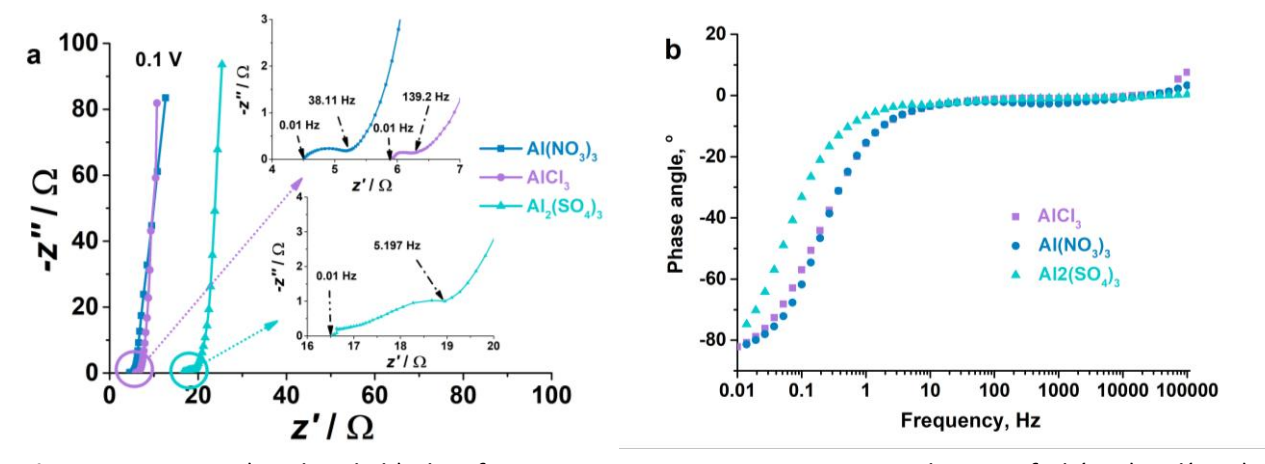


Figure 3. Nyquist a) and Bode b) plots for $AC_{vs}700$ pristine in 1 M aqueous solutions of $Al_2(SO_4)_3$, $Al(NO_3)_3$ and $AlCl_3$ measured in a three-electrode cell. Inset shows enlarged high-frequency part of the Nyquist plot

Dependence of the phase angle (φ) on the frequency (Figure 3b) indicates the almost ideal capacitor-like response with the low-frequency φ values very close to -90°, for all electrolytes. Dunn analysis of $AC_{vs}700$ in $Al_2(SO_4)_3$ [13] revealed that the electrical double layer capacitance (EDLC) dominates the total charge storage process (71 % at 5 mV s⁻¹ and 83 % at 50 mV s⁻¹). Based on the phase angle-frequency dependence, this contribution is slightly higher for $AlCl_3$ and $Al(NO_3)_3$. The real and imaginary parts of the capacitance (Figure S2a and b) were obtained as a function of frequency by applying complex capacitance analysis. Figure S2a shows the characteristic real capacitance-frequency dependence with a high degree of ion pore-filling where the plateau is not fully achieved especially for the $Al_2(SO_4)_3$ electrolyte. Comparative capacitance values observed within the frequency region of 0.1 to 1 Hz follow the trend measured by CV at scan rates from 20 mV s⁻¹. There is a deviation in the low-frequency capacitance values (around 0.01 Hz) from those obtained by CV at lower scan rates (< 20 mV s⁻¹). This can be attributed to the nitrate-involved redox and water electrolysis reactions since the CV was measured over the extended voltage window, while the impedance diagrams were collected at a fixed potential corresponding to the CV maximum. The typical dependence of the imaginary capacitance part of the frequency, including the existence of the maximum at the frequency

 f_0 , was presented in Figure S2b. The time constant, $\tau_0 = 1/f_0$, when the system changed behaviour from the resistor to the capacitor one, was found to be around 9.9, 7.3 and 19.8 s for AlCl₃, Al(NO₃)₃ and Al₂(SO₄)₃, respectively. The time-constant trend in different electrolytes follows the corresponding changes of CV with the scan rate increase. The highest τ_0 for Al₂(SO₄)₃ indicates the most limited rate capability, which is in accordance with the large deviation of CV upon switching the scan rate to 400 mV s⁻¹, Figure S2b. A somewhat higher τ_0 value for AlCl₃ compared to Al(NO₃)₃ corresponds to a more pronounced CV deviation at high scan rates, Figure 2.

Exploring AC_{vs}700 charge storage ability in different Al-based full cells

To further investigate the stability of the material in the symmetric supercapacitor cell using all three Al-containing electrolytes, galvanostatic testing has been performed, Figure 4. The different shape of the charge/discharge curves in $Al_2(SO_4)_3$ and $AlCl_3$ compared to $Al(NO_3)_3$ indicates a different charge storage mechanism within the higher voltage range (1.2-1.5 V at 5 A g⁻¹), Figure 4a. In $Al(NO_3)_3$ electrolyte, the sloping part is evidenced within this range and diminishes with time. This can be attributed to the irreversible redox processes of NO_3 , which are reduced in the vicinity of the positive electrode, thus oxidizing the carbon surface at higher voltages [19]. That contributes to significantly higher initial charge capacitance and slightly higher initial discharge capacitance for NO_3 ions compared to SO_4 and Cl, resulting in low initial efficiency. No similar behaviour is observed for SO_4 and Cl.

The irreversibility of the NO_3 -involved process is responsible for the notable short-term capacitance fade in $Al(NO_3)_3$ at 5 A g^{-1} (Figure 4b), more pronounced at the lower current of 1 A g^{-1} (Figure S3), after which the capacitance becomes stable over 5000 cycles, with good efficiency. Stabilized capacitance values in $Al(NO_3)_3$ (\approx 75 F g^{-1} at 5000 cycles) are almost two times lower than in the other two electrolytes (130 F g^{-1} in $Al_2(SO_4)_3$ and 125 F g^{-1} in $AlCl_3$). The corresponding specific energy of the cell is also notably lower for $Al(NO_3)_3$ (5.8 Wh kg^{-1}) when compared to $Al_2(SO_4)_3$ and $AlCl_3$ (10.2 and 9.9 Wh kg^{-1} , respectively). Generated oxygen groups on the carbon surface at limiting potentials decrease specific surface area [30] and specific capacitance/energy. Therefore, $Al_2(SO_4)_3$ and $AlCl_3$ appear as more promising than $Al(NO_3)_3$. It can be seen that the carbon oxidation also occurs in $Al_2(SO_4)_3$ and $AlCl_3$ at lower current rates of 1 A g^{-1} (slightly more pronounced in $Al_2(SO_4)_3$), resulting in the difference between charge and discharge capacitance, Figure S3, but it does not significantly deteriorate its value upon cycling.

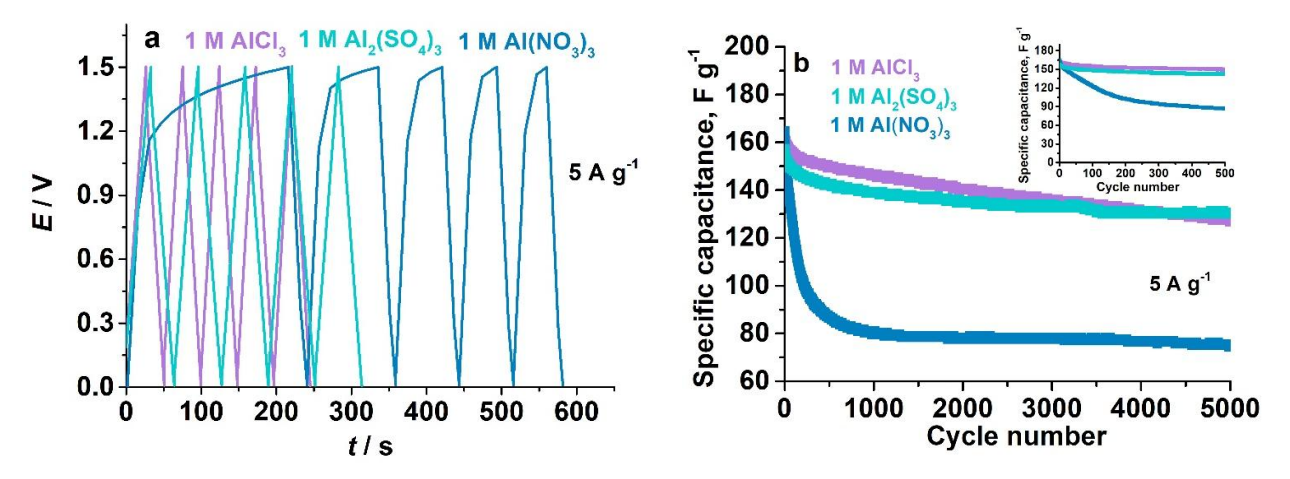


Figure 4. $AC_{vs}700$ -based supercapacitors with Al-ion containing electrolytes ($Al_2(SO_4)_3$, $Al(NO_3)_3$ and $AlCl_3$): (a) first five charge/discharge curves at 5 A g^{-1} , (b) specific capacitance vs. number of cycles for 5000 cycles at 5 A g^{-1} . Inset shows enlarged graph part within 0 to 500 cycles

Unlike their Li analogues [18], the use of Al(NO₃)₃ does not offer an advantage over the other two Al-based electrolytes in terms of initial delivered energy. For both Li and Al aqueous salts, NO₃-based electrolytes deteriorate the long-term stability of carbon (Fig 4b, inset).

The described galvanostatic behaviour from the two-electrode arrangement is reflected well through the impedance response of individual electrodes. Significant oxidation of the positive electrode in Al(NO₃)₃ over 5000 cycles responsible for the capacitance fade is evidenced through the appearance of the large semicircle, Figure 5a. Higher resistance values over the total frequency range measured in Al(NO₃)₃ also reflect the capacitance deterioration during cycling. The semicircle is not observed after cycling in Al₂(SO₄)₃ and AlCl₃, which correlates with good capacitance retention. Also, better wettability of the electrodes during charge/discharge can improve the transport of ions through pores and can result in depression of the initial semicircle measured before cycling. Since a certain degree of oxidation still occurs at the positive electrode at 1 A g⁻¹ (the current density at which the cell was previously cycled) and is more pronounced for Al₂(SO₄)₃ than for AlCl₃, lower highfrequency intercept was observed for SO₄²⁻ containing electrolyte. Therefore, oxidation of the polarized positive electrode controls the high-frequency intercept by altering the wettability of the surface. The opposite effect was observed at a negative electrode, Figure 5b. Different processes at positive and negative electrodes are reflected in different phase angle-frequency profiles for specific electrolytes, Figures 5c and 5d. The peak-shaped phase angle response was measured for the positive electrode in Al(NO₃)₃ (after 5000 cycles) due to its strong oxidation (Figure 5c). This is a consequence of the aggravated penetration of ions through pores and their interaction with generated oxygen groups. This influence is not observed at the negative electrode, where the phase angle retains its characteristic initial shape (Figure 5d).

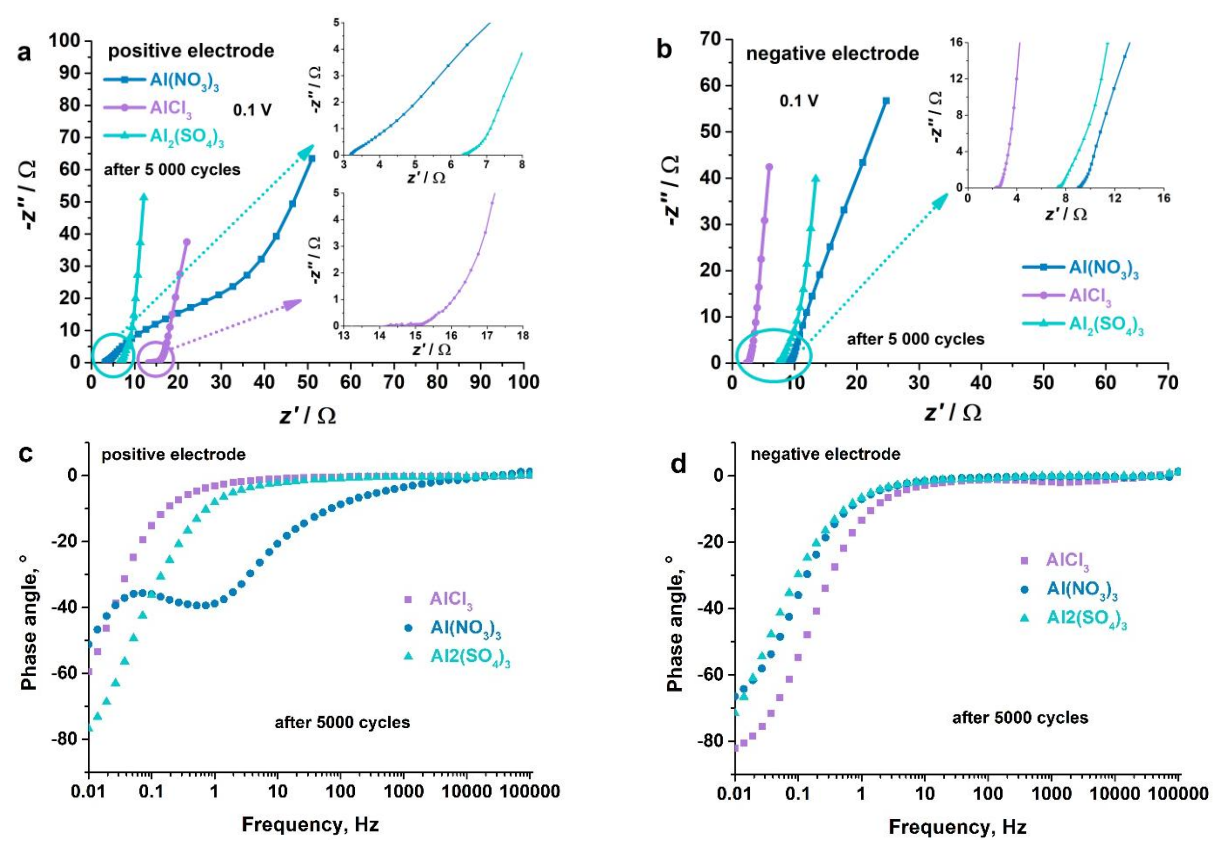


Figure 5. Nyquist (a, b) and Bode (c, d) plots for positive and negative $AC_{vs}700$ electrodes measured in a three-electrode cell after 5,000 cycles using 1 M aqueous solutions of $Al_2(SO_4)_3$, $Al(NO_3)_3$ and $AlCl_3$. Inset shows enlarged high-frequency part of the Nyquist plot

To further observe if there are crucial differences between $Al_2(SO_4)_3$ and $AlCl_3$, the long-term stability test was performed over 15,000 cycles (Figure 6a). The notable difference is observed only after 10,000 cycles, where the capacitance in $AlCl_3$ starts to fade significantly and $Al_2(SO_4)_3$ keeps the same trend. The capacity retention of ACvs700/ACvs700 cells amounts to ≈ 83 , ≈ 75 and ≈ 65 % in $Al_2(SO_4)_3$, while the corresponding values for $AlCl_3$ are ≈ 77 , ≈ 67 and ≈ 30 % after 5,000, 10,000 and 15,000 cycles, respectively. Considering that the CV distortion in $Al_2(SO_4)_3$ starts after 20 mV s⁻¹ (the current maximum corresponds to ≈ 5 A g⁻¹), excellent capacitance performance is still achieved at a current of 5 A g⁻¹.

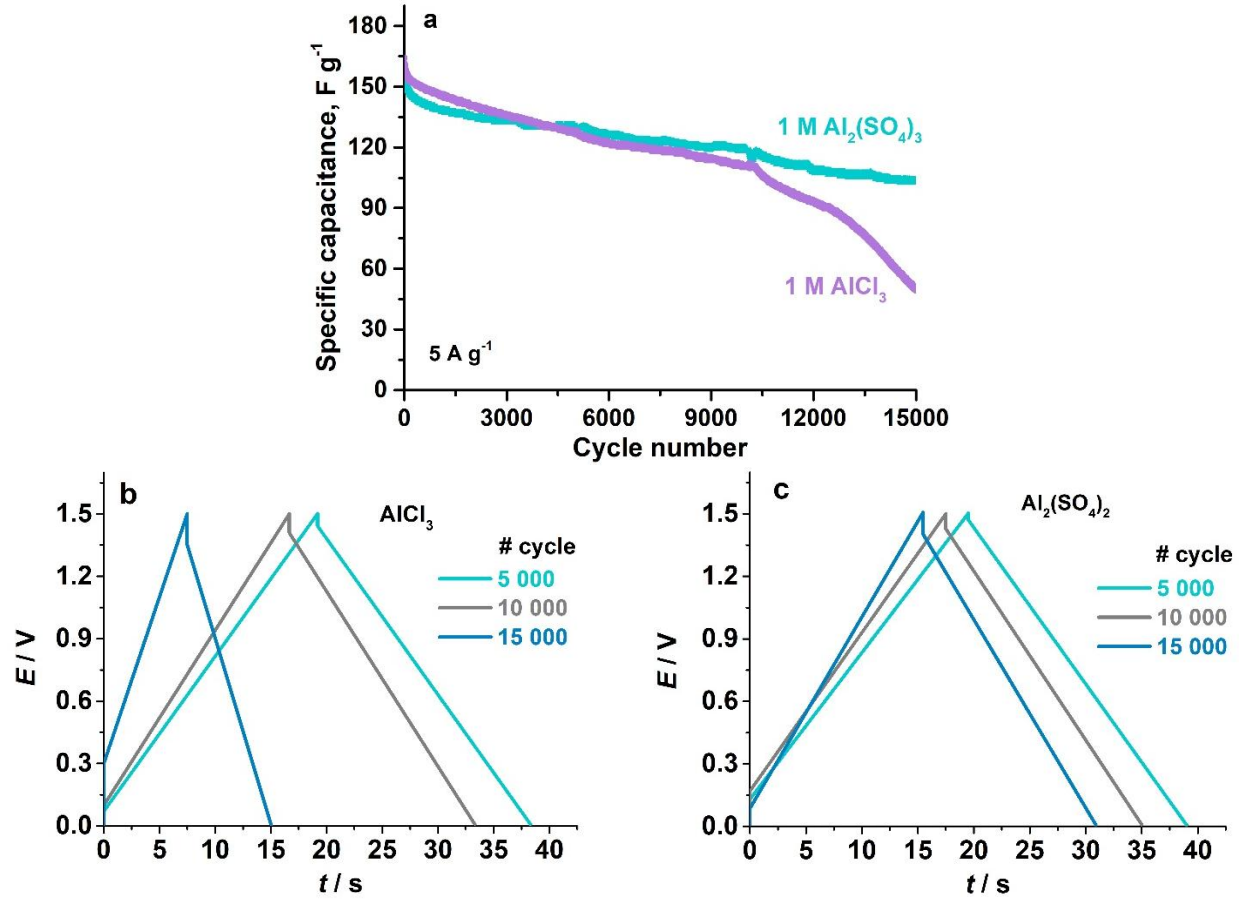


Figure 6. a) Specific discharge capacitance vs. number of cycles $AC_{vs}700/AICI_3/AC_{vs}700$ and $AC_{vs}700/AI_2(SO_4)_3/AC_{vs}700$ for 15000 cycles; b) charge/discharge curves of $AC_{vs}700/AICI_3/AC_{vs}700$ and c) $AC_{vs}700/AI_2(SO_4)_3/AC_{vs}700$ at different cycles

To summarize, $Al_2(SO_4)_3$ electrolyte delivered the best performance in terms of long-term stability, as evidenced also by the preservation of both charge/discharge (Figure 6c) and Nyquist curves of individual electrodes after 15,000 cycles (Figures 7c and d). On the other hand, these curves change in shape upon cycling ACvs700 in $AlCl_3$ after 10,000 cycles, in accordance with the decrease in capacitance. In the Nyquist plot, this is evidenced by the appearance of the large semicircle for the positive electrode (Figure 7a), which indicates more pronounced carbon oxidation during this cycling period. The oxidation also shifts the high-frequency intercept point to lower values (Figure 7a) and changes the shape of the phase angle-frequency profile, Figure 8a.

When the complex impedance analysis is applied, it can be seen that cycling limitations originate from the positive electrode (C_{real} + < C_{real} - and τ_{o} + > τ_{o} -, Figure S4), especially after 15,000 cycles. All these effects are not observed in Al₂(SO₄)₃, thus confirming the low degree of oxidation during cycling within the potential window of 1.5 V and, consequently, good capacitance behaviour.

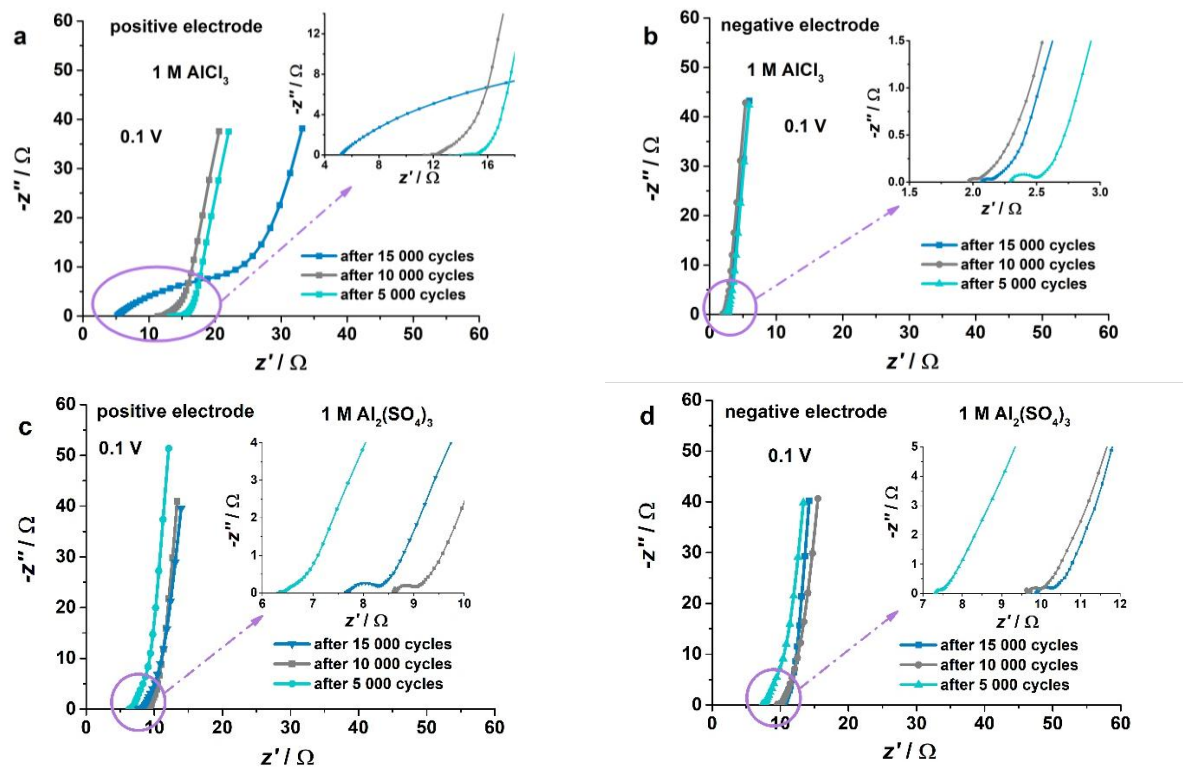


Figure 7. Nyquist plots individual AC_{vs} 700 electrodes measured in a three-electrode cell after 5,000, 10,000 and 15,000 cycles using 1 M aqueous solutions of $AlCl_3$ (a, b) and $Al_2(SO_4)_3$ (c, d). Inset shows enlarged high-frequency part of the Nyquist plot

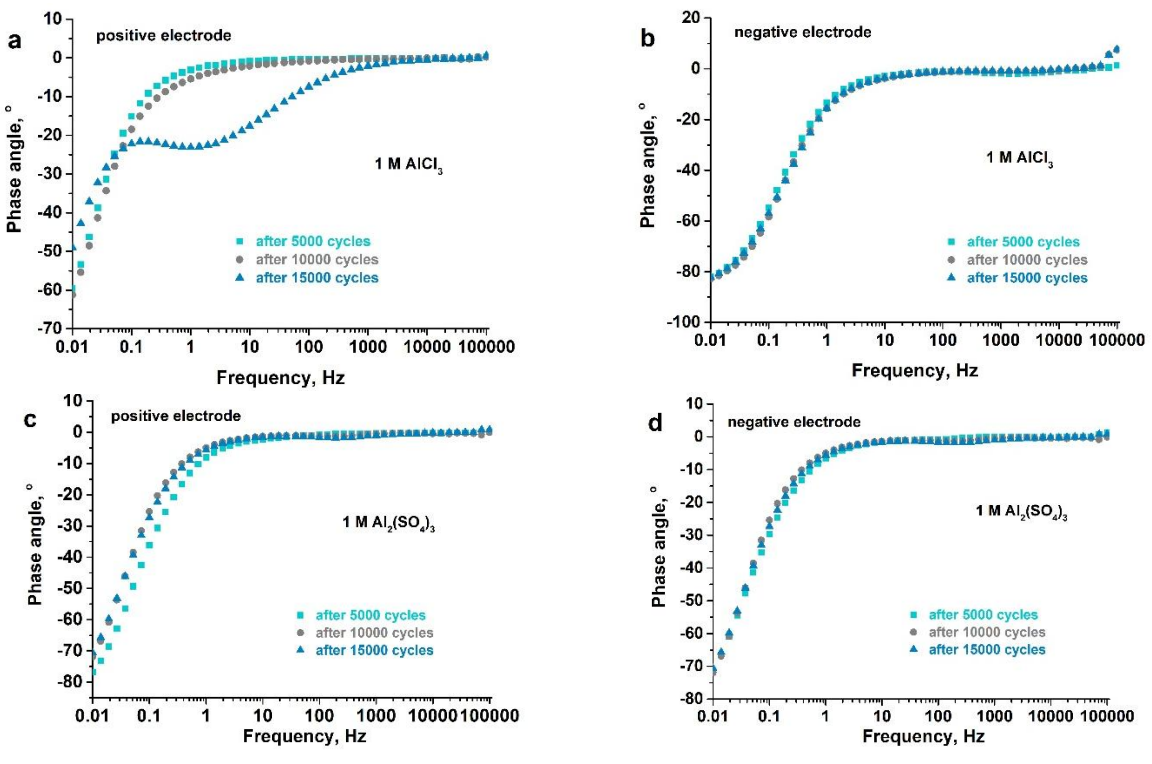


Figure 8. Bode plots for positive and negative $AC_{vs}700$ electrodes measured in a three-electrode cell after 5,000, 10,000 and 15,000 cycles using 1 M aqueous solutions of $AICl_3$ (a, b) and $Al_2(SO_4)_3$ (c, d)

Conclusions

High-surface area vine shoots-derived activated carbon was examined as an electrode material in three Al-based aqueous electrolytes for non-conventional supercapacitors. Typical capacitance behaviour was observed in all examined electrolytes (Al₂(SO₄)₃, Al(NO₃)₃ and AlCl₃), while the type of

anion determines the rate capability and capacitance retention. Due to the larger size of SO₄²⁻ than NO₃⁻ and Cl⁻ ions, their penetration into pores is aggravated, which causes strong CV deviation at extremely high scan rates above 50 mV s⁻¹. This was not as pronounced for the other two salts, offering them an advantage. On the other hand, the presence of NO₃⁻ and Cl⁻ deterioration of the capacitance of 1.5 V ACvs700/ACvs700 cells at different levels of cycling depth. Due to the capability to be reduced in the proximity of the positive carbon electrode, NO₃ progressively oxidizes its surface during initial cycling, thus causing the capacitance fade of the cell (up to ≈1000 cycles) to the stabilized value of ≈75 F g⁻¹ after 5000 cycles. In AlCl₃, this oxidation process was delayed, thus producing significant capacitance fading only after 10,000 cycles (from \approx 110 F g⁻¹ after 10,000 cycles to \approx 50 F g⁻¹ after 15,000 cycles). In both Al(NO₃)₃ and AlCl₃, these processes can be evidenced through the appearance of the larger semicircle in the Nyquist diagram and the shifting of its high-frequency intercept point towards lower resistance values (better wettability due to in-situ generated oxygen groups). Pronounced oxidation is not observed for Al₂(SO₄)₃, as verified through the unchanged shape of charge/discharge and Nyquist curves throughout long-term cycling. As a result, carbon pores are more available for electrolyte ions, leading to higher capacitance values of the cell in Al₂(SO₄)₃ (≈131 F g⁻¹ after 5,000 cycles) than in Al(NO₃)₃ (\approx 75 F g⁻¹ after 5,000 cycles) and AlCl₃ (127 F g⁻¹ after 5,000 cycles). Calculated energy density is also higher for Al₂(SO₄)₃ -based supercapacitor cell (10.2 Wh kg⁻¹ after 5,000 cycles) than for Al(NO₃)₃- and AlCl₃-based supercapacitors (5.8 and 9.9 Wh kg⁻¹ after 5,000 cycles, respectively). The best cyclic stability was observed in Al₂(SO₄)₃, demonstrated by relatively high values of \approx 103 and 119 F g⁻¹ after 10,000 and 15,000 cycles, respectively.

Supplementary material: Additional data are available electronically on article page of the journal's website: https://pub.iapchem.org/ojs/index.php/JESE/article/view/2532, or from the corresponding author upon request.

Acknowledgements: This research was supported by NATO Science for Peace and Security (SPS) Programme under grant G5836-SUPERCAR. Authors gratefully acknowledge the financial support from the bilateral project Montenegro-Slovenia "Biomass-derived carbons as anodes in sodium-ion batteries". M. Vujković acknowledges the Ministry of Science, Technological Development and Innovation of the Republic of Serbia for support through the national programme (Contract number: 451-03-66/2024-03/200146).

References

- [1] D. Jiménez-Cordero, F. Heras, M. A. Gilarranz, E. Raymundo-Piñero, Grape seed carbons for studying the influence of texture on supercapacitor behaviour in aqueous electrolytes, *Carbon* **71** (2014) 127-138 https://doi.org/10.1016/j.carbon.2014.01.021.
- [2] L. Guardia, L. Suárez, N. Querejeta, V. Vretenár, P. Kotrusz, V. Skákalová, T.A. Centeno, Biomass waste-carbon/reduced graphene oxide composite electrodes for enhanced supercapacitors, *Electrochimica Acta* **298** (2019) 910-917 https://doi.org/10.1016/j.electacta.2018.12.160.
- [3] L. Alcaraz, A. Adán-Más, P. Arévalo-Cid, M. de F. Montemor, F. A. López, Activated Carbons From Winemaking Biowastes for Electrochemical Double-Layer Capacitors, *Frontiers in Chemistry* **8** (2020) 1-10 https://doi.org/10.3389/fchem.2020.00686.
- [4] L. Suárez, T.A. Centeno, Unravelling the volumetric performance of activated carbons from biomass wastes in supercapacitors, *Journal of Power Sources* **448** (2020) 227413 https://doi.org/10.1016/j.jpowsour.2019.227413.
- [5] J. Zhang, H. Chen, J. Bai, M. Xu, C. Luo, L. Yang, L. Bai, D. Wei, W. Wang, H. Yang, N-doped

- hierarchically porous carbon derived from grape marcs for high-performance supercapacitors, *Journal of Alloys and Compounds* **854** (2021) 157207 https://doi.org/10.1016/j.jallcom.2020.157207.
- [6] L. Guardia, L. Suárez, N. Querejeta, C. Pevida, T.A. Centeno, Winery wastes as precursors of sustainable porous carbons for environmental applications, *Journal of Cleaner Production* **193** (2018) 614-624 https://doi.org/10.1016/j.jclepro.2018.05.085.
- [7] J. J. Manyà, B. González, M. Azuara, G. Arner, Ultra-microporous adsorbents prepared from vine shoots-derived biochar with high CO₂ uptake and CO₂/N₂ selectivity, *Chemical Engineering Journal* **345** (2018) 631-639 https://doi.org/10.1016/j.cej.2018.01.092.
- [8] M. Erdem, R. Orhan, M. Şahin, E. Aydın, Preparation and Characterization of a Novel Activated Carbon from Vine Shoots by ZnCl₂ Activation and Investigation of Its Rifampicine Removal Capability, *Water, Air, & Soil Pollution* **227** (2016) https://doi.org/10.1007/s11270-016-2929-5.
- [9] M. Ruiz-Fernández, M. Alexandre-Franco, C. Fernández-González, V. Gómez-Serrano, Adsorption isotherms of methylene blue in aqueous solution onto activated carbons developed from vine shoots (vitis vinifera) by physical and chemical methods, *Adsorption Science & Technology* **28** (2010) 751-759 https://doi.org/10.1260/0263-6174.28.8-9.751.
- [10] B. Corcho-Corral, M. Olivares-Marín, E. Valdes-Sánchez, C. Fernández-González, A. Macías-García, V. Gómez-Serrano, Development of activated carbon using vine shoots (Vitis Vinifera) and its use for wine treatment, *Journal of Agricultural and Food Chemistry* **53** (2005) 644-650 https://doi.org/10.1021/jf048824d.
- [11] J. A. S. B. Cardoso, B. Šljukić, M. Erdem, C. A. C. Sequeira, D. M. F. Santos, Vine shoots and grape stalks as carbon sources for hydrogen evolution reaction electrocatalyst supports, *Catalysts* **8** (2018) https://doi.org/10.3390/catal8020050.
- [12] D. Alvira, D. Antorán, M. Vidal, V. Sebastian, Vine Shoots-Derived Hard Carbons as Anodes for Sodium- Ion Batteries: Role of Annealing Temperature in Regulating Their Structure and Morphology, *Batteries and Supercapacitors* **6** (2023) e202300233 https://doi.org/10.1002/batt.202300233.
- [13] A. Gezović, J. Mišurović, B. Milovanović, M. Etinski, J. Krstić, V. Grudić, R. Dominko, S. Mentus, M.J. Vujković, High Al-ion storage of vine shoots-derived activated carbon New concept for affordable and sustainable supercapacitors, *Journal of Power Sources* **538** (2022) 231561 https://doi.org/10.1016/j.jpowsour.2022.231561.
- [14] M. P. Bichat, E. Raymundo-Piñero, F. Béguin, High voltage supercapacitor built with seaweed carbons in neutral aqueous electrolyte, *Carbon* **48** (2010) 4351-4361 https://doi.org/10.1016/j.carbon.2010.07.049.
- [15] L. Deng, G. Zhang, L. Kang, Z. Lei, C. Liu, Z.H. Liu, Graphene/VO₂ hybrid material for high performance electrochemical capacitor, *Electrochimica Acta* **112** (2013) 448-457 https://doi.org/10.1016/j.electacta.2013.08.158.
- [16] L. Demarconnay, E. Raymundo-Piñero, F. Béguin, A symmetric carbon/carbon supercapacitor operating at 1.6 V by using a neutral aqueous solution, *Electrochemistry Communications* **12** (2010) 1275-1278 https://doi.org/10.1016/j.elecom.2010.06.036.
- [17] K. Fic, G. Lota, M. Meller, E. Frackowiak, Novel insight into neutral medium as electrolyte for high-voltage supercapacitors, *Energy & Environmental Science* **5** (2012) 5842-5850 https://doi.org/10.1039/c1ee02262h.
- [18] K. Fic, M. He, E.J. Berg, P. Novák, E. Frackowiak, Comparative operando study of degradation mechanisms in carbon-based electrochemical capacitors with Li₂SO₄ and LiNO₃ electrolytes, *Carbon* **120** (2017) 281-293 https://doi.org/10.1016/j.carbon.2017.05.061.
- [19] J. Piwek, A. Platek, E. Frackowiak, K. Fic, Mechanisms of the performance fading of carbon-based electrochemical capacitors operating in a LiNO₃ electrolyte, *Journal of Power Sources*



- 438 (2019) 227029 https://doi.org/10.1016/j.jpowsour.2019.227029.
- [20] J. Piwek, A. Platek-Mielczarek, E. Frackowiak, K. Fic, Enhancing capacitor lifetime by alternate constant polarization, *Journal of Power Sources* **506** (2021) 230131 https://doi.org/10.1016/j.jpowsour.2021.230131.
- [21] J. M. V. Nabais, C. Laginhas, P. J. M. Carrott, M. M. L. R. Carrott, Thermal conversion of a novel biomass agricultural residue (vine shoots) into activated carbon using activation with CO₂, Journal of Analytical and Applied Pyrolysis **87** (2010) 8-13 https://doi.org/10.1016/j.jaap.2009.09.004.
- [22] H. A. Andreas, B. E. Conway, Examination of the double-layer capacitance of an high specificarea C-cloth electrode as titrated from acidic to alkaline pHs, *Electrochimica Acta* **51** (2006) 6510-6520 https://doi.org/10.1016/j.electacta.2006.04.045.
- [23] A. Śliwak, B. Grzyb, J. Ćwikła, G. Gryglewicz, Influence of wet oxidation of herringbone carbon nanofibers on the pseudocapacitance effect, *Carbon* **64** (2013) 324-333 https://doi.org/10.1016/j.carbon.2013.07.082.
- [24] S. Garcia-Segura, M. Lanzarini-Lopes, K. Hristovski, P. Westerhoff, Electrocatalytic reduction of nitrate: Fundamentals to full-scale water treatment applications, *Applied Catalysis B:*Environment and Energy 236 (2018) 546-568 https://doi.org/10.1016/j.apcatb.2018.05.041.
- [25] M. Endo, T. Maeda, T. Takeda, Y.J. Kim, K. Koshiba, H. Hara, M.S. Dresselhaus, Capacitance and Pore-Size Distribution in Aqueous and Nonaqueous Electrolytes Using Various Activated Carbon Electrodes, *Journal of The Electrochemical Society* **148** (2001) A910 https://doi.org/10.1149/1.1382589.
- [26] H. Wu, X. Wang, L. Jiang, C. Wu, Q. Zhao, X. Liu, B. Hu, L. Yi, The effects of electrolyte on the supercapacitive performance of activated calcium carbide-derived carbon, *Journal of Power Sources* **226** (2013) 202-209 https://doi.org/10.1016/j.jpowsour.2012.11.014.
- [27] Y. Marcus, Ionic radii in aqueous solutions, *Chemical Reviews* **88** (1989) 1475-1798 http://dx.doi.org/10.1021/cr00090a003.
- [28] D. W. Smith, Ionic hydration enthalpies, *Journal of Chemical Education* **54** (1977) 540-542 https://doi.org/10.1021/ed054p540.
- [29] X. Yang, Q. Xie, S. Yao, A comparative study on polyaniline degradation by an electrochemical quartz crystal impedance system: Electrode and solution effects, *Synthetic Metals* **143** (2004) 119-128 https://doi.org/10.1016/j.synthmet.2003.10.027.
- [30] K. Fic, M. Meller, J. Menzel, E. Frackowiak, Around the thermodynamic limitations of supercapacitors operating in aqueous electrolytes, *Electrochimica Acta* **206** (2016) 496-503 https://doi.org/10.1016/j.electacta.2016.02.077.

© 2024 by the authors; licensee IAPC, Zagreb, Croatia. This article is an open-access article distributed under the terms and conditions of the Creative Commons Attribution license (https://creativecommons.org/licenses/by/4.0/)



Open Access:: ISSN 1847-9286 www.jESE-online.org

Original scientific paper

Self-healing efficiency of ceria-doped Zn-Co coatings: Insights into particle-free *versus* biphasic plating baths

Marija Mitrović^{1,⊠}, Anđela Simović², Regina Fuchs-Godec³, Milorad Tomić^{1,4} and Jelena Bajat⁵

¹University of East Sarajevo, Faculty of Technology Zvornik, Karakaj 34A 75400 Zvornik, Republic of Srpska, Bosnia and Herzegovina

²University of Belgrade, Institute of Chemistry, Technology and Metallurgy, National Institute of the Republic of Serbia, Njegoševa 12, 11000 Belgrade, Serbia

³University of Maribor, Faculty of Chemistry and Chemical Engineering, Smetanova ulica 17, 2000 Maribor, Slovenia

⁴Engineering Academy of Serbia, Kneza Miloša 9/I, 11000 Belgrade, Serbia

⁵University of Belgrade, Faculty of Technology and Metallurgy, Karnegijeva 4, 11000 Belgrade, Serbia Corresponding authors: [™]marija.ridjosic@tfzv.ues.rs.ba; Tel.: 0038756260190; Fax: 0038756260190 Received: October 8, 2024; Accepted: October 23, 2024; Published: October 26, 2024

Abstract

Achieving the superior properties of nanocomposite materials involves addressing several challenges, particularly the agglomeration of nanoparticles in the plating bath. This study focuses on the electrodeposition and characterization of Zn-Co-CeO₂ composite coatings using a particle-free plating bath, an effective strategy for mitigating agglomeration. For comparison, the composite coatings were also deposited from a traditional biphasic plating solution. The coatings were deposited galvanostatically at various current densities. Scanning electron microscopy revealed that using a particle-free plating solution in conjunction with lower current densities enhanced the compactness and the overall quality of the coatings. Lower current densities favoured the codeposition of particles, as indicated by energy-dispersive X-ray spectroscopy results. Notably, the coatings produced from the particle-free bath exhibited significantly improved corrosion resistance and durability in chloride-rich environments, attributed to their self-healing properties, as shown by electrochemical impedance spectroscopy.

Keywords

Zn-Co-CeO₂; smart nanomaterials; self-repair; ceria-doping; nanocomposite

Introduction

The electrodeposition of nanocomposite coatings has emerged as a significant area of research within materials engineering, owing to their versatile applications and the ability to tailor properties

for specific uses. While various methods exist for producing nanocomposite coatings, electrodeposition offers distinct advantages, including operation at room temperature, precise control over coating thickness, applicability to complex geometries, and reduced equipment costs.

However, the electrochemical deposition of composite coatings is influenced by numerous parameters. These include the composition of the deposition solution (specifically the concentration of metal ions and particles), characteristics of the particles (such as size, shape, and surface charge), the presence of additives, pH levels, and deposition parameters (including deposition mode, potential, current density, temperature, and agitation) [1-10]. Additionally, the geometry of the electrodes and the deposition solution plays a critical role in the process. A significant challenge in electrochemical deposition is the low dispersion stability of particles in high ionic strength solutions, which can lead to particle agglomeration in biphasic media [11-14]. To mitigate this issue, several techniques have been employed, including mechanical mixing and wet ball milling prior to or during deposition. Ultrasonic mixing has also proven effective in preventing agglomeration and enhancing the properties of nanocomposite coatings [15-22]. Nonetheless, despite these methods, the inherent tendency of nanoparticles to agglomerate poses ongoing challenges, often resulting in rough, porous, and poorly distributed coatings. This non-uniformity can induce microstress in the coating and reduce key properties such as hardness, wear and corrosion resistance.

In terms of corrosion protection, ceria particles have demonstrated efficacy as corrosion inhibitors and are frequently integral to self-healing materials [23-29]. Self-healing materials are categorized as smart materials capable of autonomously repairing microscopic damage without external intervention. This inherent ability to self-repair enhances the longevity and durability of materials, making ceria-based composites particularly valuable in applications requiring sustained performance under harsh conditions. Ceria conversion films deposited via cathodic electrodeposition on steel, aluminium, pure zinc and zinc alloys exhibit high corrosion resistance [30,31]. Moreover, Zn-CeO₂ composite coatings demonstrate enhanced corrosion protection compared to pure zinc coatings [32-34]. The incorporation of ceria into the zinc and zinc alloy matrix imparts self-healing properties, which are critical for addressing the primary limitation of zinc coatings: their durability in corrosive environments.

Thus, the goal of this study is to produce Zn-Co-CeO₂ composite coatings from a particle-free deposition solution and to compare their morphology, composition, and corrosion resistance with those of coatings produced from biphasic solutions. This approach may address the main challenge in the composite production field, particle agglomeration and enhance the overall performance of composite coatings. Also, the aim of this study is the optimization of the deposition current density, which is a critical parameter influencing the amount of particles incorporated into the metal matrix [35-37]. While it is generally observed that particle content tends to increase with increasing current density and particle loading in the bath until a saturation point is reached, establishing a direct correlation between current density and particle content can be complex and may vary significantly based on the specific particles used. In some cases, the incorporation rate of particles may continuously decrease or display a peak as current density increases [12,38,39]. This behaviour is closely related to the dynamics of metal deposition and highlights the need for careful optimization to achieve the desired particle distribution within the coating and final properties of the coating.

Experimental

The preparation of AISI-1010 steel plates for the coating deposition process involves several steps. Initially, the steel is ground using silicon carbide abrasive paper of varying grits (No. 600, 800,

1000). This is followed by rinsing with distilled water, degreasing in a saturated NaOH solution in ethanol for 30 seconds, and then rinsing again with distilled water. The substrates are then etched in a HCl: H_2O (1:1 v/v) solution for 30 seconds and subsequently rinsed with distilled water. Composite coatings are deposited at various current densities: j = 1, 2, 3, 5, and 8 A dm⁻². A zinc anode with a purity of 99.99% is employed during the deposition. Two distinct solutions containing different sources of cerium ions (pH 5.5) are used. All used chemicals were analytical grade and produced by Sigma Aldrich. Both deposition solutions contain the following components: 0.1 M ZnCl₂; 0.8 M H₃BO₃; 3 M KCl; 0.03 M CoCl₂. In particle-free solution, 2 g/L of CeCl₃ is added, while the biphase solution contains 2 g/L of solid CeO₂ particles (particles size <50nm, according to producer). The plating solutions were stirred during the deposition by a magnetic stirrer at 300 rpm in order to minimize particle agglomeration. Also, the solutions were stirred for 10 minutes before electrodeposition to ensure the homogeneous distribution of particles in the plating solution throughout the deposition process. The deposition time for the composite coatings was calculated based on Faraday's law to achieve a target thickness of 10 µm. The morphology of the composite coatings was examined by scanning electron microscopy (SEM) (Tescan Mira) and composition was determined by energy dispersive X-ray spectroscopy (EDAX). Corrosion testing of the composite coatings is performed using a ZRA Reference 600 potentiostat from Gamry Instruments, utilizing electrochemical impedance spectroscopy (EIS) for analysis. The impedance spectra are recorded within a Faraday cage at the open circuit potential, spanning a frequency range of 100 kHz to 10 mHz, with an alternating voltage amplitude of 10 mV. A platinum mesh is employed as the counter electrode, while a saturated calomel electrode serves as the reference electrode, positioned in a Luggin capillary opposite the sample. The experimental data are subsequently analysed and fitted using the Gamry Echem Analyst software.

Results and discussion

Morphology of composite coatings

The morphology of electrodeposited composite coatings as a function of the deposition current density, as well as a function of the type of the Ce source, is shown in Figures 1 and 2. The morphology of the composite coatings produced at the lowest tested current density (1 A dm⁻²) exhibited significant heterogeneity. The coating surface displayed irregularly distributed agglomerates interspersed with smaller structures. An increase in the deposition current density to 2 and 3 A dm⁻² resulted in a more uniform and globular surface morphology characterized by grains of consistent size, albeit with pronounced porosity. At a further increase to 5 A dm⁻², the coatings developed smaller agglomerates. The furrows and cavities on the surface are likely attributed to the intense hydrogen evolution during the deposition process. In coatings utilizing CeO₂ solid participles as a source of Ce, higher current densities lead to the formation of increasingly inhomogeneous structures. Notably, the initially smooth and compact morphology observed at lower current densities transitions to a rougher and more irregular surface as deposition current density rises. At a current density of 5 A dm⁻², the emergence of cauliflower-like structures is evident, with these agglomerates exhibiting larger sizes that progressively coalesce into larger formations over time. This phenomenon is likely attributable to the uneven distribution of current density across the coating surface. As protrusions develop, ions preferentially undergo reduction at these elevated points, which consequently results in a greater variety of irregular morphologies during the deposition process. The increase in deposition current density to 8 A dm⁻² leads to heterogeneous morphology with visible CeO₂ agglomerates on the coating surface. The EDAX spot analyses of the white agglomerates on the surface (Figure 2 (e)) verify the presence of cerium, confirming the considerable agglomeration phenomenon present in the biphasic plating solution.

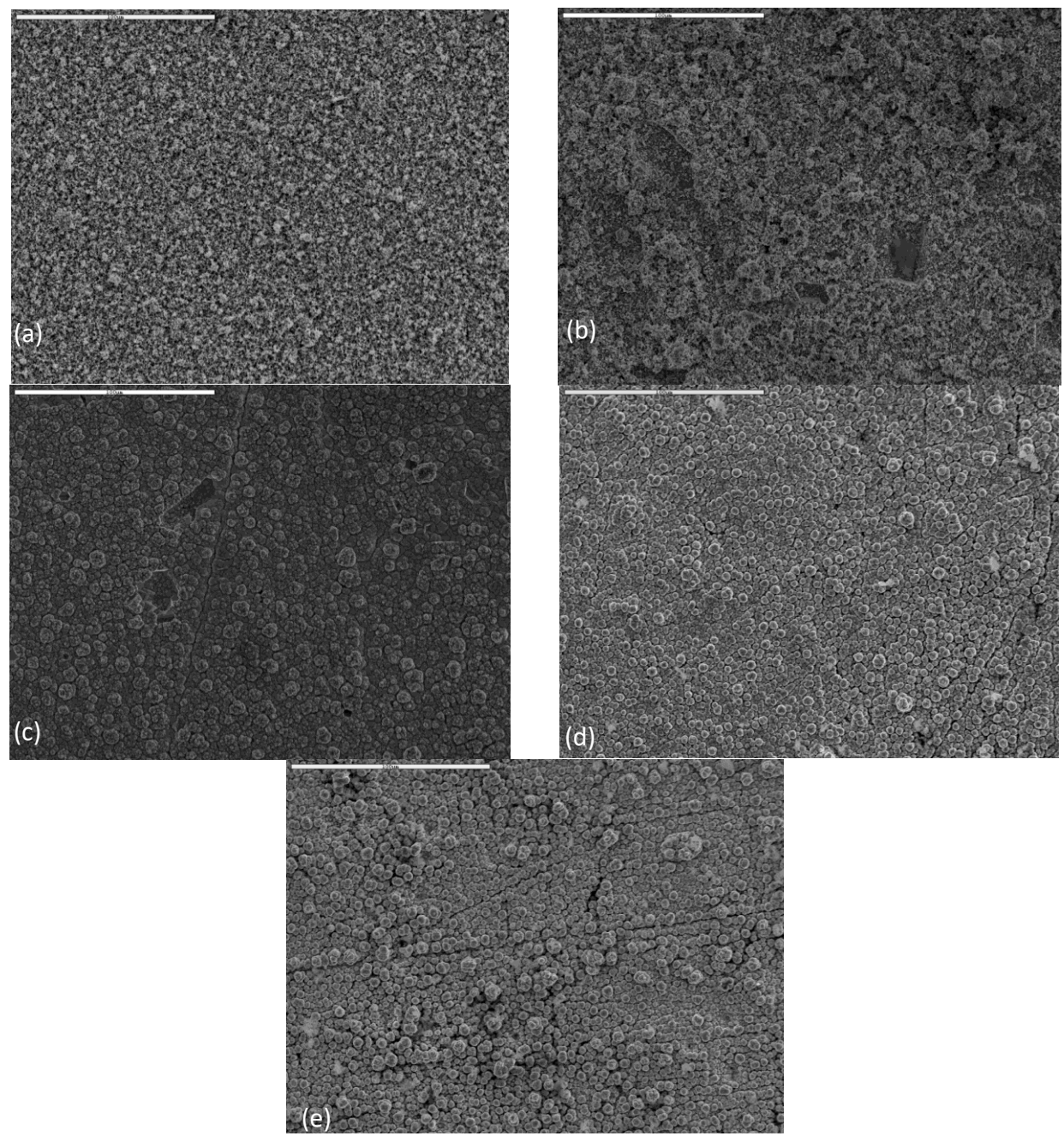


Figure 1. Morphology of the Zn-Co-CeO₂ composite coatings deposited at: (a) 1, (b) 2, (c) 3, (d) 5 and (e) 8 A dm⁻² from particles free plating solution (CeCl₃ as Ce source). Scale bars 100 μ m

The coatings produced through deposition using $CeCl_3$ as the source of cerium ions exhibit a significantly more compact structure. Microscopic imaging reveals that these coatings are more homogeneous at lower current densities of 1 and 2 A dm⁻². Even at elevated current densities, there is a lack of pronounced larger agglomerates, contrasting sharply with the coatings derived from biphasic plating solution, which display more pronounced agglomeration. Also, there is a lack of agglomerates on the surface of the composite coatings deposited from particles-free solution even at 8 A dm⁻², which confirms the primary goal of this work. The reduction of the coating porosity is also more than evident when a particle-free plating bath is used ($CeCl_3$, Figure 1).

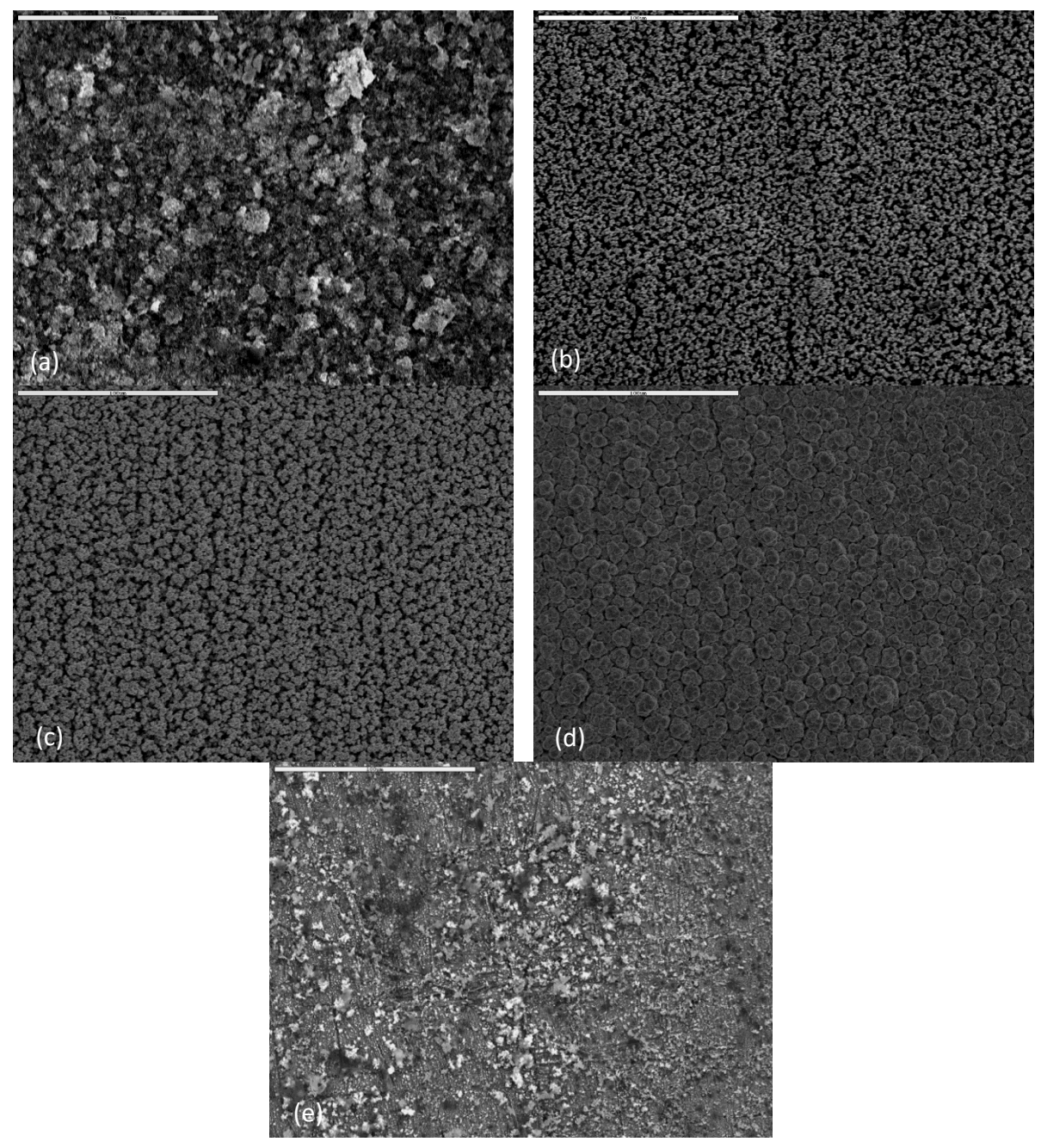


Figure 2. Morphology of the Zn-Co-CeO₂ composite coatings deposited at: (a)1, (b) 2, (c) 3, (d) 5 and (e) 8 A dm⁻² from plating solution with solid CeO₂ particles. Scale bars 100 μ m

This phenomenon arises from the distinct mechanisms of particle deposition. When using insoluble CeO₂ nanoparticles, agitation plays a crucial role in the codeposition process. The fluid flow predominantly transports the particles to the growing deposit layer, with electrophoresis contributing to a lesser extent. The nanoparticles are subsequently incorporated into the deposit primarily through entrapment within the growing layer. Conversely, when CeCl₃ is used, it dissolves in the plating solution. During the deposition process, specific local physico-chemical conditions at the zinc cobalt film interface promote the formation of a secondary phase consisting of cerium-based hydroxides. This occurs due to localized alkalinisation resulting from the reduction of dissolved oxygen and water, which can be described as a coprecipitation process [40]. The formed cerium-hydroxide oxidizes to the CeO₂ [41,42]. As a result, the lack of microstress and internal straining within the coatings leads to a more homogeneous and compact structure.

The chemical composition of the composite coatings

The chemical content of composite coatings deposited from particle-free and biphasic plating solution as a function of the deposition current density is shown in Figure 3.

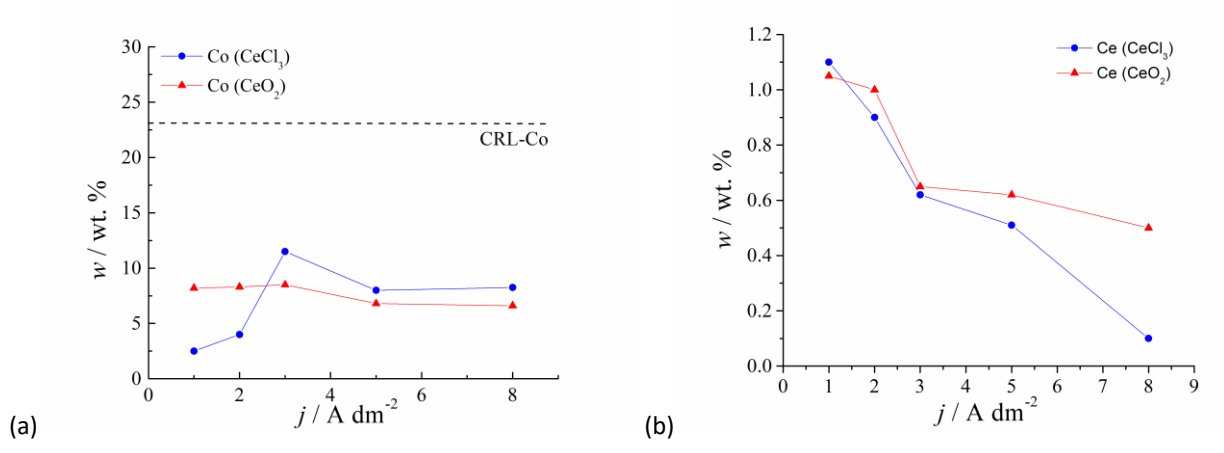


Figure 3. Dependence of the (a) Co and (b) Ce contents in Zn-Co-CeO₂ coatings on the deposition current density for the coatings deposited from the particles free (CeCl₃ as a source of Ce) and biphasic plating solution (CeO₂ solid particles)

From Figure 3(a), it can be noted that the cobalt content in the composite coatings increases with an increase in deposition current density when using $CeCl_3$ as Ce source, reaching a maximum of approximately 12 wt.% at j=3 A dm⁻², after which it levels off. In contrast, the influence of current density on Co content in composites derived from biphasic plating solution (CeO_2 particles) is negligible. Brenner categorized the electrochemical deposition of Co alloys as anomalous, where zinc, being more electronegative, is preferentially deposited. The line labelled CRL-Co in Figure 3(a) serves as a control reference line, indicating the ratio of Co^{2+} ions to the total concentration of metal ions (Co^{2+} and Co^{2+}) in the deposition solution. Since the Co content in the composite alloys deposited from both solutions is substantially below the CRL, we can infer that the deposition occurs via an anomalous mechanism and that the presence of the ceria in the solution does not affect the deposition process of the Co content in the coatings remains low (below 1.2 wt.%), which aligns with the low concentration of Ce in the deposition solution.

The use of a particles-free plating bath did not lead to an increase in cerium content in the composite coating, which is in agreement with existing literature [40]. Furthermore, higher cerium content does not necessarily correlate with improved properties, as morphology and compactness also play a significant role in determining coating performance. Scanning electron microscopy observations indicate that the use of a particle-free plating solution enhances the compactness and overall appearance of the coatings (Figure 1). Unlike Co, the Ce content decreases with increasing deposition current density in both solutions. During the initial stage of deposition, nucleation and growth of nuclei compete. At high current densities, the reaction rate is higher, leading to a nucleation rate surpassing the growth rate of the nuclei. Conversely, at low current densities, the growth rate of the nuclei predominates. Consequently, the enhanced deposition rate at higher current densities limits the ability of CeO₂ particles to be incorporated. The concentration of metal ions in the pre-electrode layer surpasses the particles, leading to a faster reduction of the metal ions.

Corrosion resistance of the composite coatings

The effects of using single versus biphasic plating solutions and variation of the deposition current densities on corrosion resistance and durability of the deposited composite coatings in a

chloride-rich environment were evaluated by electrochemical impedance spectroscopy. The Nyquist diagrams, revealing the corrosion resistance of coatings produced at various current densities (1, 2, 3 and 5 A dm⁻²) from biphasic plating solution in the presence of CeO₂, are illustrated in Figure 4(a), (c), (e) and (g). These diagrams exhibit two depressed semicircles, indicating two distinct time constants within the investigated frequency range. Notably, the diameter of the dominant semicircle, which represents the charge transfer process, increases upon exposure to NaCl solution. This impedance growth may be attributed to the formation of a pseudo-passive protective layer composed of corrosion products on the metal surface in contact with the corrosive medium, or it may reflect a self-healing effect of the substrate. Coatings deposited at a current density of 1 A dm⁻² demonstrate significantly lower initial resistance compared to those obtained at 2 A dm⁻². Both samples exhibit an increase in resistance over the exposure to NaCl, with the coatings produced at 2 A dm⁻² displaying superior corrosion stability. Coatings deposited at 3 A dm⁻² exhibited lower impedance values compared to those obtained at 2 A dm⁻², although both showed an increase in impedance value over time. In contrast, the resistivity of coatings deposited at 5 A dm⁻² consistently decreased over time, likely due to their inhomogeneous morphology, which includes porosity and defects. This structural irregularity may compromise the integrity of the protective layer, leading to reduced corrosion resistance.

Coatings produced with CeCl₃ as the source of cerium ions exhibited similar behaviour, as evidenced by the Nyquist diagrams in Figure 4(b), (d), (f), (h), although the resistivity of these samples was significantly higher compared to coatings produced from the biphasic plating solution. The durability of these coatings in aggressive corrosion media, like chloride-rich solution, was significantly increased. There could be several explanations for this phenomenon. The more homogenous morphology and increased compactness is surely one of the reasons, as a consequence of the utilization of the particle-free plating bath and suppressed incorporation of agglomerates inside the coating. In addition, since the deposition mechanism incorporating CeO₂ is changed in this case, a better distribution of the particles in the coatings is achieved. When homogeneously distributed cerium is throughout the coating, it could be accessible for the formation of CeO₂ through a pHdriven process [40], which, in turn, results in repairing the damage on the substrate surface after attack of the Cl⁻ anions and oxygen present in the corrosive media. Since ceria is known to have the self-healing effect [12,17,23,27,29], along with the passive layer formed on the coatings surfaces, it provided good corrosion protection during 2 weeks in NaCl solution for Zn-Co-CeO2 coatings produced from particles free plating bath. The same coatings deposited from the biphasic plating solution were able to protect the steel only for up to 5 days in the same corrosive media.

For nearly all current densities tested, the impedance values for Zn-Co-CeO₂ coatings deposited from particle-free plating bath (CeCl₃) were higher than those for Zn-Co-CeO₂ coatings deposited from biphasic plating solution (CeO₂) (Figures 4 to 6). Notably, the coatings deposited at a current density of 3 A dm⁻² showed the best performance, maintaining high resistance values throughout the 2-week testing period. The phase angle versus frequency diagrams clearly exhibit two time constants during the initial exposure to NaCl solution (Figures 5 and 6). The time constant observed at medium frequencies is associated with the resistance of solution penetration through the composite coating and the passive layer made of corrosion products formed on its surface [43].

The second time constant, occurring at lower frequencies, pertains to the electrochemical processes at the substrate/composite coating interface [44]. The Zn-Co-CeO₂ composite coatings result in only temporary corrosion protection of the underlying steel due to their porosity.

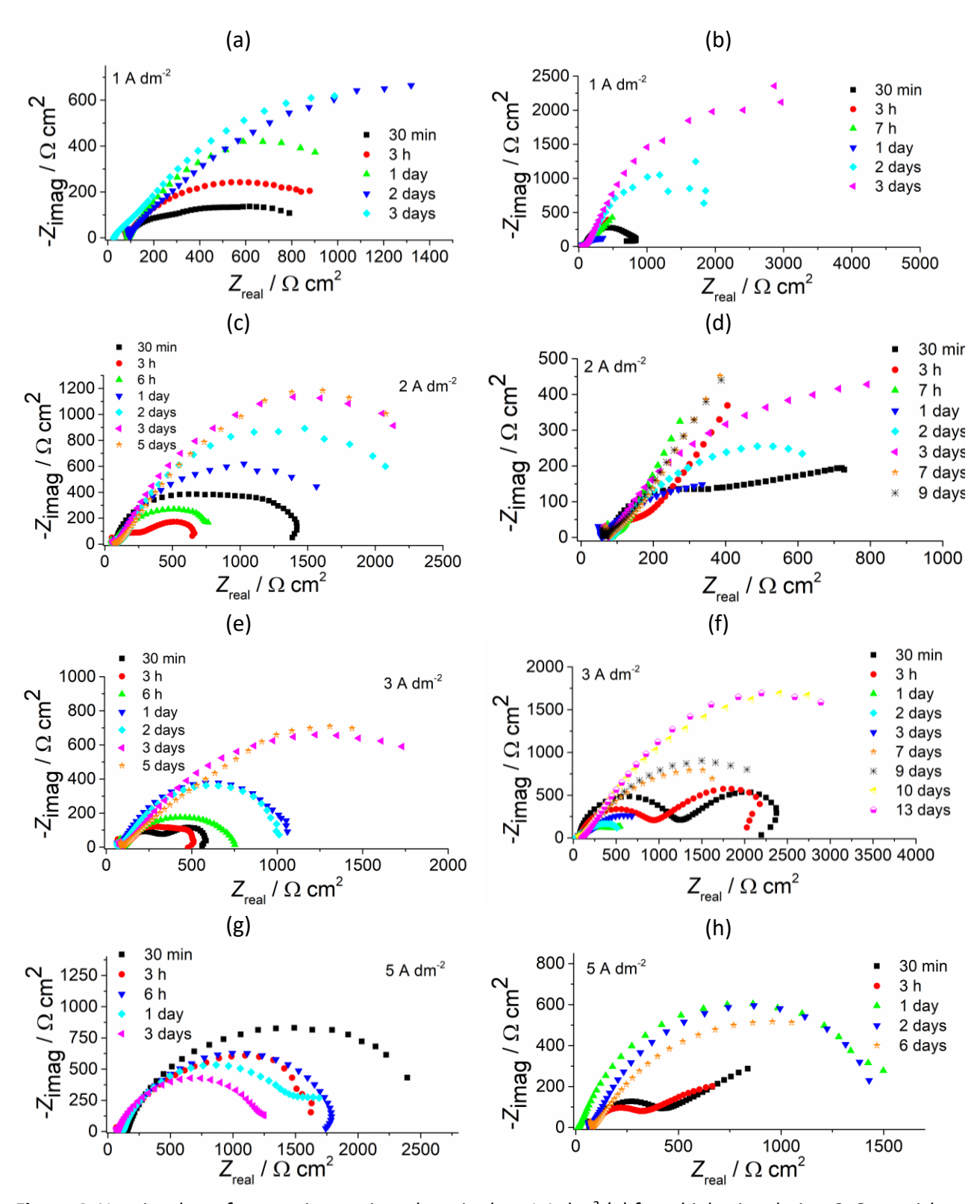


Figure 4. Nyquist plots of composite coatings deposited at: 1 A dm⁻² (a) from biphasic solution-CeO₂ particles, (b) particles free solution-CeCl₃; 2 A dm⁻² (c) from biphasic solution, (d) particles free solution; 3 A dm⁻² (e) from biphasic solution, (f) particles free solution; 5 A dm⁻², (g) from biphasic solution and (h) particles free solution

The impedance values at low frequencies decreased in NaCl after some time (Figures 5 and 6), indicating electrolyte infiltration through the coating and subsequent corrosion progression.

(cc) BY

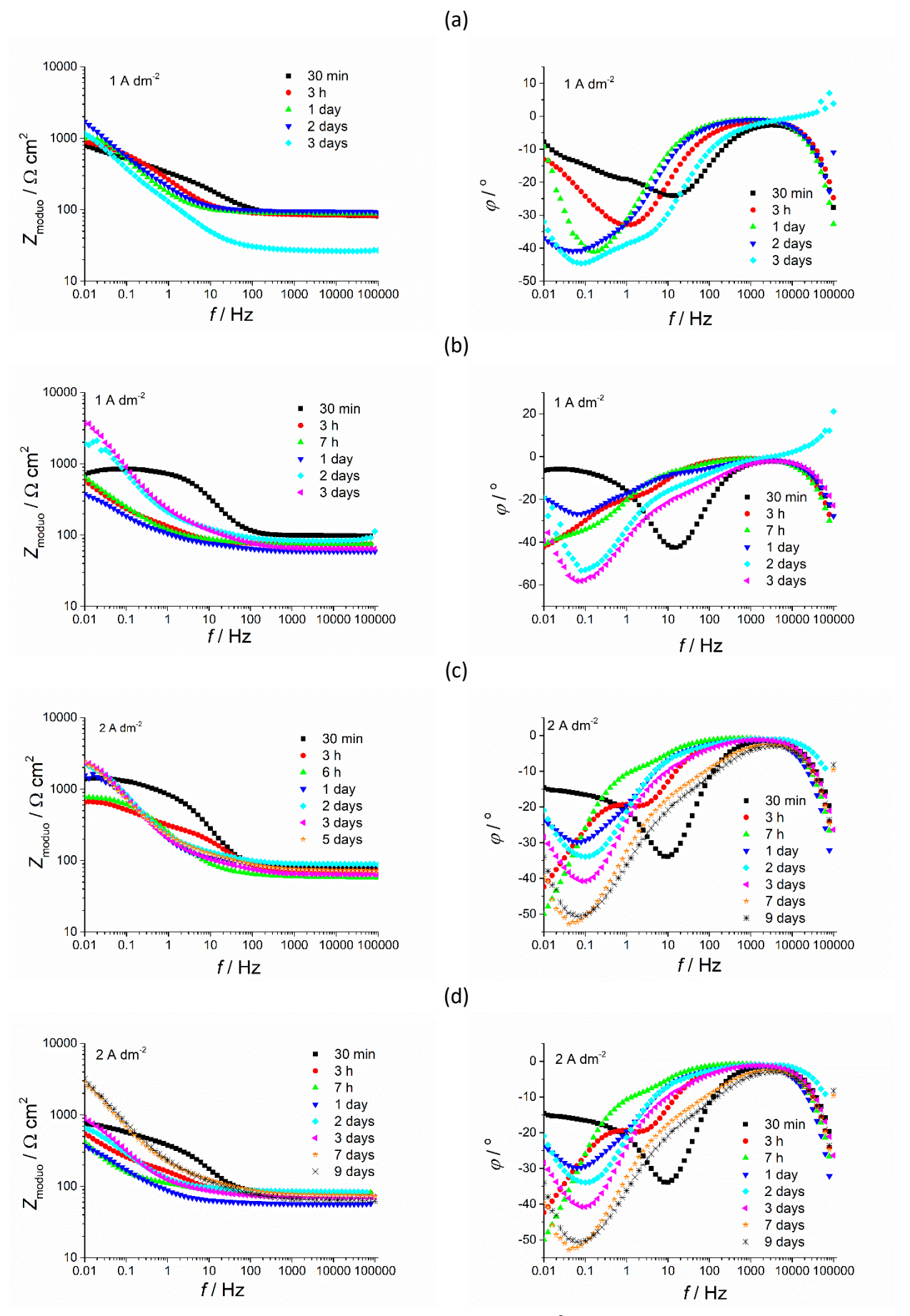


Figure 5. Bode plots of composite coatings deposited at 1 A dm⁻² (a) from biphasic plating solution-CeO₂ particles, (b) particles free solution -CeCl₃; 2 A dm⁻² (c) from biphasic plating solution, (d) particles free solution; 3 A dm⁻²

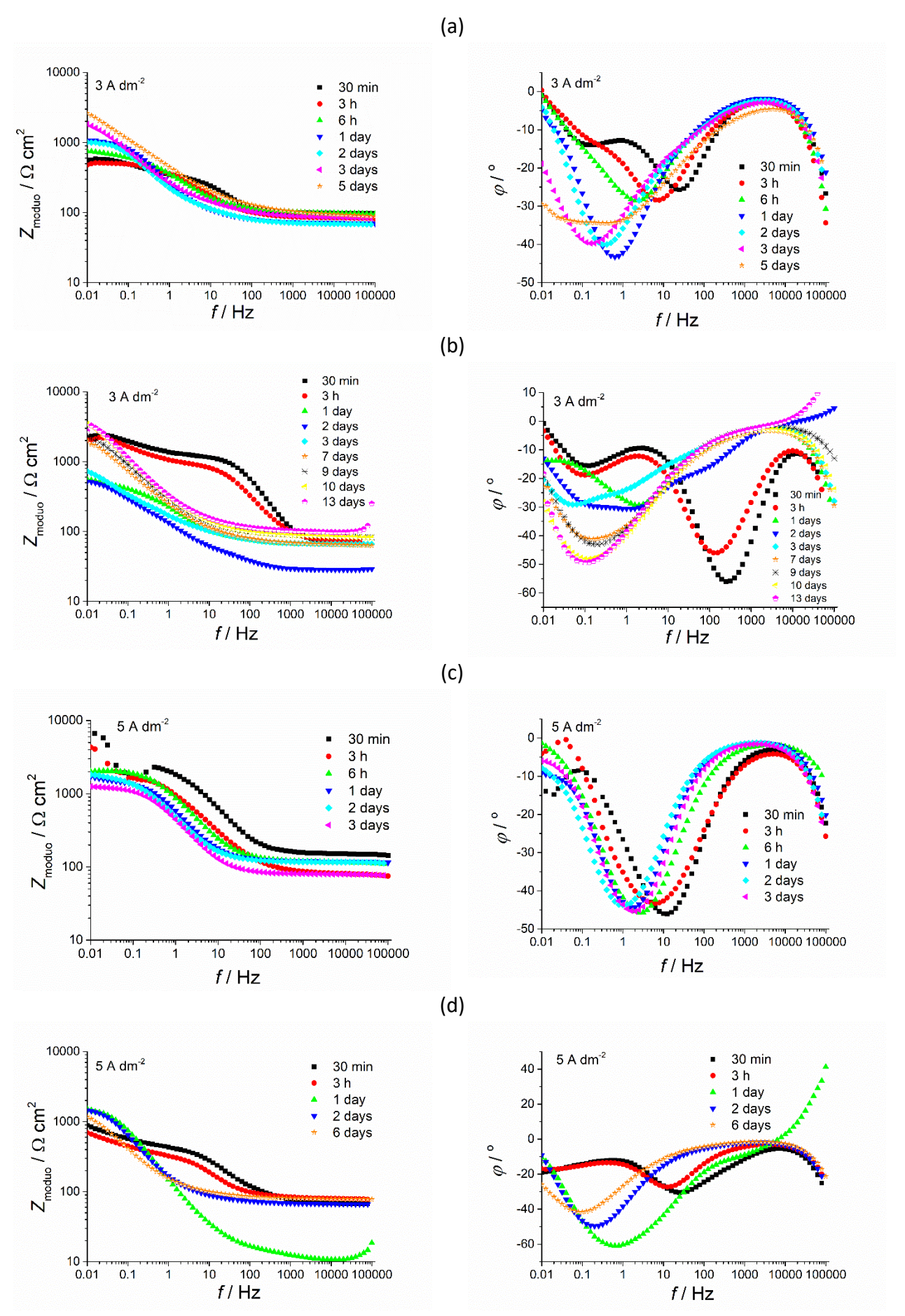


Figure 6. Bode plots of composite coatings deposited at: 1 A dm⁻² (a) from biphasic plating solution, (b) particles free solution; 5 A dm⁻² (c) from biphasic plating solution, (d) particles free solution

However, over a longer time in the NaCl environment, the impedance values at low frequencies increase again, and only the second time constant remains visible. Eventually, the phase angle exhibits a single maximum position between the original two. This behaviour is often characteristic of coatings that facilitate a self-healing effect. As the electrolyte continued to penetrate, CeO_2 particles diffused through the coating and accumulated at the active sites on the steel substrate. Given that CeO_2 has a low solubility [44], the observed high impedance values at low frequencies are to be expected. This behaviour suggests that the presence of CeO_2 particles contributes to the formation of a protective layer that enhances the corrosion resistance of the substrate. By fitting the obtained EIS results using the equivalent electrical circuits shown in Figure 7, where R_{Ω} denotes the solution resistance, R_p is the resistance of the coating, C_c capacitance of the coating, CPE denotes the constant phase element corresponding to the double layer capacitance in parallel with the charge transfer resistance (R_{ct}), it is possible to determine the charge transfer resistance values.

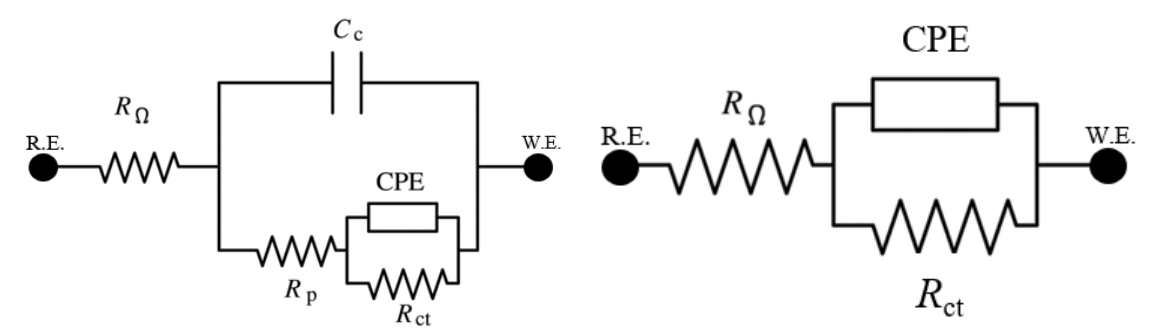


Figure 7. Equivalent electric circuits used for fitting the electrochemical impedance data; R.E. reference electrode, W.E. working electrode

Figure 8 illustrates the dependence of R_{ct} values on the exposure time of the coatings deposited at various current densities (1, 2, 3, and 5 A dm⁻²) and from different plating solutions (containing CeO₂ or CeCl₃) to the NaCl solution. Initially, all tested coatings at all current densities exhibit a decrease in R_{ct} values, which can be attributed to the contact of the metal surface with the electrolyte. After a certain exposure time, the R_{ct} values of the composite coatings begin to increase and then stabilize, reaching a plateau of nearly constant values. This behaviour suggests a gradual development of a protective layer, enhancing the corrosion resistance of the coatings over time. The plateau in R_{ct} values corresponds to the formation of a passive layer of corrosion products on the metal surface, effectively hindering further substrate activity.

Notably, significantly higher R_{ct} values were observed for the Zn-Co-CeO₂ composite coating produced from particle-free plating solution compared to the Zn-Co-CeO₂ coating from the biphasic solution, confirming the superior corrosion stability of the coatings derived from CeCl₃ containing bath. The persistence of this phenomenon over extended exposure to NaCl suggests the presence of a layer with a low solubility product from the CeO₂ layer, indicative of a self-healing effect of the substrate. Based on the EIS results, it can be concluded that composite coatings based on Zn-Co alloy and cerium obtained from CeCl₃ exhibit better corrosion stability than those deposited from CeO₂ based bath. When CeO₂ particles are utilized for composite alloy formation, they tend to precipitate at the site of damage, where corrosion processes have initiated, likely forming a physisorbed layer of CeO₂. In contrast, the cerium-based layer produced via a pH-driven process in coatings produced from solution with CeCl₃ appears to provide enhanced protection. Cerium can undergo oxidation-reduction cycles between Ce(III) and Ce(IV) due to the presence of oxygen vacancies and the small energy difference between its 4f inner and outer valence electrons [45]. The Ce(IV) hydroxides begin to precipitate around pH 4 [46], while Ce(III) hydroxides start to form

at around pH 8 [46]. These hydroxides serve as reaction intermediates for the formation of CeO_2 . In CeO_2 , cerium atoms predominantly exist in the +4 oxidation state. However, the presence of missing lattice oxygen atoms in this highly reducible oxide indicates that two Ce(III) ions are situated near each oxygen vacancy [45]. Thus, the formed protection layer always consists of a mixture of Ce(III) and Ce(IV) species, along with Zn and Co oxides/hydroxides. A key factor in the superior performance of the CeO_2 layer is its adhesion to the metal substrate, which is likely stronger when formed in situ from Ce(III) through a pH-driven process. In contrast, CeO_2 particles precipitated from the alloy during corrosion may not bond as effectively with the substrate.

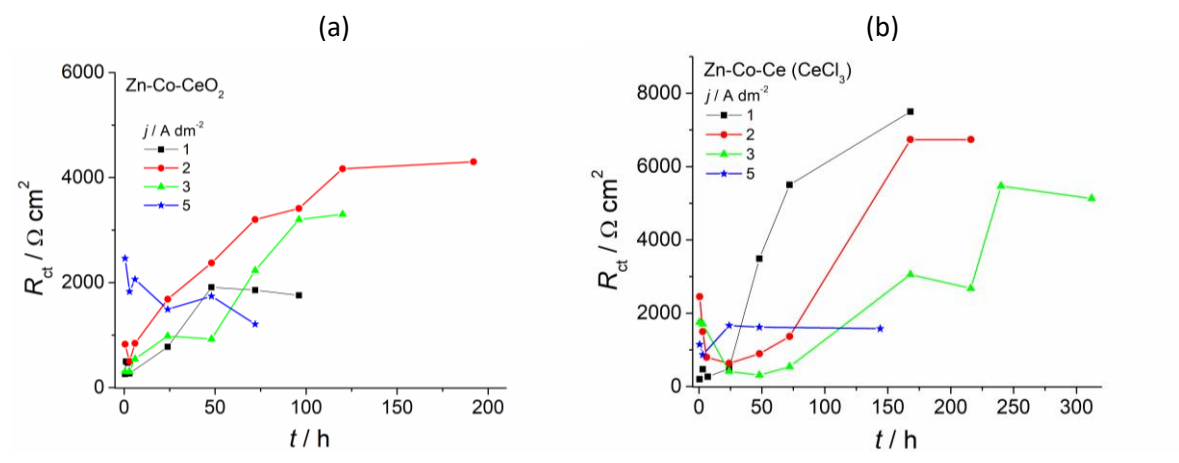


Figure 8. Charge transfer resistance values (R_{ct}) of composite coatings deposited from (a) biphasic plating solution - CeO₂ particles and (b) single plating solution - CeOl₃ as Ce source

Conclusions

The results shown indicate that deposition current density significantly influences the morphology, chemical composition, and corrosion resistance of composite coatings, irrespective of the particle source. Specifically, lower current densities yield finer-grained coatings with strong adhesion to the substrate and enhanced compactness. In contrast, higher current densities produce uneven coatings that exhibit reduced compactness and visible surface porosity as a consequence of uneven current distribution. Additionally, increased current density correlates with lower incorporation of CeO₂ particles within the coating. Given that cobalt concentrations were significantly below the critical reduction limit, the presence of particles in the plating solution did not alter the deposition mechanism of the Zn-Co alloy, which remained anomalous regardless of the ceria source. Utilizing a single plating solution effectively suppressed particle agglomeration, resulting in coatings that were more homogeneous, denser, and demonstrated improved corrosion resistance and durability due to their self-healing ability in chloride-rich environments.

Acknowledgements: The Ministry of Scientific and Technological Development and Higher Education of the Republic of Srpska (Grant No. 19.032/431-1-34/23) and the Ministry of Science, Technological Development and Innovation of the Republic of Serbia (Contract No. 451-03-65/2024-03/200135) are gratefully acknowledged for funding this research.

References

[1] A. Vlasa, S. Varvara, A. Pop, C. Bulea, L. M. Muresan, Electrodeposited Zn–TiO₂ nanocomposite coatings and their corrosion behavior, *Journal of Applied Electrochemistry* **40** (2010) 1519-1527. https://doi.org/10.1007/s10800-010-0130-x

- [2] K. Vathsala, T. V. Venkatesha, Zn–ZrO₂ nanocomposite coatings: Electrodeposition and evaluation of corrosion resistance, *Applied Surface Science* 257(21) (2011) 8929-8936. https://doi.org/10.1016/j.apsusc.2011.05.0
- [3] M. Sajjadnejad, S. Karkon, S. M. S. Haghshenas, Corrosion characteristics of Zn-TiO₂ nanocomposite coatings fabricated by electro-codeposition process, *Advanced Journal of Chemistry A* **7(2)** (2024) 209-226. https://doi.org/10.48309/ajca.2024.418391.1425
- [4] K. K. Maniam, S. Paul, Corrosion performance of electrodeposited zinc and zinc-alloy coatings in marine environment, *Corrosion and Materials Degradation* 2(2) (2021) 163-189. https://doi.org/10.3390/cmd2020010
- [5] C. M. P. Kumar, A. Lakshmikanthan, M. P. G. Chandrashekarappa, D. Y. Pimenov, K. Giasin, Electrodeposition based preparation of Zn–Ni alloy and Zn–Ni–WC nanocomposite coatings for corrosion-resistant applications, *Coatings* 11(6) (2021) 712. https://doi.org/10.3390/coatings11060712
- [6] M. Klekotka, K. Zielińska, A. Stankiewicz, M. Kuciej, Tribological and anticorrosion performance of electroplated zinc based nanocomposite coatings, *Coatings* 10)6) (2020) 594. https://doi.org/10.3390/coatings10060594
- [7] M. Egbuhuzor, C. Akalezi, S. Ulaeto, D. Njoku, B. Onyeachu, E. Oguzie, Electro-deposited nanocomposite coatings and their behaviours against aqueous and high-temperature corrosion: A review, *Hybrid Advances* **5** (2024) 100180. https://doi.org/10.1016/j.hybadv.2024.100180
- [8] A. Cabral, A. O. Junior, G. Koga, I. Rigoli, C. Rocha, C. Souza, Electrodeposited Zinc Cellulose Nanocrystals Composite Coatings: Morphology, Structure, Corrosion Resistance and Electrodeposition Process, *Journal of Materials Research and Technology* 33 (2024) 1569-1580 https://doi.org/10.1016/j.jmrt.2024.09.153
- [9] M. M. K. Azar, H. S. Gugtapeh, M. Rezaei, Evaluation of corrosion protection performance of electroplated zinc and zinc-graphene oxide nanocomposite coatings in air saturated 3.5 wt.% NaCl solution, *Colloids and Surfaces A: Physicochemical and Engineering Aspects* 601 (2020) 125051. https://doi.org/10.1016/j.colsurfa.2020.125051
- [10] S. Anwar, F. Khan, Y. Zhang, Corrosion behaviour of Zn-Ni alloy and Zn-Ni-nano-TiO₂ composite coatings electrodeposited from ammonium citrate baths, *Process Safety and Environmental Protection* **141** (2020) 366-379. https://doi.org/10.1016/j.psep.2020.05.048
- [11] H. Srivastav, A. Z. Weber, C. J. Radke, Colloidal Stability of PFSA-Ionomer Dispersions. Part I. Single-Ion Electrostatic Interaction Potential Energies, *Langmuir* **40(13)** (2024) 6654-6665. https://pubs.acs.org/doi/abs/10.1021/acs.langmuir.3c03903
- [12] M. Riđošić, M. Bučko, A. Salicio-Paz, E. García-Lecina, L. S. Živković, J. B. Bajat, Ceria particles as efficient dopant in the electrodeposition of Zn-Co-CeO₂ composite coatings with enhanced corrosion resistance: The effect of current density and particle concentration, *Molecules* **26(15)** (2021) 4578. https://doi.org/10.3390/molecules26154578
- [13] R. Daneshfar, B. S. Soulgani, S. Ashoori, Identifying the mechanisms behind the stability of silica nano-and micro-particles: effects of particle size, electrolyte concentration and type of ionic species, *Journal of Molecular Liquids* 397 (2024) 124059. https://doi.org/10.1016/j.molliq.2024.124059
- [14] X. Wang, T. Sun, H. Zhu, T. Han, J. Wang, H. Dai, Roles of pH, cation valence, and ionic strength in the stability and aggregation behavior of zinc oxide nanoparticles, *Journal of Environmental Management* 267 (2020) 110656. https://doi.org/10.1016/j.jenvman.2020.110656
- [15] M. Riđošić, A. Salicio-Paz, E. Garcia-Lecina, P. Zabinski, L. S. Živković, J. B. Bajat, The effect of the ultrasound agitation and source of ceria particles on the morphology and structure of

- the Zn–Co–CeO₂ composite coatings, *Journal of Materials Research and Technology* **13** (2021) 1336-1349. https://doi.org/10.1016/j.jmrt.2021.05.064
- [16] M. Bucko, M. Ridošić, J. Kovačina, M. Tomić, J. Bajat, Hardness and corrosion resistance of Zn- Mn/Al₂O₃ composite coatings produced by electrochemical deposition, *Indian Journal of Engineering and Materials Sciences* 29(4) (2022) 540-549. http://op.niscpr.res.in/index.php/IJEMS/article/view/47785/0
- [17] M. Riđošić, N. D. Nikolić, A. Salicio-Paz, E. García-Lecina, L. S. Živković, J. B. Bajat, Zn-Co-CeO₂ vs. Zn-Co Coatings: Effect of CeO₂ Sol in the Enhancement of the Corrosion Performance of Electrodeposited Composite Coatings, *Metals* **11(5)** (2021) 704. https://doi.org/10.3390/met11050704
- [18] J. M. Costa, A. F. de Almeida Neto, Ultrasound-assisted electrodeposition and synthesis of alloys and composite materials: A review, *Ultrasonics Sonochemistry* **68** (2020) 105193. https://doi.org/10.1016/j.ultsonch.2020.105193
- [19] M. Akbarpour, F. G. Asl, Fabrication of high-performance graphene/nickel-cobalt composite coatings using ultrasonic-assisted pulse electrodeposition, *Ceramics International* 49(9) (2023) 13829-13835. https://doi.org/10.1016/j.ceramint.2022.12.262
- [20] C. Liu, X. Huang, R. Xu, Y. Mai, L. Zhang, X. Jie, Microstructure and properties of nanocrystalline Ni-Mo coatings prepared by ultrasound-assisted pulse electrodeposition, *Journal of Materials Engineering and Performance* 30 (2021) 2514-2525. https://doi.org/10.1007/s11665-021-05570-1
- [21] H. Zhang, J. Wang, S. Chen, H. Wang, Y. He, C. Ma, Ni–SiC composite coatings with improved wear and corrosion resistance synthesized via ultrasonic electrodeposition, *Ceramics International* **47(7)** (2021) 9437-9446. https://doi.org/10.1016/j.ceramint.2020.12.076
- [22] C. Ma, D. Zhao, F. Xia, H. Xia, T. Williams, H. Xing, Ultrasonic-assisted electrodeposition of Ni-Al₂O₃ nanocomposites at various ultrasonic powers, *Ceramics International* **46(5)** (2020) 6115-6123. https://doi.org/10.1016/j.ceramint.2019.11.075
- [23] X. Gong, M. Luo, M. Wang, W. Niu, Y. Wang, B. Lei, Injectable self-healing ceria-based nanocomposite hydrogel with ROS-scavenging activity for skin wound repair, *Regenerative Biomaterials* **9** (2022) rbab074. https://doi.org/10.1093/rb/rbab074
- [24] S. V. Harb, A. Trentin, T. A. C. de Souza, M. Magnani, S. H. Pulcinelli, C. V. Santilli, P. Hammer, Effective corrosion protection by eco-friendly self-healing PMMA-cerium oxide coatings, *Chemical Engineering Journal* **383** (2020) 123219. https://doi.org/10.1016/j.cej.2019.123219
- [25] V. Hernández-Montes, R. Buitrago-Sierra, M. Echeverry-Rendón, J. Santa-Marín, Ceria-based coatings on magnesium alloys for biomedical applications: a literature review, RSC Advances 13(2) (2023) 1422-1433. https://doi.org/10.1039/D2RA06312C
- [26] B. Fotovvat, M. Behzadnasab, S. Mirabedini, H. E. Mohammadloo, Anti-corrosion performance and mechanical properties of epoxy coatings containing microcapsules filled with linseed oil and modified ceria nanoparticles, *Colloids and Surfaces A: Physicochemical and Engineering Aspects* **648** (2022) 129157. https://doi.org/10.1016/j.colsurfa.2022.129157
- [27] S. Habib, E. Fayyad, M. Nawaz, A. Khan, R. A. Shakoor, R. Kahraman, A. Abdullah, Cerium dioxide nanoparticles as smart carriers for self-healing coatings, *Nanomaterials* **10(4)** (2020) 791. https://doi.org/10.3390/nano10040791
- [28] H. Zhang, H. Bian, X. Zhang, L. Zhang, Y. Chen, Y. Yang, Z. Zhang, Preparation and characterization of hollow ceria based smart anti-corrosive coatings on copper, *Surfaces and Interfaces* **45** (2024) 103930. https://doi.org/10.1016/j.surfin.2024.103930
- [29] A. Kirdeikiene, O. Girčiene, L. Gudavičiūte, V. Jasulaitiene, A. Selskis, S. Tutliene, M. Skruodiene, J. Pilipavičius, J. Juodkazyte, R. Ramanauskas, Self-healing properties of cerium-modified molybdate conversion coating on steel, *Coatings* 11(2) (2021) 194. https://doi.org/10.3390/coatings11020194

- [30] S. V. Kozhukharov, C. Girginov, N. Boshkova, A. Tzanev, Impact of the final thermal sealing of combined zinc/cerium oxide protective coating primers formed on low carbon steel. Journal of Electrochemical Science and Engineering 12(4) (2022) 685-701. http://dx.doi.org/10.5599/jese.1297
- [31] J. Gulicovski, J. Bajat, V. Mišković-Stanković, B. Jokić, V. Panić, S. Milonjić, Cerium oxide as conversion coating for the corrosion protection of aluminum, Journal of Electrochemical Science and Engineering **3(4)** (2013) 151-156. https://doi.org/10.5599/jese.2013.0037
- [32] L. Exbrayat, C. Rébéré, R. Milet, E. Calvié, P. Steyer, J. Creus, Corrosion Behavior in Saline Solution of Electrodeposited Nanocomposite Zn-CeO₂ Coatings Deposited onto Low Alloyed Steel, Coatings 13(10) (2023) 1688. https://doi.org/10.3390/coatings13101688
- [33] P. I. Nemes, M. Lekka, L. Fedrizzi, L. M. Muresan, Influence of the electrodeposition current regime on the corrosion resistance of Zn-CeO₂ nanocomposite coatings, Surface and Coatings Technology 252 (2014) 102-107. https://doi.org/10.1016/j.surfcoat.2014.04.051
- [34] S. Ranganatha, T. Venkatesha, K. Vathsala, Electrochemical studies on Zn/nano-CeO₂ electrodeposited composite coatings, Surface and Coatings Technology 208 (2012) 64-72. https://doi.org/10.1016/j.surfcoat.2012.08.004
- [35] S. Lajevardi, T. Shahrabi, Effects of pulse electrodeposition parameters on the properties of Ni-TiO₂ nanocomposite coatings, Applied Surface Science **256(22)** (2010) 6775-6781. https://doi.org/10.1016/j.apsusc.2010.04.088
- [36] E. Beltowska-Lehman, P. Indyka, A. Bigos, M. J. Szczerba, J. Guspiel, H. Koscielny, M. Kot, Effect of current density on properties of Ni–W nanocomposite coatings reinforced with zirconia particles, Materials Chemistry and Physics 173 (2016) 524-533. https://doi.org/10.1016/j.matchemphys.2016.02.050
- [37] Z. Zhang, B. Li, S. Chen, Z. Yuan, C. Xu, W. Zhang, Influences of Al particles and current density on structural, mechanical and anti-corrosion properties of electrodeposited Ni-Co/Al composite coatings, Ceramics International 50(7) (2024) 11804-11816. https://doi.org/10.1016/j.ceramint.2024.01.085
- [38] F. Walsh, C. Ponce de Leon, A review of the electrodeposition of metal matrix composite coatings by inclusion of particles in a metal layer: an established and diversifying technology, Transactions of the IMF **92(5)** (2014) 83-98. https://doi.org/10.1179/0020296713Z.000000000161
- [39] T. J. Tuaweri, G. D. Wilcox, Influence of SiO₂ particles on zinc–nickel electrodeposition, *Transactions of the IMF* **85(5)** (2007) 245-253. https://doi.org/10.1179/174591907X229608
- [40] L. Exbrayat, J. Creus, Synthesis of Zn-Ceria Nanocomposite Coatings from Particle-Free Aqueous Bath in a one Electrodeposition Step Process, Colloid and Interface Science Communications 25 (2018) 31-35. https://doi.org/https://doi.org/10.1016/j.colcom.2018.06.004
- [41] Y. Hamlaoui, F. Pedraza, C. Remazeilles, S. Cohendoz, C. Rébéré, L. Tifouti, J. Creus, Cathodic electrodeposition of cerium-based oxides on carbon steel from concentrated cerium nitrate solutions: Part I. Electrochemical and analytical characterisation, Materials Chemistry and Physics 113(2) (2009) 650-657.
 - https://doi.org/https://doi.org/10.1016/j.matchemphys.2008.08.027
- [42] L. Martínez, E. Román, J. L. de Segovia, S. Poupard, J. Creus, F. Pedraza, Surface study of cerium oxide based coatings obtained by cathodic electrodeposition on zinc, Applied Surface Science 257(14) (2011) 6202-6207.
 - https://doi.org/https://doi.org/10.1016/j.apsusc.2011.02.033
- [43] A. M. Simões, J. Torres, R. Picciochi, J. C. S. Fernandes, Corrosion inhibition at galvanized steel cut edges by phosphate pigments, Electrochimica Acta 54(15) (2009) 3857-3865. https://doi.org/10.1016/j.electacta.2009.01.065

- [44] T. V. Plakhova, A. Y. Romanchuk, S. N. Yakunin, T. Dumas, S. Demir, S. Wang, S. G. Minasian, D. K. Shuh, T. Tyliszczak, A. A. Shiryaev, A. V. Egorov, V. K. Ivanov, S. N. Kalmykov, Solubility of Nanocrystalline Cerium Dioxide: Experimental Data and Thermodynamic Modeling, *The Journal of Physical Chemistry C* 120(39) (2016) 22615-22626. https://doi.org/10.1021/acs.jpcc.6b05650
- [45] C. E. Castano, M. J. O'Keefe, W. G. Fahrenholtz, Cerium-based oxide coatings, *Current Opinion in Solid State and Materials Science* **19(2)** (2015) 69-76. https://doi.org/10.1016/j.cossms.2014.11.005
- [46] B. Bouchaud, J. Balmain, G. Bonnet, F. Pedraza, pH-distribution of cerium species in aqueous systems, *Journal of Rare Earths* 30(6) (2012) 559-562. https://doi.org/10.1016/S1002-0721(12)60091-X
- [47] S. A. Hayes, P. Yu, T. J. O'Keefe, M. J. O'Keefe, J. O. Stoffer, The Phase Stability of Cerium Species in Aqueous Systems: I. E-pH Diagram for the System Ce-HClO₄-H₂O system, *Journal of The Electrochemical Society* **149(12)** (2002) C623-C630. https://doi.org/10.1149/1.1516775



Open Access:: ISSN 1847-9286 www.jESE-online.org

Original scientific paper

Al-Mg electrodeposition using chloride-based molten salts

Sreesvarna Bhaskaramohan¹, M. J. N. V. Prasad², G. V. Dattu Jonnalagadda³ and Sankara Sarma V. Tatiparti $^{1, \boxtimes}$

¹Department of Energy Science and Engineering, Indian Institute of Technology Bombay, Mumbai 400076, India

²Department of Metallurgical Engineering and Materials Science, Indian Institute of Technology Bombay, Mumbai 400076, India

³John F Welch Technology Centre, General Electric India Industrial Pvt. Ltd. Bangalore 560066, India Corresponding authors: [™] sankara@iitb.ac.in; Tel.: +91-22-2576-7672; Fax: +91-22-2576-4890 Received: October 1, 2024; Accepted: November 9, 2024; Published: November 14, 2024

Abstract

Al-Mg alloys were potentiostatically electrodeposited from electrolyte with AlCl₃, NaCl, KCl and MgCl₂ at 180 °C for aircraft applications. The electrode setup includes a Cu cathode, Pt-mesh anode, and Al-rod pseudo-reference electrode. Cyclic voltammetry (CV) reveals the Al deposition sources as Al₂Cl₇ and AlCl₄. The Mg deposition source can be a reaction between Al₂Cl₇ and MgCl₂, and MgCl₂ dissociation (both releasing Mg²⁺). Depositions at overpotentials: -1.03, -1.05, -1.06, and -1.10 V show current density-time curves with almost steady-state j, indicating planar diffusional growth. This is confirmed by layer-like morphologies with near-globular growth features. The average feature size decreases to -1.06 V and increases slightly at -1.10 V due to further deposition over the existing features. The deposit composition (Mg content) increases from 0.36 to 5.68 at.% from -1.03 to -1.10 V. Such a wide range of Mg content is obtained through minimal compositional changes in spent electrolytes, indicating the ease of less-noble Mg deposition. Al-Mg deposition scheme is devised with Al and Mg deposition perceived as Al³⁺ + 3e⁻ \rightarrow Al and Mg²⁺ + 2e⁻ \rightarrow Mg; and 2Cl \rightarrow Cl₂(\uparrow)+ 2e⁻ supplying electrons for deposition.

Keywords

Aluminum; magnesium; potentiostatic deposition; morphology; composition; scheme

Introduction

Aluminum (Al) - magnesium (Mg) alloys are very promising in aircraft applications due to their light weight and good corrosion resistance [1-5]. Al-Mg alloys have been conventionally produced through thermal processing, casting, conventional metal forming techniques, vapor phase deposition, etc. [6,7]. However, these methods of producing Al-Mg alloys incorporate defects such as internal, stresses, pores, and inhomogeneities in compositions and yield undesired morphologies, etc. [7].

Electrodeposition is a versatile technique for Al-Mg deposition due to its advantages, such as obtaining desired morphologies, uniform alloy composition, lower heat stress in the core alloy, and control over the thickness of the deposit [8]. Electrodeposition offers several parameters, such as potential/current, electrolyte composition, temperature, agitation, pH, etc, for achieving control over the deposit characteristics [9].

Electrodeposition of Al-Mg alloys is a challenge and has been attempted by only a few groups [9-18]. Aqueous electrolytes cannot be used for the electrodeposition of Al and Mg as the reduction potentials of Al (-1.67 V vs. NHE) and Mg (-2.356 V vs. NHE) are lower than that for water electrolysis ($E^{o}_{H_2O|OH}$ = -0.828 V vs. NHE) [18]. Hence, water electrolysis occurs preferentially when attempting to deposit Al and Mg from aqueous solutions. Also, it is noteworthy that Al is nobler than Mg and, hence, can deposit preferentially over Mg. This creates a problem of not being able to deposit Mg to a desired composition when depositing Al and Mg together using non-aqueous electrolytes.

Electrodeposition Al and its alloys have been carried out using non-aqueous molten salts [13], ionic liquids [12,15-17,19], Grignard reagents [11], and organometallic electrolyte systems [9,10,18]. Due to their hygroscopic and/or moisture-sensitive nature, the non-aqueous electrolytes are handled in inert atmosphere conditions, which offers another challenge. In literature, deposition of a maximum of ~13.3 at.% Mg in Al-Mg alloys was reported by using ionic liquids by adding AlCl₃ to a 1,3-dialkyl-imidazolium chloride or benzene in the presence of tetrahydrofuran/crotyl alcohol [17]. Also, deposition cannot occur if the ionic liquid is basic [15]. Further, a clear trend of deposit compositions versus overpotentials/current densities is absent from these electrolyte systems [12,15-17,19]. In a work by Mayer, electrolytes comprising of NaF, KF, Al(C_2H_5)₃, Al(C_2H_5)₃, tri-iso-butyl-aluminum (iBu₃Al, where Bu = -C₄H₉) and Mg(C_2H_5)₂ prepared from Grignard reagents deposited Al-Mg alloys only if aluminum alkyl/magnesium alkyl mole ratio is \geq 3.5, else pure Mg was deposited [11,20].

In our earlier extensive work on Al-Mg deposition from organometallic-based electrolytes, we reported the deposition of a wide range of compositions and morphologies of Al-Mg alloys by employing Na[Al(C_2H_5)₄] + 2Na[(C_2H_5)₃Al-H-Al(C_2H_5)₃] + 2.5Al(C_2H_5)₃ + 6toluene [18,21]. For example, morphologies with crystallographically consistent facets/feather-like morphology always possess 1 to 7 at.% Mg [22]. Smooth globular dendrites contain ~20 at.% Mg [21]. Rough globular dendrites, which always form over the smooth ones, possess ~65 to 80 at.% Mg [23]. Unfortunately, most of these electrolyte systems discussed here are very difficult to handle requiring extra precautions, are costly, and are banned in some countries.

Molten salt-based electrolytes, *e.g.* chloride-based, *etc.*, are relatively easier to handle, cheaper, and widely available in several countries. However, they are relatively less explored for the deposition of Al-Mg alloys, with systematic studies being scarce in the literature. For example, a stand-alone study by Li *et al.* [13] demonstrated Al-Mg composition in the range 2.41-9.14 at.% Mg using AlCl₃-MgCl₂-NaCl-KCl molten salt electrolytes. However, this system has yet to establish clear trends in Mg content with overpotential [13]. A trend of deposit compositions with overpotentials/current densities, relations between the compositions of deposits and electrolytes, and Al-Mg deposition schemes from molten salts are yet to be established. Most of the reported studies extensively deposited pure Al and its alloys (Al-Ti, Al-Sn, Al-Mn) on copper substrate.

In the present study, Al-Mg alloy films were deposited using a chloride-based molten salt electrolyte containing $AlCl_3$, NaCl, KCl, and $MgCl_2$ at $180\,^{\circ}C$. Here, a copper (Cu) strip was used as the working electrode to deposit Al-Mg alloys to facilitate the direct comparison of the obtained results with those reported in the literature. Potentiostatic techniques with overpotentials of -1.03, -1.05, -1.06 and -1.10 V with respect to open circuit potential were used for deposition. The current density-

time (*j-t*) curves obtained from these depositions exhibit the typical characteristics and attain almost a steady-state current density, indicating planar diffusional growth (layer-like) of the deposits. This is confirmed by the morphologies of these deposits, which exhibit near-globular growth features in these Al-Mg layers. The average size of these features decreases up to -1.06 V. At -1.10 V, the size is slightly larger due to their growth by further deposition occurring over the already existing features. The composition (Mg content) of the deposits increases monotonously with the magnitude of overpotential. For example, 0.36 at.% Mg is obtained at -1.03 V and 5.68 at.% Mg is achieved at -1.10 V. This wide range of Mg content is achieved in the deposits through minimal changes in the spent electrolytes. This indicates that the present Al-Mg system has no obstacles to depositing lessnoble Mg under the employed conditions. Also, a possible Al-Mg deposition scheme is devised by considering the electrochemical (from cyclic voltammetry) and non-electrochemical reactions in this system. The Al and Mg deposition can be perceived as $Al^{3+} + 3e^{-} \rightarrow Al$ and $Mg^{2+} + 2e^{-} \rightarrow Mg$ at the cathode. The electrons for these depositions are supplied by chlorine gas evolution (from CV) according to $2Cl^{-} \rightarrow Cl_{2(\uparrow)} + 2e^{-}$ at the anode.

Experimental

Electrodeposition of Al-Mg was conducted using a chloride-based molten salt electrolyte containing AlCl₃, NaCl, KCl, MgCl₂ (due to a non-disclosure agreement with the industry collaborators, the actual composition could not be revealed). Aluminium chloride (Reagent Plus®, 99 %) was procured from SIGMA; sodium chloride and potassium chloride (analysis grade) were purchased from EMPARTA; and magnesium chloride (anhydrous, \geq 98 %) was obtained from SIGMA. Since the chemicals are moisture and oxygen-sensitive, they were handled in a glovebox (MBRAUN EASYlabproi 4-port) under argon (Ar) atmosphere, which maintained O₂ and moisture (H₂O) at < 0.1 ppm. These salts were melted together in the above-mentioned composition at 180 °C in a 10 ml beaker (electrochemical cell) to prepare the electrolyte. Several complexes can form in the electrolyte in its molten state. The complexes of Al, such as Al₂Cl₇-and AlCl₄- are well established in the literature [24-28]. However, the complexes of Mg are not established in the literature. Nevertheless, there are suggestions for forming complexes such as Mg(AlCl₄)₂ in the literature [24]. Also, MgCl₂ can combine with Al₂Cl₇- to form AlCl₄- and Mg²⁺, according to Eqation (1) [15,16].

$$2Al_2Cl_7^- + MgCl_2^* \rightleftharpoons 4AlCl_4^- + Mg^{2+}$$

$$*Mg^{2+} can exist as complex$$
(1)

All the electrochemical experiments were conducted using a fresh stationary electrolyte at 180 °C in this cell and a CHI660E electrochemical workstation. A commercial Copper (Cu, 98 % pure, Patel) strip was used as the working electrode (WE). Prior to the experiments, this Cu strip was polished manually using sand papers (120C, 200C, 400C, 800C, 1000C, 2000C) followed by diamond paste (6 to 12 μ m and 3 to 5 μ m), alumina powder (1 μ m) and finally by diamond paste (0.5 to 1 μ m). Platinum mesh (Pt, 99.9 % pure, CH Instruments) was used as the counter electrode (CE), and an Aluminum (Al, 99.99 % pure, PureSynth) strip was employed as the pseudo-reference electrode (RE). The Al RE was polished using sandpapers (80C, 120C, 200C, 800C, 1000C) before employing it. Prior to the electrochemical experiments, open circuit potential (OCP) was measured. In order to identify various anodic activities such as Al-Mg dissolution, Cu dissolution and Cl₂ evolution, linear sweep voltammetry (LSV) was performed from OCP on (i) Cu strip with Al-Mg deposit on it, (ii) Pt rod with Al-Mg deposit on it and (iii) bare Pt rod. The results from these LSVs are shown in Figure 1(a). From Figure 1(a), the bare Pt rod substrate exhibits a signature of only Cl₂ evolution [29]. The Pt rod with an Al-Mg deposit on it, however, exhibits a wide anodic peak and plateau for Al-Mg dissolution [25,30] and for Cl₂

evolution [29], as indicated in Figure 1(a). From these results, the peaks for Al-Mg dissolution, Cu dissolution and Cl₂ evolution can be clearly distinguished in the LSV curve from the Cu strip with an Al-Mg deposit on it, as seen in Figure 1(a). Moreover, it must be noted that though Cu dissolution exhibits the highest activity (in terms of the current density), this anodic reaction would not happen during Al-Mg deposition on Cu. Cyclic voltammetry (CV) was performed by starting from OCP and between the switching potentials of -2.00 and +2.00 V vs. Al at a scan rate of 10 mV s⁻¹. The results of the potentiostatic electrodeposition experiments are reported here in terms of the overpotentials. The overpotentials were calculated as the difference between the applied potentials and OCP. The potentiostatic electrodeposition experiments were performed for 120 s at the applied potentials of -0.52, -0.55, -0.57 and -0.60 V vs. Al. These applied potentials correspond to the overpotentials of -1.03, -1.05, -1.06 and -1.10 V, respectively. Following the electrodeposition experiments, the WE were cleaned to remove any adhered solidified molten salt by ultrasonicating it in distilled water for 15 minutes. After every electrodeposition experiment, the spent electrolyte was transferred to an alumina crucible within the glove box. After the spent electrolyte in the crucible was solidified, it was brought outside the glovebox. The solidified spent electrolyte was handled in a fume hood by adding a few drops of water for neutralizing. The electrolyte was not disturbed until the end of fuming. Once the fuming ended, the spent electrolyte turned transparent and dried in a hot air oven at 120 °C. Eventually, this spent electrolyte was sent for compositional analysis.

Morphological and compositional analyses were performed on the deposits in as-deposited conditions on the Cu strip. For morphological analysis of the deposits, a JEOL FEG-SEM (JSM-7600F) scanning electron microscope (SEM) was employed in gentle beam-low (GB-L) mode. Compositional analysis was performed on both deposits and the spent electrolytes using an energy dispersive spectrometer (EDS) as an accessory to the SEM. The phase analysis was performed using Rigaku X-ray diffractometer (XRD, SmarLab 9 kW, Cu, K_{α} , λ = 0.15406 nm, 160 mA, 45 kV). The phases were indexed using ICSD code 44321.

Results and discussion

Cyclic voltammetry

Figure 1(b) shows the cyclic voltammogram for the electrodeposition of Al-Mg alloys from the employed molten salt. The scan begins from OCP (+0.48 V vs. Al) and eventually progresses into the cathodic segment towards -2.00 V vs. Al. The scan direction is shown by the arrows in Figure 1(b). While progressing in the cathodic segment, the scan exhibits a slight cathodic hump with a subtle peak at around -0.41 V vs. Al due to the Al deposition from Al_2Cl_7 according to Equation (2) [25-28].

$$4Al_2Cl_7 \rightleftharpoons 7AlCl_4 + Al^{3+} \tag{2}$$

Further progress of the scan results in another cathodic hump in the cathodic segment around a peak value of around -1.04 V vs. Al. This cathodic peak arises from the Al deposition from $AlCl_4$ according to Equation (3) [25-28].

$$AICI_4^- \rightleftharpoons AI^{3+} + 4CI^- \tag{3}$$

A careful observation suggests that the peak of Al deposition from $AlCl_4^-$ is relatively more pronounced than Al deposition from $Al_2Cl_7^-$. This suggests that the concentration of $Al_2Cl_7^-$ is possibly smaller (than that of $AlCl_4^-$) at the beginning of the CV. With the progress of CV, more $AlCl_4^-$ is produced according to Equations (1) and (2). This additionally produced $AlCl_4^-$, apart from its originally present concentration in the electrolyte, could lead to the pronounced peak for Al

deposition from $AlCl_4^-$. It should be noted that both $Al_2Cl_7^-$ and $AlCl_4^-$ can indulge in a non-electrochemical reaction according to Equation (4) to produce Cl^- [29,30].

$$2AICI_4^- \rightleftharpoons AI_2CI_7^- + CI^- \tag{4}$$

The progress of CV towards negative potential beyond the AI deposition from AICI₄⁻ (Equation (3)) results in a steep increase in the current density to a very high value (Figure 1(b)), rendering an appearance of developing towards a large cathodic peak. However, such a cathodic peak is not attained by the time the scan reaches the negative switching potential of -2.00 V vs. AI. Hence, a trivial and partial reason for this large cathodic peak to be still in its developmental stage is that the scan was retracted towards a potential positive to the switching potential of -2.00 V vs. AI. The other reason this peak is still in its developmental stage is the deposition of Mg²⁺ from the electrolyte within these potentials. Mg can deposit from the employed chloride-based molten salt system according to Equation (1). Moreover, the possibility of Mg²⁺ deposition from un-complexed MgCl₂ according to Equation (5) [11,31-34] cannot be ruled out. From Figure 1(b), it is evident that the system did not reach diffusion limitation with respect to the concentration of Mg²⁺, leading to this cathodic peak still being in its developmental stage.

$$MgCl_2 \rightleftharpoons Mg^{2+} + 2Cl^{-} \tag{5}$$

Upon retracting the CV scan in the anodic segment, the first prominent anodic peak was obtained at +0.45 V vs. Al (Figure 1).

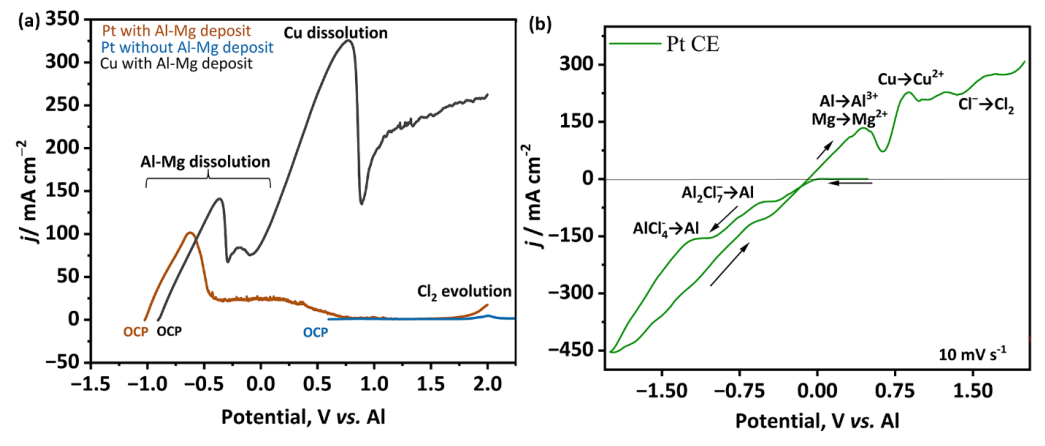


Figure 1. (a) Anodic linear sweep voltammetry curves from Pt substrates with and without Al-Mg deposit and Cu substrate with Al-Mg deposit on them. (b) Cyclic voltammogram on Cu using the present electrolyte system employing Pt CE

This peak is asymmetric and arises due to the anodic dissolution of Al and Mg that were deposited in the cathodic segment. Further progress of the scan towards the potentials more positive this anodic dissolution of Al and Mg lead to the appearance of another anodic peak due to the dissolution of Cu from WE. At the potentials immediately adjacent to the Cu-dissolution peak, the CV flutters in a wavy form mainly due to the chlorine gas evolution according to Equation (6). The source of this chlorine gas are Equations (3) to (5) [29].

$$2CI^{-} \rightarrow CI_{2(\uparrow)} + 2e^{-} \tag{6}$$

Cyclic voltammetry was used in the present study to identify various electrochemical reactions that can take place in this system and to choose potentials for electrodeposition.

Potentiostatic electrodeposition of Al-Mg

The current density-time curves from the potentiostatic deposition experiments are shown in Figure 2(a). The obtained curves are typical of electrodeposition and exhibit the following

characteristic stages (i) a steeply rising feature in the current density values corresponding to (Al-Mg) nucleation events (ii) a decreasing current density after the peak corresponding to the overlapping of diffusion zones of these nuclei; (iii) an almost steady-state current density due to the planar diffusional growth of the deposits [35]. The *j-t* curve of the deposit at -1.10 V is not as flat as that of the rest of the deposits (Figure 2(a)). As expected, the peak and the steady-state current density values are generally higher at the higher overpotentials. The steady-state current density values are plotted against overpotential in Figure 2(b). The steady-state current density from the deposit at -1.10 V is way higher than that from -1.06 V. Those from deposits at -1.05 and -1.06 V are similar and higher than that from the deposit at -1.03 V. Figure 2(b) also shows a guideline delineating the expected morphologies for the chosen overpotentials in this study. The shape of the guideline and the expected morphologies are almost universal (irrespective of the system)[36]. However, the values of the overpotentials and the steady-state current densities spanning this guideline can depend on the alloy system being deposited [36]. From Figure 2(b), all the obtained steady-state current densities fall in the regime where layer-like or film morphology is expected.

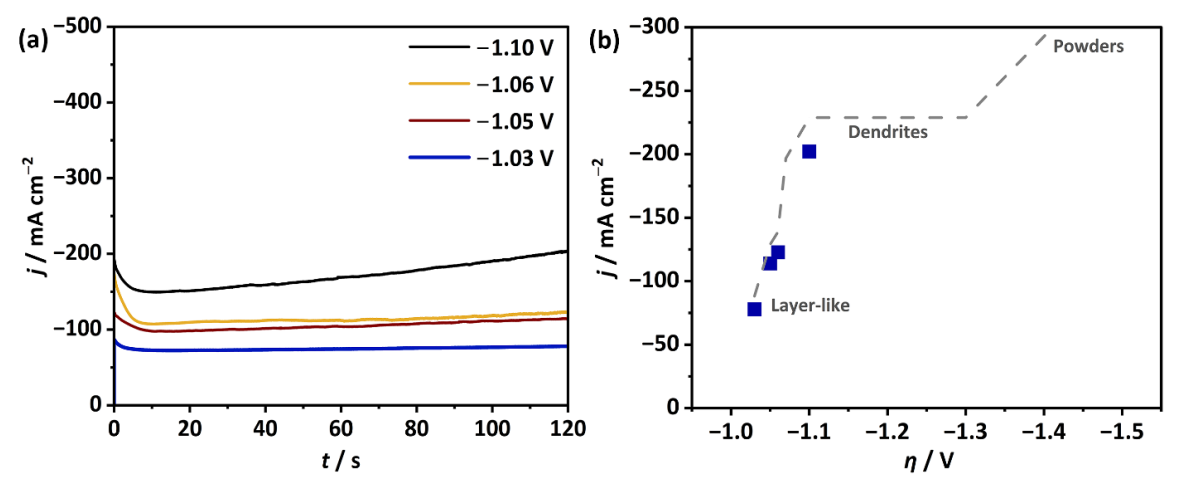


Figure 2. (a) Current density - time curves of Al-Mg electrodeposition on Cu; (b) Steady-state current densities versus overpotential with guidelines delineating expected morphologies

Morphologies, composition and phases of the Al-Mg deposits

The morphologies of all the deposits are shown in Figures 3(a)-(d) and possess near-globular features. The morphology within any given deposit is uniform as a consequence of potentiostatic deposition [37]. These morphologies represent the scenarios in the steady-state current density regimes since they are characterized at the end of the deposition. During the steady-state regime of the current density, the diffusion zones around the individual nuclei that were growing in the initial stages overlap, resulting in a blanket-like effect and ultimately yielding planar diffusion zones and growth. Such planar diffusional growth of morphologies offers good coverage on the substrate (i.e., WE). For instance, the range of thickness obtained in the deposits is approximately between 350-500 nm. At such an advanced stage of the deposition (where planar, i.e., film-like, growth is prevalent), the variation of morphology with thickness is expected to be very minimal, as seen here. However, the size of the near-globular features can change with the magnitude of the overpotential. For example, the obtained near-globular features are the coarsest in the deposit at -1.03 V and refine with the increase in the overpotential. The average size of these features (encircled in Figures 3(a) to 3(d)) is plotted as a function of overpotential in Figure 3(e). From Figure 3(e), it can be seen that the extent of the refinement of the features is the highest in the deposit at -1.06 V. From Figures 2(b) and 3(e), a significant increase in the steady-state current density from -1.03 to



-1.05 V leads to significant refinement in the feature size in the morphologies. Similarly, a small increase in the steady-state current density corresponding to the overpotentials from -1.05 to -1.06 V (Figures 2(b)) results in only a smaller extent of refinement in the average size of the features from these deposits. Interestingly, the average feature sizes are only slightly different in the deposits from -1.06 and -1.10 V, despite the very large difference in the steady-state current density between -1.06 and -1.10 V. This clearly shows that the average feature size is more sensitive to overpotentials up to -1.06 V, beyond which it becomes less sensitive. The reason for such a refinement up to -1.06 V is due to the increased charge transfer rate from -1.03 to -1.06 V. In addition, the number densities of the nuclei increase from -1.03 to -1.06 V, as more sites can get activated with an increase in the overpotential. The larger number density leads to the smaller feature size, as seen in Figure 3(e). In the deposit at -1.06 V, the density of the depositing nuclei is so high that no further nuclei can be accommodated beyond this overpotential. This leads to saturation in the number of nuclei depositing from -1.06 to -1.10 V. At -1.10 V, the additional energy supplied (*i.e.*, charge transfer) by the overpotential contributes to the growth of the near-globular features by further deposition over the already existing features.

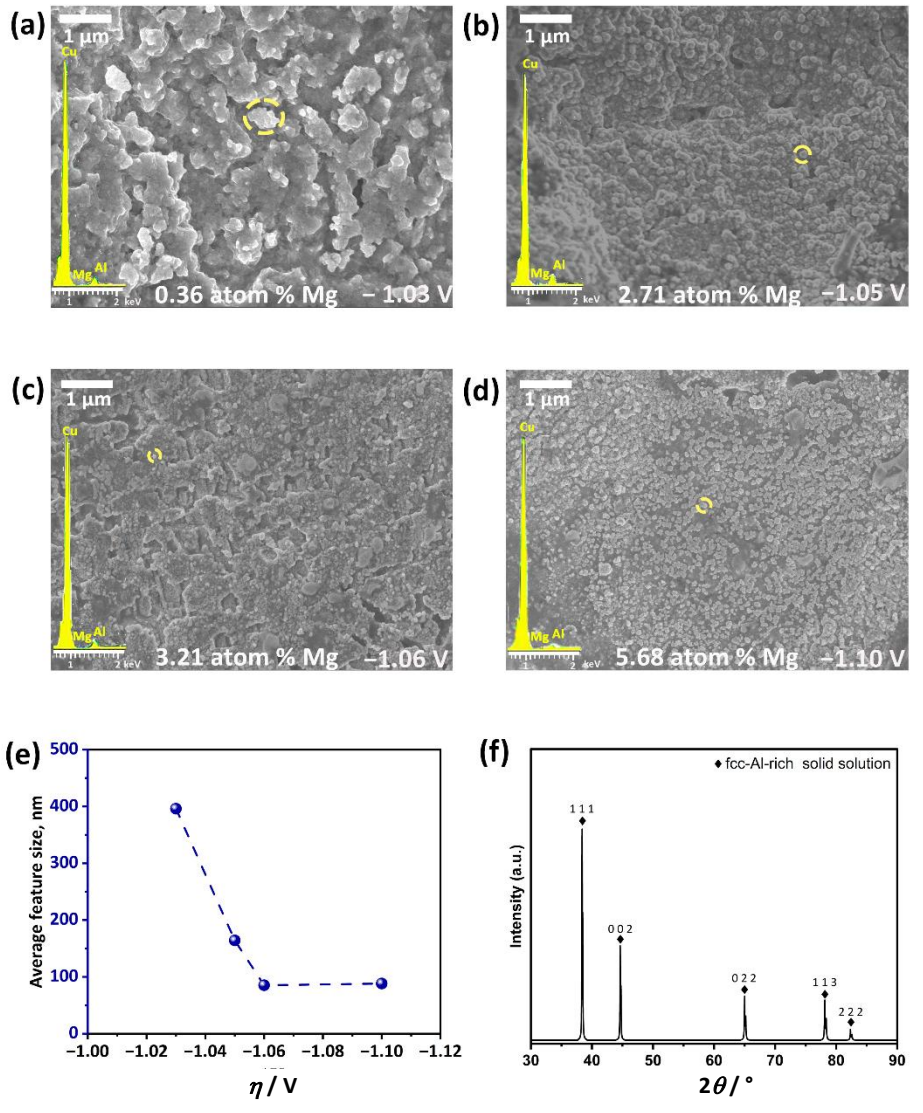


Figure 3. Morphologies of deposits at overpotentials (a) -1.03 V, (b) -1.05 V, (c) -1.06 V, (d) -1.10 V (representative near-globular features encircled), (e) average feature size versus overpotential, (f) representative X-ray diffraction pattern of Al-Mg deposits

This is probably because of the lower density of sites available for nucleation on the WE in this deposit for further nucleation events. This is why the *j-t* curve of the deposit is not as flat as that of the rest (Figure 2(a)). In fact, such a growth on the already existing features yields slightly coarsened near-globular features in the deposit at -1.10 V than that at -1.06 V (Figure 3(e)).

The compositions were analyzed from EDS spectra, which are embedded in the SEM images for the respective deposits. All the spectra show strong signals of Cu arising from the Cu substrate. The signals for Al and Mg can also be seen in these spectra. While estimating the composition in terms of Al and Mg, the contribution from Cu was neglected. Moreover, the absorption and fluorescence effects were also taken into consideration while estimating the compositions. As seen from Figures 3(a) to 3(d), the Mg content in the deposit increases with overpotential.

The XRD patterns of all the deposits are almost identical, with peaks corresponding to the face-centred cubic (fcc) phase. A representative XRD pattern from these deposits is shown in Figure 3(f). Hence, all the morphologies shown in Figure 3(a) to 3(d), containing compositions in the range of 0.36-5.68 at.% Mg, are supersaturated fcc-Al-rich solid solutions according to the equilibrium phase diagram of Al-Mg system [38]. This is expected as these deposits were obtained under highly non-equilibrium conditions, as evidenced by the high magnitudes of the current densities (Figure 2(a)).

Composition analysis

The Mg contents in the deposits and those in the spent electrolytes are plotted versus overpotential in Figure 4(a). From Figure 4(a), higher Mg is obtained in the deposits at the higher overpotentials. For example, the Mg content in the deposit at -1.03 V is 0.36 at.% and increases monotonously to 5.68 at.% in the deposit at -1.10 V. The standard reduction potentials of deposition ($E^o_{M^+|M}$, M =metal) of Al and Mg are -1.676 and -2.356 V vs. NHE, rendering Al nobler [39]. Hence, the deposition of the less-noble Mg is expected to be encouraged by overpotential, as is the case here (Figure 4(a)). Besides, the Mg content in the spent electrolyte does not significantly change with overpotential, as seen in Figure 4(a). In other words, a wide range of deposit compositions (i.e. Mg contents) can be obtained through minimal changes in the spent electrolyte compositions, as seen from the plot between the Mg content in the deposit versus that in the spent electrolyte in Figure 4(b).

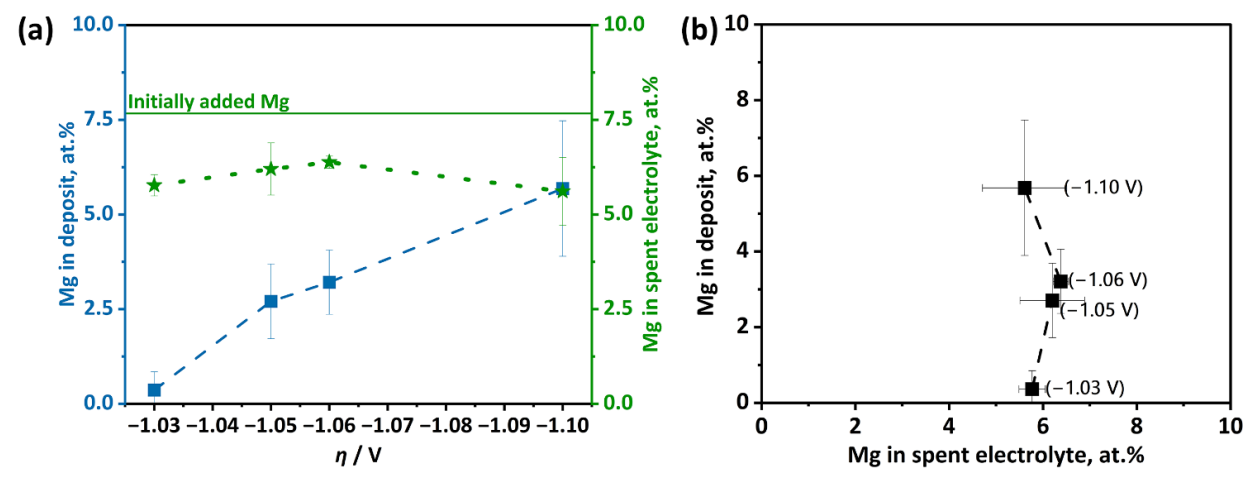


Figure 4. (a) Mg in the deposit and spent electrolyte versus overpotential; (b) Mg in the deposit versus Mg in the spent electrolyte

For clarity, the overpotentials at which the depositions were performed are also indicated in parentheses in Figure 4(b) adjacent to every point. This is a crucial result as it indicates that the present Al-Mg system does not encounter any obstacles to incorporating Mg in the deposits under

the employed conditions. Such ease in obtaining deposits with a wide range of Mg contents suggests that the deposition scheme can be simple.

Scheme of Al-Mg deposition

A possible scheme of Al-Mg deposition is devised by considering the initial composition of the electrolyte prior to the deposition, various electrochemical (deciphered from CV), and non-electrochemical reactions presented in Equations (1) to (5), and is shown in Figure 5. From the previous section, the deposition of Mg is envisaged as easy. The deposition of Al is, anyway, easy as it is a nobler metal, and its content in the deposits is much higher (Figures 4(a) and 4(b)).

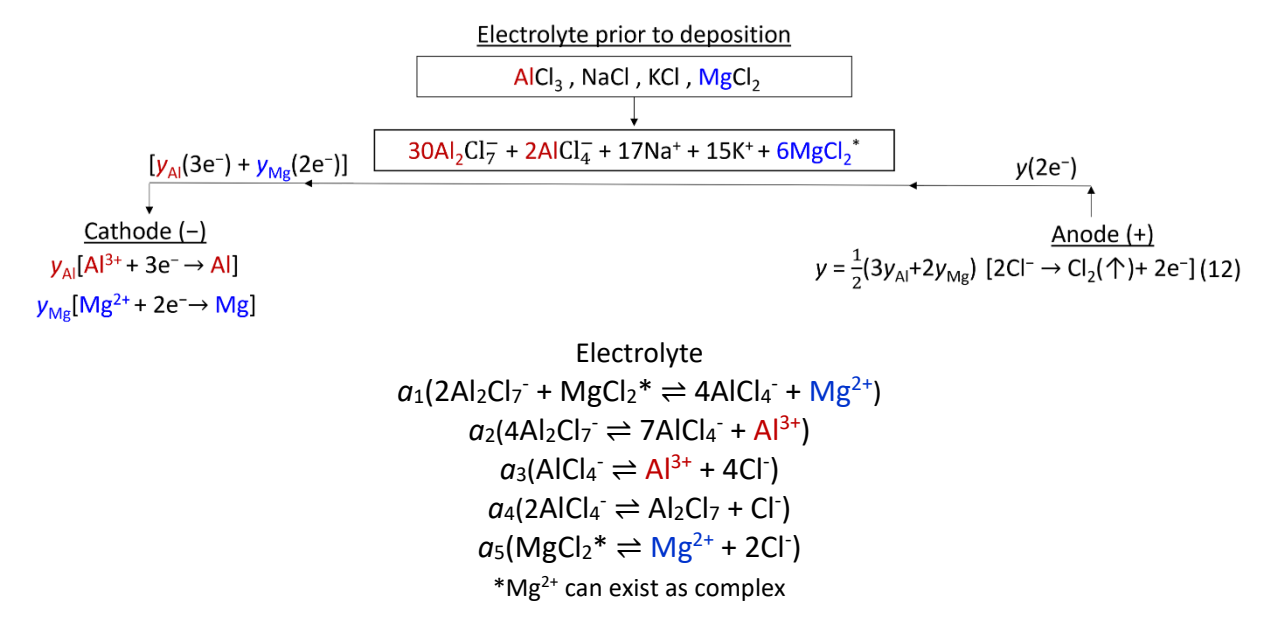


Figure 5. Proposed scheme of Al-Mg electrodeposition using chloride-based molten salt electrolyte system employing Pt CE

Hence, the electrochemical equations for the deposition of Al and Mg can be perceived as $Al^{3+} + 3e^- \rightarrow Al$ and $Mg^{2+} + 2e^- \rightarrow Mg$, both occurring at the cathode (Figure 5). Among all the electrochemical reactions perceived here, chlorine evolution (Figure 1) is the only anodic reaction (Figure 5). Hence, this is the reaction that supplies electrons for Al-Mg deposition. All the Equations (1) to (5) discussed above are shown in Figure 5. As mentioned earlier, it is assumed that $MgCl_2$ can combine with Al_2Cl_7 to form $AlCl_4$ and Mg^{2+} , according to Equation (1) [15,16]. Combined with Equation (5), this equation can serve as the source of Mg for its eventual deposition. The sources of Al for its deposition are Equations (2) and (3); and those for chlorine evolution are Equations (3) to (5), all occurring within the electrolyte (Figure 5). These reactions can happen to various extents in respective regions (*i.e.*, the electrodes and the electrolyte). The extents of reactions within the electrolyte are denoted with variables a_i (i = 1 to 5) in Figure 5. Those for Al and Mg deposition at the cathode are denoted as y_{Al} and y_{Mg} . Collectively, they are used to denote the extent of anodic reaction as y (Figure 5). Thus, Figure 5 represents the deposition scheme of Al-Mg alloys from the present chloride-based electrolyte system.

Conclusions

Al-Mg alloys with desired morphology and composition were potentiostatically electrodeposited from a chloride-based molten salt electrolyte containing AlCl₃, NaCl, KCl, and MgCl₂ at 180 °C for aircraft applications. The alloys were deposited on a Cu cathode (working electrode)

employing a Pt-mesh anode (counter electrode) and an Al rod as the pseudo-reference electrode. Prior to conducting the deposition experiments, cyclic voltammetry (CV) was performed to identify various electrochemical reactions in this system and to facilitate the choice of potentials for deposition. CV reveals that Al₂Cl₇⁻ and AlCl₄⁻ are the sources for depositing Al. Mg can deposit due to the reaction between Al₂Cl₇⁻ and AlCl₄⁻ (releasing Mg²⁺) and the dissociation of MgCl₂ to Mg²⁺ and Cl⁻. Eventually, potentiostatic deposition was performed for 120 s at overpotentials of -1.03, -1.05, -1.06 and -1.10 V with respect to open circuit potential. The current density-time curves exhibit the typical characteristics such as an initially rising j-t portion due to nucleation events, followed by a steeply dropping portion suggesting the overlapping of diffusion zones of these nuclei, and finally, an almost steady-state current density portion indicating the prevalence of planar diffusional growth of the deposits. The steady-state current densities fall in the regime of obtaining layer-like morphology. This is confirmed by the morphologies of the deposits, all of which exhibit near-globular growth features in the layers of Al-Mg alloys. The average size of these features decreases up to -1.06 V. At -1.10 V. However, the size increases slightly due to the growth of these features as further deposition occurs over the already existing features. The composition (Mg content) of the deposits increases monotonously with the magnitude of overpotential (i.e. 0.36 at.% at -1.03 V; 5.68 at.% at -1.10 V). Such a wide range of Mg content in the deposits is obtained through minimal changes in the spent electrolytes. This indicates that the present Al-Mg system does not encounter obstacles to incorporating less-noble Mg in the deposits under the employed conditions. A possible Al-Mg deposition scheme is devised by considering the electrochemical (from CV) and non-electrochemical reactions in this system. The Al and Mg deposition can be perceived as $Al^{3+} + 3e^{-} \rightarrow Al$ and $Mg^{2+} + 2e^{-} \rightarrow Mg$, both occurring at the cathode. The electrons for these depositions are supplied by chlorine gas evolution (from CV) according to $2Cl^{-} \rightarrow Cl_{2(\uparrow)} + 2e^{-}$, occurring at the anode.

Conflicts of interest: The authors declare no conflict of interest.

Acknowledgements: Financial support from Department of Science and Technology, India and General Electric India Industrial Pvt. Ltd. under IMPRINT II C (File No.: IMP/2019/000241) is appreciated. FEG-SEM and EDS facilities at Sophisticated Analytical Instrument Facility (SAIF), IIT Bombay are acknowledged.

References

- [1] W. S. Miller, L. Zhuang, J. Bottema, A. J. Wittebrood, P. De Smet, A. Haszler, A. Vieregge. Recent development in aluminium alloys for the automotive industry. *Materials Science & Engineering A* **A280** (2000) 37-49. https://doi.org/10.1016/S0921-5093(99)00653-X
- [2] E. Georgantzia, M. Gkantou, G.S. Kamaris. Aluminium alloys as structural material: A review of research. *Engineering Structures* **227** (2021) 111372 https://doi.org/10.1016/j.engstruct.2020.111372
- [3] S. V. Kozhukharov, C. Girginov, S. Portolesi, A. Tsanev, V. Lilova, M. Georgieva, E. Lilov, P. Petkov. Sealing of cerium oxide coating primers on anodized AA2024-T3 alloy by boiling in Lourier buffers. *Journal of Electrochemical Science and Engineering* **14** (2024) 559-582. https://doi.org/10.5599/jese.1949
- [4] C. Kammer, Aluminum and aluminum alloys, in Springer Handbook of Materials Data, W. Martinessen, H. Warlimont, Eds., Springer Nature, Switzerland, 2018, p. 157 https://doi.org/10.1007/978-3-319-69743-7
- [5] K. K. Sankaran, R. S. Mishra, *Metallurgy and Design of Alloys with Hierarchical Microstructures,* Elsevier, 2017, p. 57. ISBN 978-0-12-812068-2



- [6] M. Leary, Materials selection and substitution using aluminium alloys, in Fundamentals of Aluminium Metallurgy: Production, Processing and Applications, M. Leary, Ed., Woodhead Publishing Limited, 2010, p. 784 https://doi.org/10.1533/9780857090256.3.784
- [7] I. C. Park, S. J. Kim. Electrochemical characteristics in seawater for cold thermal spray-coated Al-Mg alloy layer, *Acta Metallurgica Sinica (English Letters)* **29** (2016) 727-734 https://doi.org/10.1007/s40195-016-0437-7
- [8] M. Ueda. Overview over studies of electrodeposition of Al or Al alloys from low temperature chloroaluminate molten salts. *Journal of Solid State Electrochemistry* **21** (2017) 641-647 https://doi.org/10.1007/s10008-016-3428-8
- [9] S.S. V. Tatiparti, F. Ebrahimi. An understanding of the electrodeposition process of Al-Mg alloys using an organometallic-based electrolyte. *Journal of Applied Electrochemistry* **40** (2010) 2091-2098 https://doi.org/10.1007/s10800-010-0190-y
- [10] H. Lehmkuhl, K. Mehler, B. Reinhold, H. Bongard, B. Tesche. Deposition of Aluminum-Magnesium Alloys from Electrolytes Containing Organo-Aluminum Complexes. *Advances in Engineering Materials* 3 (2001) 412-417 https://doi.org/1438-1656/01/0606-0412
- [11] A. Mayer. Electrodeposition of Aluminum, Aluminum/Magnesium Alloys, and Magnesium from Organometallic Electrolytes. *Journal of the Electrochemical Society* **137** (1990) 2806-2809. https://doi.org/10.1149/1.2087078
- [12] M. Morimitsu, T. Tanaka, M. Matsunaga, *Electrodeposition of Al-Mg Alloys from Lewis acidic AlCl₃-EMIC-MgCl₂ room temperature molten salts*, Electrochemical Society Proceedings Series, Molten Salts XIII: Proceedings of the international symposium, United States of America, 2002, p. 671-676. https://www.electrochem.org/dl/ma/201/pdfs/1459.pdf
- [13] Y. Li, P. Zhao, Y. Dai, M. Yao, H. Gan, W. Hu. Electrochemical deposition of Al-Mg alloys on tungsten wires from AlCl₃-NaCl-KCl melts. *Fusion Engineering and Design* **103** (2016) 8-12 https://doi.org/10.1016/j.fusengdes.2015.11.053
- [14] M. Morimitsu, N. Tanaka, M. Matsunaga. Induced Codeposition of Al-Mg Alloys in Lewis acidic AlCl₃-EMIC room temperature molten salts. *Chemistry Letters* (2000) 1028-1029. https://doi.org/10.1246/cl.2000.1028
- [15] M.R. Ali, A. P. Abbott, K.S. Ryder. Electrodeposition of Al-Mg Alloys from Acidic AlCl₃-EMIC-MgCl₂ room temperature ionic liquids. *Journal of Electrochemistry* 21 (2015) 172-180 https://doi.org/10.13208/j.electrochem.140603
- [16] H-M. Kan, S-S. Zhu, N. Zhang, X-Y. Wang. Electrodeposition of aluminum and aluminum—magnesium alloys at room temperature. *Journal of Central South University* **22** (2015) 3689-3697 https://doi.org/10.1007/s11771-015-2911-1
- [17] L. Shen, B. Cui, S. Li, Y. Lei, Z. Shi. Electrodeposition of Al-Mg coating in the electrolyte system of $C_4H_8O-C_6H_6$ -LiAlH₄-AlCl₃-MgX₂ (X=Cl, Br). *Journal of Materials Research and Technology* **22** (2023) 1349-1361 https://doi.org/10.1016/j.jmrt.2022.12.018
- [18] S.S.V. Tatiparti, F. Ebrahimi. Electrodeposition of Al-Mg alloy powders. *Journal of the Electrochemical Society* **155** (2008) D363-D368 https://doi.org/10.1149/1.2885016
- [19] X. Zhang, A. Liu, F. Liu, Z. Shi, B. Zhang, X. Wang. Electrodeposition of aluminum-magnesium alloys from an aluminum-containing solvate ionic liquid at room temperature. *Electrochemical Communications* 133 (2021) 107160 https://doi.org/10.1016/j.elecom.2021.107160
- [20] A. Mayer, Electrodeposition of aluminum, aluminum/magnesium alloys, and magnesium from organometallic electrolytes, 1. international congress on high-tech-materials and finishing, Berlin, F.R. Germany, 12 -14 March 1989, pp. 1-11. https://www.osti.gov/servlets/purl/6418518

- [21] S. S. V. Tatiparti, F. Ebrahimi. The formation of morphologies and microstructures in electrodeposited nanocrystalline Al-Mg alloy powders. *Journal of The Electrochemical Society* **157** (2010) E167-E171 https://doi.org/10.1149/1.3468939
- [22] S. S. V. Tatiparti, F. Ebrahimi. Preferred orientation and shape of electrodeposited nanocrystalline Al-Mg alloy dendrites. *Materials Letters* 65 (2011) 1915-1918 https://doi.org/10.1016/j.matlet.2011.04.018
- [23] S. S. V. Tatiparti. Extended solubility in the electrodeposited nanocrystalline Al-Mg alloy dendrites. *Materials Letters* 65 (2011) 3173-3175 https://doi.org/10.1016/j.matlet.2011.06.112
- [24] G. R. Stafford, T. Tsuda, C. L. Hussey. The structure of electrodeposited aluminum alloys from chloroaluminate ionic liquids: Let's not ignore the temperature. *ECS Transactions* **64** (2014) 535-547 https://doi.org/10.1149/06404.0535ecst
- [25] G. R. Stafford, G.M. Haarberg. The electrodeposition of Al-Nb alloys from chloroaluminate electrolytes, *Plasmas & Ions* 1 (1999) 35-44. https://doi.org/10.1016/S1288-3255(99)80010-0
- [26] C. G. Fink, D. N. Solanki. Aluminum from a Fused Chloride Bath. *ECS Transactions* **91** (1947) 203-219 https://doi.org/10.1149/1.3071777
- [27] R. C. Howie, D. W. Macmillan. The electrodeposition of aluminium from molten aluminium chloride/sodium chloride. *Journal of Applied Electrochemistry* **2** (1972) 217-222. https://doi.org/10.1007/BF02354979
- [28] B. Nayak, M. M. Misra. The electrodeposition of aluminium on brass from a molten aluminium chloride-sodium chloride bath. *Journal of Applied Electrochemistry* 7 (1977) 45-50. https://doi.org/10.1007/BF00615529
- [29] H-M. Kan, Z-W. Wang, X-Y. Wang, N. Zhang. Electrochemical deposition of aluminum on W electrode from AlCl₃-NaCl melts. *Transactions of Nonferrous Metals Society of China (English Edition)* **20** (2010) 158-164 https://doi.org/10.1016/S1003-6326(09)60114-X
- [30] G. R. Stafford. The electrodeposition of Al₃Ti from chloroaluminate electrolytes. *Journal of the Electrochemical Society* **141(4)** (1994) 945-953. https://doi.org/10.1149/1.2054863
- [31] G. T. Cheek, W. O'Grady, S. Z. El Abedin, E. M. Moustafa, F. Endres. Electrochemical studies of magnesium deposition in ionic liquids. ECS Transactions 3 (2007) 269-279 https://doi.org/10.1149/1.2798670
- [32] T. Watkins, A. Kumar, D. A. Buttry. Designer ionic liquids for reversible electrochemical deposition/dissolution of magnesium. *Journal of American Chemical Society* **138** (2016) 641-650 https://doi.org/10.1021/jacs.5b11031
- [33] A. M. Martínez, B. Børresen, G. M. Haarberg, Y. Castrillejo, R. Tunold. Electrodeposition of magnesium from CaCl₂-NaCl-KCl-MgCl₂ melts. *Journal of the Electrochemical Society* 151 (2004) C508-C513 https://doi.org/10.1149/1.1758814
- [34] B. Bøsrresen, G.M. Haarberg, R. Tunold. Electrodeposition of magnesium from halide meltscharge transfer and diffusion kinetics. *Electrochimica Acta* 42 (1997) 1613-1622 https://doi.org/10.1016/S0013-4686(96)00322-2
- [35] M. Pise, M. Muduli, A. Chatterjee, B. P. Kashyap, R. N. Singh, S. S. V. Tatiparti.
 Instantaneous-Progressive nucleation and growth of pal ladium during electrodeposition.

 Results in Surfaces and Interfaces 6 (2022) 100044

 https://doi.org/10.1016/j.rsurfi.2022.100044
- [36] F. C. Walsh, M. E. Herron. Electrocrystallization and electrochemical control of crystal growth: Fundamental considerations and electrodeposition of metals. *Journal of Physics D:*Applied Physics 24 (1991) 217-225 https://doi.org/10.1088/0022-3727/24/2/019



- [37] S. S. V. Tatiparti, F. Ebrahimi. Potentiostatic versus galvanostatic electrodeposition of nanocrystalline Al-Mg alloy powders. *Journal of Solid State Electrochemistry* **16** (2012) 1255-1262 https://doi.org/10.1007/s10008-011-1522-5
- [38] J. L Murray, The Al-Mg (Aluminum-Magnesium) system, *Bulletin of Alloy Phase Diagrams*, (3) 1982, 60-74. https://doi.org/10.1007/BF02873413
- [39] A. Brenner, Practical Considerations Involved in the Electrodeposition of Alloys in Electrodeposition of Alloys, Principles and Practice, Volume I, Academic Press, New York, United States of America, 1963, p.44. https://doi.org/10.1016/B978-1-4831-9808-8.50011-3

© 2024 by the authors; licensee IAPC, Zagreb, Croatia. This article is an open-access article distributed under the terms and conditions of the Creative Commons Attribution license (https://creativecommons.org/licenses/by/4.0/)



Open Access : : ISSN 1847-9286

www.jESE-online.org

Original scientific paper

Polymer-modified screen-printed electrode-based electrochemical sensors for doxorubicin detection

Iva Dimitrievska[⊠], Perica Paunović and Anita Grozdanov

Ss. Cyril and Methodius University in Skopje, Faculty of Technology and Metallurgy, Rugjer Boshković 16, 1000 Skopje, North Macedonia

Corresponding author: [™]iva@tmf.ukim.edu.mk

Received: October 1, 2024; Accepted: November 27, 2024; Published: December 4, 2024

Abstract

In the last decade, intensive research has been performed in the field of analytical electrochemistry, seeking designs of electrochemical sensors capable of providing better analytical characteristics in terms of sensitivity, selectivity, reliability, ease of fabrication and use, and low cost, especially for pharmaceutical drug monitoring. Our research has primarily focused on developing screen-printed electrode-based sensors and their application as electrochemical platforms for drug determination and monitoring, specifically emphasizing their suitability for surface modification. A commercial screen-printed graphene electrode was used as the electrochemical sensing component, which was subsequently modified with polymers, such as polyvinylidene fluoride and chitosan. All studied electrodes were tested using a doxorubicin hydrochloride (DOX) solution with a concentration of 0.002 mol L⁻¹ dissolved in 0.1 mol L⁻¹ phosphate-buffered saline at pH 6.7. Cyclic voltammetry was used as an electrochemical characterization technique to gather data on all tested electrodes' electrochemical activity. The morphological characterization of the electrodes was done using scanning electron microscopy. The changes in the electrolyte during the electrochemical measurements were followed through ultraviolet-visible spectroscopy. The modified electrodes demonstrated a favorable electrochemical response to DOX and exhibited higher electrical conductivity than the commercial one. The characterization results indicated that the Ch-modified electrode exhibited excellent electrochemical conductivity and demonstrated strong electrochemical performance. The evaluations of this electrode comprised the definition of the lowest limit of detection and limit of quantification among the tested electrodes, with values of 9.822 and 32.741 μ mol L^{-1} , respectively, within a linear concentration range from 1.5 to 7.4 μ mol L^{-1} . Additionally, the electrodes showed excellent repeatability, stability, and reproducibility, confirming their suitability for sensitive DOX detection.

Keywords

Graphene; polyvinylidene fluoride; chitosan; anticancer medication, sensing

Introduction

Doxorubicin hydrochloride (DOX) is a potent and widely used anticancer medication in the anthracyclines class. Commonly referred to as the "golden standard", DOX is highly effective against a broad

spectrum of malignancies, including breast cancer, lymphomas, leukemias, and sarcomas. DOX's anticancer and antitumor mechanism of action is related to the inhibition of DNA replication and transcription processes through intercalation between base pairs, thereby leading to cell death [1]. Additionally, it can generate cytotoxic reactive oxygen species, leading to oxidative stress and induction of apoptosis, effectively targeting rapidly dividing cancer cells and exerting cellular damage [2].

Despite its remarkable efficiency, DOX has limitations because of its severe acute and long-term side effects. One major concern is raised regarding its dose-dependent cardiotoxicity, which can lead to irreversible damage to the heart muscle and potentially compromise the long-term health of cancer survivors [3]. Therefore, monitoring and keeping the DOX concentration under control in patients following cancer treatment is critical to minimize the side effects during clinical trials, assess toxicity, and follow the therapeutic efficiency.

Numerous analytical methods have already been reported for DOX determination and monitoring, using techniques such as high-performance liquid chromatography (HPLC), liquid chromatography coupled with mass spectroscopy (LC-MS), ultraviolet-visible spectroscopy (UV-Vis), fluorescence, etc. [4-15]. Although HPLC and LC/MS methods present the highest selectivity and sensitivity towards pharmaceutical molecules, all these techniques demand complicated and time-consuming sample preparation, making them unsuitable for rapid detection. Electrochemical methods receive much consideration due to their ease of use, inexpensive equipment, simple and fast manipulation, and real-time sensing. Electrochemical sensors have been reported as one of the most favorable and practical methods for pharmaceutical compound detection in human blood samples, offering unique advantages such as miniaturization, portability, rapid response, and satisfactory selectivity and sensitivity [16]. Implementing nanotechnology to conventional electrochemical sensors results in enhanced sensing mechanisms due to nanomaterials' superior properties. Electrochemical sensors based on nanomaterials show incredible performance due to their large specific surface area and high reactivity, making them a highly popular topic among researchers.

Researchers continuously work towards improving the surface kinetics of electrodes to design electrochemical sensors with advanced performance and satisfactory results. Extensive research has been focused on screen-printed electrode (SPE) based sensors as electrochemical sensors for drug determination, particularly suitable for surface modification. Carbon nanomaterials (graphene, carbon nanotubes, carbon nanorods, carbon nanoflakes, etc.) are the most widely used nanostructures as electrode modifiers and an excellent choice for electrochemical sensor performance improvement [17]. Graphene is suitable for electrochemical sensing applications because of its dimensions and improvement of the overall sensitivity when increasing the number of surface electroactive centers and enhancing the rate of electron transfer [18]. Moreover, polymeric modification by coating onto electrode surfaces offers significant flexibility. Polymers contain diverse functional groups, allowing for exceptional high surface coverage through thick multilayer coating [19]. Some commonly used polymers are chitosan (CH) and polyvinylidene fluoride (PVDF). Chitosan, a natural biopolymer, is a highly biocompatible amino saccharide, which can also be considered environmentally friendly due to its low toxicity [20,21]. Chitosan's surface can be chemically modified with many functional groups, allowing chitosan-modified sensors to interact with the target analyte, such as DOX (Figure 1). There are active amino groups in the chitosan's structure, allowing the attachment of the functional groups of other analytes. The amino groups are also determining the chitosan's cationic nature. Moreover, using chitosan nanoforms enhances the sensing platform [21]. PVDF is a highly nonreactive thermoplastic fluoropolymer known for its superior chemical resistance, versatility, and robustness, among other exceptional properties [22]. PVDF is a highly hydrophobic polymer,

allowing the analytes to adsorb on its surface through van der Waals forces and hydrophobic interactions. A unique combination of physicochemical characteristics has led to PVDF's significant use in a wide range of applications. Over time, PVDF has emerged as the most extensively used material in electrochemical applications, where attributes such as high sensitivity, stability, and rapid response are needed [23].

Figure 1. Chemical structure of doxorubicin hydrochloride

The aforementioned materials are extensively used for sensor development, as reported in the literature. Zhao et al. [24] developed an electrochemical sensor for the sensitive detection of DOX based on a novel synthesized electrode material that includes gold nanoparticles and multiwalled carbon nanotubes decorated with a covalent organic framework used for glassy carbon electrode modification. The designed sensor showed improved distribution of electroactive sites and higher affinity towards DOX, contributing to enhanced electrocatalytic sensor activity. The authors reported an improved linear range for DOX from 0.08 to 25 µmol L⁻¹ with a low detection limit of 16 nmol L⁻¹ in spiked human serum and cell lysate samples. A novel, two-dimensional nanocomposite with a mediator role in DOX's detection has been proposed by Mehmandoust et al. [25]. The synthesized nanocomposite based on two-dimensional graphitic carbon nitride/sodium dodecyl sulfate/graphene nanoplatelets has been used for surface modification of screen-printed electrodes. The authors reported excellent electrochemical performance of the sensor, including a wide dynamic linear range from 0.03 to 1.0 μ mol L⁻¹ and 1.0 to 13.5 μ mol L⁻¹ with a low detection limit of 10.0 nmol L⁻¹. Upon testing, the developed sensor showed excellent sensitivity, stability, good reproducibility, and repeatability toward DOX detection in real human plasma and urine samples, with correlation and variation coefficients below 6.0 %.

An electrochemical sensor designed using tryptophan/(polyethylene glycol)ylated-CoFe₂O₄ nanoparticles to modify glassy carbon electrodes for sensing DOX in clinical fluids has been proposed by Abbasi *et al.* [26]. Under optimized conditions, the proposed sensor exhibits a low quantification limit of 30 ng mL⁻¹ and dynamic linear limits from 30 ng mL⁻¹ to 1.0 μ g and 1.0 to 5.0 μ g mL⁻¹, respectively. Guo *et al.* [27] synthesized ternary nanocomposites with silver nanoparticles (AgNPs), carbon dots (CDs), and reduced graphene oxide (rGO), which were electrodeposited on a glass carbon electrode (GCE) and reported superior electrocatalytic activities for DOX reduction. They reported superior electrocatalytic activities for DOX reduction in the range from 0.01 to 2.5 μ mol L⁻¹ (R^2 = 0.9956), and a low detection limit of 2 nmol L⁻¹. An electrochemical device based on a screen-printed diamond electrode (SPDE) for a single drop quantification of DOX has been reported by Stanković *et al.* [28]. The authors observed high electroactivity over a wide range of pHs and a working linear range for DOX from 0.1 to 2.5 μ mol L⁻¹.

Behravan et al. [29] developed an electrochemical sensor based on reduced graphene oxide (rGO)//gold (Au) nanoparticles/polypyrrole (PPy)/nanocomposite-modified glassy carbon electrode (GCE) for the detection of DOX. The optimization process determined pH 5.5 to be the optimal value. The

authors reported a high sensitivity of $185~\mu\text{A}$ mmol $^{-1}$ L, a low detection limit of $0.02~\mu\text{mol}$ L $^{-1}$, a wide linear range of $0.02~\mu\text{mol}$ L $^{-1}$ to 25~mmol L $^{-1}$, and excellent reproducibility and stability properties. Carbon dots/cerium oxide (CDs/CeO $_2$) nanocomposites modified screen-printed carbon electrode has been developed by Thakurb *et al.* [30] for sensitive detection of DOX. The nanocomposite consisting of 5 wt.% CDs (CDs-5.0/CeO $_2$) was reported to have the highest oxidation response to DOX (20 μ mol L $^{-1}$) in a solution with a pH of 5. Moreover, the authors reported a linear concentration range of 0.2 to $20~\mu$ mol L $^{-1}$ and a low detection limit of $0.09~\mu$ mol L $^{-1}$. In addition to this, the modified sensor showed superior selectivity and sensitivity towards DOX. Other authors, Abhishek Singh *et al.* [31], also reported the use of carbon dots-based electrochemical sensors based on screen-printed carbon electrodes, but their nanocomposites consisted of carbon dots and magnesium oxide (CDs/MgO). They reported that the modification with 5 wt.% CDs (CDs-5.0/MgO) exhibited the highest oxidation response for DOX (10 μ mol L $^{-1}$) at pH 5 and a scan rate of 50 mV s $^{-1}$. The testing was done in a linear concentration range of 0.1 to 1 μ mol L $^{-1}$ and a low detection limit of 0.09 μ mol L $^{-1}$. The proposed sensor showed superior selectivity towards DOX upon testing the effect of the common interfering agents.

Sun *et al.* [32] developed a new acetylene black (AB) glassy carbon electrode (GCE) for the detection of DOX in human serum. The authors report detailed optimization of scanning rate, AB volume, concentration, DOX enrichment time, and pH as the main parameters that affect electrochemical detection. The oxidative peak current has been reported to be linearly proportional to DOX's concentration in the ranges of 0.01 to 2.5 μ mol L⁻¹, with a detection limit of 3.006 nmol L⁻¹. The method was found to be implemented for quantitative analysis of spiked samples of human serum with a satisfactory recovery from 91.22 to 101.34 %. Gold nanoparticles decorated-multi-walled carbon nanotubes (MWCNTs) have been used as an ultrasensitive electrochemical sensor by Sharifi *et al.* [33] for the detection of DOX. The authors report an efficient electrocatalytic reduction activity of DOX, which leads to a peak current density increase and a reduction in over-potential decrease. The modified electrode has demonstrated a wide linear concentration range from 10⁻⁵ to 1 μ mol L⁻¹, with a low limit of detection (6.5 pmol L⁻¹). The developed sensor exhibited appropriate selectivity, reproducibility, repeatability, and long-term stability.

Alavi-Tabari *et al.* [34] worked on the simultaneous detection of DOX and dasatinib (DAS) using a ZnO nanoparticle/1-butyl-3-methylimidazolium tetrafluoroborate modified carbon paste electrode (ZnO-NPs/BMTFB/ /CPE). The modified electrode has been reported to exhibit a good oxidation response of DOX in a linear concentration range of 0.07 to 500 μmol L⁻¹. The limit of detection was reported to be 9.0 nmol L⁻¹. An electrochemical sensor for simultaneous detection of DOX and methotrexate (MTX) using carbon black (CB), cooper nanoparticles (CuNPs), and Nafion-modified glassy carbon electrode (CuNPs-CB-Nafion/GCE) has been reported by Materon *et al.* [35]. Under optimized conditions, the modified electrode showed a linear response range of 0.45 to 5.1 μmol L⁻¹, with a limit of detection of 24 nmol L⁻¹. The authors demonstrated a successful application of the sensor to determine DOX and MTX in human urine and water river samples, with a spike recovery of nearly 100 % under optimized conditions.

As a novel DOX sensor, Rahimi *et al.* [36] designed a modified screen-printed electrode with a bird nest-like nanostructured NiCo2O4 (BNNS-NiCo₂O₄/SPE). Their sensor exhibited a linear concentration range between 0.01 and 600.0 μ mol L⁻¹, with a detection limit of 9.4 nmol L⁻¹. Graphene quantum dot (GQD)-modified glassy carbon electrode for determination of DOX has been investigated by Hashemzadeh *et al.* [37]. The authors determined a substantial decrease in the overvoltage (-0.56 V) of the oxidation reaction of DOX at low potential compared to ordinary electrodes. A wide linear concentration range of the modified electrode was reported from 0.018 to 3.600 μ M, with a suitable

limit of detection of 0.016 μ mol L⁻¹ and a limit of quantification of 0.050 μ mol L⁻¹. The developed sensor has good linearity (R^2 = 0.9971), inter-day precision (3.33 % RSD), intra-day precision (5.03 % RSD), and accuracy. Mohammadi *et al.* [38] fabricated a sensor based on Ni-Fe layered double hydroxide (Ni-Fe LDH)-modified screen-printed electrode (Ni-Fe LDH/SPE) for the detection of DOX and DAS. The proposed sensor exhibited a broad linear concentration range from 0.04 to 585.0 μ mol L⁻¹, with a narrow limit of detection of 0.01 μ mol L⁻¹. The authors confirmed the practical application of the developed sensor by sensing DOX and DAS in biological matrices.

An electrochemical sensor based on screen-printed electrodes for simultaneous detection of DOX and simvastatin (SMV) has been published by Rus *et al.* [39]. Different materials such as graphite, gold nanoparticles-decorated graphite, gold, platinum, and pencil graphite. have been implemented as working electrodes. The authors reported that the use of amperometry allowed for a better limit of detection (0.1 μ g mL⁻¹ for DOX) than the one obtained in voltammetry (1.5 μ g mL⁻¹). The limit of quantification using amperometry was 0.5 μ g mL⁻¹ in the dynamic concentration range of 0.5 to 65 μ g mL⁻¹, while using voltammetry was 1 μ g mL⁻¹ in the dynamic range from 1 to 100 μ g mL⁻¹. The authors concluded that the graphite electrodes showed the highest oxidation peak intensity for DOX and that the oxidation is reversible, involving the exchange of two protons and two electrons.

Wang *et al.* [40] demonstrated the use of electrochemically pretreated glassy carbon electrodes (p-GCE) modified with vertically ordered mesoporous silica films (VMSF) for determination of DOX. The authors emphasize the pretreatment process as a simple and cost-effective way to improve the catalytic properties on the interface, allowing for stable growth of VMSF without using adhesive layers. The proposed sensor exhibits ultrahigh sensitivity of $23.94 \,\mu\text{A} \,\mu\text{M}^{-1}$, a low detection limit of 0.2 nmol L⁻¹, along with a wide linear concentration range from 0.5 nmol L⁻¹ to 23 μ mol L⁻¹. An electrochemical sensor based on a cyclodextrin-graphene hybrid nanosheet-modified glassy carbon electrode (CD-GNs/GCE) has been reported by Guo *et al.* [41] for the detection of DOX and MTX. The linear response range under optimized conditions of the proposed sensor was 10 nmol L⁻¹ to 0.2 μ mol L⁻¹, with a detection limit of 0.1 nmol L⁻¹. Another sensor based on vertically ordered mesoporous silica films (VMSFs) and N-doped graphene quantum dots (NGQDs)-modified indium tin oxide (ITO) has been proposed by Zhang *et al.* [42]. The proposed sensor resulted in good analytical performance, such as a wide linear range (5 nmol L⁻¹ to 0.1 μ mol L⁻¹ and 0.1 to 1 μ mol L⁻¹), high sensitivity (30.4 μ A μ mol⁻¹ L), and a low limit of detection (0.5 nmol L⁻¹). The authors reported good selectivity and recoveries of 97.0 to 109 % upon testing the modified sensor in human serum and urine samples.

Haghshenas *et al.* [43] fabricated an oxidized multiwalled carbon nanotube/glassy carbon electrode (OMWCNT/GCE)-based sensor used for simultaneous detection of dopamine (DA) and DOX. Under optimal conditions, the modified electrode operated in the concentration range of 0.04 to 90 μ mol L⁻¹, with a detection limit of 9.4 nmol L⁻¹. The authors successfully demonstrated the practical application of the modified electrode in human blood serum and urine samples. A nano-titania (nano-TiO₂)/Nafion composite film-modified GCE has been synthesized and developed by Fei *et al.* [44]. The modified electrode greatly enhanced the reduction of DOX compared to the bare GCE. The authors reported a linear response of DOX in the range from 5.0 nmol L⁻¹ to 2.0 μ mol L⁻¹, with a detection limit of 1.0 nmol L⁻¹. The RSD of the inter-electrode is reported as 5.1 %, indicating the reproducibility of the method. The stability of the modified electrode was tested after 2-week air exposure, with a decrease of only 3.8 % in the initial response. The recovery of the modified electrode ranged from 94.9 to 104.4 % in human plasma samples. A DOX sensor based on multiwalled carbon nanotubes (MWCNTs) and spinel-structured cobalt ferrite (CoFe₂O₄) magnetic nanoparticles (MNPs)-modified carbon paste

electrode has been developed by Taei *et al.* [45]. The proposed sensor under optimized conditions is characterized by a concentration range of 0.05 to 1150 nM, and a low detection limit of 10 pM.

Electrochemical sensors have seen various innovations, as highlighted by recent studies [46-52]. The literature review conducted for this research focuses on implementing a specific and unique combination of materials tailored for DOX detection. Although all these studies valuably contribute to the field, none investigate the approach proposed in this manuscript: a polymer-modified screen-printed electrode as a sensing substrate designed for sensitive and repeatable DOX detection. Our simple, cost-effective modification offers improved sensitivity and is optimized specifically for targeted DOX applications. The advantages of our developed sensor underscore the originality of our approach, presenting a novel and practical pathway in the electrochemical detection of pharmaceuticals.

In this study, we investigated graphene-based screen-printed electrodes (SPEs) modified with polymers for the detection of DOX in a simulated biological matrix. The bare graphene SPEs were surface-modified using chitosan and polyvinylidene fluoride (PVDF) and their electrochemical performance was compared to that of commercial graphene SPEs. This paper presents a comparative analysis of the electrochemical and physical properties of the polymer-modified graphene SPEs, aiming to develop a simple electrochemical sensor for detecting clinical concentrations of DOX.

Experimental

Commercially available SPEs, based on graphene (G) (model DS1100) were purchased from Dropsens Ltd, Llanera, Asturias, Spain, and further modified with polymeric coatings.

All chemicals used were of analytical grade and used without further purification. Biocompatible natural polymer chitosan (Ch) and electroactive polymer polyvinylidene fluoride (PVDF), purchased from Sigma Aldrich, were used as electrode modifiers. PVDF was dissolved in N,N-dimethylacetamide at 2 wt.% concentration, deposited onto the surface of the commercial graphene SPE, and allowed to dry at room temperature. The same preparation method was used for the chitosan 2 wt.% solution.

Doxorubicin hydrochloride was purchased as Adrimisin $^{\circ}$, Saba (2 mg mL $^{-1}$) from a local pharmacy. The pure powdered active pharmaceutical ingredient was dissolved in distilled water to a concentration of 0.01 mol L $^{-1}$. 0.1 mol L $^{-1}$ phosphate buffer saline (PBS) was prepared following the method given in European Pharmacopoeia 11.0 (4014300), using sodium dihydrogen phosphate and disodium hydrogen phosphate dihydrate. The PBS was adjusted to pH 6.7 to simulate the normal human blood pH range. The electrolyte for the electrochemical measurements was prepared by adding a corresponding amount of the dissolved DOX solution to 20 mL of PBS, with a final concentration of 0.002 mol L $^{-1}$. A calibration curve constructed from 1.5 to 7.4 µmol L $^{-1}$ was used to estimate the limit of detection (LOD) and quantification (LOQ). LOD and LOQ were calculated based on S/N = 3 and S/N = 10, respectively. All electrochemical measurements were performed in triplicate at 25 °C by immersing the SPEs in the electrolyte solution. Figure 4 shows good contact between the solution and the three-electrode system.

The electrochemical behavior of the modified electrodes towards DOX was investigated by cyclic voltammetry (CV). The experimental setup of the electrochemical measurements is shown in Figure 2. All CV measurements were obtained in the potential range from -0.05 to +0.6 V, under automatic current, with 5 scans. Various scan rates (20, 50, 100, 200, and 300 mV s⁻¹) were employed for the determination of the electroanalytical parameters related to the DOX's oxidation/reduction processes: the rate-determining step (adsorption or diffusion), electrochemical mechanism (Tafel's

slope b, charge transfer coefficient α , and number of transferred electrons n), and double-layer capacitance C_{dl} . After an optimization process, the scan rate range was carefully chosen to balance the sensitivity and stability of the redox signals for DOX. Lower scan rates (e.g., 10 mV s⁻¹) could result in a prolonged analysis and might increase the potential for adsorptive interference, while higher scan rates (e.g., 400 mV s⁻¹) may cause peak broadening or shift due to kinetic limitations and potential electrode surface effects. Thus, the chosen range provides robust, reproducible data while maintaining adequate signal clarity. The measurements were performed at room temperature, using the potentiostat/galvanostat SPELEC "Dropsens", Spain, operated with the Dropview software.

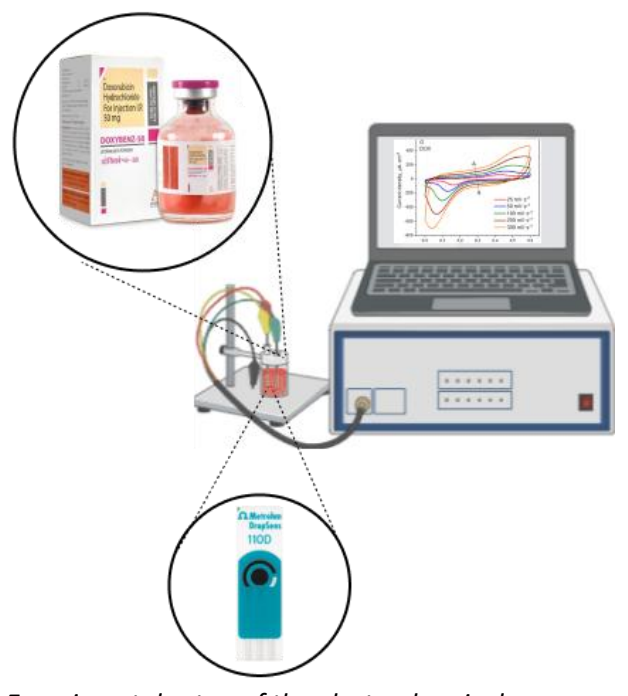


Figure 2. Experimental setup of the electrochemical measurements

Physical characterization of the SPEs was performed by scanning electron microscopy (SEM). The surface morphology of the SPEs was analyzed with FEI Quanta 2000 SEM, using a secondary electron detector and acceleration voltage of 30 kV, under a high vacuum. Before and after CV measurements, the electrolyte was investigated using UV-Vis spectroscopy. UV-Vis measurements were conducted using a Spectroquant Prove 600 spectrophotometer within a wavelength scan range of 200-800 nm.

Results and discussion

Electrochemical detection of doxorubicin hydrochloride

The electrochemical profile of the modified SPEs and their sensitivity towards DOX were followed by CV in 0.1 mol L⁻¹ PBS with pH 6.7. Three SPE systems were investigated, including commercial graphene (G), chitosan-modified graphene (G/Ch), and PVDF-modified graphene SPE (G/PVDF). The characteristic cyclic voltammograms of the tested electrodes, in 0.1 mol L⁻¹ PBS and 0.002 mol L⁻¹ DOX solution, are shown in Figure 3a and 3b, respectively. Additionally, Figures 3c, 3d, and 3e display the individual voltammograms as a correlation between the current density (j) and the potential (E), along with the calculated values for the oxidation peak potential ($P_{ox.}$), reduction peak potential ($P_{red.}$), and peak-to-peak separation potential ($P_{ox.}$). All voltammograms were scanned in the potential range of -0.05 to 0.6 V at a scan rate of 25 mV s⁻¹.

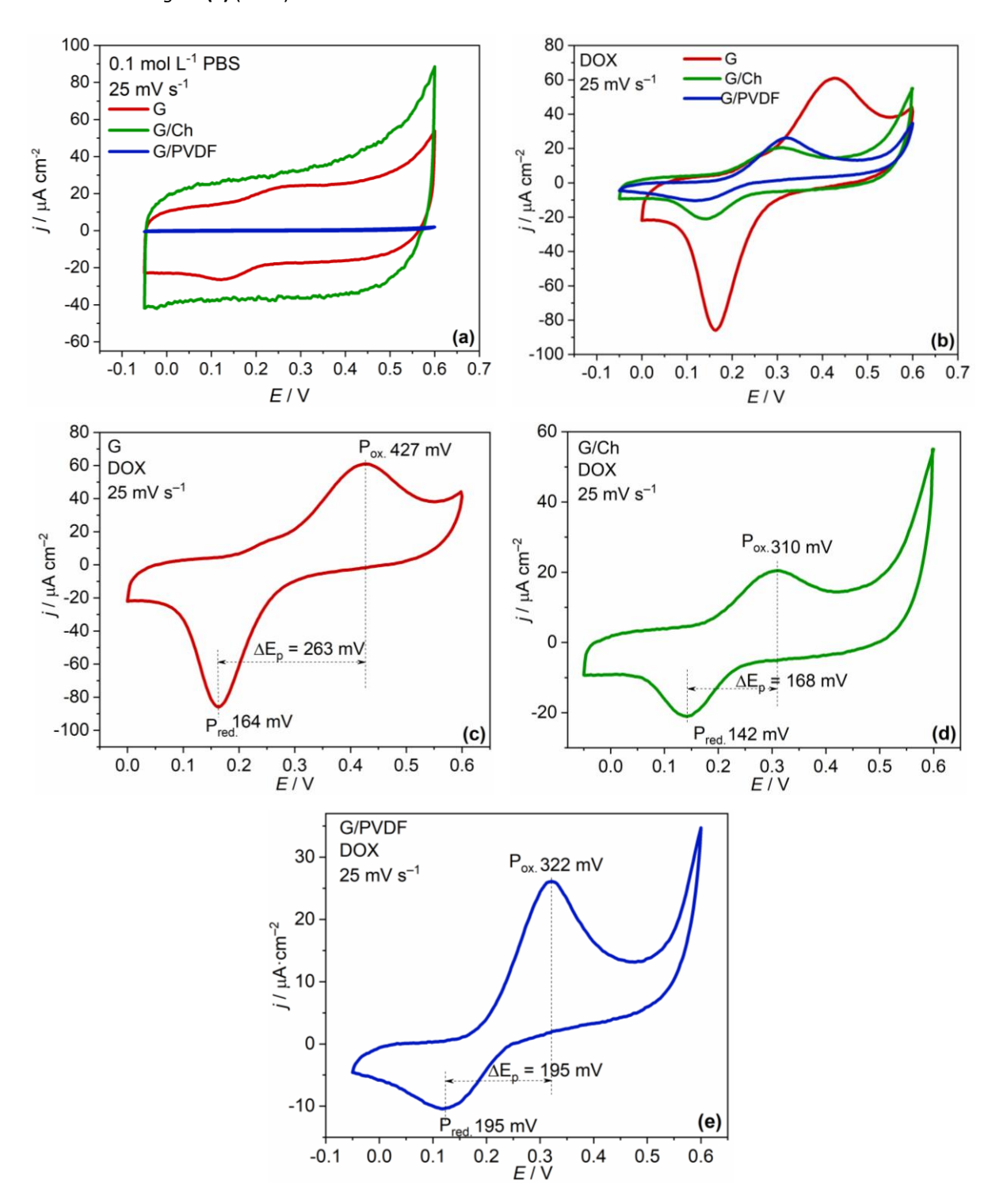


Figure 3. Electrochemical detection of DOX. Tested SPEs' cyclic voltammograms comparison in (a) 0.1 mol L⁻¹ PBS and (b) 0.002 mol L⁻¹ DOX solution. Electrochemical parameters were calculated for (c) commercial graphene electrode; (d) chitosan-modified electrode and (e) PVDF-modified electrode in 0.002 mol L⁻¹ DOX solution.

The voltammograms in Figure 3a correspond to the measurements done in 0.1 mol L⁻¹ PBS solution. The absence of peaks in PBS suggests that the electrolyte solution does not contain redoxactive species under the applied experimental conditions. PBS, being a buffer, is commonly used as a background electrolyte because it does not contain electroactive compounds that undergo oxidation or reduction at the applied potential range. The lack of peaks confirms that the SPEs exhibit minimal background current in PBS, ensuring a stable measurement baseline and a clear

distinction between the background response and any electrochemical signals that may appear upon adding an analyte, such as DOX.

Two characteristic current peaks are observed in the electrochemical spectrum of the tested SPEs in the 0.002 mol L⁻¹ DOX solution (Figure 3b), originating from the analyte. The peak labeled as $P_{\text{ox.}}$ in the anodic region of the voltammogram corresponds to DOX's oxidation, while the peak labeled $P_{\text{red.}}$ in the cathodic region corresponds to DOX's reverse reaction of reduction. This indicates a reversible reaction on the electrode surface, which can proceed in both directions, as shown in Figure 4 [53].

Figure 4. Electrochemical oxidation of doxorubicin

The reversibility of this reaction is contingent upon the electrode in which it takes place. The reaction is fully reversible when the oxidation (Pox.) and reduction (Pred.) peaks are situated at the same potential and exhibit equal intensities. Conversely, if the peak potentials are disparate and their intensities vary, the reversibility is substantially reduced.

Upon comparing the obtained voltammograms, it is evident that the commercial graphene SPE (G) exhibits the strongest current response, which is expected according to the literature and may be ascribed to the superior conductivity and large surface area of graphene [54,55]. The commercial graphene SPE exhibited the most prominent anodic peak, attributed to its electrocatalytic effect and higher background current [56]. In addition, the oxidation ($P_{ox.}$) peaked at 427 mV, surpassing the values of other modified electrodes by over 100 mV. Moreover, the potential difference between the anodic (oxidation) and cathodic (reduction) peaks, also known as peak-to-peak separation potential (ΔE_p), showed a significant increase compared to other systems, reaching 263 mV. This indicates that the DOX oxidation reaction on the commercial graphene SPE is less reversible [57-59]. The polymer-modified graphene SPEs with chitosan (G/Ch) and polyvinylidene fluoride (G/PVDF), demonstrate satisfactory electrochemical responses in comparison to the commercial graphene electrode. The intensified current density of the peaks $(j_{Pox.} = 20.5 \,\mu\text{A cm}^{-2} \,\text{for G/Ch})$ and $j_{Pox.} = 26 \,\mu\text{A cm}^{-2} \,\text{for}$ G/PVDF), lower potentials at which they appear ($E_{P_{\text{ox.}}}$ = 310 mV for G/Ch and $E_{P_{\text{ox.}}}$ = 322 mV for G/PVDF), and smaller peak-to-peak separation potentials ($\Delta E_p = 168$ mV for G/Ch and $\Delta E_p = 195$ mV for G/PVDF) indicate a faster and more reversible electron exchange in the redox reaction shown in Figure 4 [57]. This is mainly attributed to the strong interaction of DOX with G/Ch and G/PVDF. DOX, having an aromatic structure, can interact with graphene through π - π and hydrophobic interactions, chitosan through hydrophobic and electrostatic interactions, and PVDF through surface adsorption [57,60,61]. The interaction mechanism between the surface-modified electrodes and DOX typically relies on functional groups' reactions through hydrogen bonding, van der Waals forces, and hydrophobic interactions.

After comparing the modified sensor electrodes, it can be concluded that the G/PVDF system exhibits a slightly stronger current response over the G/Ch system (26 compared to 20.5 μ A cm⁻²). Conversely, the G/Ch system has the advantage of a lower potential for the oxidation reaction of

DOX (310 mV compared to 322 mV) and a smaller ΔE_p (168 mV compared to 195 mV), indicating a relatively higher reversibility of the reaction.

The quantitative determination of DOX was performed under optimal conditions. A range of increasing DOX concentrations (1.5 to 7.4 μ mol L⁻¹) was used to establish the relationship between the concentration and the analytical signal, and this data was used for calibration curve construction. The sensitivity, LOD, and LOQ were also calculated from the calibration data.

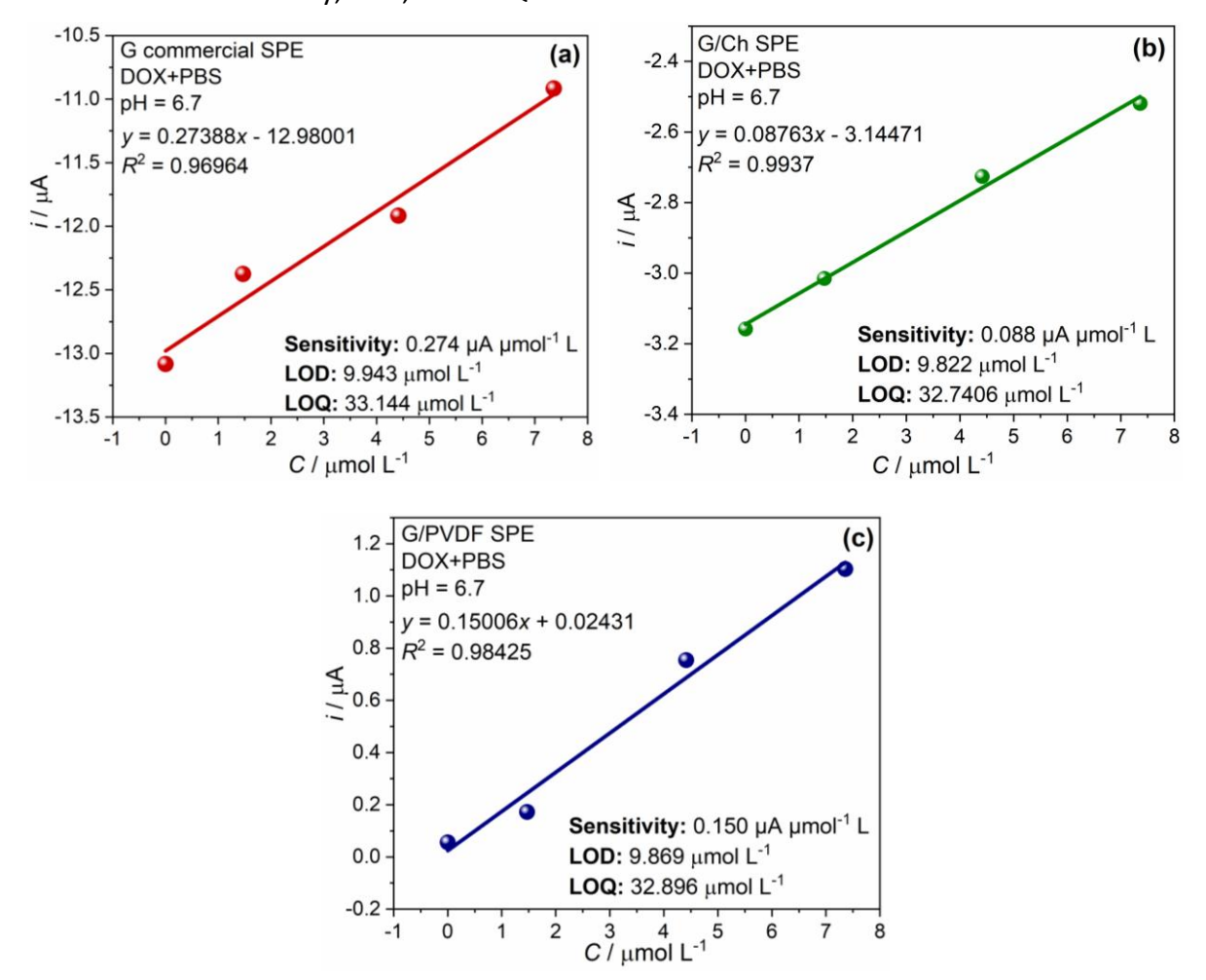


Figure 5. Linear correspondence between the current and DOX's concentration for the (a) commercial graphene electrode; (b) chitosan-modified electrode and (c) PVDF-modified electrode

Figure 5 illustrates the linear correlation between DOX concentration and the oxidation peak current for commercial and modified SPEs across various DOX concentrations. The modified electrodes exhibit strong linearity, with the chitosan-modified SPE showing the highest linear correlation, as described by $i_{ox.} = 0.08763C - 3.14471$ ($R^2 = 0.9937$). The PVDF-modified electrode follows a linear equation of $i_{ox.} = 0.15006C + 0.02431$ ($R^2 = 0.98425$). For comparison, the commercial, unmodified graphene SPE displays a linear relationship of $i_{ox.} = 0.27388C - 12.98001$ ($R^2 = 0.96964$). These results highlight the improved electrochemical performance and linearity of the modified sensors, particularly the chitosan modification.

The sensitivity was determined to be 0.088 μ A μ mol⁻¹ L for the chitosan-modified and 0.150 μ A μ mol⁻¹ L for the PVDF-modified SPE, compared to a slope of 0.274 μ A μ mol⁻¹ L for the commercial electrode. Additionally, LOD and LOQ were calculated within the same concentration range used for linear correlation. The chitosan-modified SPE achieved the lowest LOD and LOQ among the electrodes, with values of 9.822 and 32.7406 μ mol L⁻¹, respectively. For the PVDF-modified SPE, the

LOD and LOQ were calculated to be 9.869 and 32.896 μ mol L⁻¹, respectively, showing moderate sensitivity compared to the chitosan-modified electrode. The commercial electrode had the highest LOD and LOQ values, at 9.943 and 33.144 μ mol L⁻¹, respectively. The results focus on the chitosan-modified SPE exhibiting the lowest detection and quantification limits, indicating its superior sensitivity among the tested electrodes.

Kinetic analysis and electrochemical mechanism determination of DOX's oxidation

Cyclic voltammograms scanned at different scan rates can usually be used for kinetic analysis of the oxidation process of DOX. The dependence of the current density at the oxidation peak $P_{\text{ox.}}$ on the scan rate can serve as a criterion for determining the reaction mechanism, specifically to identify the slow step of DOX oxidation, known as the rate-determining step. This helps to determine whether the reaction is controlled by an adsorption or a diffusion process of the reactants participating in the reaction. Figure 6 shows the voltammograms for both the commercial and polymer-modified SPEs.

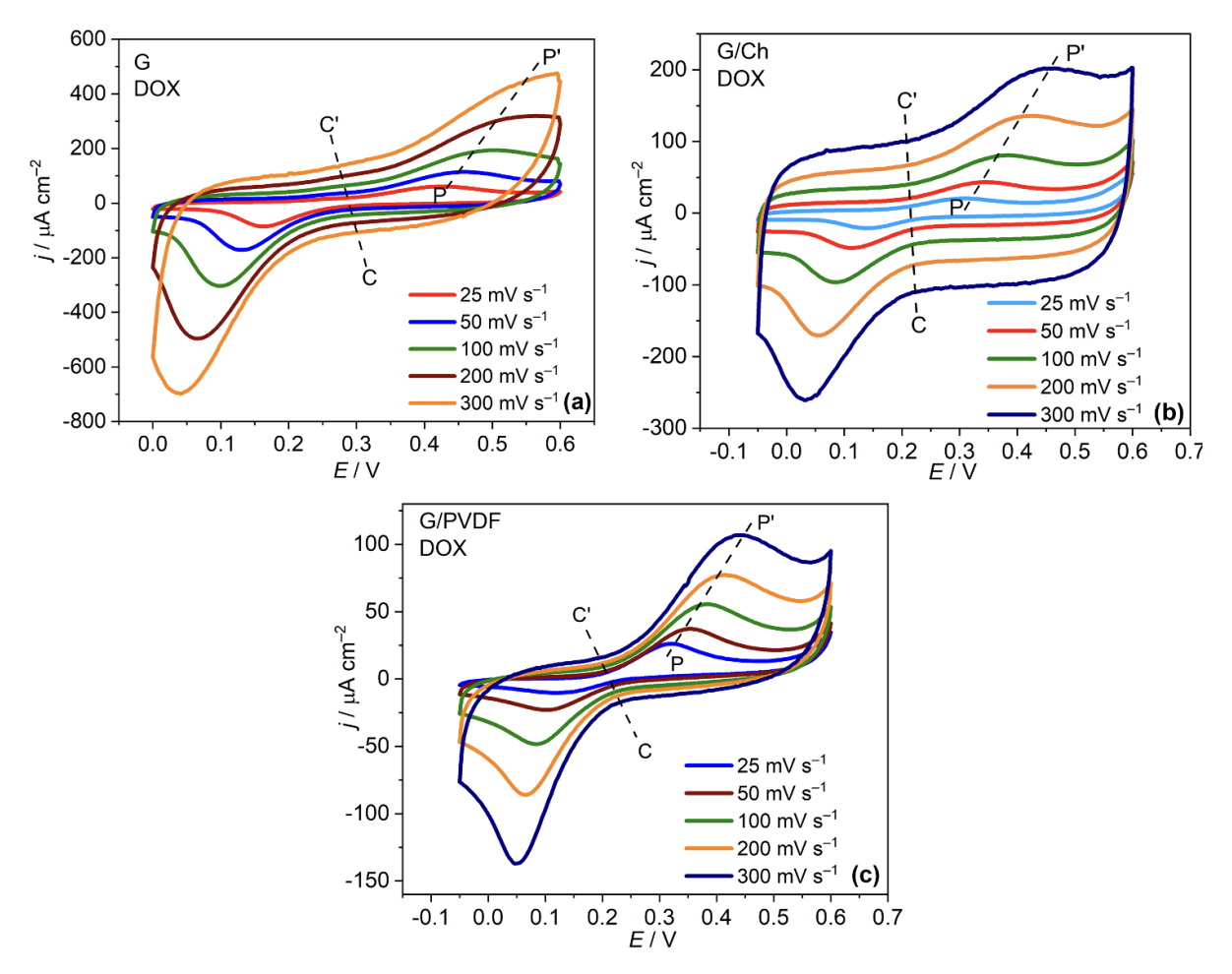


Figure 6. Cyclic voltammograms scanned at various scan rates for scan rate influence and kinetic analysis of the oxidation process of DOX onto (a) commercial G; (b) G/Ch and (c) G/PVDF modified electrode surface

As the scan rate increases while testing the electrodes, the current density of all peaks increases. Moreover, the corresponding oxidation peak potentials shift towards the anodic direction (positive potential), while the reduction peaks shift towards the cathodic direction (negative potential).

The criteria for determining the rate-determining step of the electrochemical oxidation of DOX could be $j_{P_{\text{OX.}}}$ vs. v, $j_{P_{\text{OX.}}}$ vs. $v^{1/2}$, and $\log j_{P_{\text{OX.}}}$ vs. $\log v$ plots are derived from the cyclic voltammograms shown in Figure 5 at the intersection line P-P'. The most eligible and confident criterion is the

 $\log j_{P_{\rm OX.}} vs. \log v$ plot [62,63]. The value of the linear slope is the criterion for the rate-determining step of the reaction. If it is less than 0.5, the rate-determining step is the diffusion of the reactants, and if it is greater than 0.5, then the rate-determining step is adsorption [62,64]. The plots and the calculation for the limiting step are presented in Figure 7.

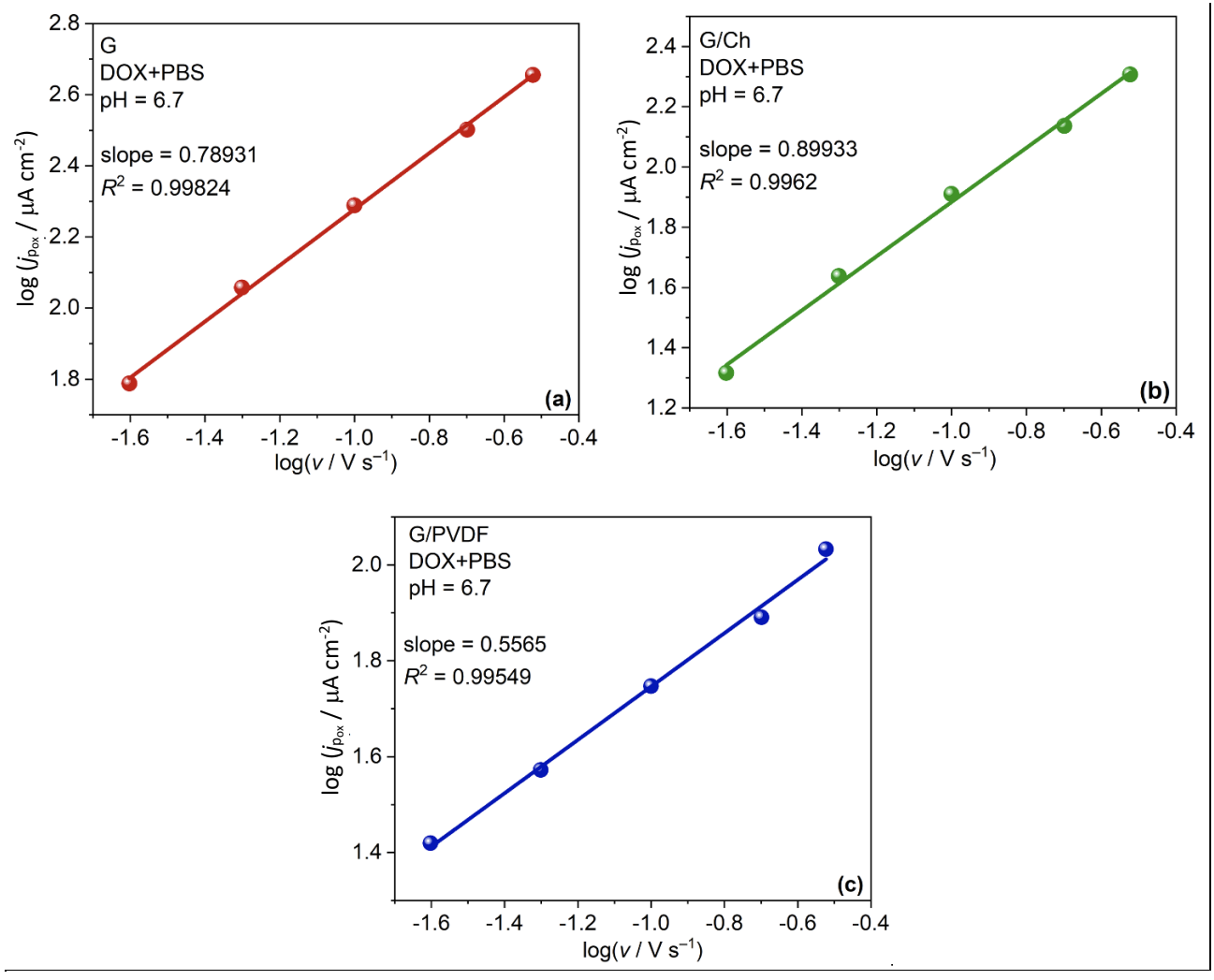


Figure 7. Linear dependence of log j_{Pox.} vs. log v for (a) commercial G; (b) G/Ch and (c) G/PVDF SPEs

The linear dependence of all three plots is characterized by a very high correlation (>0.99). The slope for the commercial graphene and the chitosan-modified electrode has a calculated value of 0.789 (Figure 7a) and 0.899 (Figure 7b), respectively, unambiguously indicating that the rate-determining step of both processes is adsorption [65]. The PVDF-modified SPE has a slope value of 0.556 (Figure 7c), slightly higher than the boundary criterion, implying an adsorption or mixed control process [66,67].

The linear dependence between the potential (E_{Pox}) of the oxidation current maximum $(P_{ox.})$ and the logarithm of the scan rate (log v) can be used to determine the electrochemical mechanism of the process, such as Tafel slope (b) and the number of exchanged electrons (n). The Tafel slope can be calculated using the Eq. (1) and (2) [68,69]:

$$E_{P_{\text{ox}}} = \frac{b}{2} \log v + \text{const.} \tag{1}$$

$$\frac{\mathrm{d}E_{P_{\mathrm{ox}}}}{\mathrm{d}\log v} = \frac{b}{2} \tag{2}$$

The constant term (const.) in Eq. 1 represents the integration constant, as this equation describes the integral relationship between the oxidation potential (E_{Pox}) and the logarithm of the scan rate (log v). In Eq. (2), which depicts the differential form of this relationship, the constant term is not applicable and has been removed to reflect the correct mathematical representation.

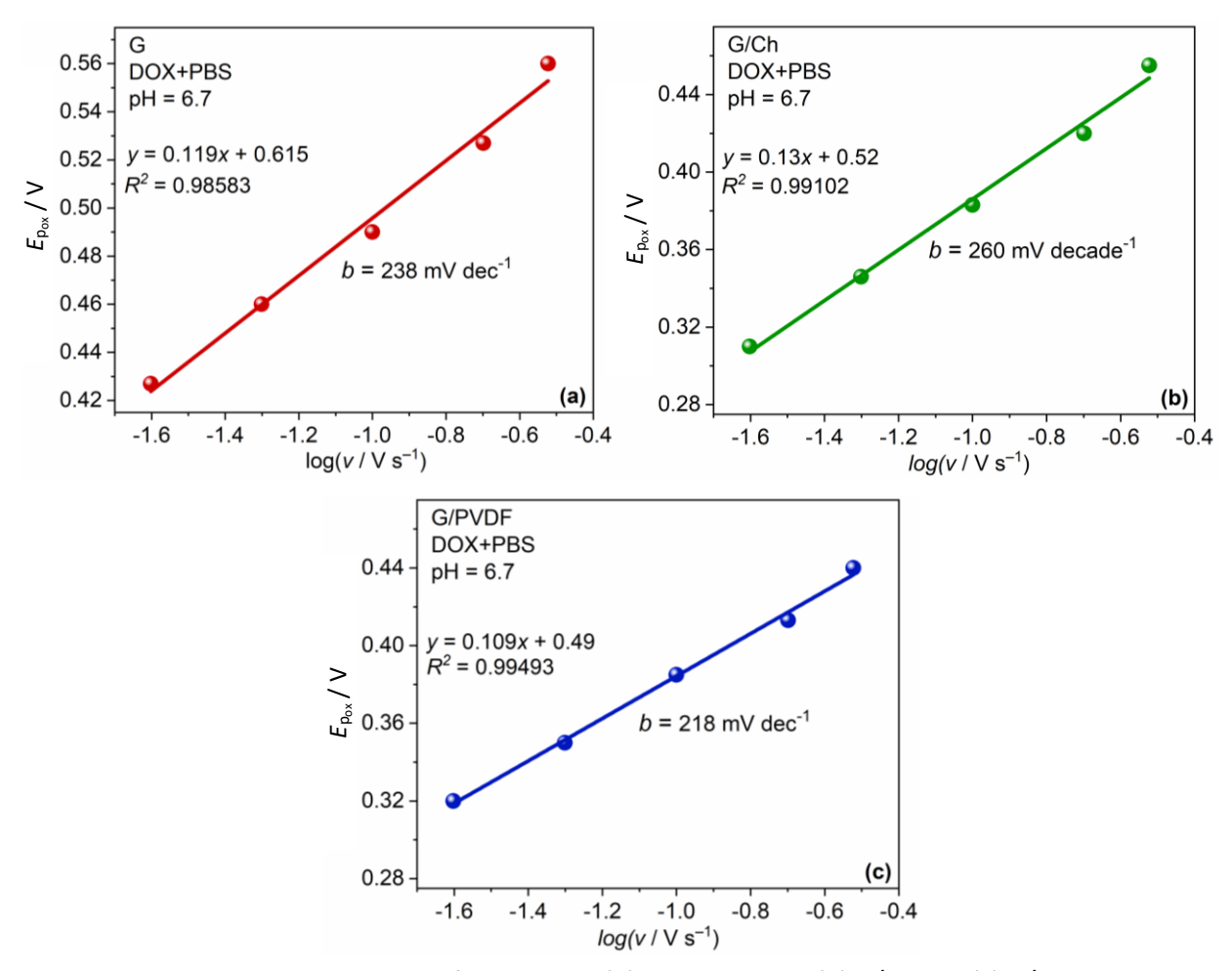


Figure 8. Linear dependence of E_{Pox} vs. logv (a) commercial G; (b) G/Ch and (c) G/PVDF SPE

Figure 8 presents the E_{Pox} and log v dependence for the studied systems and the linear equation for each system is given in the plots. Tafel's slope values calculated using the data from the plots are 238 mV dec⁻¹ for the commercial graphene, 260 mV dec⁻¹ for the chitosan-modified, and 218 mV dec⁻¹ for the PVDF-modified SPE. The values are shown in Table 1.

To calculate the number of transferred electrons, n, firstly, the charge transferred, q, needs to be calculated using the Eq. (3) [63]:

$$q = \frac{2.303 \ k_{\rm B}T}{b \alpha} \tag{3}$$

where k_B is the Boltzmann constant (1.38×10⁻²³ J K⁻¹) and T is the temperature of 298 K. The electron transfer coefficient, α , can be calculated using the Eq. (4) [70]:

$$\alpha = \frac{2.303RT}{bF} \tag{4}$$

where R is the universal gas constant (8.134 J K⁻¹ mol⁻¹), and F is the Faraday constant (96485 C mol⁻¹). Finally, the number of transferred electrons, n, was calculated using the Eq. (5):

$$n = \frac{q}{1.6 \times 10^{-19}} \tag{5}$$

where the value 1.6×10^{-19} corresponds to the charge of one electron. The electrochemical oxidation of DOX involves an exchange of one electron for all three systems. All calculated values are shown in Table 1. The estimated values for the Tafel slope of graphene SPEs correlate with the literature data for the electrochemical oxidation of DOX in the range between 210 and 260 mV dec⁻¹ [71]. These values indicate that the one-electron transfer process is the determining step in the electrochemical oxidation of DOX for all studied systems.

Table 1. Electrochemical parameters (Tafel slope (b), electron transfer coefficient (α), number of transferred electrons (n)) calculated for all three studied systems

Electrode	b / mV dec ⁻¹	α	n
G	238	0.25	1
G/Ch	260	0.23	1
G/PVDF	218	0.27	1

Double-layer capacitance

The double-layer capacitance ($C_{\rm dl}$) is intricately linked to the actual surface area of the electrodes. It can be calculated from the cyclic voltammograms shown in Figure 6. At the intersection C-C', in the region where the electrochemical double layer charge and discharge, a log $C_{\rm dl}$ vs. v plot can be derived. $C_{\rm dl}$ can be calculated using Eq. (6) [72]:

$$C_{\rm dl} = \frac{\mathrm{d}j_{cap.}}{\mathrm{d}\left(\frac{\partial E}{\partial t}\right)} = \frac{\mathrm{d}j_{\rm cap.}}{v} \tag{6}$$

where E is the potential, v is the scan rate and $j_{\text{cap.}}$ is the capacitance current density, calculated as the average value of the absolute values of the anodic and cathodic currents densities at the C-C' intersection potential points, or following Eq. (7):

$$j_{\text{cap.}} = \frac{\left|j_{\text{cat.}}\right| + \left|j_{\text{anod.}}\right|}{2} \tag{7}$$

The change of the capacitance current density with the scan rate (j_{cap} . vs. v) exhibits a strong linear dependence, as presented in Figure 9.

The slope of this linear dependence determines the double-layer capacity, $C_{\rm dl}$, summarized in Table 2.

Table 2. Double-layer capacitance calculated values for the studied systems

Electrode	C _{dl} / mF cm ⁻²
G	0.384
G/Ch	0.338
G/PVDF	0.046

The commercial G electrode exhibits the highest double-layer capacitance of 0.384 mF cm⁻², indicating the greatest surface roughness (largest active surface), as confirmed by the SEM analysis. However, the capacitance decreases after the electrode is coated with either chitosan or PVDF, with the values calculated as 0.338 and 0.046 mF cm⁻², respectively. In the case of the chitosan-modified SPE, the reduction in capacitance is not significant. It is somewhat comparable to the commercial electrode, while it is more pronounced for the one modified with PVDF. The addition of PVDF to the surface results in graphene flakes being visibly covered with polymer clusters in the form of spherical particles.

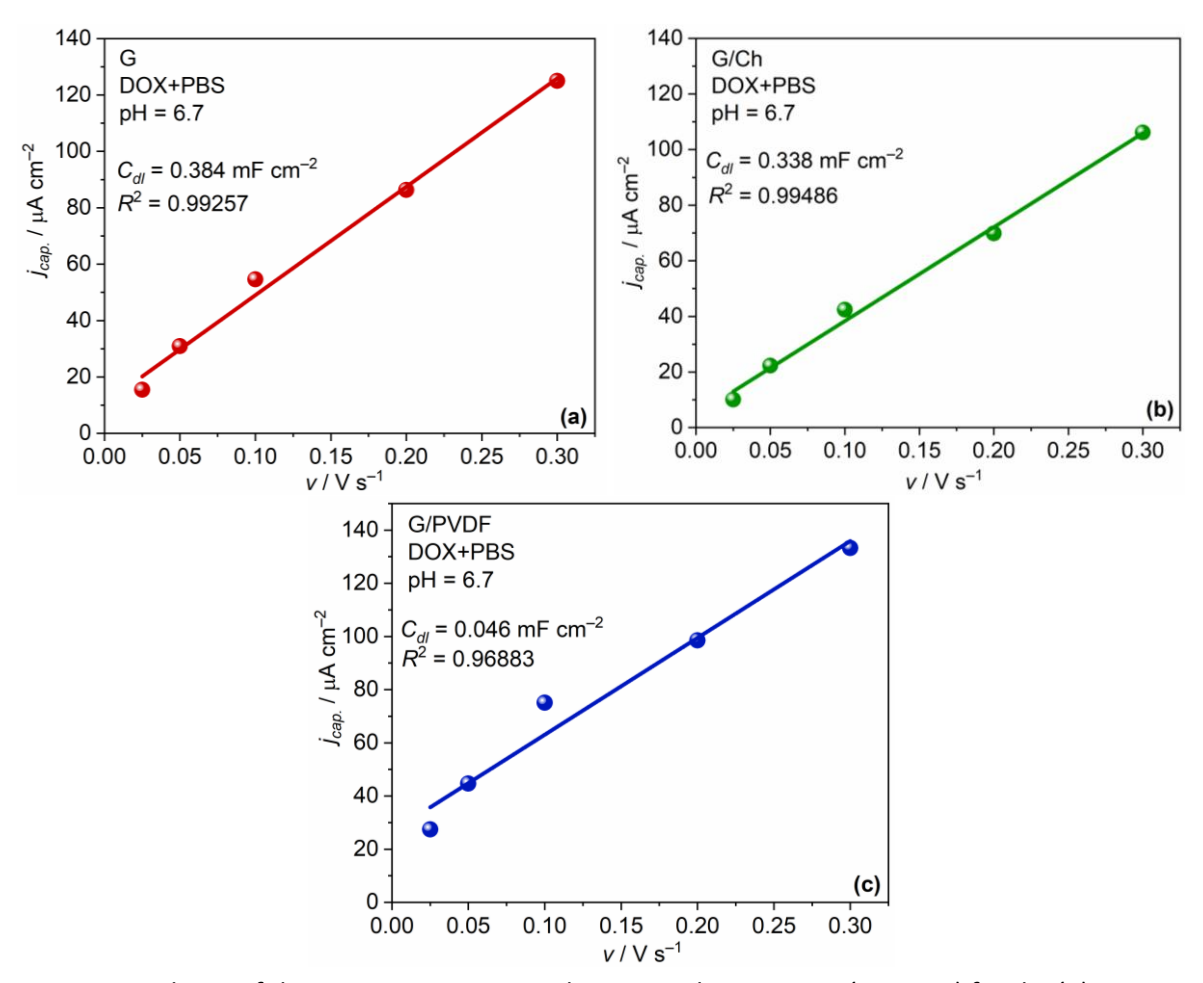


Figure 9. Dependence of the capacitance current density on the scan rate ($j_{cap.}$ vs. v) for the (a) commercial G, (b) G/Ch, and (c) G/PVDF SPE

The PVDF spherical particles appear to surround the graphene, filling the vacancies and leading to reduced surface porosity. This suggests a substantial reduction in surface roughness upon PVDF incorporation.

Repeatability, stability and reproducibility

The repeatability of the modified electrochemical sensors' response was assessed using 10 consecutive CV measurements to detect 0.002 mol L⁻¹ DOX in 0.1 mol L⁻¹ PBS at pH 6.7. The relative standard deviation (RSD) values obtained for triplicate experiments were 3.6 % for the chitosan-modified and 4.9 % for the PVDF-modified SPE, indicating reliable repeatability. Sensor stability was further evaluated by recording CV signals of 0.002 mol L⁻¹ DOX over seven days. After one week, the chitosan-modified electrode exhibited a 10.2 % decrease in oxidation peak current from the initial values, demonstrating good long-term stability. The PVDF-modified SPE retained 86.0 % of its initial current response over the same period. After each use, the SPEs were rinsed thoroughly with 0.1 mol L⁻¹ PBS and distilled water and then air-dried at room temperature. These results highlight the stability of the modifications, reflecting not only strong analytical performance but also enhanced physical protection of the working electrode. The findings suggest that, with appropriate handling, these electrodes can be reused despite the manufacturer Metrohm DropSens recommending them as disposable, single-use platforms for optimal performance. Reproducibility, indicating the precision of the modified electrodes, was investigated by testing three separate electrodes from each modification for 0.002 mol L⁻¹ DOX detection, resulting in RSD values of 4.1 %

and 5.0 % for the chitosan and PVDF-modified SPE, respectively. These findings confirm that both modifications provide stable and repeatable measurements for DOX detection.

Physical characterization

SEM was used as a powerful visual technique to obtain detailed information about the electrodes' morphology and surface characteristics. The micrographs shown in Figure 10 present the commercial (10a and 10b), PVDF (10c and 10d), and Ch-modified (10e and 10f) graphene electrodes, respectively.

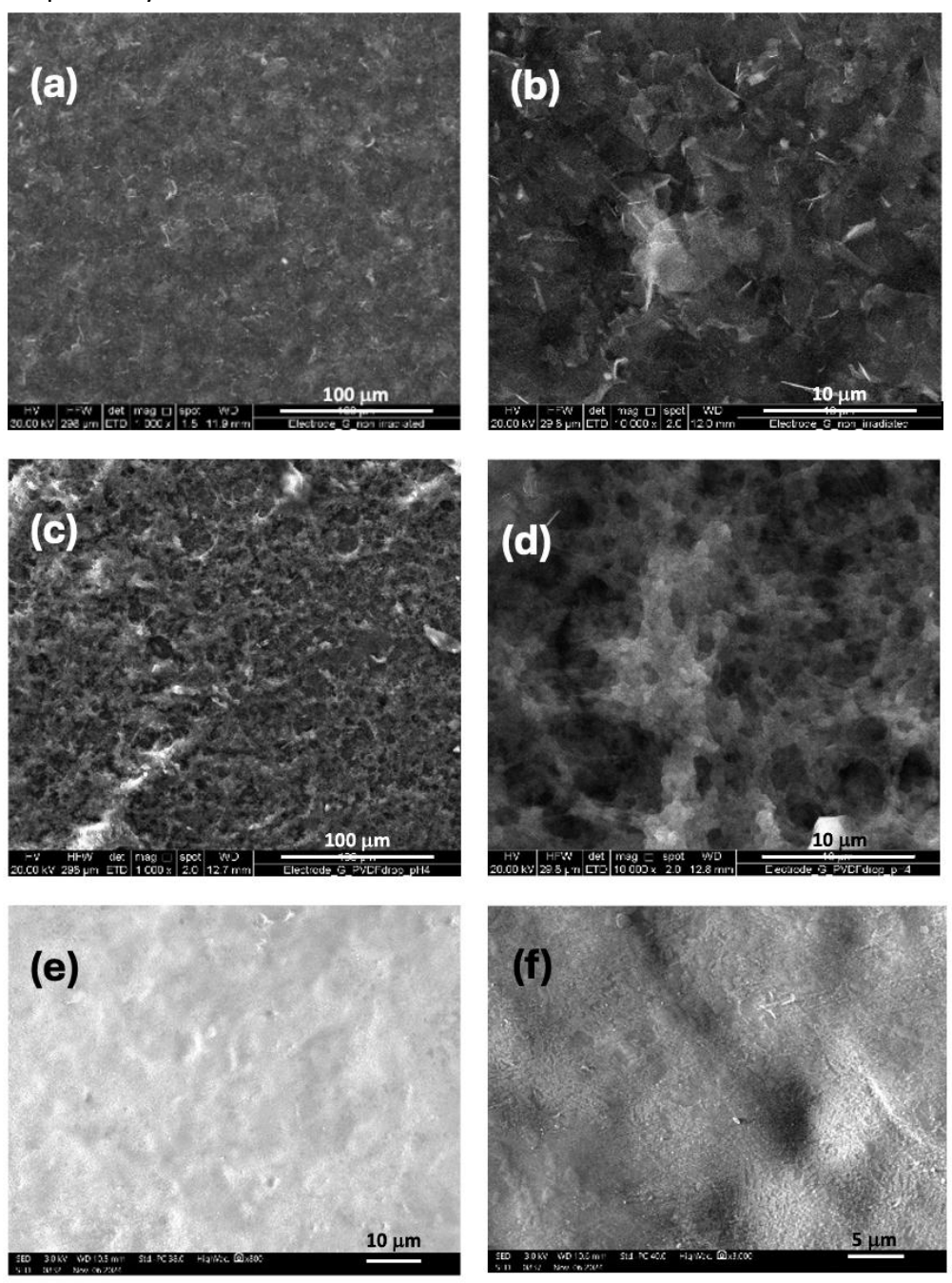


Figure 10. SEM micrographs of a commercial G electrode under (a) $1000 \times$ and (b) $10\,000 \times$ magnification, PVDF-modified electrode under (c) $1000 \times$ and (d) $10\,000 \times$ magnification, and chitosan-modified electrode under (e) $800 \times$ and (f) $6000 \times$ magnification

The micrographs of the commercial SPE observed with a magnification of $1000 \times$ (Figure 10a) and $10000 \times$ (Figure 10b) depict the characteristic structure of the graphene, revealing layers of graphene

flakes with irregular structure and random orientation. This results in a working electrode with a rough surface and a large active area, two strongly favorable properties in the electrochemical sensor design. The micrographs of the PVDF-modified graphene electrode under magnification of $1000 \times$ (Figure 10c) and $10000 \times$ (Figure 10d) reveal the fibrous structure of the polymer film. PDVF's deposition onto the electrode's surface adds porosity upon evaporation of the solvent, contributing to a larger active area and a better response while detecting the analyte, thus enhancing the sensor's performance. The chitosan-modified graphene SPE demonstrates a uniform and continuous polymer film, as shown in the micrographs in Figures 10e and 10f. The chitosan coating fully covers the rough graphene surface, conforming closely to its heterogeneous morphology, indicating a strong interaction between the chitosan film and the graphene substrate. The microroughness observed in the micrograph taken at higher magnification provides potential adsorption sites, enhancing the electrode's effectiveness in detecting DOX. This morphology supports the interaction mechanism based on adsorption, highlighting the superiority of this electrode for DOX detection.

The electrolyte solution used for the CV measurements (0.002 mol L⁻¹ DOX in 0.1 mol L⁻¹ PBS, pH 6.7) was studied using ultraviolet-visible (UV-Vis) spectroscopy. The absorbance measurements and their corresponding spectra before and after exposing the electrolyte to the voltammetric measurements (to at least nine consecutive measurements - three electrodes tested in triplicates) are given in Figure 11. The analysis suggests that the electrolyte solution undergoes changes induced by the current when the electrochemical response is monitored through cyclic voltammetry. A current-induced change in the absorption of the solution at a wavelength of 482 nm was noted as a decrease from 2.75 to 1.58. While DOX generally undergoes reversible redox processes (discussed in the Electrochemical detection part), the observed decrease in absorption could indicate partial or temporary adsorption of DOX onto the electrode surface, resulting in lower solution concentration. This absorption correlates to the interaction mechanism of DOX with the SPE. For further clarification, the maximal absorbance wavelengths for both redox forms of DOX are 485 nm for the oxidized and 480 to 490 nm for the reduced form, depending on the environmental conditions [73-75]. The maximal excitation noted in Figure 11 corresponds to the DOX's oxidized form rather than the product of reduction - doxorubicinol.

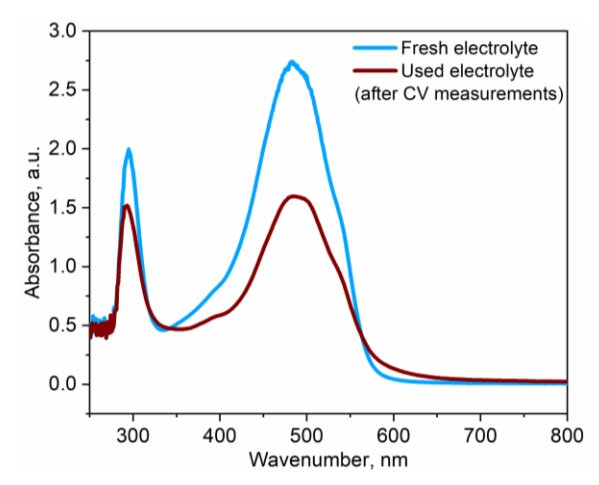


Figure 11. UV-Vis spectra of 0.1M PBS solution (pH 6.7)

Conclusions

Simple electrochemical sensors based on screen-printed graphene electrodes were applied to detect a chemotherapy medication, doxorubicin hydrochloride, in a simulated biological environment with pH 6.7. While studies in the literature contribute to the field, no other researcher investigated the proposed polymer-modified sensor, underscoring its novelty. Our simple design

approach consists of a screen-printed electrode platform, modified by drop deposition of chitosan and PVDF as thin polymeric films onto the electrode's surface. The electrochemical reactivity and performance of the electrodes were tested and compared to the commercial graphene SPE using cyclic voltammetry. The presence of DOX in the solutions induced characteristic redox peaks in the voltammograms and led to the appearance of a reversible reaction. Polymer-modified graphene electrodes exhibited a broad current intensity and achieved the desired rectangular form in the voltammograms due to their exceptional electrical properties. The electrochemical behavior confirmed that both modified electrodes displayed excellent electrochemical properties for the determination and monitoring of DOX, with a promising application in the field of pharmaceutical drug detection. However, according to the thoroughly conducted electrochemical analysis, the chitosan-modified electrode exhibits superior properties compared to the PVDF-modified one, such as lower Pox., higher reversibility, lower LOD and LOQ, and higher double-layer capacitance i.e., larger active surface area. The electrodes demonstrated excellent repeatability, stability, and reproducibility, confirming their suitability for sensitive DOX detection. The simplicity and costeffectiveness of the polymer-modified screen-printed electrodes make them promising candidates for pharmaceutical drug analysis and on-site in vivo diagnostics.

Conflict of interest: The authors declare no conflict of interest.

References

- [1] C. Carvalho, R. X. Santos, S. Cardoso, S. Correia, P. J. Oliveira, M. S. Santos, P. I. Moreira, Doxorubicin: the good, the bad and the ugly effect, *Current Medicinal Chemistry* **16(25)** (2009) 3267-3285 https://doi.org/10.2174/092986709788803312.
- [2] G. Minotti, S. Recalcati, A. Mordente, G. Liberi, A. M. Calafiore, C. Mancuso, P. Preziosi, G. Cairo, The secondary alcohol metabolite of doxorubicin irreversibly inactivates aconitase/iron regulatory protein-1 in cytosolic fractions from human myocardium. *Federation of American Societies for Experimental Biology Journal* **12(7)** (1998) 541-52 https://doi.org/10.1096/fasebj.12.7.541.
- [3] M. A. Mitry, J. G. Edwards, Doxorubicin induced heart failure: Phenotype and molecular mechanisms, International Journal of Cardiology Heart & Vasculature 10(17-24) (2016) 17-24 http://doi.org/10.1016/j.ijcha.2015.11.004.
- [4] J. H. Beijnen, P. L. Meenhorst, R. Van Gijn, M. Fromme, H. Rosing, W. J. M. Underberg, HPLC determination of doxorubicin, doxorubicinol and four aglycone metabolites in plasma of AIDS patients, *Journal of Pharmaceutical and Biomedical Analysis* 9(10-12) (1991) 995-1002 https://doi.org/10.1016/0731-7085(91)80036-9.
- [5] K. Alhareth, C. Vauthier, C. Gueutin, G. Ponchel, F. Moussa, HPLC quantification of doxorubicin in plasma and tissues of rats treated with doxorubicin loaded poly(alkylcyanoacrylate) nanoparticles, *Journal of Chromatography B* 887-888 (2012) 128-132 https://doi.org/10.1016/j.jchromb.2012.01.025.
- [6] S. Ahmed, N. Kishikawa, K. Ohyama, M. Wada, K. Nakashima, N. Kuroda, Selective determination of doxorubicin and doxorubicinol in rat plasma by HPLC with photosensitization reaction followed by chemiluminescence detection, *Talanta*, **78(1)** (2009) 94-100 https://doi.org/10.1016/j.talanta.2008.10.043.
- [7] C. Mazuel, J. Grove, G. Gerin, K. P. Keenan, HPLC-MS/MS determination of a peptide conjugate prodrug of doxorubicin, and its active metabolites, leucine-doxorubicin and doxorubicin, in dog and rat plasma, *Journal of Pharmaceutical and Biomedical Analysis*, **33(5)** (2003) 1093-1102 https://doi.org/10.1016/S0731-7085(03)00434-5.
- [8] A. S. Rodrigues and others, Development of an Analytical Methodology for Simultaneous Determination of Vincristine and Doxorubicin in Pharmaceutical Preparations for Oncology by HPLC—UV, Journal of Chromatographic Science, 47(5) 387-391 https://doi.org/10.1093/chromsci/47.5.387.
- [9] E. Configliacchi, G. Razzano, V. Rizzo, A. Vigevani, HPLC methods for the determination of bound and free doxorubicin, and of bound and free galactosamine, in methacrylamide polymer-drug conjugates,



- Journal of Pharmaceutical and Biomedical Analysis, **15(1)** (1996) 123-129 https://doi.org/10.1016/0731-7085(96)01825-0.
- [10] Q. Zhou, B. Chowbay, Determination of doxorubicin and its metabolites in rat serum and bile by LC: application to preclinical pharmacokinetic studies, *Journal of Pharmaceutical and Biomedical Analysis*, **30(4)** (2002), 1063-1074 https://doi.org/10.1016/S0731-7085(02)00442-9.
- [11] W. Ma, J. Wang, Q. Guo, P. Tu, Simultaneous determination of doxorubicin and curcumin in rat plasma by LC-MS/MS and its application to pharmacokinetic study, *Journal of Pharmaceutical and Biomedical Analysis* **111** (2015) https://doi.org/10.1016/j.jpba.2015.04.007.
- [12] Y. Xie, N. Shao, Y. Jin, L. Zhang, H. Jiang, N. Xiong, F. Su, H. Xu, Determination of non-liposomal and liposomal doxorubicin in plasma by LC-MS/MS coupled with an effective solid phase extraction: In comparison with ultrafiltration technique and application to a pharmacokinetic study, *Journal of Chromatography B* **1072** (2018) 149-160 https://doi.org/10.1016/j.jchromb.2017.11.020.
- [13] M. Janicka, A. Kot-Wasik, J.Paradziej-Łukowicz, G. Sularz-Peszyńska, A. Bartoszek, J. Namieśnik, LC-MS/MS Determination of Isoprostanes in Plasma Samples Collected from Mice Exposed to Doxorubicin or Tert-Butyl Hydroperoxide, *International Journal of Molecular Sciences* 14(3) (2013) 6157-6169 https://doi.org/10.3390/ijms14036157.
- [14] C. Bobin-Dubigeon and others, A New, Validated Wipe-Sampling Procedure Coupled to LC-MS Analysis for the Simultaneous Determination of 5-Fluorouracil, Doxorubicin and Cyclophosphamide in Surface Contamination, *Journal of Analytical Toxicology* **37(7)** (2013) 433-439 https://doi.org/10.1093/jat/bkt045.
- [15] S. Mazzucchelli, A. Ravelli, F. Gigli, M. Minoli, F. Corsi, P. Ciuffreda, R. Ottria, LC-MS/MS method development for quantification of doxorubicin and its metabolite 13-hydroxy doxorubicin in mice biological matrices: Application to a pharmaco-delivery study, *Biomedical Chromatography* **31(4)** 2017 https://doi.org/10.1002/bmc.3863.
- [16] I. Dimitrievska, P. Paunovic, A. Grozdanov, Recent advancements in nano sensors for air and water pollution control, *Material Science and Engineering* 7(2) (2023) 113–128 https://doi.org/10.15406/mseij.2023.07.00214.
- [17] M. Hossein Ghanbari, Z. Norouzi, A new nanostructure consisting of nitrogen-doped carbon nanoonions for an electrochemical sensor to the determination of doxorubicin, *Microchemical Journal* **157(9)** (2020) https://doi.org/10.1016/j.microc.2020.105098.
- [18] I. M. Apetrei, C. Apetrei, Voltammetric determination of melatonin using a graphene-based sensor in pharmaceutical products, *International Journal of Nanomedicine* 11 (2016) 1859-1866 https://doi.org/10.2147/IJN.S104941.
- [19] J. Soleymani, M. Hasanzadeh, M. Eskandani, M. Khoubnasabjafari, N. Shadjou, A. Jouyban, Electrochemical sensing of doxorubicin in unprocessed whole blood, cell lysate, and human plasma samples using thin film of poly-arginine modified glassy carbon electrode, *Materials Science and Engineering: C* 77 (2017) 790-802 https://doi.org/10.1016/j.msec.2017.03.257.
- [20] I. A. Mattioli, P. Cervini, É. T. G. Cavalheiro, Screen-printed disposable electrodes using graphite-polyurethane composites modified with magnetite and chitosan-coated magnetite nanoparticles for voltammetric epinephrine sensing: a comparative study, *Microchimica Acta* **187(6)** (2020) https://doi.org/10.1007/s00604-020-04259-x.
- [21] N. A. Negm, H. A. Abubshait, S. A. Abubshait, M. T. H. Abou Kana, E. A. Mohamed, M. M. Betiha, Performance of chitosan polymer as platform during sensors fabrication and sensing applications, International Journal of Biological Macromolecules 165 (2020) 402-435 https://doi.org/10.1016/j.ijbiomac.2020.09.13.
- [22] R. Dallaev, T. Pisarenko, D. Sobola, F. Orudzhev, S. Ramazanov, T. Trčka, Brief Review of PVDF Properties and Applications Potential, *Polymers* 14(22) (2022) 4793 https://doi.org/10.3390/polym14224793.
- [23] M. Sobhy, R. M. Khafagy, A. A. Soliman, *et al.*, Design of Biosensor Based on Graphene Oxide/ WO3/ Polyvinylidene Fluoride, *Optical and Quantum Electronics* **55** (2023) 789 https://doi.org/10.21203/rs.3.rs-2710142/v1.
- [24] H. Zhao, K. Shi, C. Zhang, J. Ren, M. Cui, N. Li, X. Ji, R. Wang, Spherical COFs decorated with gold nanoparticles and multiwalled carbon nanotubes as signal amplifier for sensitive electrochemical

- detection of doxorubicin, *Microchemical Journal* **182** (2022) https://doi.org/10.1016/j.microc.2022.107865.
- [25] M. Mehmandoust, Y. Khoshnavaz, F. Karimi, S. Çakar, M. Özacar, N. Erk, A novel 2-dimensional nanocomposite as a mediator for the determination of doxorubicin in biological samples, *Environmental Research* **213** (2022) https://doi.org/10.1016/j.envres.2022.113590.
- [26] M. Abbasi, M. Ezazi, A. Jouyban, E. Lulek, K. Asadpour-Zeynali, Y. Nuri Ertas, J. Houshyar, A. Mokhtarzadeh, A. Soleymani, An ultrasensitive and preprocessing-free electrochemical platform for the detection of doxorubicin based on tryptophan/polyethylene glycol-cobalt ferrite nanoparticles modified electrodes, *Microchemical Journal* 183 (2022) https://doi.org/10.102916/j.microc.2022.108055.
- [27] H. Guo, H. Jin, R. Gui, Z. Wang, J. Xia, F. Zhang, Electrodeposition one-step preparation of silver nanoparticles/carbon dots/reduced graphene oxide ternary dendritic nanocomposites for sensitive detection of doxorubicin, *Sensors and Actuators B: Chemical* **253** (2017) 50-57 https://doi.org/10.1016/j.snb.2017.06.095.
- [28] D. M. Stanković, Z. Milanović, L. Švorc, V. Stanković, D. Janković, M. Mirković, S. Vranješ Đurić, Screen printed diamond electrode as efficient "point-of-care" platform for submicromolar determination of cytostatic drug in biological fluids and pharmaceutical product, *Diamond and Related Materials* **113** (2021) https://doi.org/10.1016/j.diamond.2021.108277
- [29] M. Behravan, H. Aghaie, M. Giahi, L. Maleknia, Determination of doxorubicin by reduced graphene oxide/gold/polypyrrole modified glassy carbon electrode: A new preparation strategy, *Diamond and Related Materials* **117** (2021) https://doi.org/10.1016/j.diamond.2021.108478.
- [30] N. Thakur, V. Sharma, T. Abhishek Singh, A. Pabbathi, J. Das, Fabrication of novel carbon dots/cerium oxide nanocomposites for highly sensitive electrochemical detection of doxorubicin, *Diamond and Related Materials* **125** (2022) https://doi.org/10.1016/j.diamond.2022.109037.
- [31] T. Abhishek Singh, V. Sharma, N. Thakur, N. Tejwan, A. Sharma, J. Das, Selective and sensitive electrochemical detection of doxorubicin via a novel magnesium oxide/carbon dot nanocomposite based sensor, *Inorganic Chemistry Communications* **150** (2023) https://doi.org/10.1016/j.inoche.2023.110527.
- [32] S. Sun, X. Xu, N. Aiu, Z. Sun, Y. Zhai, S. Li, C. Xuan, Y. Zhou, X. Yang, T. Zhou, Q. Tian, Novel Electrochemical Sensor Based on Acetylene Black for the Determination of Doxorubicin in Serum Samples, *International Journal of Electrochemical Science* 17 (2022) https://doi.org/10.20964/2022.11.82.
- [33] J. Sharifi, H. Fayazfar, Highly sensitive determination of doxorubicin hydrochloride antitumor agent via a carbon nanotube/gold nanoparticle based nanocomposite biosensor, *Bioelectrochemistry* **139** (2021) https://doi.org/10.1016/j.bioelechem.2021.107741.
- [34] A. R. Alavi-Tabari, A. Khalilzadeh, H. Karimi-Maleh, Simultaneous determination of doxorubicin and dasatinib as two breast anticancer drugs uses an amplified sensor with ionic liquid and ZnO nanoparticle, *Journal of Electroanalytical Chemistry* **811** (2018) 84-88 https://doi.org/10.1016/j.jelechem.2018.01.034.
- [35] E. M. Materon, A. Wong, O. Fatibello-Filho, R. Censi Faria, Development of a simple electrochemical sensor for the simultaneous detection of anticancer drugs, *Journal of Electroanalytical Chemistry* **827** (2018) 64-72 https://doi.org/10.1016/j.jelechem.2018.09.010.
- [36] M. Rahimi, G. Bagheri, S. Jamilaldin Fatemi, A new sensor consisting of bird nest-like nanostructured nickel cobaltite as the sensing element for electrochemical determination of doxorubicin, *Journal of Electroanalytical Chemistry* **848** (2019) https://doi.org/10.1016/j.jelechem.2019.113333.
- [37] N. Hashemzadeh, M. Hasanzadeh, N. Shadjou, J. Eivazi-Ziaei, M. Khoubnasabjafari, A. Jouyban, Graphene quantum dot modified glassy carbon electrode for the determination of doxorubicin hydrochloride in human plasma, *Journal of Pharmaceutical Analysis* **6(4)** (2016) 235-241 https://doi.org/10.1016/j.jpha.2016.03.003.
- [38] S. Zia Mohammadi, F. Mousazadeh, S. Tajik, Simultaneous Determination of Doxorubicin and Dasatinib by using Screen-Printed Electrode/Ni-Fe Layered Double Hydroxide, *Industrial & Engineering Chemistry Research* **62(11)** (2023) 4646-4654 https://doi.org/10.1021/acs.iecr.2c03105.



- [39] I. Rus, M. Tertis, C. Barb`alat`a, A. Porfire, I. Tomut`a, R. S`andulescu, C. Cristea, An Electrochemical Strategy for the Simultaneous Detection of Doxorubicin and Simvastatin for Their Potential Use in the Treatment of Cancer, *Biosensors* **11(15)** (2021) https://doi.org/10.3390/bios11010015.
- [40] M. Wang, J. Lin, J. Gong, M. Ma, H. Tang, J. Liu, F. Yan, Rapid and sensitive determination of doxorubicin in human whole blood by vertically-ordered mesoporous silica film modified electrochemically pretreated glassy carbon electrodes, *Royal Society of Chemistry Advances* **11** (2021) 9021 https://doi.org/10.1039/d0ra10000e.
- [41] Y. Guo, Y. Chen, Q. Zhao, S. Shuang, C. Dong, Electrochemical Sensor for Ultrasensitive Determination of Doxorubicin and Methotrexate Based on Cyclodextrin-Graphene Hybrid Nanosheets, *Electroanalysis* **23** (2011) 2400 2407 https://doi.org/10.1002/elan.201100259.
- [42] C. Zhang, X. Zhou, F. Yan, J. Lin, N-Doped Graphene Quantum Dots Confined within Silica Nanochannels for Enhanced Electrochemical Detection of Doxorubicin *Molecules* **28** (2023) 6443 https://doi.org/10.3390/molecules28186443.
- [43] E. Haghshenas, T. Madrakian, A. Afkhami, Electrochemically oxidized multiwalled carbon nanotube/glassy carbon electrode as a probe for simultaneous determination of dopamine and doxorubicin in biological samples, *Analytical and Bioanalytical Chemistry* **408** (2016) 2577-2586 https://doi.org/10.1007/s00216-016-9361-y.
- [44] J. Fei, X. Wen, Y. Zhang, L. Yi, X. Chen, H. Cao Voltammetric determination of trace doxorubicin at a nano-titania/nafion composite film modified electrode in the presence of cetyltrimethylammonium bromide, *Microchimica Acta* **164** (2009) 85-91, https://doi.org/10.1007/s00604-008-0037-y.
- [45] M. Taei, F. Hasanpour, H. Salavati, S. Mohammadian, Fast and sensitive determination of doxorubicin using multi-walled carbon nanotubes as a sensor and CoFe2O4 magnetic nanoparticles as a mediator, *Microchimica Acta* **183** (2016) 49-56, https://doi.org/10.1007/s00604-015-1588-3.
- [46] S. Kummari, L. Panicker, K.V. Gobi, R. Narayan, Y.G. Kotagiri, Electrochemical Strip Sensor Based on a Silver Nanoparticle-Embedded Conducting Polymer for Sensitive In Vitro Detection of an Antiviral Drug, ACS Applied Nano Materials 6(13) (2023) 12381-12392 https://doi.org/10.1021/acsanm.3c02080.
- [47] G. Krishnaswamy, G. Shivaraja, S. Sreenivasa, Aruna Kumar D. B, Votammetric applications in Drug detection: Mini Review, *Volatmmetry for Sensing Applications* **11** (2022) 281-305 https://doi.org/10.2174/9789815039719122010013.
- [48] S. Sadak, I. Atay, S. Kurbanoglu, B. Uslu, Disposable Electrochemical Sensors for Biomedical Applications, *ACS Recent Developments of Green Electrochemical Sensors* **1437(8)** (2023) 157-191 https://doi.org/10.1021/bk-2023-1437.ch008.
- [49] Z. Bagheri Nasab, F. Garkani Nejad, Electrochemical Sensor Based on a Modified Graphite Screen Printed Electrode for Amitriptyline Determination, *Surface Engineering and Applied Electrochemistry* **58** (2022) 100-108 https://doi.org/10.3103/S1068375522010070.
- [50] B. Bozal-Palabiyik, B. Dogan-Topal, S. A. Ozkan, B. Uslu, New trends in Electrochemical sensor modified with carbon nanotubes and graphene for pharmaceutical analysis, *Recent Advances in Analytical Techniques* **2** (2018) 249-301 https://doi.org/10.2174/9781681085746118020009.
- [51] A. V. Bounegru, I. Bounegru, Chitosan-Based Electrochemical Sensors for Pharmaceuticals and Clinical Applications, *Polymers* **15(17)** (2023) 3539; https://doi.org/10.3390/polym15173539.
- [52] S. Traipop, W. Jesadabundit, W. Khamcharoen, T. Pholsiri, S. Naorungroj, S. Jampasa, O. Chailapakul, Nanomaterial-based Electrochemical Sensors for Multiplex Medicinal Applications, *Current Topics in Medicinal Chemistry* 24(11) (2024) 986 - 1009 https://doi.org/10.2174/0115680266304711240327072348
- [53] M. Wang, J. Lin, J. Gong, M. Ma, H. Tang, J. Liu, F. Yan F, Rapid and sensitive determination of doxorubicin in human whole blood by vertically-ordered mesoporous silica film modified electrochemically pretreated glassy carbon electrodes, *Royal Society of Chemistry Advances* 11 (2021) 9021-9028 https://doi.org/10.1039/DORA10000E.
- [54] Y. Guo, Y. Chen, Q. Zhao, S. Shuang, C. Dong, Electrochemical Sensor for Ultrasensitive Determination of Doxorubicin and Methotrexate Based on Cyclodextrin-Graphene Hybrid Nanosheets, *Electroanalysis* **23(10)** (2011) 2400-2407 https://doi.org/10.1002/elan.201100259.
- [55] J. Soleymani, M. Hasanzadeh, N. Shadjou, M. Khoubnasab Jafari, J. V. Gharamaleki, M. Yadollahi, A. Jouyban, A new kinetic-mechanistic approach to elucidate electrooxidation of doxorubicin

- hydrochloride in unprocessed human fluids using magnetic graphene-based nanocomposite modified glassy carbon electrode, *Materials Science and Engineering: C* **61** (2016) 638-650 https://doi.org/10.1016/j.msec.2016.01.003.
- [56] S. M. Ilies, B. Schinteie, A. Pop, S. Negrea, C. Cretu, E. I. Szerb, F. Manea, Graphene Quantum Dots and Cu(I) Liquid Crystal for Advanced Electrochemical Detection of Doxorubicin in Aqueous Solutions, *Nanomaterials* **11** (2021) 2788 https://doi.org/10.3390/nano11112788.
- [57] F. Chekin, V. Myshin, R. Ye, S. Melinte, S. K. Singh, S. Kurungot, R. Boukherroub, S. Szunerits, Graphene-modified electrodes for sensing doxorubicin hydrochloride in human plasma, *Analytical and Bioanalytical Chemistry* **411** (2019) 1509-1516, https://doi.org/10.1007/s00216-019-01611-w.
- [58] E. Hghshenas, T. Madrakian, A. Afkhami, Electrochemically oxidized multiwalled carbon nanotube/glassy carbon electrode as a probe for simultaneous determination of dopamine and doxorubicin in biological samples, *Analytical and Bioanalytical Chemistry* **408** (2019) 2577-2586 https://doi.org/10.1007/s00216-016-9361-y.
- [59] P. Paunović, A. Grozdanov, I. Dimitrievska, A. Tomova, Voltammetric Detection of Diclofenac with Screen-printed Electrodes Based on Graphene and PVDF-Modified Graphene, *Chemistry in Industry* **73(7-8)** (2024) 293-302 https://doi.org/10.15255/KUI.2023.058.
- [60] H. Imran, Y. Tang, S. Wang, X. Yan, C. Liu, L. Guo, E. Wang, C. Xu, Optimized DOX Drug Deliveries via Chitosan-Mediated Nanoparticles and Stimuli Responses in Cancer Chemotherapy: A Review, *Molecules* 29(1) 2024 31 https://doi.org/10.3390/molecules29010031.
- [61] I. M. Apetrei, C. Apetrei, Voltametric determination of melatonin using a graphene-based sensor in pharmaceutical products, *International Journal of Nanomedicine* 11 (2016) 1859-1866 http://doi.org/10.2147/IJN.S104941.
- [62] R. C. Carvalho, A. J. Betts, J. F. Cassidy, Diclofenac determination using CeO2 nanoparticle modified screen-printed electrodes A study of background correction, *Microchemical Journal* **158** (2020) 105258 https://doi.org/10.1016/j.microc.2020.105258.
- [63] U. Ciltas, B. Yilmaz, S. Kaban, B. K. Akcay, G. Nazik, Study on the interaction between isatin-β-thiosemicarbazone and calf thymus DNA by spectroscopic techniques. *Iranian Journal of Pharmaceutical Research* **15** (2014) 715-722 https://doi.org/10.22037/ijpr.2015.1691.
- [64] E. S. Gil, R. O. Couto, Flavonoid electrochemistry: a review on the electroanalytical applications, *Brazilian Journal of Pharmacognosy* **23** (2013) 542-558 https://doi.org/10.1590/S0102-695X2013005000031.
- [65] J. A. Gothi Grace, A. Gomathi, C. Vedhi, Electrochemical behaviour of 1,4-diaminoanthra-9,10-quinone at conducting polymer based modified electrode, *Journal of Advanced Chemical Sciences* **2(3)** (2016) 366-368 ISSN: 2394-5311.
- [66] S. Guan, X. Fu, B. Zhang, M. Lei, Z. Peng, Cation-exchange-assisted formation of NiS/SnS2 porous nanowalls with ultrahigh energy density for battery-supercapacitor hybrid devices, *Journal of Materials Chemistry A* **6** (2020) 3300-3310 https://doi.org/10.1039/C9TA11517J.
- [67] G. A. J. Merghani, A. A. Elbashir, Development of chemically modified electrode using cucurbit(6)uril to detect ranitidine hydrochloride in pharmaceutical formulation by voltammetry, *Journal of Analytical and Pharmaceutical Research* **7** (2018) 634-639 https://doi.org/10.15406/japlr.2018.07.00294.
- [68] H. Beitollahi, M. Hamzavi, M. Torkzadeh-Mahani, Electrochemical determination of hydrochlorothiazide and folic acid in real samples using a modified graphene oxide sheet paste electrode, *Materials Science and Engineering: C* 52 (2015) 297-305 https://doi.org/10.1016/j.msec.2015.03.031.
- [69] W. He, Y. Ding, W. Zhang, L. Ji, X. Zhang, F. Yang, A highly sensitive sensor for simultaneous determination of ascorbic acid, dopamine and uric acid based on ultra-small Ni nanoparticles, *Journal of Electroanalytical Chemistry* **775** (2016) 205-211 https://doi.org/10.1016/j.jelechem.2016.06.001.
- [70] P. Paunović, A. Grozdanov, I. Dimitrievska, M. Paunović, M. Mitevska, *Sofia Electrochemical Days, Irradiation Treatment on Sensing Performances of Screen-Printed Electrodes Aimed for Monitoring of Anticancer Drug Doxorubicin*, Varna, Bulgaria, 2024, p. 14.
- [71] E. Gileadi, *Electrode Kinetics for Chemists, Chemical Engineers, and Materials Scientists*, VCH Publishers Inc., New York, USA, 1993, ISBN: 978-0-471-18858-2.



- [72] L. M. Silva, L. A. Faria, J. F. C. Boodts, Determination of the morphology factor of oxide layers, *Electrochimica Acta* **47** (2001) 395-403 https://doi.org/10.1016/S0013-4686(01)00738-1.
- [73] Y. Chen, Y. Zhang, Z. Wu, X. Peng, T. Su, J. Cao, B. He, S. Li, Biodegradable poly(ethylene glycol)-poly(ε-carprolactone) polymeric micelles with different tailored topological amphiphilies for doxorubicin (DOX) drug delivery, *Royal Society of Chemistry Advances* **63** (2016) http://doi.org/10.1039/C6RA06040D.
- [74] J. Liang, Z. Zhang, H. Zhao, S. Wan, X. Zhai, J. Zhou, R. Liang, Q. Deng, Y. Wu, G. Lin, Simple and rapid monitoring of doxorubicin using streptavidin-modified microparticle-based time-resolved fluorescence immunoassay, *Royal Society of Chemistry Advances* 8 (2018) 15621-15631 https://doi.org/10.1039/C8RA01807C.
- [75] R. Bartzatt, E. Weidner, Analysis for doxorubicin by spectrophotometry and reversed phase high performance liquid chromatography (HPLC), *Current Topics in Analytical Chemistry* **9** (2012) 63-69 (PDF) Analysis for doxorubicin by spectrophotometry and reversed phase high performance liquid chromatography (HPLC)

© 2024 by the authors; licensee IAPC, Zagreb, Croatia. This article is an open-access article distributed under the terms and conditions of the Creative Commons Attribution license (https://creativecommons.org/licenses/by/4.0/)



Open Access : : ISSN 1847-9286

www.jESE-online.org

Original scientific paper

Preparation and optimization of $La_{0.6}Sr_{0.4}Fe_{1-y}Co_yO_{3-\delta}$ cathodes for intermediate temperature solid oxide fuel cells

Jesús Tartaj[™] and Alvaro Vázquez

ELAMAT Group, Ceramics and Glass Institute (CSIC), Kelsen 5, 28049 Madrid, Spain

Corresponding authors: [™] <u>itartaj@icv.csic.es</u>; Tel.: +34917355853; Fax: +34917355843

Received: September 27, 2024; Accepted: October 30, 2024; Published: November 7, 2024

Abstract

It is shown in this work that a synthetic route based on the auto-combustion of an ethylene glycol-metal nitrate polymerized gel precursor can be efficiently used to easily produce a range of $La_{0.6}Sr_{0.4}Fe_{1-v}Co_vO_{3-\delta}$ nanopowders at moderate temperatures. We have been able to determine on air-sintered samples the effect of sintering temperature on the microstructure. At sintering temperatures as low as 1100 to 1200 °C, grains are well defined with a uniform round spherical morphology and have a homogeneous sub-micrometer size distribution showing a highly densified microstructure. The electronic conductivity and thermal expansion coefficients (TEC) of sintered LSFC samples have been determined according to the variation of Fe/Co composition. Both measures clearly increase with the Co content. These materials also must exhibit chemical stability with electrolytes, most commonly used for intermediate temperature solid oxide fuel cells (IT-SOFCs). In this way, the material obtained is optimized in terms of chemical homogeneity and good stoichiometric control, microstructural characteristics of sintered samples, and finally, the adequate cobalt content to avoid high TEC mismatch with other components of the SOFC. This is a crucial issue as it causes an important thermomechanical stress, promotes extensive microcraking and causes significant performance degradation. Finally, these cathodes must exhibit acceptable electrochemical parameters for use in IT-SOFC.

Keywords

Ferro-cobaltite cathodes; electrochemical properties; thermal expansion coefficients; chemical compatibility

Introduction

Fuel cells represent a viable alternative for producing electricity with high efficiency, low pollution and cost-effectiveness. In recent years, among the different types of fuel cells, the interest in solid oxide fuel cells (SOFCs) has increased enormously as a commercially viable power source [1]. Additional advantages of this type of fuel cells are the high tolerance to impurities and the possibility of internal reforming, which leads to the possibility of using different fuels [2]. In addition, the

possibility of producing cogenerative energy from heat waste during the operation process results in being very attractive for this kind of fuel cell [3]. However, considering the high working temperature (around 900 to 1000 °C), some difficulties limit the use of SOFCs, among them the selection of interconnects, sealing materials, coefficient thermal expansion (CTE) mismatch and chemical compatibility of cell components [4]. Therefore, a lower operating temperature (600 to 800 °C) is necessary to reduce manufacturing costs and increase durability. For that purpose, new materials are required that can efficiently operate at a lower temperature, *i.e.*, electrolytes with higher conductivity such as doped-CeO₂ [5] or La(Sr)Ga(Mg)O₃ [6] and also, it is crucial the development of more effective cathode materials with increased electrocatalytic activity [7].

The new cathode materials should be characterized by increased oxide ion transport in addition to high electronic conductivity. La_{1-x}Sr_xFeO₃ (LSF) has demonstrated higher electrical and ionic conductivity than the conventional La_{1-x}Sr_xMnO₃ (LSM), which may extend the cathode reaction sites beyond the triple-phase boundaries [8,9]. In this same way, La_{1-x}Sr_xCoO₃ (LSC) can be considered as a promising cathode for IT-SOFCs with high values of conductivity. However, the good electrocatalytic performance of this Cobalt-based-cathode is somehow limited by a thermal expansion coefficient (TEC) mismatch with other components of the SOFC, causing significant thermosmechanical stress between these thermally mismatched components and finally leading to significant performance degradation that may be rapid and catastrophic. TECs of both the electrolyte and electrode layers should be well matched to ensure long-term operational stability of the SOFCs, either by modifying existing cathodes or designing new ones [10]. Considering all the above aspects, alternative materials could be ferrite/cobaltite cathodes such as La_{0.6}Sr_{0.4}Fe_{1-γ}Co_γO_{3-δ} (LSFC). The electronic conductivity of these samples in air is characterized by the higher values at increasing Co contents because the activation energy of LSF is higher than that for Co-doped ferrites [11,12]. It must be considered that the presence of Fe helps to minimize mechanical stresses as it can reduce the TEC mismatch. Also, it should be ensured that there are no reaction phases on the electrode/electrolyte interfaces since this could be detrimental to the efficiency of the cell. Furthermore, cation interdiffusion must be precluded because it may negatively modify the properties of the electrode and electrolyte. In recent years, many studies have proposed relevant mechanisms and solutions [13].

On the other hand, the solid-state reaction of the corresponding oxides is an easy synthesis process to obtain ceramic powders of different materials. However, it requires high processing temperatures and the homogeneity of the final synthesized powder is poor. Due to the number of cations involved, the compositional complexity of the materials mentioned above requires a synthesis method that ensures optimal chemical homogeneity and good stoichiometric control in which cations involved are distributed uniformly at an atomic scale. Thus, chemical methods of processing are highly recommended techniques to produce these materials [14-17]. Here, we use a low-cost and simple synthesis alternative method, which was previously studied and has excellent results [18]. It is based on the chelation of complex cations leading to the formation of an intermediate resin, which, on charring and calcining, leads to a sinterable powder that can be efficiently used to easily produce a range of $La_{0.6}Sr_{0.4}Fe_{1-y}Co_yO_{3-\delta}$ (LSFC) at moderate temperatures.

Therefore, the purpose of this work is to prepare LSFC cathodes using a low-cost and simple synthesis method with adequate electrochemical properties and thermomechanical compatibility with the electrolyte. First, to optimize these materials, microstructural control is necessary by determining the adequate sintering temperature. In addition, the chemical compatibility between electrodes and electrolytes is an important issue for successfully operating the fuel cells. It is also

crucial to determine the LSFC composition that avoids microstructural problems caused by the TEC's mismatch with the electrolyte and adequate electrochemical performance in terms of electrical conductivity and polarization resistance.

Experimental

 $La_{0.6}Sr_{0.4}Fe_{1-v}Co_vO_{3-\delta}$ nanopowders with compositions y = 0 to 1 were prepared by the ethylene glycol-metal nitrate polymerized complex process. Aqueous solutions (≈0.5 M) of corresponding nitrates were mixed by stirring nitric acid (65 %) and ethylene glycol to make a gel. It was treated thermally at different temperatures [18]. The as-obtained powder was calcined at 900 °C for 5 h and then attrition milled for 1 h in ethanol with zirconia ball media. For sintering, the powders were isopressed in pellets at 200 MPa and thermally treated at temperatures between 1000 and 1200 °C after drying. The powders were characterized by differential thermal (DTA) and thermogravimetric (TG) analysis (Perkin-Elmer 7). The calcined powders and sintered samples were characterized by X-ray diffraction (XRD) with a Bruker D8 Advance diffractometer (Cu $K\alpha_1$ radiation). After polishing and thermal etching, the microstructures of the sintered samples were examined by Scanning Electron Microscopy (SEM) in a Zeiss Microscope (model DSM 950, Germany). Shrinkage during sintering, at a heating rate of 5 °C min⁻¹ without holding, was followed in a dilatometer Netzsch Gerätebau (model 402 EP, Selb-Bayern Germany) by the conventional rampant-holding methods. The TECs were measured using the above-mentioned dilatometer in air from room temperature to 800 °C on air-sintered rectangular shapes. For determining the total electrical conductivity, impedance was measured at 800 °C in argon using a potentiostat/galvanostat (Autolab PGSTAT302 N). The platinum paste is used as a current-collecting electrode on either side of the sintered pellet and the electrode is cured at 950 °C for 2 h before the electrical conductivity measurements. To study the effect on the microstructure of the electrode/electrolyte TEC mismatch, LSFC powders were fixed on the sintered electrolyte of La_{0.9}Sr_{0.15}Ga_{0.8}Mg_{0.2}O_{3-δ} (LSGM) by uniaxial pressing. The sandwich electrode/electrolyte was co-fired at 1200 °C for 5 h and continuously subjected to 10 cycles of rise and fall of temperature (25 to 800 °C). The microstructures of these samples were examined by SEM. Energy dispersive X-ray analysis (EDX) was performed to study the possibility of cations diffusion through the cathode-electrolyte interfaces. The measurements of area-specific resistance (ASR) dependence with temperature were carried out in a half cell with a 3-electrode configuration, using Ce_{0.9}Gd_{0.1}O_{2-δ} (CGO, Cerpotech) as electrolyte. In this study, pellets of electrolyte powder were uniaxial pressed and sintered at 1500 °C for 6 hours. A mix of a commercial organic solvent, Decoflux, and the studied electrodes were deposited using a 6 mm-diameter mask on both sides. The electrode-electrolyte pellets were then co-fired at 1200 °C for 6 h. A reference platinum electrode was deposited in the edge of the pellet to make 3-probe electrode polarization measurements. Impedance spectroscopy was carried out with a Metrohm Autolab PGSTAT302 N, employing a signal amplitude of 1 mA across a frequency range of 0.1 to 10⁶ Hz and a temperature range of 600 to 950 °C. Energy dispersive X-ray analysis (EDX) was performed to study the possibility of cations diffusion.

Results and discussion

The simultaneous TG/DTA curves of a representative LSFC polymeric gel are shown in Figure 1. In the DTA curve, the more relevant feature corresponded to that present at about 230 °C, in which an abrupt exothermal peak is detected and associated with the decomposition-oxidation of the metal chelates and the evolved gases. This process continues around 300 to 350 °C. The TG curve shows a total weight loss

of about 60 % up to 900 °C. Also, Figure 1 shows the XRD analysis of LSFC powders calcined at 900 °C for 5 h and sintered at 1200 °C for 12 h. Only two representative samples have been included in the XRD diagrams for better visualization. The X-ray diffraction patterns are very similar in that all peaks correspond to the pure perovskite phase [19]. In those corresponding to calcined powder, an extra peak appears at the left of the main peak. It can be attributed to the SrFeLaO₄ phase [19]. This secondary phase disappears when heated at 1200 °C, leaving a pure perovskite.

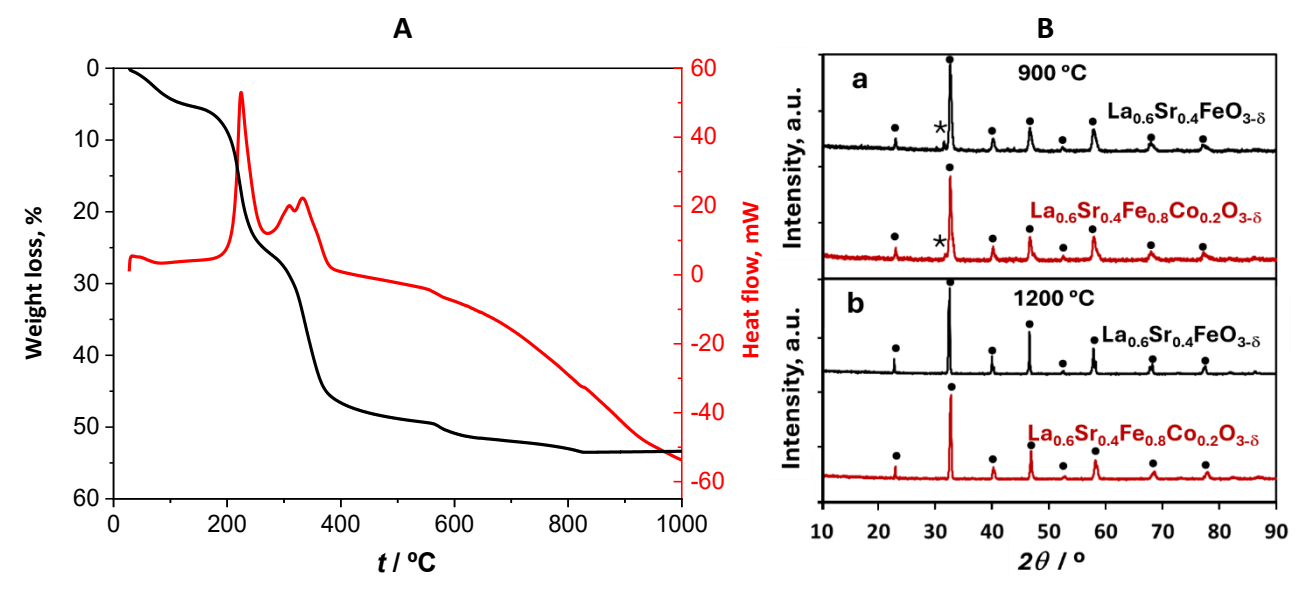


Figure 1. A - TG and DTA curve correspond to the LSFC polymeric gel precursor; B - XRD patterns of a - calcined powders at 900 °C - 5 h and b - sintered powders at 1200 °C.

• Perovskite phase, * SrFeLaO₄ phase

Linear shrinkage behavior and shrinkage rate curves of typical green compacts with temperature are shown in Figure 2. Green compacts initiate detectable bulk shrinkage at a very low temperature (\approx 1000 °C).

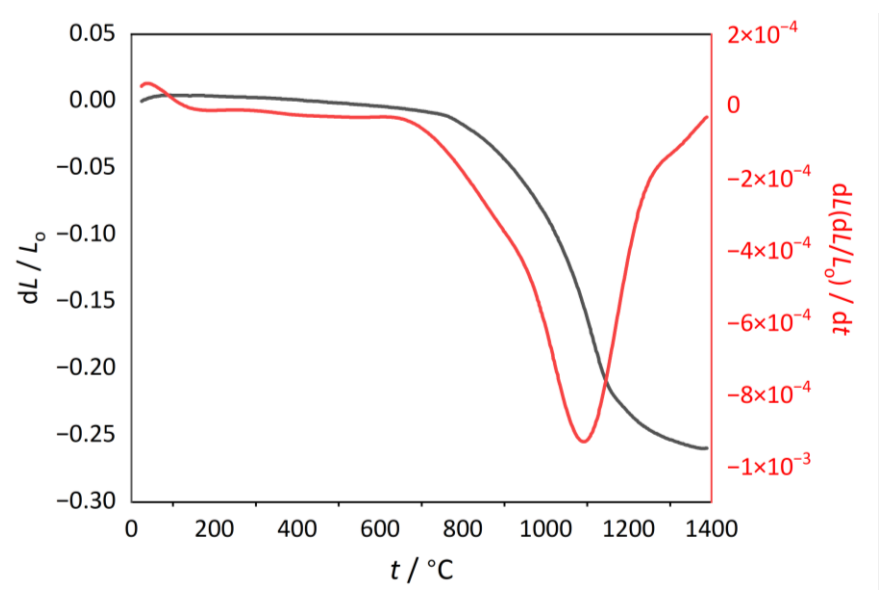


Figure 2. Typical linear shrinkage behavior and shrinkage rate curves of green LSFC compacts vs. sintering temperature.

Although several causes can contribute to this rapid sintering, such behaviour could be explained as the consequence of the nanometer size of powders and low agglomeration state and, consequently, a higher amount of intercrystallite porosity present in the green compacts, which is

rapidly eliminated [18]. The shrinkage process is clearly intensified at \approx 1100 °C temperature for maximum densification rate. At 1200 °C, most of the shrinkage process has taken place; therefore, it is close to the endpoint density.

Figure 3 reflects the effect of a sintering temperature below and above the temperature for maximum densification rate, (≈1100 °C). At 1000 °C, the microstructure showed low densification and high porosity but with sufficient integrity. Above that temperature, 1100 °C, grains are well defined with a uniform round spherical morphology and have a homogeneous sub-micrometre size distribution. The importance of this kind of microstructure is mentioned by Acuña *et al.* in their work [20]. The electrochemical properties of these materials significantly improve with decreasing grain size, and thus, the high specific surface area of these nanostructured cathodes increases the number of active sites for the oxygen reduction reaction. Finally, at 1200 °C, most of the densification process takes place; therefore, it is close to the endpoint density, showing a highly densified microstructure.

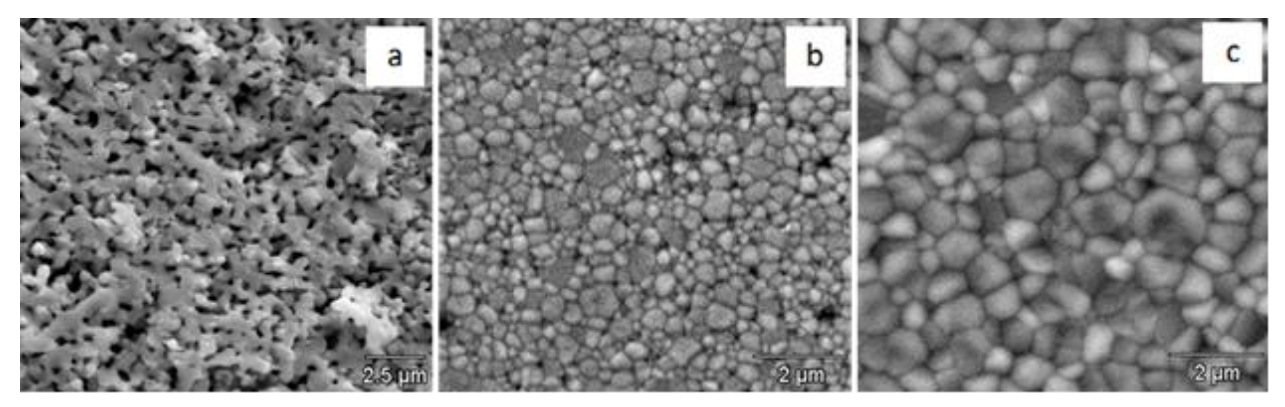


Figure 3. SEM micrographs of typical LSFC compacts sintered at a - 1000, b-1100 and c-1200 °C for 12 h.

Table 1 shows the thermal expansion coefficients (TEC) and the electronic conductivity (EC) of sintered samples as a function of the Fe and Co content, that is $La_{0.6}Sr_{0.4}Fe_{1-v}Co_vO_{3-\delta}$ (y = 0 to 1). As it is observed, the increase of the TEC and EC is influenced clearly by the increase of Co concentration. As Shah et al. [10] explain, cobalt undergoes a spin state change at high operating temperatures, resulting in a significant difference in TEC values between cobaltite perovskite cathodes and other components, such as the electrolyte material. The TEC values obtained are quite high (>17×10⁻⁶ / $^{\circ}$ C)) for samples with higher cobalt proportion, which is incompatible with the values corresponding to the electrolytes mentioned in the table and calculated by the same method as the LSFC cathodes. This produces an important thermomechanical stress. On the contrary, samples with lower Co content reduce the TEC to values that are more comparable. To highlight these considerations, Figure 4 shows cross-sectional SEM views corresponding to electrode/electrolyte interface co-fired at 1200 °C for 5 h. In both cases, the LSFC layer is strongly attached to the LSGM phase and shows a well-defined interface. It can be observed, in the case of higher Co content $(La_{0.6}Sr_{0.4}Fe_{0.5}Co_{0.5}O_{3-6})$, that an extensive microcraking is presented near the interphase. Clearly, this is a consequence of a TEC mismatch, above recommended tolerance values. On the contrary, by reducing the cobalt, (La_{0.6}Sr_{0.4}Fe_{0.8}Co_{0.2}O_{3-δ}), no delamination or other types of structural defects were formed within the laminate structure. The electronic conductivity values in Table 1 are similar to those previously reported in the literature [7]. Also, Banerjee et al. [21] report similar results in cathodes synthesized by autocombustion technique for producing powders with particulate sizes ranging 50 to 100 nm, like our procedure. An increase in conductivity is clearly observed with increasing cobalt content. Thus, very significant values of 2000 S/cm are reached for the pure cobaltite. However, a drawback of the Co-based cathodes is that TEC mismatches with those that correspond to the electrolytes. Therefore, even considering the reduction of the EC, shown in this table, the substitution of Co by Fe is strongly recommended in order to reduce the TEC values and optimize the themomechanical behavior of these materials. The substitution of Co by Fe changes the orbital configuration of Co 3d orbital and O 2p orbital, decreasing the electrical conductivity of the LSFC [11]. The objective is that TECs of both electrolyte and electrode layers should be well matched to ensure long-term operational stability of the SOFC and also maintain acceptable values of EC. Considering both parameters, of great importance for its satisfactory application in SOFCs, the recommended composition could be nearby to $La_{0.6}Sr_{0.4}Fe_{0.8}Co_{0.2}O_{3-\delta}$, with good thermomechanical stability and exhibiting and adequate electronic conductivity, 244 S/cm at 800 °C.

Table 1. Thermal expansion coefficients (25 to 800 °C) and electronic conductivity (800 °C) as a function of the Fe and Co content in La_{0.6}Sr_{0.4}Fe_{1-y}Co_yO_{3- δ} (LSF y = 0 to LSC y = 1). TEC of the most typical electrolytes for IT-SOFC are also included

TEC, 10 ⁻⁶ °C ⁻¹	σ / S cm $^{ ext{-}1}$
12.27	148
14.28	221
14.52	244
14.84	303
15.24	597
15.47	642
15.70	963
16.63	1190
17.11	1380
17.91	1800
18.62	2000
12.83	-
13.20	-
	12.27 14.28 14.52 14.84 15.24 15.47 15.70 16.63 17.11 17.91 18.62

Furthermore, the long-term stability of these materials also depends on the chemical compatibility of these cathodes with the electrolytes. It must be considered that LSC-based materials that react with ZrO₂-based electrolytes have presented serious challenges to their practical application [22]. In fact, reactivity between LSCF and yttria-stabilized zirconia (YSZ) electrolyte with the formation of insulating phases such as SrZrO₃ has been reported [9]. According to the EDX analysis, also included in Figure 4, there is no presence of any new secondary phases, that is, interfacial reactions did not take place between the cathode and the electrolyte. Fe or Co were not detected at the electrolyte surface, even close to the cathode side. Also, it is possible to observe that in the mark located in the cathode (near the interface), there are no indications of the presence of gallium and magnesium. Then, these LSFC cathodes also exhibit chemical stability with the LSGM electrolyte mentioned above. These results are in agreement with Zhang *et al.* [13], LSGM or CeO₂-based electrolytes had good chemical compatibility with the LSFC cathode materials.

LSCF emerges as the most promising cathode for IT-SOFC due to its low polarization resistance. This performance can be attributed to the increasing number of active sites for the oxygen reduction reaction. The Arrhenius representation of area-specific resistance (ASR) dependence on temperature is shown in Figure 5. For that, two electrodes without and with Co ($La_{0.6}Sr_{0.4}Fe_{0.8}Co_{0.2}O_{3-\delta}$) were deposited, in each case, on electrolytes of $Ce_{0.9}Gd_{0.1}O_{2-\delta}$.

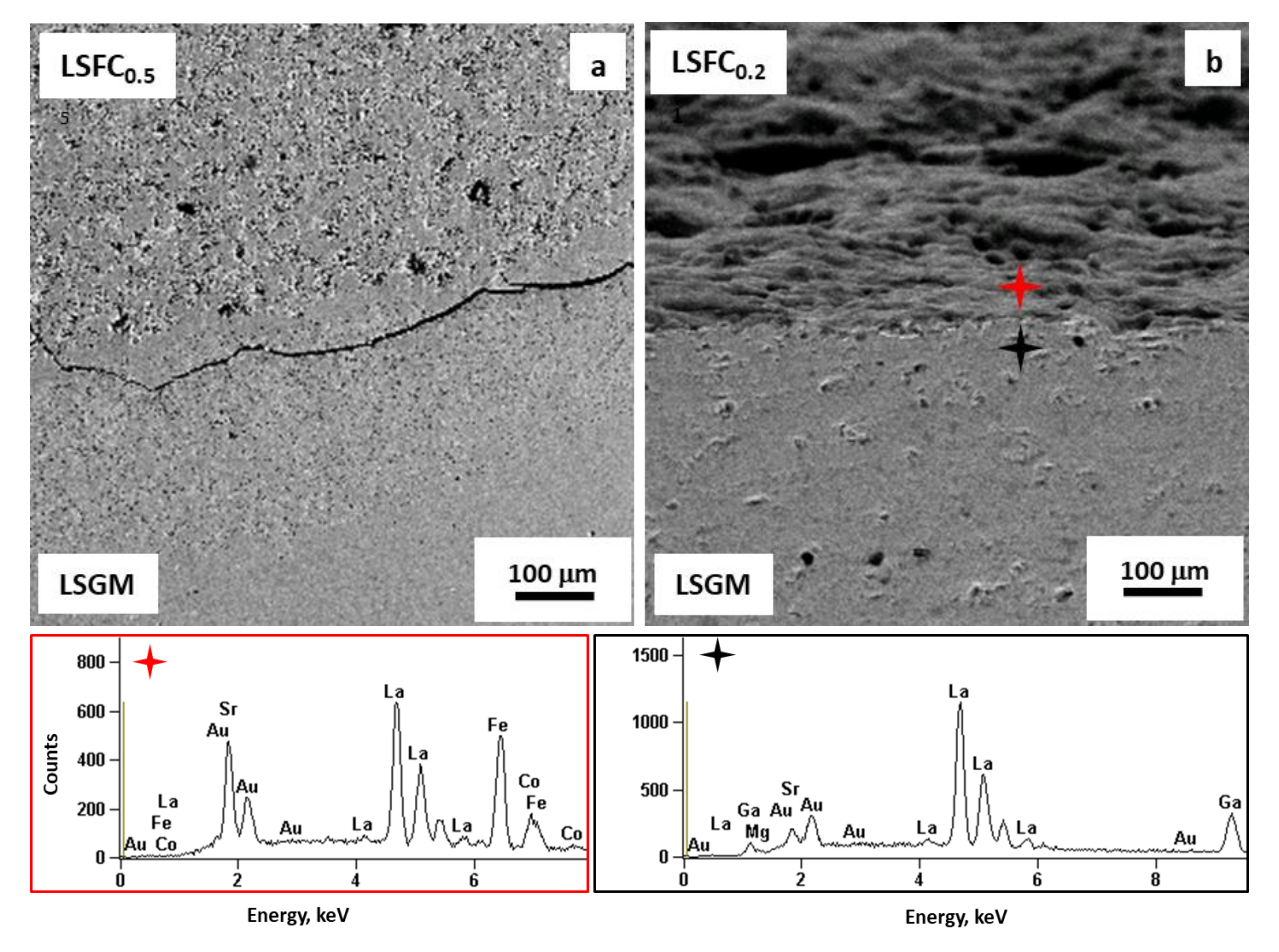


Figure 4. SEM micrographs of cathode/electrolyte pairs co-fired at 1200 °C for 5 h and treated during 10 cycles of raising and lowering of temperature (from room temperature to 800 °C). a - LSFC_{0.5} (La_{0.6}Sr_{0.4}Fe_{0.5}Co_{0.5}O_{3-δ}), b - LSFC_{0.2} (La_{0.6}Sr_{0.4}Fe_{0.8}Co_{0.2}O_{3-δ}). (LSGM: La_{0.9}Sr_{0.15}Ga_{0.8}Mg_{0.2}O_{3-δ}). Include EDX analysis on both sides of the interface corresponded to micrograph b.

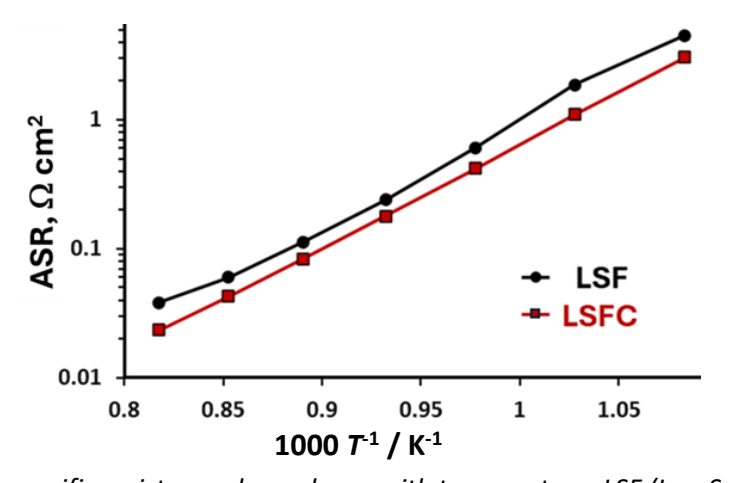


Figure 5. Area-specific resistance dependence with temperature. LSF ($La_{0.6}Sr_{0.4}FeO_{3-\delta}$) and LSFC ($La_{0.6}Sr_{0.4}Fe_{0.8}Co_{0.2}O_{3-\delta}$).

This study is carried out to verify the good electrochemical performance of these materials, specifically for that composition, which had been recommended according to thermomechanical stability and electronic conductivity, (La_{0.6}Sr_{0.4}Fe_{0.8}Co_{0.2}O_{3- δ}). The values of ASR at 700, 750 and 800 °C are 1.87, 0.61 and 0.24 Ω cm² for LSF, and 1.1, 0.42 and 0.18 Ω cm² for LFSC. First, the electrochemical performance is improved with cobalt, which has the same oxidation states as Fe³⁺ and Fe⁴⁺, but the Co-O bonds are weaker than Fe-O bonds, so oxygen ions can move more easily

through the structure. These materials exhibited adequate area-specific resistance around 0.20 Ω cm² for an operating temperature of 800 °C, showing the capability of these structures to move oxygen ions through them. Other authors as Banerjee *et al.* [21], report similar results of 0.142 Ω cm² at 800 °C for La_{0.54}Sr_{0.4}Co_{0.2}Fe_{0.80}O_{3-δ}. Also, it must be considered that the deposition process to improve the microstructure of the cathodes is important to increase their performance (decrease the ASR). La_{0.6}Sr_{0.4}Fe_{0.8}Co_{0.2}O_{3-δ}, showing excellent area-specific resistance values for an operating temperature of 800 °C, constitute a first step in understanding these promising compositions and optimizing them. Finally, the EDX analysis of these samples indicates that no cationic diffusion processes have occurred on either side of the interface. These LSFC materials also exhibit chemical stability with electrolytes based on CGO, in agreement with Zhang *et al.* [13].

Conclusions

La $_{0.6}$ Sr $_{0.4}$ Fe $_{1-\gamma}$ Co $_{\gamma}$ O $_{3-\delta}$ perovskite nanopowders were satisfactorily prepared by the polymeric organic complex solution method. The densification process of powder compacts is initiated at a very low temperature ($\approx 1000\,^{\circ}$ C) and is completed at $\approx 1200\,^{\circ}$ C. We have been able to determine on these samples, the sintering temperature conditions for an effective microstructural control, that is, materials with highly densified microstructure, an effective grain size control, and then optimum microstructures for improving the electrochemical performance of these materials. It has been established how electronic conductivity and thermal expansion coefficients change with the Fe, Co composition. TEC values obtained for LSFC samples with lower Co content are compatible with the values corresponding to the electrolytes used based on LSGM and exhibit adequate electronic conductivity. These materials also exhibit chemical stability with the LSGM and CGO electrolytes. In addition, La $_{0.6}$ Sr $_{0.4}$ Fe $_{0.8}$ Co $_{0.2}$ O $_{3-\delta}$ shows excellent area-specific resistance values for an operating temperature of even 700 °C. As a consequence of these results, it can be concluded that those compositions with a small amount of cobalt, La $_{0.6}$ Sr $_{0.4}$ Fe $_{0.8}$ Co $_{0.2}$ O $_{3-\delta}$, are highly recommended for use as cathodes for advanced IT-SOFCs.

The presented results are important not only for the synthetic route itself but also because they establish practical cathode operational parameters on sintered samples for the selection of the most suitable composition, considering the TECs of the electrolyte utilized and the operating temperature of the cell. These results regarding the development of these cathodes will contribute to the fact that solid oxide fuel cells (SOFCs) are expected to play a major role in many power generation applications.

Acknowledgements: The authors acknowledge the financial support by PID2021-123308OB-I00 project, funded by MCIN/AEI/10.13039/501100011033 in Spain and "ERDF A way of making Europe", by the European Union.

References

- [1] A. Talukdar, A. Chakrovorty, P. Sarmah, P. Paramasivam, V. Kumar, S. Kumar Yadav, S. Manickkam, A Review on Solid Oxide Fuel Cell Technology: An Efficient Energy Conversion System, *International Journal of Energy Research* (2024) 443247. https://doi.org/10.1155/2024/6443247
- [2] D. Mogensen, J.-D. Grunwaldt, P.V. Hendriksen, J.U. Nielsen, K. Dam-Johansen, Methane Steam Reforming over an Ni-YSZ Solid Oxide Fuel Cell Anode in Stack Configuration, *Journal of Chemistry* (2014) 10391. http://dx.doi.org/10.1155/2014/710391



- [3] Z. Zakaria, Z. Awang Mat, S. H. Abu Hassan, Y. B. Kar, A review of solid oxide fuel cell component fabrication methods toward lowering temperature, *International Journal of Energy Research* **44** (2020) 594-611. https://doi.org/10.1002/er.4907
- [4] M. S. Arshad, X. Y. Mbianda, I. Ali, G. Wanbing, T. Kamal, K. Kauhaniemi, S. Z. Hassan, G. Yasin, Advances and Perspectives on Solid Oxide Fuel Cells: From Nanotechnology to Power Electronics Devices, *Energy Technology* **11** (2023) 300452. https://doi.org/10.1002/ente.202300452
- [5] A. Moure, C. Moure, J. Tartaj, A significant improvement of the processing and electric properties of CeO₂ co-doped with Ca and Sm by mechanosynthesis, *Journal of Power Sources* **196** (2011) 10543-10549. https://doi.org/10.1016/j.jpowsour.2011.07.088
- [6] M. Morales, J.J. Roa, J. Tartaj, M. Segarra, A review of doped lanthanum gallates as electrolytes for intermediate temperature solid oxides fuel cells: From materials processing to electrical and thermo-mechanical properties, *Journal of the European Ceramic Society* **36** (2016) 1-16. http://dx.doi.org/10.1016/j.jeurceramsoc.2015.09.025
- [7] A. Samreen, M. S. Ali, M. Huzaifa, N. Ali, B. Hassan, F. Ullah, S. Ali, N. A. Arifin, Advancements in Perovskite-Based Cathode Materials for Solid Oxide Fuel Cells: A Comprehensive Review, *The Chemical Record* **24** (2024) 1-27. https://doi.org/10.1002/tcr.202300247
- [8] S. D. Safian, N. I. Abd Malek, Z. Jamil, S-W. Lee, C-J. Tseng, N. Osman, Study on the surface segregation of mixed ionic-electronic conductor lanthanum-based perovskite oxide La_{1-x} Sr_xCo_{1-y}Fe_yO_{3-δ} materials, *International Journal of Energy Research* **46** (2022) 7101-7117. https://doi.org/10.1002/er.7733
- [9] L. dos Santos-Gomez, J.M. Porras-Vázquez, E. R. Losilla, F. Martín, J. R. Ramos-Barrado, D. Marrero-López, Stability and performance of La_{0.6}Sr_{0.4}Co_{0.2}Fe_{0.8}O_{3-δ} nanostructured cathodes with Ce_{0.8}Gd_{0.2}O_{1.9} surface coating, *Journal of Power Sources* **347** (2017) 178-185. http://dx.doi.org/10.1016/j.jpowsour.2017.02.045
- [10] N. Shah, X. Xu, J. Love, H. Wang, Z. Zhu, L. Ge, Mitigating thermal expansion effects in solid oxide fuel cell cathodes: A critical review, *Journal of Power Sources* **599** (2024) 234211. https://doi.org/10.1016/j.jpowsour.2024.234211
- [11] U. F. Vogt, P. Holtappels, J. Sfeir, J. Richter, S. Duval, D. Wiedenmann, A. Züttel, Influence of A-Site Variation and B-Site Substitution on the Physical Properties of (La,Sr)FeO₃ Based Perovskites, *Fuel Cells* **9** (2009) 899-906. https://doi.org/10.1002/fuce.200800116
- [12] S. B. C. Duval, T.Graule, P. Holtappels, J. P. Ouweltjes, G. Rietveld, Evaluation of the Perovskite $(La_{0.8}Sr_{0.2})_{0.95}Fe_{0.8}Ni_{0.2}O_{3-\delta}$ as SOFC Cathode, *Fuel Cells* **9** (2009) 911-914. https://doi.org/10.1002/fuce.200900154
- [13] L. Zhang, G. Chen, R. Dai, X. Lv, D. Yang, S. Geng, A review of the chemical compatibility between oxide electrodes and electrolytes in solid oxide fuel cells, *Journal of Power Sources* **492** (2021) 229630. https://doi.org/10.1016/j.jpowsour.2021.229630
- [14] A. Dutta, J. Mukhopadhyay, R. N. Basu, Combustion synthesis and characterization of LSCF-based materials as cathode of intermediate temperature solid oxide fuel cells, *Journal of the European Ceramic Society* **29** (2009) 2003–2011. https://doi.org/10.1016/j.jeurceramsoc.2008.11.011
- [15] M. R. Cesario, D. A. Macedo, A. E. Martinelli, R. M. Nascimento, B. S. Barros, D. M. A. Melo, Synthesis, structure and electrochemical performance of cobaltite-based composite cathodes for IT-SOFC, *Crystal Research and Technology* **47** (2012) 723-730. https://doi.org/10.1002/crat.201100028
- [16] A. Chrzan, J. Karczewski, M. Gazda, D. Szymczewska, P. Jasinski, La_{0.6}Sr_{0.4}Co_{0.2}Fe_{0.8}O_{3-δ} oxygen electrodes for solid oxide cells prepared by polymer precursor and nitrates solution

- infiltration into gadolinium doped ceria backbone, *Journal of the European Ceramic Society* **37** (2017) 3559-3564. http://dx.doi.org/10.1016/j.jeurceramsoc.2017.04.032
- [17] I-. Hung, C-J Ciou, Y-J. Zeng, J-S. Wu, Y-C. Lee, A. Su, S-H. Chan, Conductivity and electrochemical performance of (Ba_{0.5}Sr_{0.5})_{0.8}La_{0.2}Fe_{1-x}Mn_xO_{3-δ} cathode prepared by the citrate–EDTA complexing method, *Journal of the European Ceramic Society* **31** (2011) 3095–3101. https://doi.org/10.1016/j.jeurceramsoc.2011.04.029
- [18] J. M. Perez-Falcon, A. Moure, J. Tartaj, Low-Temperature preparation of La_{0.6}Sr_{0.4}Fe_{0.8}Co_{0.2}O_{3-δ} Sinterable Nanopowders by the Polymeric Organic Complex Solution Method, *Fuel Cells* **11** (2011) 75-80. https://doi.org/10.1002/fuce.201000061
- [19] P. Plonczak, M. Gazda, B. Kusz, P. Jasinski, Fabrication of solid oxide fuel cell supported on specially performed ferrite-based perovskite cathode, *Journal of Power Sources* **181** (2008) 1-7. https://doi.org/10.1016/j.jpowsour.2007.12.019
- [20] L. M. Acuña, J. Peña-Martínez, D. Marrero-López, R. O. Fuentes, P. Nuñez, D. G. Lamas, Electrochemical performance of nanostructured La_{0.6}Sr_{0.4}CoO_{3-δ} and Sm_{0.5}Sr_{0.5}CoO_{3-δ} cathodes for IT-SOFCs, *Journal of Power Sources* **196** (2011) 9276-9283. https://doi.org/10.1016/j.jpowsour.2011.07.067
- [21] K. Banerjee, J. Mukhopadhyay, R. N. Basu, Nanocrystalline doped lanthanum cobalt ferrite and lanthanum iron cobaltite-based composite cathode for significant augmentation of electrochemical performance in solid oxide fuel cell, *International Journal of Hydrogen Energy* **39** (2014) 15754-15759. http://dx.doi.org/10.1016/j.ijhydene.2014.07.109
- [22] S. P. Simner, J. P. Shelton, M. D. Anderson, J. W. Stevenson, Interaction between La(Sr)FeO₃ SOFC cathode and YSZ electrolyte, *Solid State Ionics* **161** (2003) 11-18. https://doi.org/10.1016/S0167-2738(03)00158-9

©2024 by the authors; licensee IAPC, Zagreb, Croatia. This article is an open-access article distributed under the terms and conditions of the Creative Commons Attribution license (https://creativecommons.org/licenses/by/4.0/)





Open Access:: ISSN 1847-9286 www.jESE-online.org

Original scientific paper

Extended characteristic polynomial estimating the electrochemical behaviour of some 4-(azulen-1-yl)-2,6-divinylpyridine derivatives

Eleonora-Mihaela Ungureanu¹, Amalia Ștefaniu², Raluca Isopescu³, Cornelia-Elena Mușina³, Magdalena-Rodica Bujduveanu³ and Lorentz Jäntschi⁴,5,⊠

¹Doctoral School of Chemical Engineering and Biotechnologies, National University of Science and Technology POLITEHNICA, Bucharest, Romania

²National Institute of Chemical, Pharmaceutical Research and Development, Bucharest, Romania ³Faculty of Chemical Engineering and Biotechnologies, National University of Science and Technology POLITEHNICA, Bucharest, Romania

⁴Department of Physics and Chemistry, Technical University of Cluj-Napoca, Romania ⁵Laboratory of Electrochemistry For Advanced Materials, Technical University of Cluj-Napoca, Cluj-Napoca, Romania

Corresponding authors: □ lorentz.jantschi@chem.utcluj.ro; tel.: +4-0264-401-775

Received: June 5, 2024; Accepted: July 18, 2024; Published: July 26, 2024

Abstract

Six derivatives of 4-(azulen-1-yl)-2,6-divinylpyridine were the subject of experimental determination of oxidation and reduction potentials being reported elsewhere. In this paper, a computational study was employed in order to obtain a function of structure for these potentials. The geometry was optimized at three theory levels (MMFF94, B3LYP and M06), and the following analysis was conducted with the separately saved optimum geometry in each instance. Two families of molecular descriptors (FMPI and EChP) were used to derive structure-based descriptors. Simple linear regressions were extracted with the best of descriptors for each family and level of theory for both potentials. The study revealed that the MMFF94 optimum geometries best explained the selected electrochemical properties. Furthermore, the EChP family of descriptors, much bigger than FMPI (about 64 times), was able to better explain the connection between the structure and the property. Once more, it has been shown that the eigenproblem has deep roots in structural chemistry.

Keywords

Oxidation potential; reduction potential; structure - activity relationship; eigenproblem

Introduction

Substituting pyridine (CAS RN 110-86-1) leads to a key six-membered heterocyclic scaffold (Figure 1), structurally related to benzene and having a conjugated system of six π electrons delocalized over the ring.

$$R_2$$
 R_4
 R_5

Figure 1. Pyridine scaffold

It occurs in natural compounds, drug molecules and vitamins, being a precursor of the synthesis of larger molecules [1]. Pyridine derivatives have multiple uses. Figure 2 depicts, in increasing complexity, some pyridine derivatives.

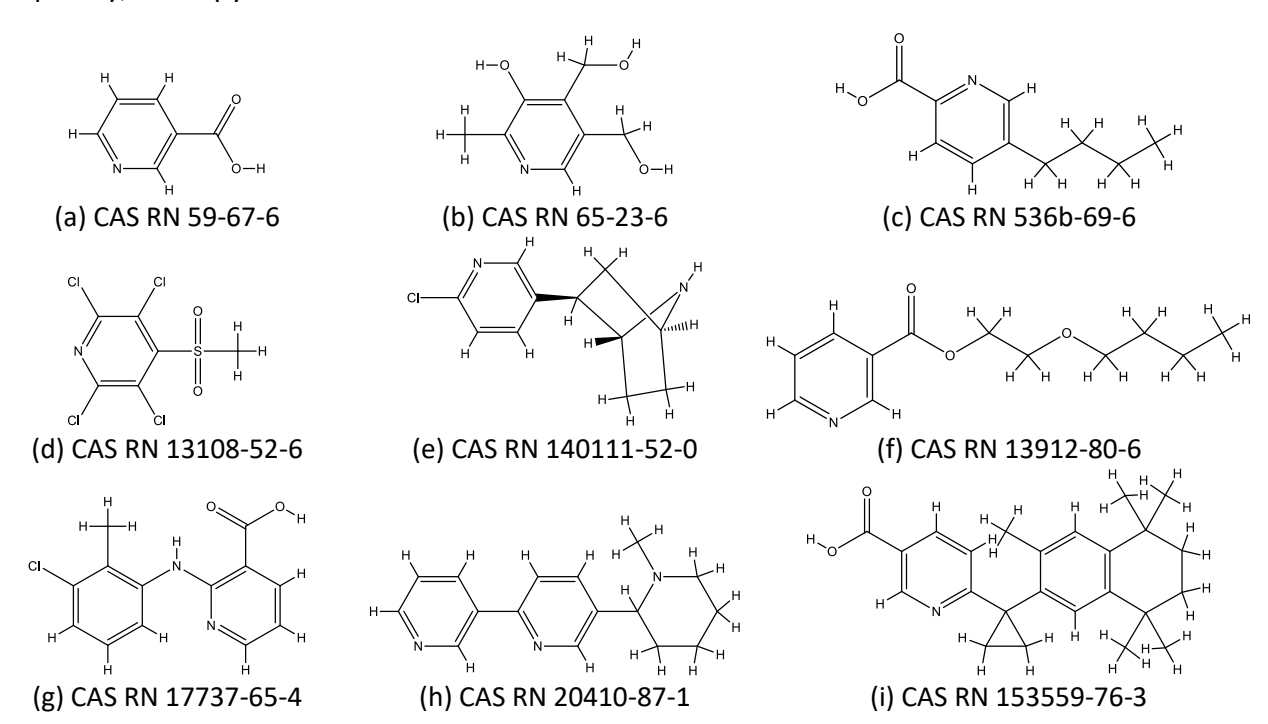


Figure 2. Some pyridine derivatives

Nicotinic acid (CID 938, C₆H₅NO₂, Figure 2a) is vitamin B3, an essential nutrient [2]; Pyridoxine (CID 1054, C₈H₁₁NO₃, Figure 2b) is vitamin B6, an important dietary supplement [3]; Fusaric acid (CID 3442, C₁₀H₁₃NO₂, Figure 2c) is a wilting agent and antibiotic [4]; Davicil (CID 61579, C₆H₃Cl₄NO₂S, Figure 2d) is a fungicide and allergen [5]; Epibatidine (CID 854023, C₁₁H₁₃ClN₂, Figure 2e) causes numbness and paralysis and may cause respiratory arrest [6]; Nicoboxil (CID 14866, C₁₂H₁₇NO₃, Figure 2f) is an analgesic effective on acute lower back pain [7]; Clonixin (CID 28718, C₁₃H₁₁ClN₂O₂, Figure 2g) is an anti-inflammatory, analgesic, antipyretic, platelet aggregation inhibitor [8]; Anabasamine (CID 161313, C₁₆H₁₉N₃, Figure 2h) is an inhibitor of acetylcholinesterase [9]; lastly, LG100268 (CID 3922, C₂₄H₂₉NO₂, Figure 2i) is a potent rexinoid [10].

As exemplified in Figure 2, the physical properties and biological activities of pyridine-containing compounds can be tuned by functional groups added to the scaffold. Of medical interest is the use of pyridine derivatives for making potent drugs. Table 1 contains some representative examples for medical use.

(cc) BY

Activity	Derivative(s)	Ref.
Antibacterial	Pyrazolo[3,4-b] Pyridine	[11]
Antibiotic	Streptonigrin	[12]
Antidiabetic	Glicaramide	[13]
Antiestrogenic	Tamoxifen analogue	[14]
Antifungal	Tetrahydroimidazo[1,2-a]pyridine	[15]
Antimicrobial	Imidazo[1,2-a]pyridine	[16]
Antimycobacterial	Isoniazid	[17]
Antineuralgic	Decumbenine B	[18]
Antioxidant	Imidazo[4,5-b]pyridines	[19]
Antiparasitic	Azamethiphos	[20]
Antispasmodic	Papaverine	[21]
Antitubercular	Ethionamide	[22]
Antitumor	Pyrrolo-pyridine benzamide	[23]
Antiviral	Indeno[1,2-b]pyridine	[24]

Table 1. Some biomedical applications of pyridines derivatives

On the other hand, if the chemical change is made into solutions, then it usually has a difference of electrical potential associated, and electrochemical methods may provide further insights about it, such as the mechanism of redox reaction, but can also be a powerful tool for the synthesis of new compounds on a gram scale [25]. The mechanisms can be treacherous and may involve models with a great deal of mathematics and numerical solving incorporated [26].

Materials and methods

Vinyl-pyridines

The 4-(azulen-1-yl)-2,6-divinylpyridine scaffold (see Figure 3) has been used to obtain and characterize six derivatives (Table 2), where experimental oxidation (E_a) and reduction (E_c) potentials were taken from [27].

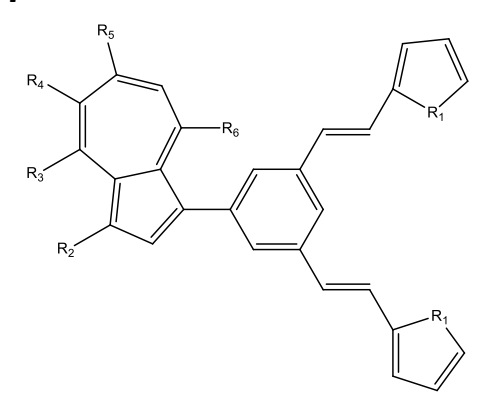


Figure 3. The 4-(azulen-1-yl)-2,6-divinylpyridine template

Table 2. Templating of 4-(azulen-1-yl)-2,6-divinylpyridine derivatives

Figure	R ₁	R_2	R_3	R ₄	R_5	R_6	Molecular formula	E_a / V	E _c / V
4a	0	CH ₃	Н	i-Pr	Н	CH₃	$C_{32}H_{29}NO_2$	0.318	-2.071
4b	0	Н	CH₃	Н	CH ₃	CH₃	$C_{30}H_{25}NO_2$	0.487	-2.084
4c	0	Н	Н	Н	Н	Н	$C_{27}H_{19}NO_2$	0.553	-1.854
4d	S	CH ₃	Н	i-Pr	Н	CH₃	$C_{32}H_{29}NS_2$	0.338	-2.065
4e	S	Н	CH₃	Н	CH₃	CH₃	$C_{30}H_{25}NS_2$	0.470	-2.090
4f	S	Н	Н	Н	Н	Н	$C_{27}H_{19}NS_2$	0.567	-1.858

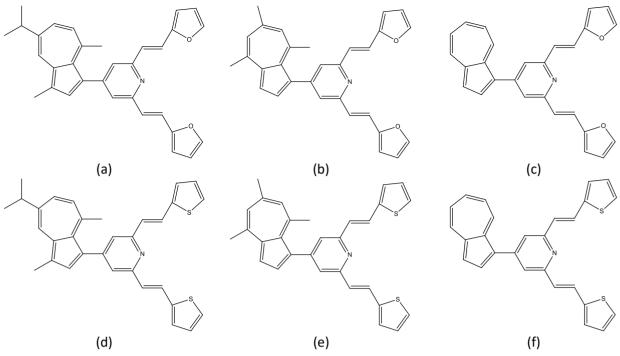


Figure 4. 4-(azulen-1-yl)-2,6-divinylpyridine derivatives

Molecular descriptors families

Physical, chemical and biological activities of chemical compounds are related to one another in a natural way since all molecules are constituted from atoms and the same forces keep the atoms together in molecules. It is thus a supported idea to construct a pool of molecular descriptors that are closely related and differ by only a choice in the construction. A series of such pools of descriptors was reported (FPIF in Chapter 7 of [28]; MDF in [29]; MDFV in [30]; SAPF in [31]; SMPI in [32], FMPI in [33]), and some notable results in the modeling of biological activities were obtained [34-37]. A thesis [38] elaborates on the issue.

For convenience, Table 3 provides the coding of the FMPI.

Table 3. Templating of FMPI

Gene		L_O				1	M_O				I	D			D_M					A_P					F_C	
Genome	- 1	R	L	Ε	F	ı	J	Ν	М	D	Ε	Р	U	G	Т	U	Α	В	С	D	Ε	F	G	М	Ν	S
Code: FMPI =	: LC	МО	IDD	ΜA	P F	C; D	esc	ripto	ors: 4	536																

The encodings from Table 3 correspond to:

- Fragmentation criteria (of the molecule) F_C with maximal fragments for $F_C = M$, with minimal fragments for $F_C = N$, and with Szeged fragments for $F_C = S$;
- Atomic property A_P with (fragment's) sum of atomic masses (in Da) for $A_P = A$, harmonic sum of atomic numbers (Z) for $A_P = B$, with sum of cardinalities for $A_P = C$, with harmonic mean of solid state density (in kg/m³) for $A_P = D$ (see page 12 in [39]), with geometrical mean of electronegativities from revised Pauling scale for $A_P = E$ (see page 16 in [39]), with average of the first ionization energy (in kJ/mol) for $A_P = F$ (see page 14 in [39]) and with power 2 mean (PM(p), p = 2) of the melting point temperatures (K) for $A_P = G$ (see page 10 in [39]);
- Distance metric D_M with (in between atoms) geometric (in nm) for $D_M = G$, topologic (in bonds) for $D_M = T$, and weighted (by bond order) topologic for $D_M = U$; interaction descriptor I_D (built with selected property and distance) with $P_{i,j}D_{i,j}$ for $I_D = E$, with $P_{i,j}/D_{i,j}$ for $I_D = U$, with $P_{i,j}$ for $I_D = D$;

(cc) BY

- Mean operation (averaging from multiple fragments of a molecule) M_O , with min. $(M_{i,j})$ for $M_O = N$, max. $(M_{i,j})$ for $M_O = M$, $\frac{1}{2}\Sigma(M_{i,j})$ for $M_O = I$, $\frac{1}{2}\Sigma(M_{i,j}M_{j,i})$ for $M_O = J$, $\frac{1}{2}\Sigma(M_{i,j}Ad_{i,j})$ for $M_O = E$, $\frac{1}{2}\Sigma(M_{i,j}M_{j,i}Ad_{i,j})$ for $M_O = F$;
- Linearization operator (adjusting the scale of the descriptor) L_O with f(x) = x for $L_O = I$, with $f(x) = x^{-1}$ for $L_O = I$, and with f(x) = I for $L_O = I$.

Extending the characteristic polynomial

The characteristic polynomial (ChP) was first expressed in the 18^{th} century in order to characterize the movement of planets [40]. Later, Hückel's method of molecular orbitals [41] was the ChP first extension approximating the treatment of π electron systems in organic molecules. An extended ChP (EChP) in a parameter (x in Equation (1)) can be associated with two particular matrices (square, of size n; A and I in Equation (1)) through the evaluation of a determinant [42]:

$$EChP(x,l,A) \leftarrow |xl-A| \tag{1}$$

In Equation (1), I should be a diagonal matrix (a matrix in which the entries outside the main diagonal are all zero), while A should be the exact opposite (a matrix from which the entries of the main diagonal were extracted). In this instance, I and A can be associated with an (edge) directed and (vertex) labeled graph with no loops. The undirected and unlabeled graph is the case that recovers the classical formula of the ChP (for instance, the one applied in [43]).

One should notice that the classical formula of the ChP is not well suited for modeling the considered congeners (Figure 4) since different chemical elements are present (nitrogen, oxygen and sulfur, in addition to carbon), while an EChP formula will take into consideration the atoms' change.

For convenience, Table 4 provides the coding of the EChP. The encodings from Table 4 correspond to (see also [42] and [44]):

Table 4. Templating of EChP

Gene		Lo					1	A							$A_{\mathcal{C}}$			C	d_0					d_1 , c	d_2 , d_3	3			
Genome	I	R	L	Α	В	С	D	Ε	F	G	Н	t	g	С	Τ	G	С	-	+	0	1	2	3	4	5	6	7	8	9
Code: EChP =	: Lo	ol _A A	c (d 0	.d₁a	2 d 3)	; De	scri	otor	s: 2	881	44																		

- Atomic identity, I_A (variable I in Equation (1)), with A = A for atomic mass divided to 294.0 (atomic mass of Oganesson), A = B for cardinality (always 1), A = C for electrostatic charges (ESP method [45]), A = D for solid-state density (in kg/m³, divided to 30000; see page 12 in [39]), A = E for electronegativity (revised Pauling, divided to 4.00, see page 16 in [39]), A = F for first ionization potential (in kJ/mol, /1312.0, see page 14 in [39]), A = G for melting point temperature (in K, divided to 3820.0, see page 10 in [39]), and A = H for the number of attached hydrogen atoms (divided to 4, the valence of a carbon atom);
- Connectivity parameter A_C (variable A in Equation (1)), with connectivity on adjacencies (classical ChP, [A] [Ad], topological adjacency matrix) for C = t, connectivity on topological distances (classical ChP, [A] [Di], topological distance matrix) for C = T, inverse of the geometrical distance for C = G, and only for adjacent atoms for C = g, inverse of the conventional bond orders for C = c, and inverse of the sum of conventional bond orders for C = C;
- Evaluation point (variable x in Equation (1)), expressed with four digits, as $\pm \overline{0.d_1d_2d_3}$, with d_1 , d_2 , $d_3 \in \{0, 1, ..., 9\}$;
- Linearization operator (adjusting the scale of the descriptor) L_0 with f(x) = x for O = I, with $f(x) = x^{-1}$ for O = R, and with f(x) = In x for O = L.

Quantitative structure-property relationship studies

For a biologist, basic units of structure define the function of all living things [46]. Since 1868, when Crum-Brown and Fraser argued about the existence of the relation between the physiological action of a substance and its composition and constitution [47], much progress has been made. Today, structure-property relationships may be considered the central dogma of chemistry [48].

A typical structure-property study (referred to as quantitative, quantitative structure-property relationship (QSPR) to express its desired outcome, a relationship expressing the property as a function of the structure) requires the collection of a series of compounds with known structure and measured properties.

Certain inclusion criteria apply. Therefore, the presence of an extreme value [49] or an outlier [50] in the series makes the derived relations unreliable, so the derivation of the structure-property relationships is desired to be obtained in the absence of those. The environment, such as water as a solute, may influence dissociations and associations of ions [51], and chemical properties [26] are also affected. Furthermore, it should be a clearly defined endpoint, an unambiguous algorithm to facilitate the reproducibility of a built model, a defined applicability domain to determine the model space associated with reliable predictions, to employ appropriate measures of goodness-of-fit, robustness and predictivity, and ideally, a mechanistic interpretation of the model in chemical structural terms [52].

One may argue that modeling of the 3D geometry is of the essence for estimating the biological activities [53], while, for physical properties, feeding the models with topologies works well (take, for instance log P [54]).

Two methods were employed: with FMPI (Table 3) and with EChP (Table 4), considering the molecules' topology and geometry. As expected, the 3D model of the computed molecular geometry depends on the selected computational model. Three models were subjected to analysis: a mechanistic one (MMFF), an in vitro one (B3LYP), and a solvent-interacting one (M06 SM8). The design of this experiment is depicted in Table 5.

Design Molecular modeling method Ref.
Raw MMFF94 [55]
In vitro B3LYP 6-311G** [56]

Table 5. Molecular methods for optimal conformations

See Table 6 in Supplementary material of [56] for the reasons of choosing B3LYP

M06 6-31G* + SM8-water

Using notation from [58], if $f = f(\underline{x}; b)$ depending on x as the random variable and having $b = (b_j)_{1 \le j \le m}$ as m population parameters) is the theoretical distribution function, then the likelihood of the sample is $f(x_1;b)f(x_2;b)...f(x_n;b)$, and it is maximum when all its derivatives vanish. The maximum likelihood estimation (MLE) method was used here.

Results and discussion

In vivo

Modeling the oxidation and reduction potential of vynil-pyridines

There are six observation points for each electrochemical property in Table 3 (n = 6), which is, at the minimum required to conduct an association analysis. However, in [59], it is pointed out that at n < 8, both false positives and false negatives may appear if the association is used to do a classification (which is not the case here). At the same time, other studies (including Google's AI) suggest at least n = 10. A sample size calculation can be employed [60], but it is useful only when sampling is available. Therefore, this deficiency must be alleviated by better testing the sample's quality.

[57]

Outlier and extreme values analysis was conducted. Normal distribution (\mathcal{N}) population parameters (μ and σ), associated with the sample for the given measurements of the properties, were obtained using MLE and are given in Table 6. One should note that the usage of MLE, unlike the method of central moments, does not reduce the number of degrees of freedom associated with the sample [61].

Table 6. Gaussian distribution population parameters of the 4-(azulen-1-yl)- 2,6-divinylpyridine derivatives by maximizing the likelihood for the samples from Table 2

Potential \Parameters	μ	σ
Oxidation (E _a)	0.4555	0.10569
Reduction (E _c)	-2.0037	0.11474

 μ : mean; σ : standard deviation; σ^2 : variance

The results in Table 6 have been used to obtain the cumulative probabilities associated with each observation. Table 7 contains these results.

Table 7. Cumulative probabilities (data in Table 2; parameters in Table 6)

i	1	2	3	4	5	6
		Oxi	dation potentials	(sorted data)		
Xi	0.318	0.3380	0.47	0.487	0.5530	0.567
pi	0.0966	0.1331	0.5546	0.6172	0.8219	0.8543
		Red	uction potentials	(sorted data)		
Xi	-2.09	-2.084	-2.071	-2.065	-1.858	-1.854
p _i	0.226	0.242	0.2788	0.2966	0.8979	0.904

 $p_i = \int_{x \le x} f(x;b) dx$ are the cumulative probabilities

A series of order statistics was calculated. Table 8 contains these results. The analysis from Table 8 reveals that there are 99.4 % worse draws of a normal (\mathcal{N}) sample than the sample of E_a values and 44.5 % worse draws of a normal (\mathcal{N}) sample than the sample of E_c values. Both probabilities (p values in boldface in Table 8) are greater than the conventional level of 5 %, so the assumption that the samples of E_a values and E_c values are drawn from normal distributions (\mathcal{N}) cannot be rejected.

Table 8. Order statistics on rejecting the hypothesis of samples normality

Statistic	CM	WU	KS	KV	AD	H1	g1	TS	FCS
k	1	2	3	4	5	6	7	8	
	Sta	tistics and a	associated _i	probabilitie	s for the se	eries of obs	erved E _a va	lues	
Value	0.36302	0.54199	0.05696	1.03250	0.05596	2.94610	0.40337	0.29957	2.44592
p_k	0.829	0.875	0.857	0.606	0.710	0.564	0.724	0.792	0.994
	Sta	tistics and o	associated	probabilitie	es for the se	eries of obs	erved E _c va	lues	
Value	0.87742	0.90647	0.15756	1.47290	0.15358	2.93340	0.40400	0.29486	8.88016
p_k	0.422	0.304	0.373	0.096	0.089	0.575	0.722	0.818	0.445

FCS: Fisher's chi-square statistic; ECS=-In $\sum_{k=1}^{8} p_k$; p_{rcs} =1-CDF_{χ^2} (FCS,8)

Modeling with raw geometries

Table 9 contains step-by-step results for modeling with SAPF and EChP using optimum geometries from the MMFF94 molecular mechanics approach. One should note that the descriptors from EChP are able to better explain both E_a and E_c electrochemical properties than the ones from FMPI (see r^2_{adj} values in Table 9).

Table 9. Staged selection of the best descriptors for linear associations with the descriptors from raw geometries

Family	Stage	For E _a dataset	For E _c dataset	Result
FMPI	1	2275	2275	Number of adapted descriptors
FMPI	2	2069	2198	Number of linearly associated descriptors
FMPI	2	LNUTGM	INEGEM	Best performing descriptors
FMPI	2	0.9894	0.9949	r ² with above descriptors
EChP	1	265411	265411	Number of adapted descriptors
EchP	2	252120	243742	Number of linearly associated descriptors
EChP	2	RDCN0940	LEGN0705	Best performing descriptors
EChP	2	0.9977	0.9996	r ² with above descriptors
	•	<u> </u>	•	·

RDCN0940 = $(EChP(-0.940; I_D, A_C))^{-1}$, LEGN0705 = $In(EChP(-0.705; I_E, A_G))$ in Equation (1) and Table 4

With MMFF94 obtained geometries, for the considered 4-(azulen-1-yl)-2,6-divinylpyridine derivatives, from the EChP selected descriptors, it can be inferred that the solid-state density is selected as the influential property for E_a acting on the inverse of the sums of conventional bond orders ($I \leftarrow I_D$ and $A \leftarrow A_C$ extending the ChP, see Equation 4.1 and Table 9). On the other hand, E_C is expressed by the electronegativity acting on the inverse of the geometrical distance ($I \leftarrow I_E$ and $A \leftarrow A_G$ extending the ChP, see Equation 4.1 and Table 9). However, FMPI, with only 1.6 % of the size of EChP, explains over 99 % of the variance in the E_a and E_c values and can be used as a first approximation level, just as MMFF is used for molecular geometry. Going further with the analysis of the FMPI selected descriptors, E_a is related to the structure on a logarithmic scale ("L" letter in LNUTGM), while E_c is related on an identity scale ("I" letter in INEGEM), both E_a and E_c were seen through FMPI perspective as localized properties (properties characterized by minimal fragments, usually single atoms - "N" as the second letter in LNUTGM and INEGEM descriptors' names, see Table 9 and Table 3 encodings), interacting like a potential (property over distance "U" as third letter in the LNUTGM name, see Table 9 and Table 3 encodings) and like a elastic force (property multiplied with the distance "E" as third letter in the INEGEM name, see Table 9 and Table 3 encodings) respectively, being affected mainly by the topology of the molecules ("T" as third letter in LNUTGM), and by the geometry ("G" as third letter in INEGEM) respectively. The differences are not at the level of the fragmentation criteria (for both E_a and E_c is minimal, "M" as last letter in LNUTGM and INEGEM), but at the elemental property relating the best (for E_a is the melting point temperature, "G" letter in LNUTGM, and for E_c is the electronegativity, "E" before last letter in INEGEM).

Table 10 lists the calculated values of the descriptors for each molecule from the set.

Table 10. Calculated values of the descriptors from raw geometries

Doscriptor	Family			Con	npounds	from Fi	gure	
Descriptor	raililly		4a	4b	4c	4d	4e	4f
LNUTGM	FMPI	Values estimating E_a	7.326	7.367	7.392	7.326	7.367	7.393
INEGEM	FMPI	Values estimating E _c	3.426	3.425	3.432	3.426	3.425	3.432
-10 ⁵ RDCN0940	EChP	Values estimating E _a	15.21	6.158	2.642	14.37	7.003	2.477
-10 ¹ LEGN0705	EChP	Values estimating E_c	3.608	3.677	2.775	3.581	3.685	2.781

10⁵ and 10¹ are scaling factors; Conventionally slope and intercept from Table 11 have units of V; then here values are adimensional

One can notice that INEGEM descriptor from FMPI does not distinguish between Oxygen and Sulphur (furan and thiophen rings in Figure 4), LNUTGM barely distinguishes between 4c and 4f, while the EChP descriptors make the distinction (see the numeric values in the 4a, 4b, 4c group vs. 4d, 4e, 4f group in Table 10). The obtained linear models expressing E_a and E_c as functions of derivatives structure are provided in Table 11.



Prope	rty Family	Model	$ ho_{\scriptscriptstyleF}$
Ea	FMPI	$y = -25.4_{\pm 3.3} + 3.51_{\pm 0.45}$ LNUTGM	3×10 ⁻⁵
Ea	EChP	$y = 0.606_{\pm 0.011} + 1.89_{\pm 0.11} \cdot 10^{-7} \cdot (\text{EChP}(-0.940_{\pm 0.0005}; I_A = D, A_C = C))^{-1}$	10 ⁻⁶
E c	FMPI	$y = -118_{\pm 10} + 33.8_{\pm 3.0}$ INEGEM	6×10 ⁻⁶
E _c	EChP	$y = -1.141_{\pm 0.022} + 0.026_{\pm 0.01} \cdot ln(EChP(-0.705_{\pm 0.0005}; I_A = E, A_C = G))$	4×10 ⁻⁸

Table 11. Models and associated statistics with the descriptors from raw geometries

 $y \sim \text{lin}(x), y \in \{E_a, E_c\}, x \in \text{FMPI or } x \in \text{EChP, lin}(x) \in \{c_0x, c_1x + c_2\}, c_0, c_1, c_2 \in \Re^*$; slope and intercept have units of V

In both instances (for E_a and E_c), with the use of the EChP approach, the precision of the models is improved.

Modeling with in vitro geometries.

Table 12 contains step-by-step results of modeling with SAPF and EChP using optimum geometries from B3LYP 6-311G** theory level.

Table 12. Staged selection of the best descriptors for linear associations with descriptors from in vitro geometries

Family	Stage	For E _a dataset	For E _c dataset	Result
FMPI	1	2218	2218	Number of adapted descriptors
FMPI	2	2049	2041	Number of linearly associated descriptors
FMPI	2	LNUTGM	LNEGCM	Best performing descriptors
FMPI	2	0.9894	0.9909	r^2_{adj} with above descriptors
EChP	1	265750	265750	Number of adapted descriptors
EChP	2	247097	238368	Number of linearly associated descriptors
EChP	2	RDCN0940	ICtN0193	Best performing descriptors
EChP	2	0.9977	0.9995	r^2_{adj} with above descriptors
			-11 1	

RDCN0940 = $(EChP(-0.940; I_A = D, A_C = C))^{-1}$, $ICtN0193 = EChP(-0.193; I_A = C, A_C = t)$ in Equation (1)

One should note that the descriptors from EChP are able to better explain both E_a and E_c electrochemical properties than the ones from FMPI (see r^2 values in Table 12).

With B3LYP obtained geometries, for the considered 4-(azulen-1-yl)-2,6-divinylpyridine derivatives, from the EChP selected descriptors, can be inferred that the solid-state density is selected as the influential property for E_a acting on the inverse of the sums of conventional bond orders ($I \leftarrow I_D$ and $A \leftarrow A_C$ extending the ChP, see Equation (1) and Table 9). On the other hand, E_C is expressed by the electrostatic charges acting on adjacencies ($I \leftarrow I_C$ and $A \leftarrow I$) extending the ChP, see Equation (1) and Table 12).

Through the perspective of FMPI selected descriptors, E_a and E_c are related with the structure on a logarithmic scale ("L" letter in LNUTGM and LNEGCM), both E_a and E_c were seen through FMPI perspective as localized properties (properties characterized by minimal fragments, usually single atoms - "N" as second letter in LNUTGM and LNEGCM descriptors names, see Table 9 and Table 3 encodings), interacting like a potential (property over distance - "U" as third letter in LNUTGM name, see Table 9 and Table 3 encodings) and like an elastic force (property multiplied with the distance - "E" as third letter in LNEGCM name, see Table 9 and Table 3 encodings) respectively, being affected mainly by the topology of the molecules ("T" as third letter in LNUTGM), and by the geometry ("G" as third letter in LNEGCM) respectively. The differences are not at the level of the fragmentation criteria (for both E_a and E_c , it is minimal, "M" as last letter in LNUTGM and INEGEM) but at the elemental property relating the best (for E_a is the melting point temperature, "G" letter in LNUTGM, and for E_c is the cardinality (size of the fragment), "C" before last letter in LNEGCM).

Table 13 lists the calculated values of the descriptors for each molecule from the set.

Descriptor Family 4a 4b 4c 4d 4e 4f **LNUTGM FMPI** Values estimating E_a 7.326 7.367 7.392 7.326 7.367 7.393 1.702 0.4064 0.4166 **LNEGCM FMPI** Values estimating E_c 0.4065 0.4170 1.708 -105RDCN0940 **EChP** Values estimating E_a 15.21 6.158 2.642 14.37 2.477 7.003 -10°ICtN0193 **EChP** Values estimating E_c 0.1515 1.054 -10.3 .1530 1.142 -10.1

Table 13. Calculated values of the descriptors from in vitro geometries

 10^5 and 10^0 are scaling factors; Conventionally slope and intercept from Table 14 have units of V; then here values are adimensional

One can notice that the INEGEM descriptor from FMPI does not distinguish between oxygen and sulphur (furan and thiophene rings in Figure 4), LNUTGM barely distinguishes between 4c and 4f, while the EChP descriptors make the distinction (see the numeric values in the 4a, 4b, 4c group vs. 4d, 4e, 4f group in Table 13).

The obtained linear models expressing E_a and E_c depending on the structure of derivatives are provided in Table 14.

Table 14. Models and associated statistics with the descriptors from in vitro geometries

Property	Family	Model	$ ho_{\scriptscriptstyle F}$
E a	FMPI	$y = -25.4_{\pm 3.3} + 3.51_{\pm 0.45} \cdot \text{LNUTGM}$	3×10 ⁻⁵
Ea	EChP	$y = 0.606_{\pm 0.011} + 1.89_{\pm 0.11} \cdot 10^{-7} \cdot (\text{EChP}(-0.940_{\pm 0.0005}; I_D, A_C))^{-1}$	10 ⁻⁶
E _c	FMPI	$y = -2.15_{\pm 0.02} + 0.17_{\pm 0.02} \cdot \text{LNEGCM}$	2×10 ⁻⁵
E _c	EChP	$y = -2.065_{\pm 0.003} - 0.0205_{\pm 0.0006} \cdot \text{EChP}(-0.193_{\pm 0.0005}; I_C, A_t)$	6×10 ⁻⁸

 $y \sim \text{lin}(x), y \in \{E_a, E_c\}, x \in \text{FMPI or } x \in \text{EChP, lin}(x) \in \{c_0x, c_1x + c_2\}, c_0, c_1, c_2 \in \Re^*; \text{ slope and intercept have units of } V$

In both instances (for E_a and E_c), with the use of the EChP approach, the precision of the models is improved.

Modeling with in vivo (water) geometries.

Table 15 contains step-by-step results of modeling with SAPF and EChP using optimum geometries from M06 6-31G* + SM8-water theory level.

Table 15. Staged selection of the best descriptors for linear associations

Family	Stage	For E _a dataset	For E _c dataset	Result		
FMPI	1	2220	2220	Number of adapted descriptors		
FMPI	2	2050	2052	Number of linearly associated descriptors		
FMPI	2	LNUTGM	RNUTCM	Best performing descriptors		
FMPI	2	0.9894	0.9923	r^2_{adj} with above descriptors		
EChP	1	265964	265964	Number of adapted descriptors		
EChP	2	251531	243044	Number of linearly associated descriptors		
EChP	2	RDCN0940	ICtN0176	Best performing descriptors		
EChP	2	0.9977	0.9994	r^2_{adj} with above descriptors		

RDCN0940 = (EChP(-0.940; I_D , A_C))-1, ICtN0176 = EChP(-0.176; I_C , A_t) in Eq. 1

One should note that the descriptors from EChP are able to explain better than the ones from FMPI, both E_a and E_c electrochemical properties (see r^2 values in Table 15).

With M06 6-31G* + SM8-water obtained geometries, for the considered 4-(azulen-1-yl)-2,6-divinyl-pyridine derivatives, the solid-state density is selected as the influential property for E_a , acting on the inverse of the sums of conventional bond orders ($I \leftarrow I_D$ and $A \leftarrow A_C$ extending the ChP, see Equation 4.1 and Table 9). On the other hand, E_C is expressed by the electrostatic charges acting on adjacencies ($I \leftarrow I_C$ and $A \leftarrow A_C$ extending the ChP, see Equation and Table 15). However, FMPI,



with only 1.6 % of the size of EChP, explains over 99 % of the variance in the E_a and E_c values and can be used as a first approximation level, just as MMFF is used for molecular geometry. Going further with the analysis of the FMPI selected descriptors, E_a is related to the structure on a logarithmic scale ("L" letter in LNUTGM) while E_c is related on a reciprocal scale ("R" letter in RNUTCM), both E_a and E_c were seen through FMPI perspective as localized properties (properties characterized by minimal fragments, usually single atoms - "N" as second letter in LNUTGM and RNUTCM descriptors names, see Table 9 and Table 3 encodings), interacting like a potential (property over distance - "U" as third letter), being affected mainly by the topology of the molecules ("T" as third letter). The differences are not at the level of the fragmentation criteria (for both E_a and E_c it is minimal, "M" as last letter in LNUTGM and RNUTCM), but at the elemental property relating the best (for E_a is the melting point temperature, "G" letter in LNUTGM, and for E_c it is the cardinality (size of the fragment), "C" before last letter in RNUTCM).

Table 16 lists the calculated values of the descriptors for each molecule from the set.

Dosarintar	Family.		Compdound						
Descriptor	Family		4a	4b	4c	4d	4e	4f	
LNUTGM	FMPI	Values estimating E _a	7.326	7.367	7.392	7.326	7.367	7.393	
RNUTCM	FMPI	Values estimating E_c	1.000	1.000	0.7143	1.000	1.000	0.7143	
-10 ⁵ RDCN0940	EChP	Values estimating E _a	15.21	6.158	2.642	14.37	7.003	2.477	
-10 ¹ ICtN0176	EChP	Values estimating E_c	-0.7679	8.225	-104.0	-0.8165	8.454	-102.4	

Table 16. Calculated values of the descriptors from in vivo geometries

10⁵ and 10¹ are scaling factors; Conventionally slope and intercept from Table 17 have units of V; then here values are adimensional

One can notice that the best descriptors from FMPI do not distinguish between 4a and 4c and between 4b and 4d, while EChP does.

The obtained linear models expressing E_a and E_c as functions of derivatives structure are provided in Table 17.

Property	Family	Model	р _ғ
Ea	FMPI	$y = -25.4_{\pm 3.3} + 3.51_{\pm 0.45} \cdot \text{LNUTGM}$	3·10 ⁻⁵
Ea	EChP	$y = 0.606_{\pm 0.011} + 1.89_{\pm 0.11} \cdot 10^{-7} \cdot (\text{EChP}(-0.940_{\pm 0.0005}; I_D, A_C))^{-1}$	1.10-6
E _c	FMPI	$y = -1.302_{\pm 0.077} - 0.775_{\pm 0.085} \cdot RNUTCM$	1.10-5
E _c	EChP	$y = -2.0697_{\pm 0.0038} + 0.0207_{\pm 0.0006} \cdot \text{EChP}(-0.176_{\pm 0.0005}; I_C, A_t)$	9·10 ⁻⁸

Table 17. Models and associated statistics

 $y \sim \text{lin}(x), y \in \{E_a, E_c\}, x \in \text{FMPI or } x \in \text{EChP, lin}(x) \in \{c_0x, c_1x + c_2\}, c_0, c_1, c_2 \in \mathfrak{R}^*$; slope and intercept have units of V

In both instances (for E_a and E_c), with the use of the EChP approach, the precision of the models is improved.

Correlated correlations analysis

Correlated correlation analysis is intended to reveal the change in the information carried by a model. The main supposition is that when changing a model, the same data was used to derive the new model, such that the association in the paired data still exists. In a classical analysis, the correlation coefficient between the experimental and the calculated is of interest. With two models: Model 1, with $y \sim \text{lin}(x_1)$, $r_{01} = r(y, x_1)$, and Model 2, with $y \sim \text{lin}(x_2)$, $r_{02} = r(y, x_2)$, the calculation of a third correlation coefficient, $r_{12} = r(x_1, x_2)$, may provide the necessary information to reveal the change in the information carried by $y \sim \text{lin}(x_1)$ model vs. $y \sim \text{lin}(x_2)$ model. Steiger [62] proposed

the use of such a test. Its approach is used here. Equation (2) has been used (conventionally positive correlations have been used, $r \leftarrow |r|$):

$$S = \left(Z_{01} - \frac{r_{01}}{2(n-1-f_1)} - Z_{01} + \frac{r_{01}}{2(n-1-f_1)}\right)\sqrt{\frac{(n-3)(1-r_a^2)^2}{2-3r_a^2 - \rho_{12}(2-4r_a^2+r_a^2\rho_{12})}}$$
 (2)

where Z_{01} , Z_{02} , and Z_{12} are the Fisher's Z transformations ($Z(r) = 0.5(\ln(1+r)/\ln(1-r))$) of the correlation coefficients (r_{01} , r_{02} , and r_{12}), $r_a = (r_{01} + r_{02})/2$, $\rho_{12} = (1-e^{2o_{12}})/(1+e^{2o_{12}})$, $o_{12} = Z_{12} - 0.5r_{12}/(n-1-f_m)$, and where f_1 , f_2 , and $f_m = (f_1 + f_2)/2$ are the degrees of freedom associated with the models. The probability is calculated from Student's t distribution with t0 degrees of freedom (t0 fre

Correlated correlation analysis is a powerful test, and when the model is changed, probabilities to gain a different model can be calculated. Thus, Table 18 contains the probabilities associated with the changes in the models.

Fixed Changing $p_t(S; 2)$ x_1 1.32 raw FMPI vs EChP E_{a} **LNUTGM RDCN0940** 0.3177 FMPI vs EChP **RNUTAN** LEGN0705 5.56 0.0309 E_{c} raw FMPI vs EChP **LNUTGM RDCN0940** 1.32 0.3177 vitro E_{a} vitro FMPI vs EChP E_{c} **LNEGCM** ICtN0193 2.52 0.1279 vivo FMPI vs EChP E_{a} **LNUTGM RDCN0940** 1.32 0.3177 vivo FMPI vs EChP E_{c} **RNUTCM** ICtN0176 2.18 0.1611 **EChP** raw vs vitro E_{c} LEGN0705 ICtN0193 0.19 0.8668 **EChP** raw vs vivo $\boldsymbol{\mathit{E}}_{c}$ LEGN0705 ICtN0176 0.35 0.7598 **EChP** ICtN0176 vitro vs vivo E_{c} ICtN0193 0.75 0.5315

Table 18. Correlated correlation analysis distinguishing between the models

Geometry - optimum from: raw - MMFF94; vitro - B3LYP 6-311G**; vivo - M06+Sm8-water 6-31G*; structure descriptors - families: fragments based - FMPI; ChP extended - EChP;

electrochemical - potentials: E_a - oxidation; E_c - reduction; S: Steiger's statistic calculated with Equaation (2)

 $(r_{01} = r(y, x_1), r_{02} = r(y, x_2), r_{12} = r(x_1, x_2)); p_t$: probability that the samples of the changing parameters to be drawn from the same population; $p_t(S; 2)$ for RNUTAN v_s LEGN0705 is statistically significant (< 5 %; in red color)

There are several models provided here (all statistically significant). Table 11 contains four models, two each for the prediction of E_a and E_c with each family of descriptors. The first two models from Table 11 are not statistically distinct one from the other (the probability of expressing the same structural information is 31.77 %, see Table 18). The last two models from Table 11 are statistically distinct from each other (the probability of expressing the same structural information is 3.09 %, see Table 18) and are the only ones in distinction, according to the results from Table 8. Table 18 supports the idea that LEGN0705 (expressing E_c from files containing raw geometries), ICtN0193 (expressing E_c from files containing in vitro geometries), and ICtN0176 (expressing E_c from files containing in vivo geometries) may essentially express the same information relating structure - reduction potential since statistical significance has not been reached to distinguish between them. Furthermore, results listed in Tables 11, 14, and 17 reveal that, when from files containing raw, in vitro and in vivo geometries, E_c is expressed with EChP descriptors, there is no change in the selection of the model best expressing the association (that is the model containing RDCN0940 molecular descriptor).

There is no coincidence in the fact that an extended family of descriptors based on the characteristic polynomial (EChP) performs better even than a fragmentation-based method (FMPI) in relating the chemical structure with electrochemical properties (here, electrode potentials of 4-(azulen-1-yl)-2,6-divinylpyridine derivatives), since the roots of the eigenproblem run deep in chemistry [63].

Conclusions

The present study has shown a significant gain in the precision of expressing the QSPR model coefficients when EChP descriptors are used instead of FMPI descriptors. At the same time, EChP descriptors have a better resolution - they distinguish between all molecules from the dataset, while the resolution of the best explanatory FMPI descriptors did not distinguish between furan and thiophene rings, and this is a positive result.

The use of higher theory-level models in geometry optimization (from MMFF94 to B3LYP and M06 + Water SM8) did not obtain the expected gain in precision and/or resolution, which is a negative result. In the case of EChP model of E_a , the selected descriptor remained the same (RDCN0940) and its values remained unchanged, while in the case of the EChP model of E_c , the selected descriptor has been changed (LEGN0705, to ICtN0193 and to ICtN0176), but not with a supplementary precision or resolution. On the contrary, a slow loss of precision was the result (r^2 from 0.9996 to 0.9995, and to 0.9994; p_F from 4×10^{-8} to 6×10^{-8} , and to 9×10^{-8}).

MMFF94 geometries proved better suited to express the E_a and E_c potentials from structure than the selected B3LYP and M06 upper theory level approaches. This is a positive result regarding MMFF94 (one should notice that this is the default theory level in providing geometries of molecules by PubChem), and perhaps supports the idea that selecting and using upper theory levels in molecular geometry optimization requires much more care and suitability analysis than expected.

Correlated correlation analysis revealed an important fact. The EChP best model (containing the LEGN0705 descriptor) is statistically distinct (evidence in Table 18), and better (evidence in Table 9) than the FMPI best model (containing the INEGEM descriptor) in expressing structure-property relationship for E_c .

Abbreviations

CAS RN: Chemical Abstracts service registry number

PubChem: http://pubchem.ncbi.nlm.nih.gov/ - chemical compounds search engine and database

online available

CID: PubChem compound identifier
FPIF: fragmental property index family
MDF: molecular descriptors family
SAPF: structural atomic property family
SMPI: Szeged matrix property indices

FMPI: fragmental matrix property indices

i-Pr: isopropyl

ChP: characteristic polynomial

EChP: extended characteristic polynomial

QSPR: quantitative structure-property relationships

DFT: density functional theory

MLE: Maximum Likelihood Estimation
CDF: cumulative distribution function
PDF: probability density function

r: Pearson's correlation coefficient [64]

 r^2_{adi} : adjusted (from r) determination coefficient

 χ^2 : chi square distribution; $PDF_{\chi^2}(x; k) = x^{k/2-1}e^{-x/2}2^{-k/2}(\Gamma(k-2))^{-1}$ \mathcal{N} : normal distribution; $PDF_{\mathcal{N}}(x; \mu, \sigma) = \sigma^{-1}(2\pi)^{-1/2}e^{-(x-\mu)^2/(2\sigma^2)}$ t: Student's t distribution [65]; PDF_t(x; v) = $(\pi v)^{-1/2} \Gamma\left(\frac{v+1}{2}\right) \left(\Gamma\left(\frac{v}{2}\right)\right)^{-1} \left(1 + \frac{x^2}{v}\right)^{-\frac{v+1}{2}}$

 \mathfrak{R}^* : the set of real non-null numbers ($R^* = R \setminus 0$)

MMFF: Merk molecular force field; MMFF94: 1994 version of MMFF [55]

B3LYP: Becke 3 parameter hybrid exchange functional and Lee-Yang-Par correlation functional

[66, 67]

M06: Minnesota density functional introduced in [68]

SM8: solvation model applicable to all solvents introduced in [69]

 p_F : probability of a wrong model, calculated from Fisher's F distribution [70]

Appendix: Generated data and data analysis

Compounds studied in the paper are not available in the PubChem database. We drawn their 2D structures and build up their 3D models. Chemdraw files are available at:

http://lori.academicdirect.ro/data/C19H15N-d/Data Chemdraw.zip.

The 3D geometries were build (with HyperChem v.8 Add H & Model Build menu option and module), exported and optimized into Spartan (v. 14) software (using three theory levels, as described in the paper). Further, structure-activity relationship search was conducted using two approaches (FMPI and EChP), as described in the paper.

The subsequent analysis is available at:

http://lori.academicdirect.ro/data/C19H15N-d/Results MMFF94.zip (the analysis with MMFF94 optimum geometries, big data file, over 30 MB),

http://lori.academicdirect.ro/data/C19H15N-d/Results MMFF94.zip (the analysis with B3LYP optimum geometries, big data file, over 40 MB), and

http://lori.academicdirect.ro/data/C19H15N-d/Results MMFF94.zip (the analysis with M06 optimum geometries, big data file, about 40 MB).

For the reproducibility of the results, the programs are provided as well. Thus, the programs supporting the study with EChP are available at:

http://lori.academicdirect.ro/data/C19H15N-d/Programs EChP.zip,

the programs supporting the study with FMPI are available at:

http://lori.academicdirect.ro/data/C19H15N-d/Programs FMPI.zip

and the programs filtering statistically the structure-based descriptors are available at:

http://lori.academicdirect.ro/data/C19H15N-d/Programs LR.zip.

One need to prepare (inspect and modify by necessity) the properties asc file listing the experimental properties in order to use the methodology on other dataset. Then the programs should be called in order.

References

- [1] M. D. Hill. Recent strategies for the synthesis of pyridine derivatives. *Chemistry A European Journal* **16** (2010) 12052-12062. http://doi.org/10.1002/chem.201001100
- [2] C. Pang, Y. Xu, X. Ma, S. Li, S. Zhou, H. Tian, M. Wang, B. Han. Design, synthesis, and evaluation of novel arecoline-linked amino acid derivatives for insecticidal and antifungal activities, *Scientific Reports* **14** (2024). http://doi.org/10.1038/s41598-024-60053-2
- [3] M. Feng, B. Gao, D. Ruiz, L. R. Garcia, Q. Sun. Bacterial vitamin b6 is required for postembryonic development in c. elegans, *Communications Biology* 7 (2024). http://doi.org/10.1038/s42003-024-05992-2
- [4] M. Kang, H. Wang, C. Chen, R. Suo, J. Sun, Q. Yue, Y. Liu. Analytical strategies based on untargeted and targeted metabolomics for the accurate authentication of organic milk from jersey and yak, *Food Chemistry X* **19** (2023). http://doi.org/10.1016/j.fochx.2023.100786



- [5] H. Svensen. Synthesis and Functionalization of 3-Nitropyridines. Ph.D. thesis, Norwegian University of Science and Technology, Trondheim, Norwey (2001). http://hdl.handle.net/11250/244442
- [6] Changgeng Qian, Tongchuan Li, T. Shen, L. Libertine-Garahan, J. Eckman, T. Biftu, S. Ip. Epibatidine is a nicotinic analgesic, *European Journal of Pharmacology* **250** (1993) R13-R14. https://doi.org/10.1016/0014-2999(93)90043-H
- [7] A. Steiner, J. M. Mayer, B. Testa. Nicotinate esters: their binding to and hydrolysis by human serum albumin, *Journal of Pharmacy and Pharmacology* **44** (1992) 745-749. http://doi.org/10.1111/j.2042-7158.1992.tb05512.x
- [8] J. S. Finch, T. J. DeKornfeld. Clonixin: A clinical evaluation of a new oral analgesic, The Journal of Clinical Pharmacology and New Drugs 11 (1971) 371-377. http://doi.org/10.1177/009127007101100508
- [9] Z. Tilyabaev, A. A. Abduvakhabov. Alkaloids of anabasis aphylla and their cholinergic activities, *Chemistry of Natural Compounds* 34 (1998) 295-297. https://doi.org/10.1007/BF02282405
- [10] A. S. Leal, K. Zydeck, S. Carapellucci, L. A. Reich, D. Zhang, J. A. Moerland, M. B. Sporn, K. T. Liby. Retinoid x receptor agonist lg100268 modulates the immune microenvironment in preclinical breast cancer models, *NPJ Breast Cancer* **5** (2019) 39. http://doi.org/10.1038/s41523-019-0135-5
- [11] E. M. A. Antibacterial evaluation and molecular properties of pyrazolo[3,4-b]pyridines and thieno[2,3-b] pyridines, *Journal of Applied Pharmaceutical Science* **11** (2021) 118-124. https://doi.org/10.7324/JAPS.2021.110614
- [12] T. J. Donohoe, C. R. Jones, A. F. Kornahrens, L. C. A. Barbosa, L. J. Walport, M. R. Tatton, M. O'Hagan, A. H. Rathi, D. B. Baker. Total synthesis of the antitumor antibiotic (±)-streptonigrin: First- and second-generation routes for de novo pyridine formation using ring-closing metathesis, *Journal of Organic Chemistry* **78** (2013) 12338-12350. https://doi.org/10.1021/jo402388f
- [13] H. Hoehn, I. Polacek, E. Schulze. Potential antidiabetic agents. pyrazolo[3,4-b]pyridines, *Journal of Medicinal Chemistry* **16** (1973) 1340-1346.

 https://doi.org/10.1021/jm00270a006
- [14] M. Croisy-Delcey, A. Croisy, D. Carrez, C. Huel, A. Chiaroni, P. Ducrot, E. Bisagni, L. Jin, G. Leclercq. Diphenyl quinolines and isoquinolines: synthesis and primary biological evaluation, *Bioorganic & Medicinal Chemistry* **8** (2000) 2629-2641. https://doi.org/10.1016/S0968-0896(00)00194-2
- [15] A. Özdemir, G. Turan-Zitouni, Z. Asım Kaplancıklı, G. İşcan, S. Khan, F. Demirci. Synthesis and the selective antifungal activity of 5,6,7,8-tetrahydroimidazo[1,2-a]pyridine derivatives, European Journal of Medicinal Chemistry 45 (2010) 2080-2084. https://doi.org/10.1016/j.ejmech.2009.12.023
- [16] M. Koudad, S. Dadou, F. Abrigach, A. E. Aatiaoui, M. Azzouzi, A. Oussaid, N. Benchat, M. Allali, K. Karrouchi. Synthesis and antimicrobial, antioxidant, ADME-T, and molecular docking studies of imidazo[1,2-a]pyridine derivatives, *Russian Journal of Organic Chemistry* **59** (2023) 1237-1247. https://doi.org/10.1134/S1070428023070163
- [17] P. Makam, R. Kankanala, A. Prakash, T. Kannan. 2-(2-hydrazinyl)thiazole derivatives: Design, synthesis and in vitro antimycobacterial studies, *European Journal of Medicinal Chemistry* **69** (2013) 564-576. https://doi.org/10.1016/j.ejmech.2013.08.054
- [18] V. Reddy, A. S. Jadhav, R. Vijaya Anand. A room-temperature protocol to access isoquinolines through ag(i) catalysed annulation of o-(1-alkynyl)arylaldehydes and ketones with nh4oac: elaboration to berberine and palmatine, *Organic and Biomolecular Chemistry* 13 (2015) 3732-3741. http://dx.doi.org/10.1039/C4OB02641A

- [19] I. Boček Pavlinac, L. Persoons, D. Daelemans, K. Starčević, R. Vianello, M. Hranjec. Novel acrylonitrile derived imidazo[4,5-b]pyridines as antioxidants and potent antiproliferative agents for pancreatic adenocarcinoma, *International Journal of Biological Macromolecules* **266** (2024) 131239. https://doi.org/10.1016/j.ijbiomac.2024.131239
- [20] S. Marın, R. Ibarra, M. Medina, P. Jansen. Sensitivity of caligus rogercresseyi (boxshall and bravo 2000) to pyrethroids and azamethiphos measured using bioassay tests—a large scale spatial study, *Preventive Veterinary Medicine* **122** (2015) 33-41. https://doi.org/10.1016/j.prevetmed.2015.09.017
- [21] M. Ferrari. Effects of papaverine on smooth muscle and their mechanisms, Pharmacological Research Communications 6 (1974) 97-115. https://doi.org/10.1016/S0031-6989(74)80018-4
- [22] M. Imran. Ethionamide and prothionamide based coumarinyl-thiazole derivatives: Synthesis, antitubercular activity, toxicity investigations and molecular docking studies, *Pharmaceutical Chemistry Journal* **56** (2022) 1215-1225. https://doi.org/10.1007/s11094-022-02782-0
- [23] J. Zhang, J. Dai, X. Lan, Y. Zhao, F. Yang, H. Zhang, S. Tang, G. Liang, X. Wang, Q. Tang. Synthesis, bioevaluation and molecular dynamics of pyrrolo-pyridine benzamide derivatives as potential antitumor agents in vitro and in vivo, *European Journal of Medicinal Chemistry* 233 (2022) 114215. https://doi.org/10.1016/j.ejmech.2022.114215
- [24] R. M. Kassab, M. H. Ibrahim, A. Rushdi, S. J. Almehmadi, M. E. Zaki, S. A. Al-Hussain, Z. A. Muhammad, T. A. Farghaly. Comprehensive study for synthesis, antiviral activity, docking and ADME study for the new fluorinated hydrazonal and indeno[1,2-b]pyridine derivatives, *J. Mol. Struct.* **1305** (2024) 137752. https://doi.org/10.1016/j.molstruc.2024.137752
- [25] B. Turovska, I. Goba, A. Lielpetere, V. Glezer. Electrochemistry of pyridine derivatives, *Journal of Solid State Electrochemistry* **27** (2023) 1717-1729. https://doi.org/10.1007/s10008-023-05425-w
- [26] L. Jäntschi. Modelling of acids and bases revisited, *Studia Universitatis Babes-Bolyai, Seria Chemia* **67** (2022) 73-92. https://doi.org/10.24193/subbchem.2022.4.05
- [27] O. Ciocirlan, E.-M. Ungureanu, A.-A. Vasile (Corbei), A. Stefaniu. Properties assessment by quantum mechanical calculations for azulenes substituted with thiophen- or furan-vinyl-pyridine, *Symmetry* **14** (2022) 354. https://doi.org/10.3390/sym14020354
- [28] M. V. Diudea, I. Gutman, L. Jäntschi, *Molecular Topology,* Nova Science Publishers, Huntington, N.Y., 2001, p. 197-232. http://lccn.loc.gov/2001031282
- [29] L. Jäntschi. MDF a new qsar/qspr molecular descriptors family, *Leonardo Journal of Sciences* **3** (2004) 68-85. http://ljs.academicdirect.org/A04/68 85.pdf
- [30] S. D. Bolboacă, L. Jäntschi. Predictivity approach for quantitative structure-property models. Application for blood-brain barrier permeation of diverse drug-like compounds, *International Journal of Molecular Sciences* **12** (2011) 4348-4364. https://doi.org/10.3390/ijms12074348
- [31] R. E. Sestras, L. Jäntschi, S. D. Bolboacă. Quantum mechanics study on a series of steroids relating separation with structure, *JPC Journal of Planar Chromatography Modern TLC* **25** (2012) 528-533. https://doi.org/10.1556/JPC.25.2012.6.7
- [32] S. D. Bolboacă, L. Jäntschi. Nanoquantitative structure-property relationship modeling on C₄₂ fullerene isomers, *Journal of Chemistry* **2016** (2016) 1791756. https://doi.org/10.1155/2016/1791756
- [33] L. Jäntschi, S. D. Bolboacă. Chapter 15: Families of molecular descriptors, in New Frontiers in Nanochemistry: Concepts, Theories, and Trends. Volume 1: Structural Nanochemistry, M. V. Putz, Ed., Apple Academic Press, Burlington, Canada, 2020, p. 143-169. https://doi.org/10.1201/9780429022937



- [34] D. M. Opris, M. V. Diudea. Peptide property modeling by cluj indices, SAR and QSAR in Environmental Research 12 (2001) 159-179. https://doi.org/10.1080/10629360108035377
- [35] L. Jäntschi, S.-D. Bolboacă. Results from the use of molecular descriptors family on structure property/activity relationships, *International Journal of Molecular Sciences* **8** (2007) 189-203. https://doi.org/10.3390/i8030189
- [36] D. Janežič, L. Jäntschi, D. S. Bolboacă. Sugars and sweeteners: Structure, properties and in silico modeling, *Current Medicinal Chemistry* **27** (2020) 5-22. https://doi.org/10.2174/0929867325666180926144401
- [37] D. Bálint, L. Jäntschi. Comparison of molecular geometry optimization methods based on molecular descriptors, *Mathematics* **9** (2021) 2855. https://doi.org/10.3390/math9222855
- [38] L. Jäntschi. *Structure vs. Property: Models and Algorithms* (Babeş-Bolyai University: Habilitation Thesis) (2012). http://lori.academicdirect.org/doctoral/advisor/HabilThesis InShort.pdf
- [39] L. Jäntschi. *General Chemistry* (3rd ed.), AcademicDirect, Cluj-Napoca, Romania, 2013, pp. 436. http://ph.academicdirect.org/GCC v3.pdf
- [40] L. Jäntschi. Eigenproblem basics and algorithms, *Symmetry* **15** (2023) 2046. https://doi.org/10.3390/sym15112046
- [41] E. Hückel. Quantentheoretische beiträge zum benzolproblem, Zeitschrift für Physik **70** (1931) 204-286. https://doi.org/10.1007/BF01339530
- [42] D.-M. Joiţa, L. Jäntschi. Extending the characteristic polynomial for characterization of C₂₀ fullerene congeners, *Mathematics* **5** (2017) 84. http://doi.org/10.3390/math5040084
- [43] S. D. Bolboacă, L. Jäntschi. How good can the characteristic polynomial be for correlations?, International Journal of Molecular Sciences 8 (2007) 335-345. https://doi.org/10.3390/i8040335
- [44] L. Jäntschi. Structure-property relationships for solubility of monosaccharides, *Applied Water Science* **9** (2019) 38. https://doi.org/10.1007/s13201-019-0912-1
- [45] T. A. Halgren. Merck molecular force field. II. MMFF94 van der waals and electrostatic parameters for intermolecular interactions, *Journal of Computational Chemistry* **17** (1996) 520-552. <a href="https://doi.org/10.1002/(SICI)1096-987X(199604)17:5/6<520::AID-JCC2>3.0.CO;2-W">https://doi.org/10.1002/(SICI)1096-987X(199604)17:5/6<520::AID-JCC2>3.0.CO;2-W
- [46] S. E. Brownell, S. Freeman, M. P. Wenderoth, A. J. Crowe. Biocore guide: A tool for interpreting the core concepts of vision and change for biology majors, *CBE-Life Sciences Education* **13** (2014) 200-211. https://doi.org/10.1187/cbe.13-12-0233
- [47] A. C. Brown, T. R. Fraser. V.—On the connection between chemical constitution and physiological action. Part. i.-On the physiological action of the salts of the ammonium bases, derived from strychnia, brucia, thebaia, codeia, morphia, and nicotia, *Transactions of the Royal Society of Edinburgh* **25** (1868) 151-203
- [48] R. S. DeFever, H. Bruce, G. Bhattacharyya. Mental rolodexing: Senior chemistry majors' understanding of chemical and physical properties, *Journal of Chemical Education* **92** (2015) 415-426. https://doi.org/10.1021/ed500360g
- [49] L. Jäntschi. Detecting extreme values with order statistics in samples from continuous distributions, *Mathematics* **8** (2020) 216. https://doi.org/10.3390/math8020216
- [50] L. Jäntschi. A test detecting the outliers for continuous distributions based on the cumulative distribution function of the data being tested, *Symmetry* **11** (2019) 835. https://doi.org/10.3390/sym11060835
- [51] L. L. Pruteanu, L. Jäntschi, M. L. Unguresan, S. D. Bolboacă. Models of monovalent ions dissolved in water, *Studia Universitatis Babes-Bolyai, Seria Chemia* **61** (2016) 151-163. https://chem.ubbcluj.ro/~studiachemia/issues/chemia2016 1/15Pruteanu etal 151 162. pdf

- [52] A. Cherkasov, E. N. Muratov, D. Fourches, A. Varnek, I. I. Baskin, M. Cronin, J. Dear-den, P. Gramatica, Y. C. Martin, R. Todeschini, V. Consonni, V. E. Kuz'min, R. Cramer, R. Benigni, C. Yang, J. Rathman, L. Terfloth, J. Gasteiger, A. Richard, A. Tropsha. Qsar modeling: Where have you been? Where are you going to?, *Journal of Medicinal Chemistry* 57 (2014) 4977-5010. https://doi.org/10.1021/jm4004285
- [53] J. Verma, V. M. Khedkar, E. C. Coutinho. 3d-qsar in drug design a review, *Current Topics in Medicinal Chemistry* **10** (2010) 95-115. https://doi.org/10.2174/156802610790232260
- [54] J. Huuskonen. Estimation of aqueous solubility for a diverse set of organic compounds based on molecular topology, *Journal of Chemical Information and Computer Sciences* **40** (2000) 773-777. https://doi.org/10.1021/ci9901338
- [55] T. A. Halgren. Merck molecular force field. i. Basis, form, scope, parame-terization, and performance of MMFF94, *Journal of Computational Chemistry* **17** (1996) 490-519. https://doi.org/10.1002/(SICI)1096-987X(199604)17:5/6<490::AID-JCC1>3.0.CO;2-P
- [56] L. Jäntschi. Triple crossed 3 C₂₆ cyclic cumulene catenane, *Fullerenes, Nanotubes and Carbon Nanostructures* **32** (2024) 1-15. https://doi.org/10.1080/1536383X.2024.2354721
- [57] S. N. Roese, J. D. Heintz, C. B. Uzat, A. J. Schmidt, G. V. Margulis, S. J. Sabatino, A. S. Paluch. Assessment of the sm12, sm8, and smd solvation models for predicting limiting activity coefficients at 298.15 K, *Processes* 8 (2020) 623. https://doi.org/10.3390/pr8050623
- [58] R. A. Fisher. On an absolute criterion for fitting frequency curves, *Messenger of Mathematics* **41** (1912) 155-160. https://hdl.handle.net/2440/15165
- [59] D. G. Jenkins, P. F. Quintana-Ascencio. A solution to minimum sample size for regressions, *PloS One* **15** (2020) e0229345. https://doi.org/10.1371/journal.pone. 0229345
- [60] K. Kelley, S. E. Maxwell. Sample size for multiple regression: Obtaining regression coefficients that are accurate, not simply significant, *Psychological Methods* **8** (2003) 305-321. https://doi.org/10.1037/1082-989X.8.3.305
- [61] L. Jäntschi. Distribution fitting 1. Parameters estimation under assumption of agreement between observation and model, *Bulletin of University of Agricultural Sciences and Veterinary Medicine Cluj-Napoca. Horticulture* **66** (2009) 684-690. https://doi.org/10.48550/arXiv.0907.2829
- [62] J. H. Steiger. Tests for comparing elements of a correlation matrix, *Psychological Bulletin* **87** (1980) 245-251. https://doi.org/10.1037/0033-2909.87.2.245
- [63] L. Jäntschi. The eigenproblem translated for alignment of molecules, *Symmetry* **11** (2019) 1027. https://doi.org/10.3390/sym11081027
- [64] K. Pearson. X. On the criterion that a given system of deviations from the probable in the case of a correlated system of variables is such that it can be reasonably supposed to have arisen from random sampling, *The Philosophical Magazine series 5* **50** (1900) 157-175. https://doi.org/10.1080/14786440009463897
- [65] W. S. Gosset. The probable error of a mean, *Biometrika* **6** (1908) 1-25. https://doi.org/10.1093/biomet/6.1.1
- [66] A. D. Becke. Density-functional thermochemistry. III. The role of exact exchange, *The Journal of Chemical Physics* **98** (1993) 5648-5652. http://doi.org/10.1063/1.464913
- [67] P. J. Stephens, F. J. Devlin, C. S. Ashvar, C. F. Chabalowski, M. J. Frisch. Theoretical calculation of vibrational circular dichroism spectra, *Faraday Discussions* **99** (1994) 103-119. http://doi.org/10.1039/FD9949900103
- [68] Y. Zhao, D. G. Truhlar. The M06 suite of density functionals for main group thermochemistry, thermochemical kinetics, noncovalent interactions, excited states, and transition elements: two new functionals and systematic testing of four M06-class functionals and 12 other functionals, *Theoretical Chemistry Accounts* **120** (2008) 215-241. https://doi.org/10.1007/s00214-007-0310-x



- [69] A. V. Marenich, R. M. Olson, C. P. Kelly, C. J. Cramer, D. G. Truhlar. Self-consistent reaction field model for aqueous and nonaqueous solutions based on accurate polarized partial charges, *Journal of Chemical Theory and Computation* 3 (2007) 2011-2033. https://doi.org/10.1021/ct7001418
- [70] R. A. Fisher. On a distribution yielding the error functions of several well known statistics, Proceedings of the International Mathematical Congress. Toronto 2 (1924) 805-813. https://hdl.handle.net/2440/ 15183

©2024 by the authors; licensee IAPC, Zagreb, Croatia. This article is an open-access article distributed under the terms and conditions of the Creative Commons Attribution license (https://creativecommons.org/licenses/by/4.0/)



Open Access:: ISSN 1847-9286 www.jESE-online.org

Original scientific paper

Electrochemical impedance spectroscopy measurements on time-variant systems: the case of the Volmer-Heyrovský corrosion reaction. Part I: theoretical description

Nicolas Murer[⊠], Jean-Paul Diard and Bogdan Petrescu

BioLogic, 4 Rue de Vaucanson, 38170 Seyssinet-Pariset, France

Corresponding authors: [™]nicolas.murer@biologic.net; Tel.: +33-476-986-831

Received: August 13, 2024; Accepted: September 10, 2024; Published: September 20, 2024

Abstract

One of the theoretical requirements of electrochemical impedance spectroscopy measurements is that the studied system should not vary with time. Unfortunately, this is rarely the case of physical systems. In the literature, quite a few methods exist to check and correct a posteriori the effect of time-variance, allowing the use of conventional equivalent circuit models to fit and interpret the data. We suggest a different approach where, for a given electrochemical mechanism and specific experimental conditions, assuming stationarity during each measurement, a time- and frequency-dependent expression of the Faradaic impedance is derived from the kinetic equations. The case of a potential relaxation at zero current following an anodic steady-state polarization is considered for a system where a Volmer-Heyrovský corrosion mechanism is supposed to take place.

Keywords

EIS; adsorption; non-stationarity; Faradaic; relaxation; potential decay

Introduction

Electrochemical impedance spectroscopy (EIS) consists of studying the frequency response of an electrochemical system submitted to an electrical modulation, leading to the determination of its transfer function, the involved electrochemical reaction mechanisms and the values of the associated parameters.

Classically, the Faradaic impedance of a given electrochemical reaction is obtained by linearizing the expression of the Faradaic current using a Taylor series limited to the first order in the neighbourhood of a stationary operating point [1].

This means that the electrical perturbation applied to the system where the given electrochemical reaction takes place should not entail a nonlinear response.

This also means that the system should be stationary. As already noted elsewhere [2,3], it is considered by the authors that stationarity includes two sub-notions, namely steady-state and time-

invariance. Steady-state is the state of a system whose response has reached a permanent regime and time-invariance is the state of a system whose parameters do not change with time.

A complete description, or at least a study, of an electrochemical reaction mechanism requires impedance measurements performed at various stationary points along the stationary *I vs. E* curve. This is generally performed by collecting impedance data after the system has settled at a constant potential.

However, in some systems, the waiting time to reach the stationary state can be considered too long, for example, in the case of an insertion battery or a corroding sample. Besides, strictly speaking, no stationary state can really be defined for those systems as the voltage measured across a battery and the mixed potential measured on a corroding electrode are not equilibrium thermodynamic potentials, so the stationary approach is not deemed relevant.

A third example is given by Harrington *et al.* [4] in the case of methanol oxidation, whose irreversible adsorption reaction leads to a full-coverage state, whichever the applied potential.

In such cases, there is no other way than to perform impedance measurements in non-stationary conditions, which goes against the requirement mentioned above unless some precautions, assumptions and corrections are taken and applied.

Stoynov *et al.* [5] were the first to knowingly perform EIS measurements on a time-variant system, namely a lead-acid battery under discharge. By choosing a low enough current and keeping the measurement time short, it was assumed that the system would not change very much during the measurement and was considered to be in a quasi-stationary state (QSS).

This is also the approach chosen by researchers combining voltammetry and EIS in techniques such as potentiodynamic DEIS [6], ac voltammetry [4,7] and dynamic EIS [8-11].

The QSS or "frozen-state" assumption allows to use, at each frequency, conventional equivalent circuit models (ECM) and Faradaic impedance expressions to interpret the data, but the values of the parameters could differ from one frequency to another.

Stoynov was, to our knowledge, the first to simulate how non-stationarity can deform impedance Nyquist diagrams and lead to wrong interpretations [12]. Stoynov *et al.* introduced an elegant correction method named 4D impedance based on the cubic spline interpolation of successive measurements, allowing for a reconstruction of instantaneous impedance spectra, which can then be interpreted using conventional ECM with time-independent parameters [13,14]. More recently, the same authors introduced the rotating Fourier transform [15,16] to directly analyze non-stationary impedance measurements without the need for correction.

Belgian researchers developed a methodology using odd multisine signals (Odd random phase multisine EIS (ORP-EIS)) to quantify the non-linearity and non-stationarity of nonlinear time-varying systems [17,18]. Non-linearities appear as additional signals at non-excited frequencies and time-variance appears as "jumps" or "skirts" at excited frequencies.

The different types of Fourier spectra of the response to sinusoidal excitation are presented in the white paper "Systems and EIS quality indicators" [19]. Non-linearity and non-stationarity indicators are also presented.

This non-exhaustive review gives an idea of the various approaches used to tackle the problem of non-stationarity. Other approaches and more details can be found in two recent review articles by Hallemans *et al.* [20] and Szekeres *et al.* [21].

These approaches all rely on a mathematical treatment of the EIS measurement, using the point of view of the physicist or the signal analyst. The point of view of the electrochemist was adopted

here, starting from the electrochemical reaction and the kinetic equations to the calculation of a time and frequency-dependent Faradaic impedance expression.

The first attempt originated from a paper by the team of Srinivasan Ramanathan, who illustrated the effect of time-variance by performing impedance measurements on a rotating disk electrode (RDE) immersed in an electrolyte containing equimolar concentrations of the classical ferri- and ferro cyanide ions and being diluted [22]. In our recent paper [2], the time and frequency-dependent Faradaic impedance expression was calculated for such a redox reaction where the concentration changes with time and showed that it was possible to use this expression to fit experimental impedance data obtained on the time-variant system directly.

The topic of linear systems with variable parameters was also studied by Berthier [23], who recalled that the main issue is that, unless the system is simple, there is no mathematical method available to solve the differential Equation (1) describing the system, which is:

$$a_n(t)y^n(t) + a_{n-1}(t)y^{n-1}(t) + \dots + a_1(t)y'(t) + a_0(t)y(t) = b_m(t)u^m(t) + \dots + b_0(t)u(t)$$
(1)

where $y^n(t)$ represents the n^{th} time derivative of the function y(t), $u^m(t)$ represents the m^{th} time derivative of the function u(t), y(t) is the time response of the considered system and u(t) the time input with a(t) and b(t) their respective time-dependent coefficients.

Baddi [24] tried to explain the passivation mechanism of iron in an acidic medium as well as the time evolution of the potential during depassivation, also named the Flade experiment. In this experiment, a constant stationary passivation current or potential is applied to the system, the current is then shut and the potential returns to its equilibrium value. This potential time evolution is calculated by using the various kinetic equations derived from the chosen depassivation mechanism. The non-stationary impedance expression is written using the stationary, voltage-dependent impedance expression and replacing the stationary voltage with the time-dependent voltage.

Harrington [25] calculated open-circuit potential decay transients following the interruption of a polarizing current for a three-step hydrogen evolution reaction (HER) and related to the evolution of the surface coverage rate of the adsorbed species.

In this paper, we chose to follow a similar approach using as a case study the Volmer-Heyrovský corrosion reaction [26-28, and references therein]. This first part shows the theoretical derivation, while the second part, to be published, will present experimental data.

Mechanism and kinetic equations

The notation and the equations of the Handbook of Electrochemical Impedance Spectroscopy Corrosion Reactions Library [29] were used.

Each reaction is considered non-inversible or irreversible, meaning the forward reaction rate is much larger than the backward reaction rate.

The two-step hydrogen reduction reaction is considered, Equations (2) and (3):

$$H^{+} + s + e^{-} \xrightarrow{\kappa_{a}} H, s \tag{2}$$

$$H^{+} + H, s + e^{-} \xrightarrow{\kappa_{a}} H_{2} + s \tag{3}$$

with s an adsorption site, K_{r1} in s^{-1} and K_{r2} in s^{-1} the reaction rate constants. H,s denotes an adsorbed H atom (or H adatom).

The oxidation reaction is the corrosion of the metal atom at the surface of the electrode M.s, which produces, in our case, for the sake of simplicity, a divalent species M^{2+} (Equation (4)):

$$M,s \xrightarrow{\kappa_{o3}} M^{2+} + s + 2e^{-}$$
 (4)

with K_{03} / s⁻¹ the reaction rate constant.

M,s and s are considered to be equivalent, which means the oxidation reaction does not lead to a variation in surface concentration of the adsorption sites.

The Langmuir isotherm is used, which means that there are no interactions between the adsorbed species, which are assumed to form an ideal condensed phase.

There is no mass transport limitation, which means that interfacial concentrations $H^+(0,t)$ are equal to bulk concentrations H^{+*} , or that interfacial concentration variations are negligible, Equation (5):

$$H^+(0,t) \approx H^{+*} \tag{5}$$

This allows us to write Equations (6) to (8):

$$K_{r1}(t) = k_{r1} \exp(-\alpha_{r1} f_N E(t)), k_{r1} = k'_{r1} H^{+*}$$
 (6)

$$K_{r_2}(t) = k_{r_2} \exp(-\alpha_{r_2} f_N E(t)), k_{r_1} = k'_{r_1} H^{+*}$$
 (7)

$$K_{o3}(t) = k_{o3} \exp(2\alpha_{o3} f_{N} E(t))$$
(8)

with $f_N = F/(RT)$, F = 96485 C mol⁻¹ the Faraday constant, R = 8.32 J mol⁻¹ K⁻¹ the perfect gas constant, T in K the absolute temperature, k_{r1} in s⁻¹ and k_{r2} in s⁻¹ the transfer kinetic parameters of the reduction reactions, k_{o3} in s⁻¹ the transfer kinetic parameter of the oxidation reaction, a_{r1} , a_{r2} and a_{o3} the symmetry factors of the reduction reactions and the oxidation reaction, respectively, E(t) in V the electrode potential and the time t in s.

With $\theta_s(t) + \theta_H(t) = 1$, the reaction rates v(t) in mol cm⁻² s⁻¹ of each step of the overall reaction can be written by Equations (9) to (11):

$$v_{1}(t) = K_{r1}(t)\Gamma(1-\theta_{H}(t)) \tag{9}$$

$$v_2(t) = K_{r2}(t)\Gamma(\theta_H(t)) \tag{10}$$

$$v_{3}(t) = K_{o3}(t) \Gamma \left(1 - \theta_{H}(t) \right) \tag{11}$$

with Γ in mol cm⁻² the total number of adsorption sites per unit area, θ_H the covering factor of the adatom H, which is defined as H/ Γ , where H in mol cm⁻² is the surface concentration of the adatom H.

The Equation (12) of the evolution of the coverage rate $d\theta_H(t)/dt$ writes¹:

$$d\theta_{H}(t)/dt = v_{H}(t)/\Gamma = -d\theta_{s}(t)/dt$$
(12)

with (Equation (13))

$$v_{H}(t) = v_{1}(t) - v_{2}(t) = -v_{s}(t)$$
 (13)

Even though the rate of the oxidation reaction $v_3(t)$ does depend on the coverage rate of the adsorbed species, it does not affect its evolution as it consumes and produces an adsorption site. Hence, $v_H(t)$ and $v_S(t)$ depend solely on $v_1(t)$ and $v_2(t)$.

Finally, the Faradaic current $i_f(t)$ writes, Equation (14):

$$i_{\rm f}(t) = -F(v_1(t) + v_2(t) - 2v_3(t))$$
 (14)

Steady-state kinetic equations

Steady-state equations are needed to determine the initial and final values of the potential, current and coverage rates.

¹ Please note the use of straight d for the derivatives as the coverage rates only depend on time.

Writing that at steady-state, Equation (15)

$$d\theta_{H}(t)/dt = d\theta_{s}(t)/dt = 0 \tag{15},$$

we have been using Equationss (9-15), to obtain Equations (16) and (17):

$$\theta_{H}(E) = K_{r1}(E) / (K_{r1}(E) + K_{r2}(E))$$
(16)

$$i_{f}(E) = \left(2F\Gamma(K_{o3}(E)K_{r2}(E)-K_{r1}(E)K_{r2}(E))\right)/(K_{r1}(E)+K_{r2}(E))$$
(17)

where E is the time-independent or steady-state potential.

The corrosion potential (Equation (18)), defined as the potential for a zero Faradaic current ($i_f(E_{corr}) = 0$), can be calculated from Equations (6) to (8) and (17):

$$E_{corr} = \ln(k_{c1}/k_{o3})/((\alpha_{c1} + 2\alpha_{o3})f_{N})$$
(18)

Figure 1 below shows the steady-state Faradaic current and the coverage rate of the adatom H as a function of the steady-state potential E for a given set of kinetic parameters (shown in the caption of Fig. 1) and using Equations (6) to (8), (16) and (17). Two points are shown in Fig. 1, the initial steady-state potential E_i and the corrosion potential E_{corr} with their corresponding Faradaic current and coverage rates.

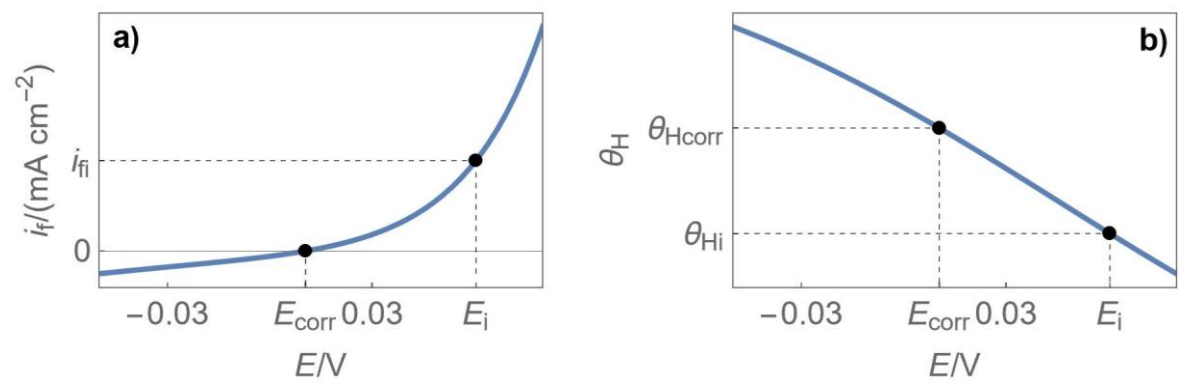


Figure 1. Steady-state evolution of (a) the current and (b) the coverage rate of the adatom H as a function of the steady-state potential E. The parameters used to plot these curves are: $\Gamma = 10^{-9}$ mol cm⁻², $f_N = 38.9 \ V^{-1}$, $\alpha_{r1} = 0.7$, $\alpha_{r2} = 0.3$, $\alpha_{o3} = 0.5$, $k_{r1} = 2 \ s^{-1}$, $k_{r2} = k_{o3} = 1 \ s^{-1}$, $E_i = E_{corr} + 0.05 \ V$

Steady-state Faradaic impedance

The steady-state Faradaic impedance of the Volmer-Heyrovský corrosion reaction Z_f is a sum of three terms [1,29], a charge transfer resistance and two surface concentration impedances related to adsorbed species s and H, Equation (19):

$$Z_{f}(p) = R_{ct} + Z_{s}(p) + Z_{H}(p)$$

$$(19)$$

with $p = 2\pi i f$, f in Hz the frequency and i the imaginary number such that $i^2 = -1$.

The details of the calculation will not be given here, but we have Equation (20):

$$Z_{f}(p) = \frac{\left(K_{r_{2}} + K_{r_{1}}\right)\left(K_{r_{2}} + K_{r_{1}} + p\right)}{f_{N}F\Gamma K_{r_{2}}\left(\alpha_{r_{1}}K_{r_{1}}\left(2\left(K_{o_{3}} + K_{r_{2}}\right) + p\right) + 4\alpha_{o_{3}}K_{o_{3}}\left(K_{r_{2}} + K_{r_{1}} + p\right) + \alpha_{r_{2}}K_{r_{1}}\left(-2K_{o_{3}} + 2K_{r_{1}} + p\right)\right)}$$
(20)

The structure of this impedance is equivalent to that of an R + C/R circuit. To obtain the electrode impedance Z(p) we need to add in parallel the double-layer capacitance $C_{\rm dl}$. The ECM that can be used to model the impedance of the Volmer-Heyrovský corrosion reaction is shown in Fig. 2 with Equations (21) to (23):

$$R_{\rm ct} = \frac{K_{\rm r2} + K_{\rm r1}}{f_N F \Gamma K_{\rm r2} \left(4\alpha_{\rm o3} K_{\rm o3} + (\alpha_{\rm r1} + \alpha_{\rm r2}) K_{\rm r1}\right)} \tag{21}$$

$$R_{\theta} = \frac{K_{r1} \left(K_{r1} - K_{r2} - 2K_{o3} \right) R_{ct} \left(\alpha_{r1} - \alpha_{r2} \right)}{4\alpha_{o3} K_{o3} \left(K_{r2} + K_{r1} \right) + 2K_{o3} K_{r1} \left(\alpha_{r1} - \alpha_{r2} \right) + 2K_{r1} \left(\alpha_{r1} K_{r2} + \alpha_{r2} K_{r1} \right)}$$
(22)

$$C_{\theta} = \frac{4\alpha_{o3}K_{o3} + \alpha_{r1}K_{r1} + \alpha_{r2}K_{r2}}{K_{r1}(K_{r1} - K_{r2} - 2K_{o3})R_{ct}(\alpha_{r1} - \alpha_{r2})}$$
(23)

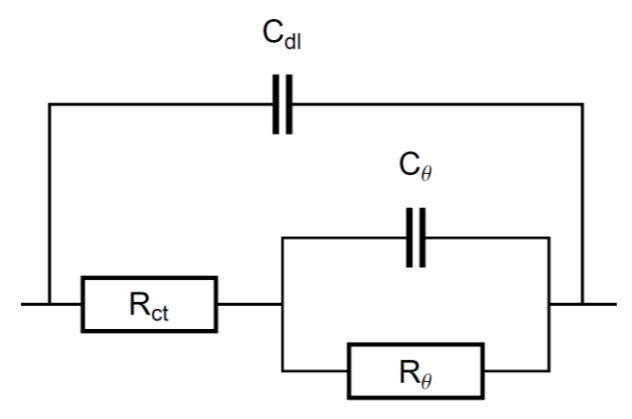


Figure 2. ECM used to model the Volmer-Heyrovský corrosion reaction

Finally, we have Equation (24):

$$Z(p) = Z_f(p) / (1 + Z_f(p)C_{d}p)$$
(24)

with Equation (25)

$$Z_{f}(p) = R_{ct} + R_{\theta} / (1 + R_{\theta}C_{\theta}p)$$
(25)

Please note that the reaction rate constants K_{r1} , K_{r2} and K_{o3} are dependent on the potential according to Equations (6) to (8). Figure 3 shows two Nyquist diagrams of the impedance Z at two different potential values, E_i and the corrosion potential E_{corr} , using the same set of parameters as in Figure 1 and C_{dl} = 10 μ F.

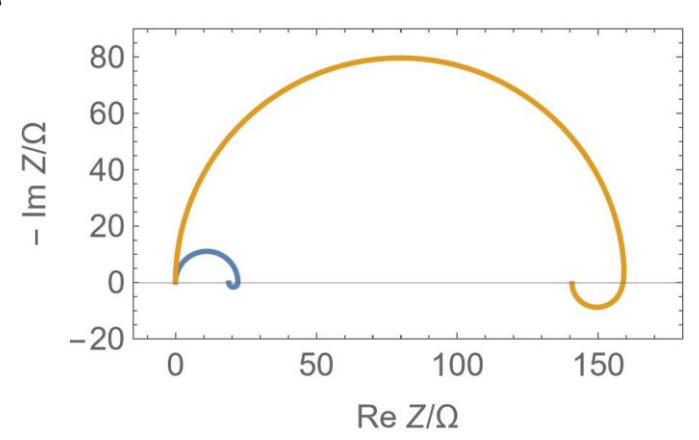


Figure 3. Nyquist diagrams of the steady-state impedance Z at two different steady-state potentials E_i (blue curve) and E_{corr} (orange curve). The parameters used to plot these curves are: $\Gamma = 10^{-9}$ mol cm⁻², $f_N = 38.9 \ V^{-1}$, $F = 96485 \ C \ mol^{-1}$, $\alpha_{r1} = 0.7$, $\alpha_{r2} = 0.3$, $a_{o3} = 0.5$, $k_{r1} = 2 \ s^{-1}$, $k_{r2} = k_{o3} = 1 \ s^{-1}$, $E_i = E_{corr} + 0.05 \ V$, $C_{di} = 10 \ \mu F$, $f_{min} = 100 \ mHz$, $f_{max} = 10 \ kHz$

Simulated experiment and objectives of this work

As depicted in Fig. 4a, it consists of a simple current interrupt experiment: the electrochemical system, described by the Volmer-Heyrovský corrosion mechanism, is polarized at an anodic

potential E_i and a current i. At t = 0, the circuit is open and the potential decays to its other steady-state value, namely E_{corr} . The first objective of this work is to calculate the transient, non-stationary evolution of the potential between E_i and E_{corr} , as illustrated in Figure 4b.

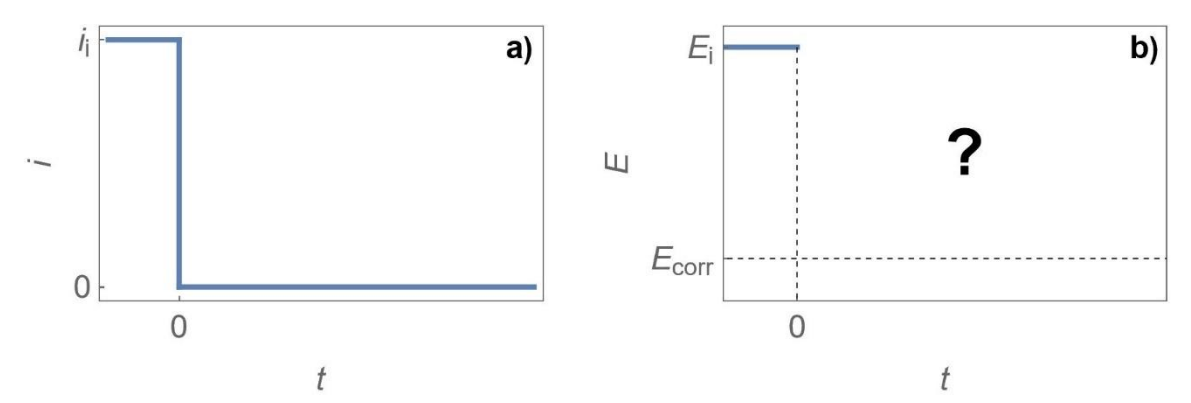


Figure 4. Illustrative depiction of a) the current interrupt experiment and b) the unknown potential time evolution during its relaxation

If the non-stationary time evolution of the potential E(t) is known, it means the time evolution of the various reaction rate constants $K_{r1}(t)$, $K_{r2}(t)$ and $K_{o3}(t)$ can also be known.

A time- and frequency-dependent impedance $Z_f(p,t)$ can then be defined using the expression of the steady-state Faradaic impedance (Equation 20), which makes the reaction rate constant and time-dependent. Similarly, $R_{ct}(t)$, $R_{\theta}(t)$, $C_{\theta}(t)$ and Z(p,t) can be defined and calculated by Equation (26).

$$Z(p,t) = Z_{f}(p,t)/(1 + Z_{f}(p,t)C_{dl}p)$$
(26)

The second objective of this work is to show the non-stationary impedance Nyquist diagrams during the relaxation of the system using Eq. (26).

E(t) and $\theta_H(t)$ determination

Assuming zero Faradaic current

Our system of equations to solve is composed of an ordinary differential equation (ODE), which is Equation (12). Using Equations (9), (10) and (13) it writes Equation (27):

$$d\theta_{H}(t)/dt = K_{r1}(E(t))(1-\theta_{H}(t))-K_{r2}(E(t))(\theta_{H}(t))$$
(27)

During the relaxation experiment, it was first assumed that $i_f = 0$. We then used Equations (9) to (11) and (14) to obtain Equation (28).

$$K_{r_1}(E(t))(1-\theta_H(t))-K_{r_2}(E(t))(\theta_H(t))-2K_{o3}(E(t))(1-\theta_H(t))=0$$
(28)

Equations (27) and (28) constitute a differential algebraic system of equations (DAE), and which can be solved numerically.

The general form of a DAEs is presented by Equations (29) and (30):

$$dx/dt = f(x(t),y(t),t)$$
(29)

$$0 = g(x(t), y(t), t)$$
(30)

In our case, $x(t) = \theta_H(t)$ and y(t) = E(t).

The NDSolve function in Mathematica 14 [30] was used to solve this DAE. The steady-state values were set as initial conditions $E(0) = E_i$ and $\theta_H(0) = \theta_H(E(0))$. The same parameters as in Figures 1 and

3 are used. In this case, the NDSolve function can only give a solution, an interpolation function defined for a given period (in our case 50 s), if the initial condition on the potential is not respected. This is shown in Figure 5: the initial potential is not E_{corr} + 0.05 V, which means the assumption needs to be revised. However, $\theta_H(t)$ seems to be correct.

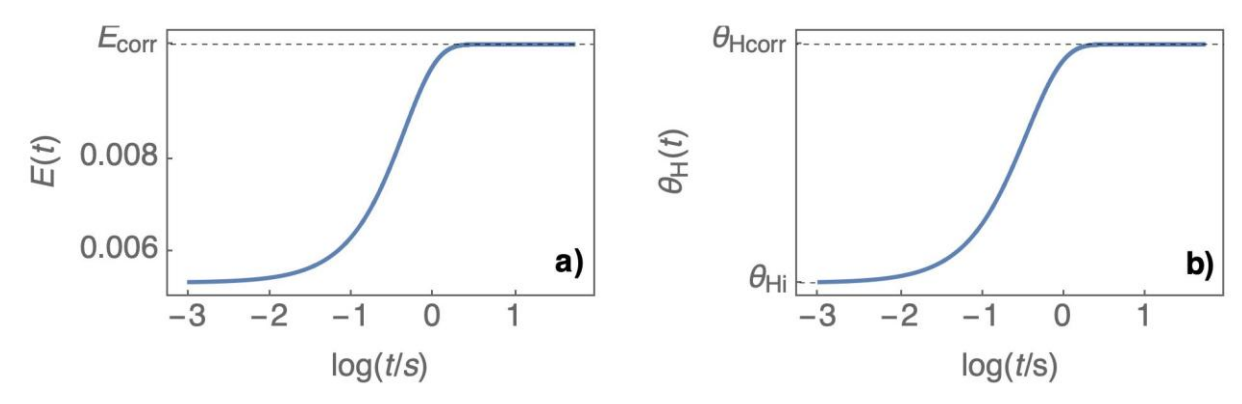


Figure 5. Simulated (a) E(t) and (b) θ_H (t) assuming a zero Faradaic current during the relaxation. The solution for E(t) is wrong as it does not fulfill the initial condition E(0) = E_i

Assuming zero total current

As the total current is the sum of the capacitive and the Faradaic current, assuming a zero total current during the relaxation leads to $i_c = -i_f$ and Equation (31):

$$C_{dl}\left(\frac{dE(t)}{dt}\right) = F\Gamma\left(K_{r1}(E(t))(1-\theta_{H}(t))-K_{r2}(E(t))(\theta_{H}(t))-2K_{o3}(E(t))(1-\theta_{H}(t))\right)$$
(31)

which is an ODE and constitutes with Equation (27) an ODE system. Using again the NDSolve function in Mathematica, two interpolation functions are obtained that both fulfil the initial conditions (Fig. 6). It is noteworthy that the transient open circuit voltage (OCV) goes below the long-time limit E_{corr} and that $\theta_H(t)$ has the same shape as in Figure 5.

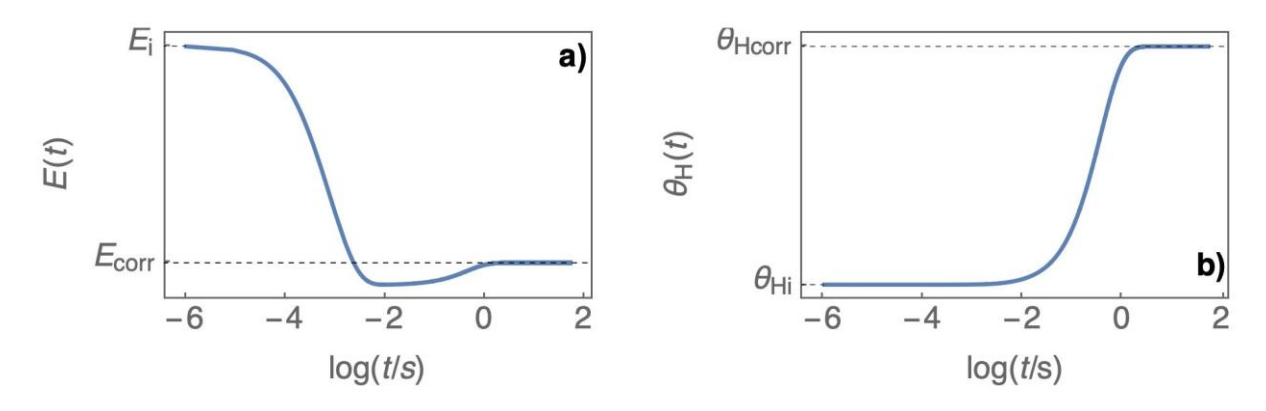
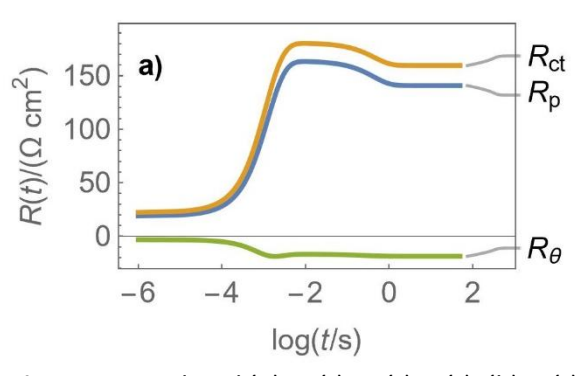


Figure 6. Simulated (a) E(t) and (b) $\theta_H(t)$ assuming a total zero current during the relaxation. Both solutions fulfill the initial conditions $\underline{E}(0) = E_i$ and $\theta_H(0) = \theta_H(E(0))$

Time-variant impedance

Now that E(t) is known, $K_{r1}(t)$, $K_{r2}(t)$ and $K_{o3}(t)$, or more explicitly $K_{r1}(E(t))$, $K_{r2}(E(t))$ and $K_{o3}(E(t))$ can be caluclated. Introducing time in Equations (21) to (23) $R_{ct}(t)$, $R_{o}(t)$, the polarization resistance $R_{p}(t) = R_{o}(t) + R_{ct}(t)$ and $C_{o}(t)$ (Figure 7) can be computed.

One can note in Fig. 7 the negative signs of $R_{\theta}(t)$ and $C_{\theta}(t)$, which was to be expected considering the shape of the impedance diagram shown in Fig. 3, with a low-frequency inductive loop, typical of a Volmer-Heyrovský mechanism [1].



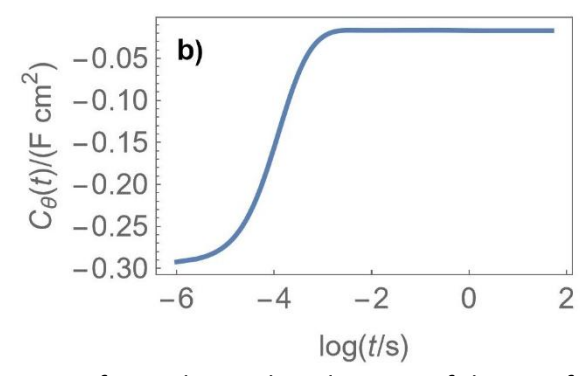


Figure 7. Simulated (a) $R_{ct}(t)$, $R_{\theta}(t)$ $R_{\rho}(t)$, (b) $C_{\theta}(t)$ as a function of time during the relaxation of the OCV for the Volmer-Heyrovský corrosion mechanism using parameters shown in Figure 3

To be able to plot the time-variant impedance measurement, for which, as a reminder, it is considered that the system is steady-state at each point, the time corresponding to each applied frequency needs to be calculated, considering that each frequency is applied sequentially from the highest to the lowest, which means we need to account for the accumulation of time.

Equation (32) was used:

$$t_{k} = \sum_{j=1}^{k} N(1 + pw)T_{j}$$
(32)

with t_k the time corresponding to the k^{th} frequency, N the number of periods chosen for the measurement and pw a percentage of the period used as a waiting time to reduce inter-frequency transient regime, and T_i is the period of the j^{th} frequency.

A list of k frequencies f_k and the corresponding list of periods $T_k = 1/f_k$ were considered. Equation (32) above gives the list of the corresponding times t_k .

Table 1 gives values for 6 frequencies over a decade.

Rank k f/Hz T/s t/s 100 0.01 0.022 1 2 68.13 0.015 0.054 3 46.42 0.022 0.102 4 31.62 0.032 0.171 5 21.54 0.046 0.273 6 14.68 0.068 0.423 7 10.00 0.10 0.643

Table 1. Numerical examples for the formula given in Equation (32) using N = 2 and pw = 10 %

Here we will try to discuss an inherent contradiction of our approach: the assumption that the system is stationary at each measurement allows us to use a Faradaic impedance expression derived from this assumption shown in Equation (20), in which a time-dependent term is "injected", here E(t). In our previous paper [2], this assumption could be verified by low values of non-stationary distortion (NSD) indicators. However, if our system is stationary at each measurement point, how can it be non-stationary over the whole measurement?

The way we exit this contradiction is by saying that the negligibility of the time-variance at each point does not hold if all points are considered. In other terms, the small error conceded at each point accumulates over the whole spectrum and becomes non-negligible. This, of course, favors the use of input modulation made of simultaneous frequencies, as mentioned in the introduction. This is exactly what is referred to by quasi-stationarity: the system has a certain "level" of non-

stationarity that can, within certain conditions, be considered negligible. The same approach is used to consider linearity: an electrochemical system is nonlinear, but it is assumed that below a certain level, its non-linearity can be considered negligible.

In case the system is "strongly" non-stationary due to a fast scan rate, for example, in a DEIS experiment or a large charge/discharge current for a battery, our approach is not valid.

Similarly, if the system behaviour is strongly nonlinear due to a very large amplitude, the measured impedance cannot be analysed in terms of "classical" Faradaic impedance or with "classical" ECMs.

Figure 8 shows the Nyquist diagram of the time-variant electrode impedance corresponding to Equations 26 and 25 (Z_{TV} , black dots) and the two steady-state impedance graphs already shown in Figure 3 ($Z_{St, t=0}$, $Z_{St, t=tmax}$), which correspond to the impedance of the system in its initial and final state. The graph distortion is visible at mid-frequencies and corresponds to the change of parameters shown in Fig. 7.

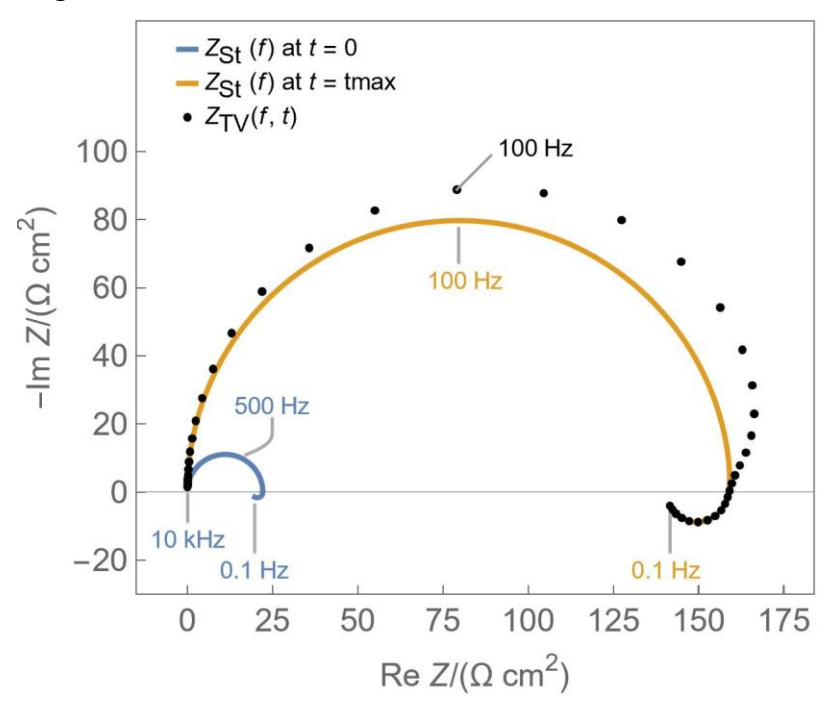


Figure 8. Simulated Nyquist diagram of the time-variant impedance expression shown in Equation (26) in black dots. The orange and blue curves correspond to the two steady-state impedance graphs already shown in Figure 3, which correspond to the initial and final state of the system. The parameters are the same as in Figure 3, with 6 points per decade, N = 2 and pw = 10%.

The larger semi-circle at mid-frequencies corresponds to $C_{\rm dl}/R_{\rm ct}$ and the low-frequency inductive loop to C_{θ}/R_{θ} . The kinetic constants and potential ranges were chosen to show a low-frequency inductive loop. For the Volmer-Heyrovský mechanism, low-frequency capacitive behaviour is expected at cathodic potentials [1,29]. The timescales shown in Figures 5 to 7 depend on the kinetic parameters chosen.

The second part of the paper will deal with the experimental validation of this theoretical approach.

Conclusion

Basically, in the literature, two approaches were adopted to deal with non-stationary impedance measurements: either a mathematical treatment and correction of the data or an adjustment of the input modulation such that the system is considered in a quasi-stationary state across the whole frequency range.

In this part of the paper, an approach based on the electrochemical reaction that takes place in the system under study was presented, for which the non-stationarity of the system can be calculated and accounted for in the Faradaic impedance expression.

The transient potential and coverage rate evolution during the relaxation of a system where the Volmer-Heyrovský corrosion mechanism takes place were calculated by solving a system of two ODEs written using the kinetic equations governing the reaction and assuming, during the relaxation, that the sum of the capacitive and Faradaic currents is equal to zero.

Stationary impedance expressions for this mechanism were given and converted into time and frequency-dependent expressions using the potential evolution previously determined. It was then possible to simulate the time and frequency-dependent impedance that would be measured during the relaxation. This approach removes the need to estimate or correct non-stationarity of the system, as it is "embedded" in the Faradaic impedance expression.

References

- [1] J.-P. Diard, B. Le Gorrec, C. Montella, *Cinétique électrochimique*, Hermann, Paris, France, 1996 (in French). ISBN-13: 978-2705662950
- [2] N. Murer, J.-P. Diard, B. Petrescu, Time-variance in EIS measurements: the simple case of dilution, *Journal of The Electrochemical Society* **170** (2023) 126506-126517. https://doi.org/10.1149/1945-7111/ad1632
- [3] N. Murer, J.-P. Diard, B. Petrescu, The effects of time-variance on impedance measurements: examples of a corroding electrode and a battery cell, *Journal of Electrochemical Science and Engineering* **10** (2020) 127-140. https://
- [4] /doi.org/10.5599/jese.725
- [5] F. Seland, R. Tunold, D. A. Harrington, Impedance study of methanol oxidation on platinum electrodes, *Electrochimica Acta* **51** (2006) 3827-3840 https://doi.org/10.1016/j.electacta.2005.10.050
- [6] M. Keddam, Z. Stoynov, H. Takenouti, Impedance measurement on Pb/H₂SO₄ batteries, Journal of Applied Electrochemistry **7** (1977) 539-544 https://doi.org/10.1007/BF00616766
- [7] G. A. Ragoisha, A. S. Bondarenko, *Chemical problems of the development of new materials and technologies, Potentiodynamic electrochemical impedance spectroscopy*, Minsk, Belarus, 2003, 138-150 https://elib.bsu.by/bitstream/123456789/21022/1/pages%20from%20Sbornik-END9.pdf
- [8] A. M. Bond, N. W. Duffy, D. M. Elton, B. D. Fleming, Characterization of nonlinear background components in voltammetry by use of large amplitude periodic perturbations and Fourier transform analysis, *Analytical Chemistry* 81 (2009) 8801-8808 https://doi.org/10.1021/ac901318r
- [9] J. Schiewe, J. Házì, V. A. Vicente-Beckett, A. M. Bond, A unified approach to trace analysis and evaluation of electrode kinetics with fast Fourier transform electrochemical instrumentation, *Journal of Electroanalytical Chemistry* **451** (1998) 129-138 https://doi.org/10.1016/S0022-0728(97)00579-2
- [10] M. J. Walters, J. E. Garland, C. M. Pettit, D. S. Zimmerman, D.R. Marr, D. Roy, Weak adsorption of anions on gold: measurement of partial charge transfer using Fast Fourier Transform electrochemical impedance spectroscopy, *Journal of Electroanalytical Chemistry* 499 (2001) 48-60 https://doi.org/10.1016/S0022-0728(00)00468-X
- [11] T. Pajkossy, M. Urs Ceblin, G. Mészáros, Dynamic electrochemical impedance spectroscopy for the charge transfer rate measurement of the ferro/ferricyanide redox couple on gold, *Journal of Electroanalytical Chemistry* **899** (2021) 115655-115663 https://doi.org/10.1016/j.jelechem.2021.115655

- [12] K. Darowicki, J. Orlikowski, G. Lentka, Instantaneous impedance spectra of a non-stationary model electrical system, *Journal of Electroanalytical Chemistry* 486 (2000) 106-110 https://doi.org/10.1016/S0022-0728(00)00111-X
- [13] Z. Stoynov, B. Savova, Instrumental error in impedance measurements of non-steady-state systems, *Journal of Electroanalytical Chemistry* **112** (1980) 157-161 https://doi.org/10.1016/S0022-0728(80)80016-7
- [14] Z. B. Stoynov, B. S. Savova-Stoynov, Impedance study of non-stationary systems: four-dimensional analysis, *Journal of Electroanalytical Chemistry* 183 (1985) 133-144 https://doi.org/10.1016/0368-1874(85)85486-1
- [15] Z. Stoynov, B. Savova-Stoynov, Non-stationary impedance analysis of lead/acid batteries, Journal of Power Sources **30** (1990) 275-285 https://doi.org/10.1016/0378-7753(93)80085-4
- [16] Z. B. Stoynov, Rotating Fourier transform: new mathematical basis for non-stationary impedance analysis, *Electrochimica Acta* 37 (1992) 2357-2359 https://doi.org/10.1016/0013-4686(92)85132-5
- [17] Z. B. Stoynov, Non-stationary impedance spectroscopy, *Electrochimica Acta* **38** (1993) 1919-1922 https://doi.org/10.1016/0013-4686(93)80315-Q
- [18] E. Van Gheem, R. Pintelon, J. Vereecken, J. Schoukens, A. Hubin, P. Verboven, O. Blajiev, Electrochemical impedance spectroscopy in the presence of nonlinear distortions and non-stationary behaviour Part I: theory and validation, *Electrochimica Acta* **49** (2004) 4753-4762 https://doi.org/10.1016/j.electacta.2004.05.039
- [19] E. Van Gheem, R. Pintelon, A. Hubin, J. Schoukens, P. Verboven, O. Blajiev, J. Vereecken, Electrochemical impedance spectroscopy in the presence of nonlinear distortions and non-stationary behaviour Part II. Application to crystallographic pitting corrosion of aluminium, *Electrochimica Acta* **51** (2006) 1443-1452 https://doi.org/10.1016/j.electacta.2005.02.096
- [20] Systems and EIS quality indicators, https://www.biologic.net/wp-content/uploads/2019/08/systems-and-eis-quality-indicators-wp2-electrochemistry.pdf (26/7/2024)
- [21] N. Hallemans, D. Howey, A. Battistel, N. F. Saniee, F. Scarpioni, B. Wouters, F. La Mantia, A. Hubin, W. D. Widanage, J. Lataire, Electrochemical impedance spectroscopy beyond linearity and stationarity, *Electrochimica Acta* **466** (2023) 142939-142962. https://doi.org/10.1016/j.electacta.2023.142939
- [22] K. J. Szekeres, S. Vesztergom, M. Ujvári, G. G. Láng, Methods for the determination of valid impedance spectra in non-stationary electrochemical systems: concepts and techniques of practical importance, *ChemElectroChem* 8 (2021) 1233-1250 https://doi.org/10.1002/celc.202100093
- [23] R. Pachimatla, M. Thomas, S. Rahman OC, R. Srinivasan, Analysis of instabilities in electrochemical systems using nonlinear electrochemical impedance spectroscopy, *Journal of The Electrochemical Society* **166** (2019) H304-H312 https://doi.org/10.1149/2.0571908jes
- [24] F. Berthier, Spectroscopie d'impédance et vitesse de corrosion : application au cas de la corrosion du zinc en milieu NaCl 3 %, Ph. D. Thesis, INP Grenoble (1989) (in French)
- [25] M. Baddi, Vérification d'un modèle réactionnel de passivation du fer en milieu acide, Ph. D. Thesis, Université Pierre et Marie Curie Paris VI (1977) (in French)
- [26] D. A. Harrington, B. E. Conway, Kinetic theory of the open-circuit potential decay method for evaluation of adsorbed intermediates: Analysis for the case of the H₂ evolution reaction, *Journal of Electroanalytical Chemistry* 221 (1987) 1-21 https://doi.org/10.1016/0022-0728(87)80242-5
- [27] J. Heyrovský, A theory of overpotential, *Recueil des travaux chimiques des Pays-Bas* **46** (1927) 582-586 https://doi.org/10.1002/recl.19270460805

- [28] T. Erdey-Grúz, M. Volmer, Zur Theorie der Wasserstoff Überspannung, Zeitschrift für Physikalische Chemie **150A** (1930) 203-213 (in German) https://doi.org/10.1515/zpch-1930-15020
- [29] J. Huang, Correlation between electrocatalytic activity and impedance shape: A Theoretical Analysis, PRX Energy 3 (2024) 023001. http://doi.org/10.1103/PRXEnergy.3.023001
- [30] J.-P. Diard, C. Montella, N. Murer. *Handbook of electrochemical impedance spectroscopy corrosion reactions library,* Self-published, Seyssinet-Pariset, France, 2012, p. 11 https://doi.org/10.13140/RG.2.2.16871.87206
- [31] Wolfram Language & System Documentation Center https://reference.wolfram.com/language/ref/NDSolve.html (31/7/2024)

©2024 by the authors; licensee IAPC, Zagreb, Croatia. This article is an open-access article distributed under the terms and conditions of the Creative Commons Attribution license (https://creativecommons.org/licenses/by/4.0/)